Kinking Nonlinear Elastic Solids: Theory and Experiments

A thesis

Submitted to the Faculty

of

Drexel University

by

Aiguo Zhou

in partial fulfillment of the

requirement for the degree

of

Doctor of Philosophy

June 2008

Dedication

To my family (parents, wife and little daughter) who always believed that I could achieve everything I wished for.

Thank you.

Acknowledgements

It is difficult if not impossible at this moment, to find appropriate words to express my gratitude to my advisor **Dr. Michel W. Barsoum** for his encouragement, continuous support, great teaching, friendly advice, inspiration and his faith in me. Thus I can simply say: THANK YOU. I have been very fortunate to learn from him so much.

I consider myself lucky and honored for having an opportunity to collaborate with a lot of wonderful people during my work on PhD Thesis. Among all of them, I would like specially to thanks:

- **Dr. Surya Kalidindi**, my co-adviser, for helping me to interpret experimental results, inspiriting discussions, great suggestions and participating in my defense committee;
- **Dr. Roger Doherty**, Drexel University, for helping me to interpret experimental results, inspiriting discussions, participating in my defense committee;
- **Antonios Zavaliangos**, Drexel University, time and interest in reviewing this thesis and participating in my defense committee;
- **Dr. David Stepp**, Army research office, for founding support, time and interest in reviewing this thesis and participating in my defense committee;
- **Dr. Gary Friedman**, ECE department of Drexel University, for inspiriting discussions and suggestions on Preisach-Mayergoyz Model;
- **Dr. Joe Horton,** Oak Ridge National Lab for selfless helping on in situ TEM;
- **Dr. Peter Finkel**, Drexel University, for inspiriting discussions and help on ultrasound test;
- **Dr. Tiejun Zhen**, for his teaching on mechanical test;
- **Dr. Sandip Basu**, for inspiriting discussions, friendly advice and co-work experience;
- **Dr ZhengMing Sun** and Dr. **Dmitry S. Filimonov**, for helping me to interpret experimental results, illuminating discussions and great suggestions;

- **Dr. Zhorro Nikolov** and **Mrs. Dee Breger**, Drexel University, for their great help on microscope and XRD;
- **Mr. Mark Shiber**, Drexel University, for doing the great job in machining the testing samples;
- **Dr. Richard Knight**, for helping and suggestion on maintaining equipment and lab;
- **Mrs. Judy Trachtman**, Drexel University, for their great help in solving everyday problems, friendly advice and support;
- All **Faculty** and **Staff members** of the **Materials Science and Engineering Department**, Drexel University;
- My fellow **graduate students** in the **Materials Science and Engineering Department** at Drexel University for making this work an enjoyable and unforgettable experience. Sincere thanks are due to my fellow research colleagues **Dr. A Murugaiah, Dr. Adrish Ganguly**, **Dr. Surojit Gupta, Dr. Elizabeth. N. Hoffman, Mr. Mathieu Fraczkiewicz, Mr. Shahram Amini, Mr. Aaron Sakulich, Alexander Moseson** and many others.

Finally, I would like to thank my parents, **Deduan Zhou** and **Xiufang Feng** and my wife **Xiumen Wan** for their comprehension, help and relentless support through all these years. Without their help, this work would not have been possible.

Philadelphia Aiguo Zhou

May 20, 2008

Table of Contents

List of Tables

List of Figures

Abstract

Kinking Nonlinear Elastic Solids: Theory and Experiments

Aiguo Zhou

Adviser: Michel Barsoum, Ph.D.

Co-adviser: Surya Kalidindi, Ph.D.

Recently it was postulated that most, if not all, plastically anisotropic solids can be classified as kinking nonlinear elastic (KNE) solids because their response to stress is nonlinear and fully reversible. Furthermore it was proposed that the large mechanical hysteresis observed was due to the fully reversible growth and shrinkage of incipient kink bands (IKBs). IKBs, the precursors of regular kink bands, are comprised of parallel dislocation loops, confined to two dimensions that remain extended if a load is applied and disappear if the load is removed.

The stress-strain curves of KNE solids can be described by 4 parameters: stress, nonlinear strain, stored nonlinear energy and dissipated energy per unit volume per cycle. In this dissertation an IKB-based microscale model is proposed to relate the four parameters. Remarkable agreement between model and experiment is achieved. The model is so powerful that a decent picture of the size, densities and distribution of the dislocations that nucleate during the reversible loops emerges. Most important, the critical resolved shear stress of the IKB dislocations is obtainable from a simple compression experiment on a polycrystalline solid.

The model was tested on select MAX phases (Ti_3SiC_2, Ti_2AlC and some of their solids solutions) and the hexagonal metals (Ti, Mg, Co). All the experimental results, and

some literature results, were shown to agree quite well with theoretical prediction. The model not only quantifies mechanical damping but also elucidates the nature of microyielding in a variety of solids, including the hexagonal metals. The nature of damping and microyielding in hexagonal metals were to date not fully understood or misunderstood for a long time.

The phenomenological Preisach-Mayergoyz model was also applied to KNE solids. From the model, the stress distributions needed to nucleate and grow the hysteretic elements – viz. the IKBs - was determined. Once determined, this distribution can then be used to predict the response of these materials to any stress history.

Based on this work there is little doubt that incipient kink bands constitute one of the last pieces in the deformation-of-solids puzzle, without which much of their early deformation cannot be understood.

1. Introduction

1.1 MAX phases

This work was triggered by the unique deformation behavior of the $M_{n+1}AX_n$ - or MAX - phases, where M is an early transition metal, A an A-group element, X carbon and/or nitrogen, and n=1-3. The MAX phases, numbering over 50, are ternary carbides and nitrides that have received considerable attention in the past decade [1-6]. The most studied and best understood is Ti_3SiC_2.

The first hint that Ti_3SiC_2 was atypical came as early as 1972, when Nick1 et al. [7], working on chemically vapor deposited single crystals, showed that Ti_3SiC_2, was anomalously soft for an early transition metal carbide. The hardness was also quite anisotropic, with the hardness normal to the basal planes roughly 3 times that parallel to them. When the authors used a solid state reaction route, the resulting material was no longer "soft". In 1987**,** Goto and Hirai [8], confirmed the results of Nick1 et al. Due to the difficulties in fabricating monolithic, bulk and dense Ti_3SiC_2, very little was known about this material and some of what was known has been shown to be incorrect later.

In 1996, Barsoum and El-Raghy made a breakthrough [3] in the synthesis of bulk, dense samples of Ti_3SiC_2 and performed extensive characterization of its properties. Barsoum and his research group at Drexel University soon identified more than 50 closely related compounds (Ti_3AlC_2, Ti_2AlC, Ti_4AlN_3, Ti_2AlN, etc.) and named them the MAX phases. Most known MAX phases are listed in Fig. 1.1 [9].

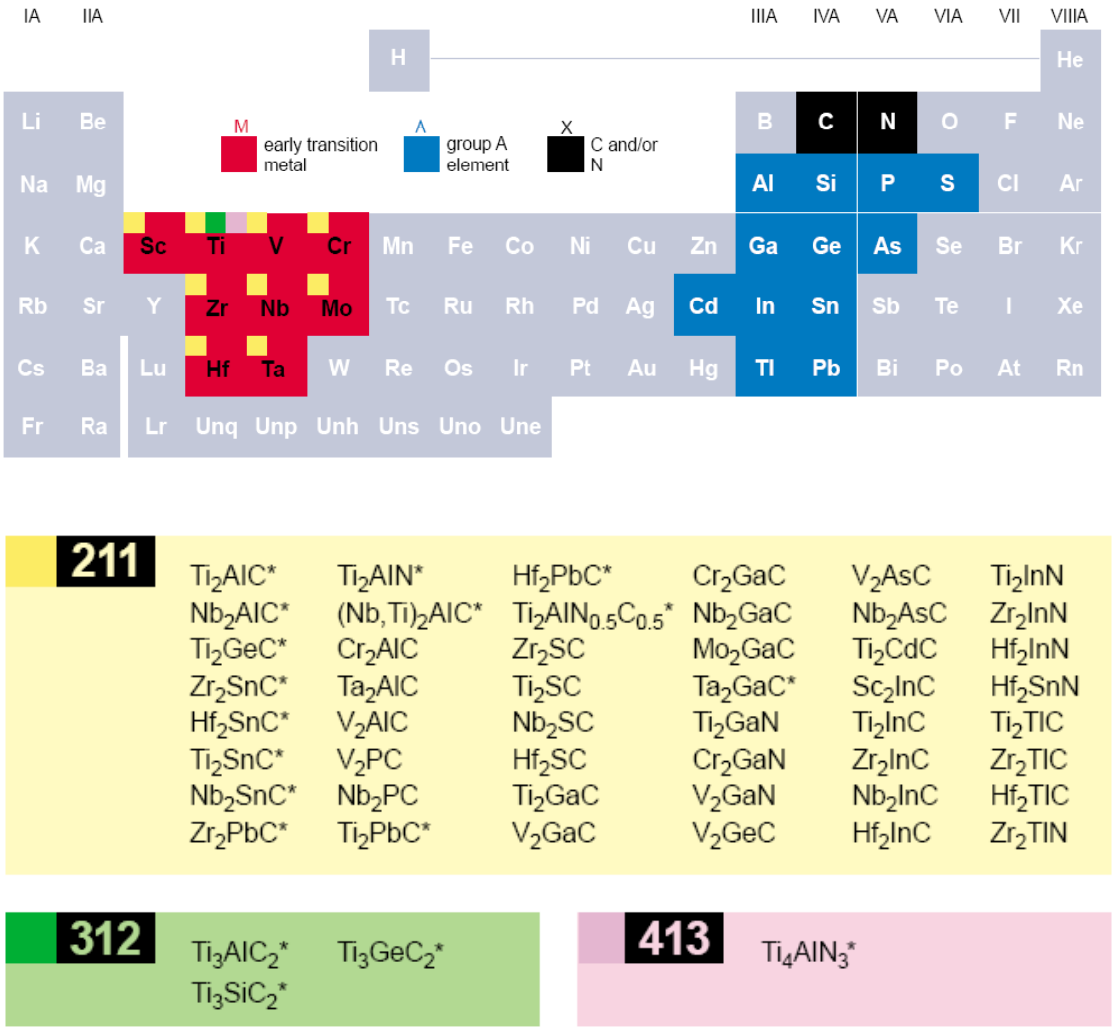

Figure 1.1: The MAX phases are made up of an early transition metal M (red) in the periodic table, an element from the A groups, usually IIIA and IVA (dark blue), and a third element, X, which is either nitrogen or carbon (black), in the composition $M_{n+1}AX_n$, where n is 1, 2 or 3. The classes of MAX phases characterized to date naturally form into three groups, based on the number of atoms of the M, A and X elements in each molecule; these groups are known as 211, 312 and 413 materials. The one's that are marked with asterisks have been synthesized successfully by Dr. Barsoum's research group at Drexel University [9].

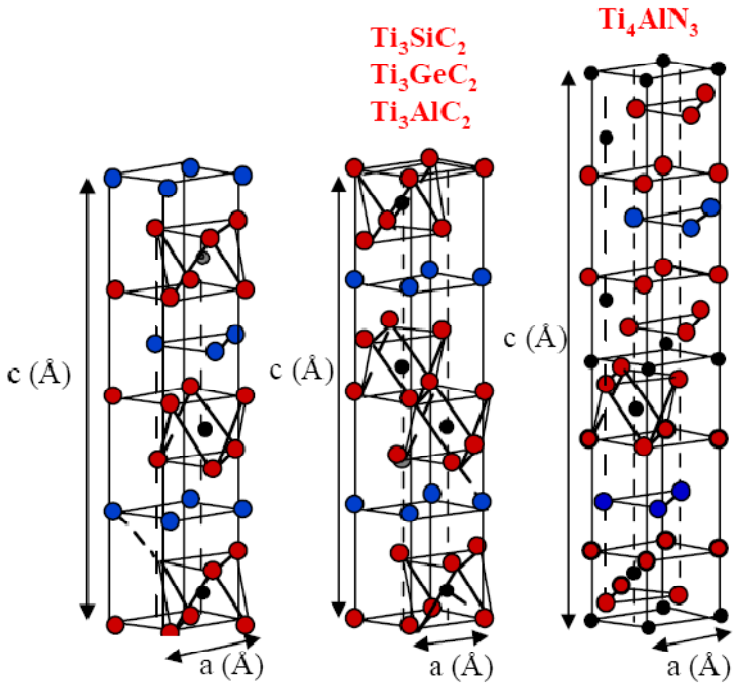

Figure 1.2: Unit cells of (a) 211 (b) 312 and (c) 413 phases. M (red) is the early transition metal, A is A groups element, usually IIIA and IVA (dark blue), and X either nitrogen or carbon (black).

As a class, the MAX phases are best described as a unique class of thermodynamically stable polycrystalline nano-laminated solids. They are layered hexagonal (space group D_{46h}-$P6_3/mmc$) with two formula units per unit cell. Figure 1.2 compares the unit cells of the 211, 312 and 413 phases, respectively [10]. In each case, near close packed layers of M layers are interleaved with layers of pure A-group element, with the X atoms filling the octahedral sites between the former. The A-group elements are located at the center of trigonal prisms that are larger than the octahedral sites and thus better able to accommodate the larger A-atoms. The M_6X octahedra are edge sharing and are identical to those found in the rock salt structure of the corresponding binary

carbides. The main difference between the structures shown in Fig. 1.2 is in the number of M layers separating the A-layers: in the 211's there are two; in the 312's three, and in the 413's four. This layered nature is of fundamental importance in understating the mechanical deformation discussed in this thesis.

Some MAX phases – most notably Ti_3SiC_2 and Ti_2AlC - are promising, lightweight candidates for high temperature structural and other applications. Their electrical and thermal conductivities are higher than those of Ti metal [3, 10]. Despite having a density (~4.5 gm/cm^3) comparable to Ti, their stiffness are roughly three times as high [11], and yet are most readily machinable [3]. With a Vickers hardness of ≈ 3 GPa, they are relatively soft, unusually thermal shock resistant [3, 12] and highly damage tolerant [3, 13]. Unlike most brittle solids, edge cracks do not emanate from the corners of hardness indentations [11, 13]. Rather, intensive kinking, buckling and bending of individual grains take place in the vicinity of the indentations, resulting in pseudo-plastic behavior at room temperature [13].

1.2 Kinking nonlinear elastic solids

In order to use Ti_3SiC_2, and the other MAX phases for structural applications, the mechanical properties, especially their moduli, need be measured. However, in 2003 [6], it was discovered that polycrystalline Ti_3SiC_2 samples don't have constant apparent modulus. The slope of their stress-strain curves are changed with stress. This is different with traditional materials. Traditional materials have linear elastic stress-strain curves with constant slopes equal to their Young's moduli, which can be measured by ultrasound. However, MAX phases are not in this case and we cannot calculate deformation from

stress. There are hysteretic loops in these samples cyclically loaded stress-strain curves, while these hysteretic loops dissipate about 25 % of the mechanical energy. These loss factors are higher than most woods, and comparable to polypropylene and nylon. The hysteretic stress-strain loops are fully reversible, rate-independent, and closed. The loops are strongly influenced by grain size, with the energy dissipated per unit volume per cycle, W_d, being significantly larger in the coarse-grained solids. In our recent papers it was established that other MAX phases [14, 15], graphite [16], mica [17, 18], sapphire [19], ZnO [20], GaN [21], $LiNbO_3$ [22] and hexagonal metals (Mg, Co, Ti, Zn etc) [23] among many others (see below), have similar deformation behavior. Our group attributed this phenomenon to the reversible growth and shrinkage of incipient kink bands (IKBs) [6, 24, 25], which is why we refer to them as kinking nonlinear elastic, KNE, solids.

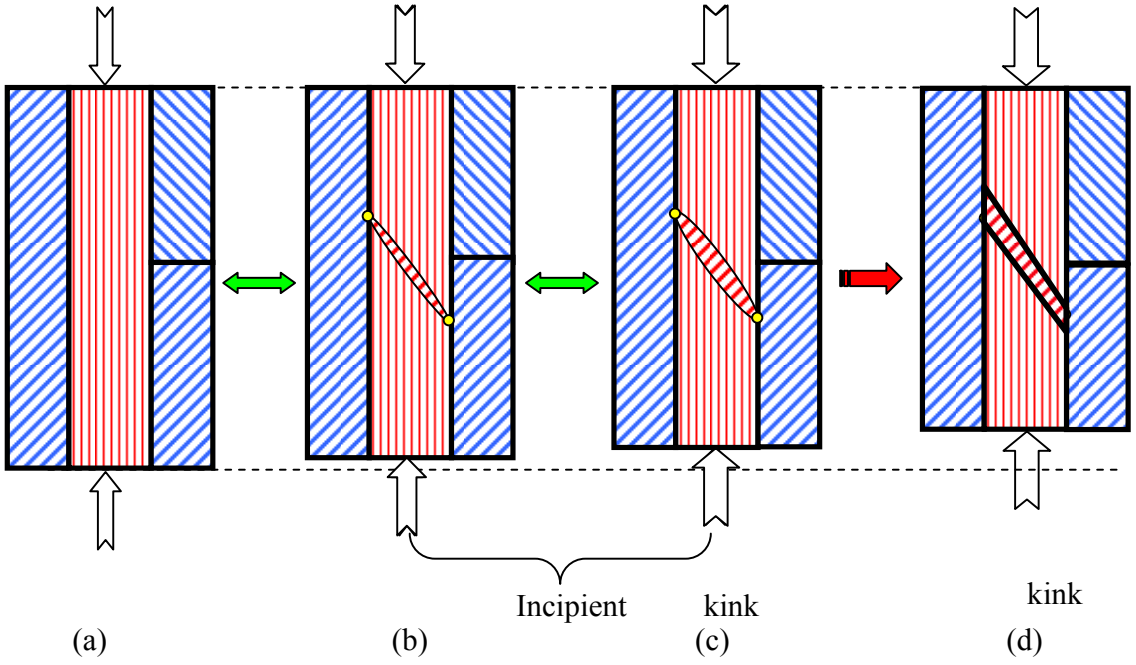

Figure 1.3: Schematic diagram of IKBs and KBs, (a) When $\sigma < \sigma_t$, the response is linear elastic. (b) At higher stresses, some hard grains form IKBs. (c) At higher σ's, the IKBs grow wider but are still reversible. (d) At even higher stresses and/or temperatures, the IKBs transform to KBs, which are irreversible.

Kink bands were first reported by Orowan [26] in single crystals of Cd loaded parallel to their basal planes. Kinking is distinct from slip or twinning in that it requires the generation of a succession of more or less regularly spaced dislocation pairs on many parallel slip planes [27, 28]. In recent papers of our group [6, 16, 25, 29-31], it was emphasized that the formation of incipient kink bands (IKBs) must precede the production of regular kink bands, KBs as shown in Fig. 1.3. IKBs are made up of near parallel walls of opposite sign dislocations that are un-dissociated, i.e. still attracted to each other at their ends (Figs. 1.3b and 1.3c). They grow when the load is increased and shrink when it is decreased. When IKBs dissociate, they produce mobile dislocation walls, MDW, and hence an irreversible or permanent deformation (Fig. 1.3d) and/or damage in the form of delaminations. It is the coalescence of mobile walls that eventually produces kink boundaries that make up the kink bands that have been documented extensively in the literature [5, 26-28, 32-35].

KNE solids are characterized by a marked anisotropy in their plastic properties at the single crystal level. One measure of that anisotropy is a high c/a ratio. It has been postulated that a sufficient condition for a solid to be KNE is a high c/a ratio [25]. This condition renders dislocations other than basal and/or basal twinning prohibitively expensive. The material can thus only deform by basal slip, which leads to kinking.

Figure 1.4a plots c_{44} vs. c/a for a number of solids, some of which are known to kink and others that are not [25]. Based on this map it is clear that KNE solids lie to the right of the vertical line and hence constitute a huge class of solids.

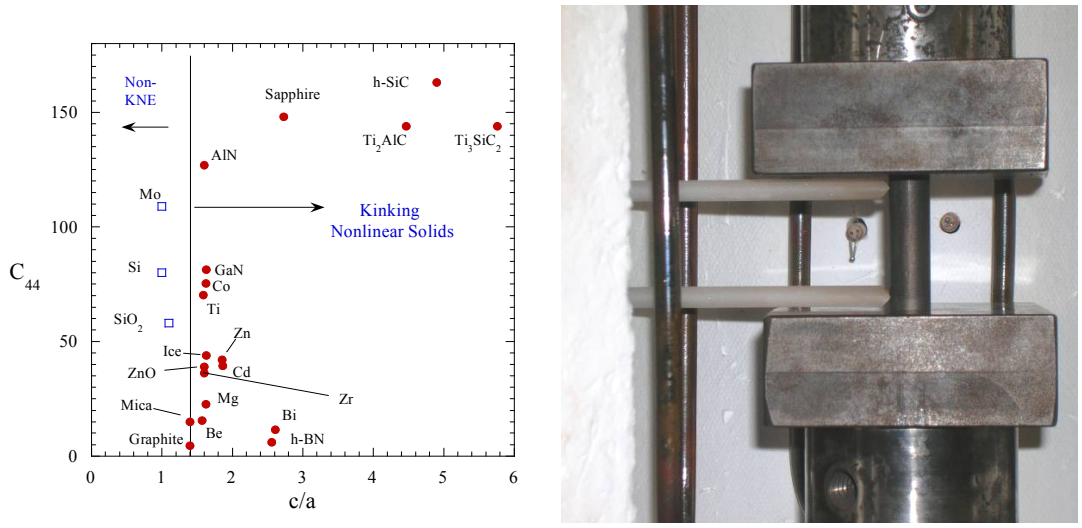

Figure 1.4: (a) Some non-KNE and currently known KNE solids and their plot of c44 versus c/a. Solids that fall to the right of the vertical line should be KNE solids (b) Compression setup and compression sample. Strain is measured by the extensometer.

Uniaxial compression is the experimental method used to characterize KNE solids in this research. As shown in Fig. 1.4b, a sample in the shape of a cylinder is cyclically compressed, to different stress levels, using a hydraulic testing machine. The strain is measured by an extensometer attached directly to the sample.

The signature of KNE deformation is the formation of fully reversible hysteresis stress-strain loops that disappear when the load is removed. Figure 1.5 shows the stress-strain curve of two typical KNE solids, Ti_3SiC_2 and Mg. As shown in Fig. 1.5a, if the compressive stress is lower than a threshold stress, σ_t, the response is linear elastic. As the stress is increases above σ_t, hysteresis loops appear and the deformation is no longer linear. For ceramics, like Ti_3SiC_2 in Fig. 1.5a, all the hysteretic loops are fully closed. But

for metals, like Mg in Fig. 1.5b, because of plastic deformation, the first cycle to a given stress level are open — i.e. results in a permanent deformation — but all subsequent cycles to the same stress are fully reversible.

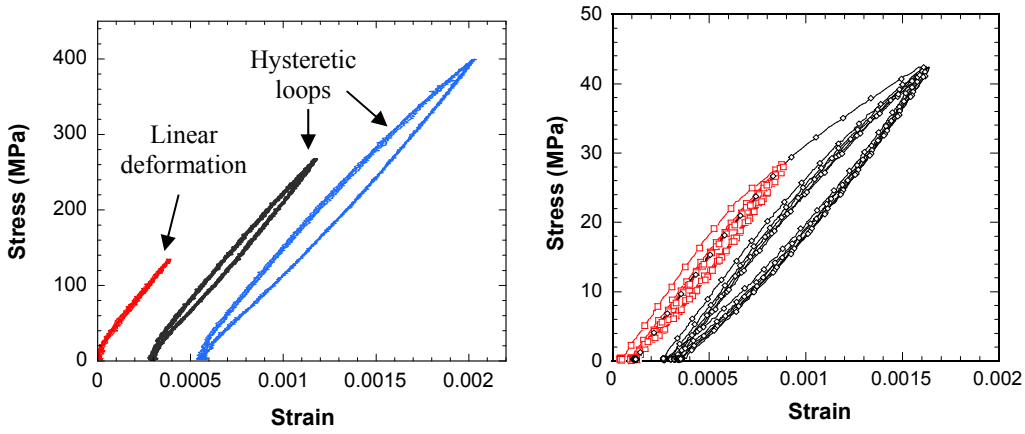

(a) (b)

Figure 1.5: Typical stress-strain curves of a KNE solid, of a) Ti_3SiC_2, and, (b) pure Mg

1.3 Kinking nonlinear elastic deformation and damping

Because large amounts of energy are dissipated per cycle, KNE solids are by necessity high damping solids. High damping means a solid can easily convert vibrational mechanical energy to heat. If high damping solids start to vibrate or oscillate for any reason, these vibrations should be rapidly quenched.

Typically, for high damping capabilities polymers and certain metals, such as Mg, are the materials of choice. Mg, a well-known high damping metals, is a typical KNE solid. We postulate in this work that IKBs in Mg sample must play a important role in

Mg's high damping. For metals, most of the current damping models - based on the classic work of Granato and Lucke,[36] G&L, who postulated that the damping was due to pining and de-pining of bowing dislocations - are, at the very least, incomplete. For example, the G&L model neither explains why Mg is such a good damping element, while Al and Cu are not, nor does it explain why a threshold strain exists to have high damping capacity for some metals. More importantly the G&L model cannot account for the strong effect of grain size on damping and/or strain thresholds.

This thesis proves that that Mg, with other HCP metals (Ti, Zn, Co and Zr) are high damping metals because of the growth and shrinkage of IKBs. It follows that understanding of KNE deformation of these metals cannot only help us engineer higher damping solids, but also understand and quantify this type of damping.

1.4 Deformation of hexagonal metals (Ti, Zr, Mg, Co, etc)

Because of their crucial technological role, the HCP metals, such as Ti, Zr, Mg, Zn, Co, have been intensively studied for decades. Zr alloys are used as cladding for nuclear reactor fuels; Ti alloys are applied for aerospace and the aircraft industry; and Mg alloys are extensively used for communication and consumer electronic applications. Consequently, the deformation mechanisms of these solids at high stresses and strains are reasonably well understood. However, how these solids deform at low strains, defined herein as strains, $\varepsilon < 1\%$, is much less understood. Normally, pure linear elastic deformation of these hexagonal metals is followed by microyielding, which indicates the activation of primary slip [37]. Thereafter recent literature claimed that secondary slips [37] or twinning [37, 38] happen after micro-yielding until macro-yielding. The early

observations of kink bands in these metals [39-42] were ignored. However, because of plastic anisotropy, the secondary slips are not operative because they have much higher critical resolved shear stress (CRSS) than primary slips [43-50]. This thesis will show that the true solution of nature to this problem is "kinking" (Ch. 6-8). The initial deformation of these metals cannot be understood until the crucial role of kink bands play in that deformation is appreciated.

1.5 Goals and motivations

The primary goal of this research is to fully understand the deformation behavior of kinking nonlinear elastic (KNE) solids. A microscale dislocation model was developed and used to predict the deformation behavior of these solids. The theoretical predictions were then experimentally verified. Using this model, the mechanical hysteresis of KNE solids, in general and the damping and microyielding of HCP metals, in particular, are explainable.

As noted above, KNE solids do not have a fixed apparent modulus and it follows that the strain of a KNE solid cannot be calculated from Hooke's law or classical stress-strain curves with hardening, etc. A universal mathematic hysteretic model (Preisach-Mayergoyz Model) was verified to be effective for this kind of hysteresis. This model assumed that any hysteresis can be modeled by invoking the presence of a large number of small independent hysteric elements. Once the distribution of independent hysteretic elements is determined, the model can be used to predict the response of these materials to any stress history.

2. Microscale Dislocation Model for Kinking Nonlinear Elastic Deformation

2.1 Four parameters to describe the hysteretic loops

The deformation of KNE solids results in stress-strain curves with large hysteretic loops as shown in Fig. 2.1(a). In this thesis, four parameters are used to describe the stress-strain curves. (a) stress, σ, (b) nonlinear strain, ε_{NL}, (c) dissipated energy, W_d and, (d) stored nonlinear energy U_{NL}.

If a sample is loaded to a stress σ, it will experience a total strain ε_{tot}. This strain, ε_{tot}, includes two parts: nonlinear strain (ε_{NL}) and linear strain (ε_L). The latter can be calculated from Hooke's law ($\varepsilon = \sigma/E$, where E is Young's modulus). In this work we are only interested in ε_{NL} which can be readily determined from the following equation:

$$\varepsilon_{NL} = \varepsilon_{tot} - \sigma/E \tag{2.1}$$

The nonlinear strain (ε_{NL}) is comprised of two components: one due to the formation of incipient kink bands, ε_{IKB}, the other to dislocation pileups, ε_{DP}. For KNE solids, dislocations are confined to the basal planes – thus both ε_{IKB} and ε_{DP} should be fully reversible. However, ε_{IKB} is much larger than ε_{DP} for KNE solids from our experimental results [25] (see Ch. 3-8). It follows that in this thesis, unless otherwise stated we assume, $\varepsilon_{IKB} \approx \varepsilon_{NL} >> \varepsilon_{DP}$.

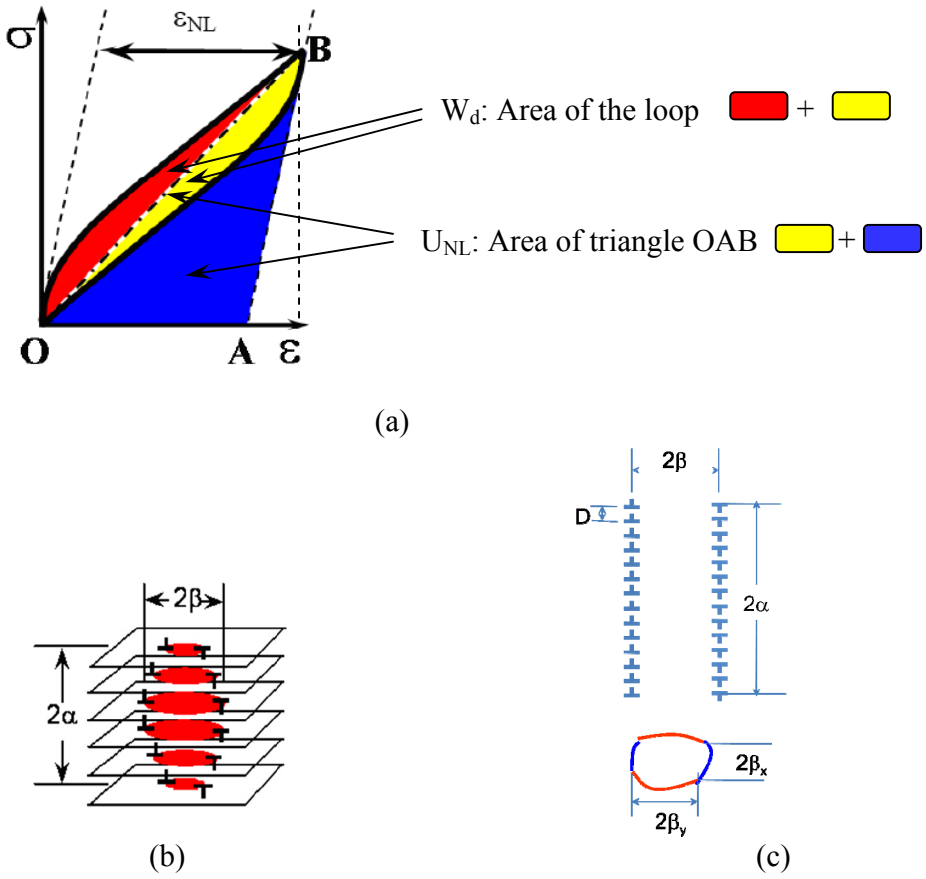

Figure 2.1: (a) Typical stress-strain curve of KNE solids with hysteretic loops. 4 parameters (σ, ε_{NL}, U_{NL} and W_d) are defined here to describe this stress-strain curve. σ is stress. ε_{NL} is nonlinear strain. U_{NL} is the area of triangle OAB (Blue + Yellow). W_d is the area of hysteretic loop (Red + Yellow). In this thesis, $U_{NL} \approx U_{IKB}$ and $\varepsilon_{NL} \approx \varepsilon_{IKB}$. (b) The schemeatic of an IKB in ellipsoid shape with the length 2α and diameter 2β. (c) Dislocation walls and dislocation loops of an IKB. D is the distance of two dislocation loops. $2\beta_x$ is the length of the edge dislocation segment; $2\beta_y$ is the length of the screw dislocation segment.

The dissipated energy per unit volume per cycle (W_d) is the loop area in Fig. 2.1a. The total stored energy (U) is the whole area under the stress-strain curve in Fig. 2.1a. The linear stored energy (U_L) (the blank triangle area at the right of AB line) is due to

linear elastic deformation. It is not of interest in this thesis. And since half the dissipated energy ($W_d/2$) is dissipated during loading and thus not stored, it follows that the nonlinear stored energy (U_{NL}) is the triangle OAB in Fig. 2.1a and can be calculated from:

$$U_{NL} = U_{tot} - U_L - W_d/2 \tag{2.2}$$

Therefore 4 parameters - $\sigma, \varepsilon_{NL}, W_d, U_{NL}$ - are needed to describe the KNE hysteretic stress-strain loops. In the next section, a dislocation-based model is proposed to relate the four parameters.

2.2 Previous Frank and Stroh's work

Frank and Stroh (F&S) [27], considered an elliptic kink band, KB, with a length 2α and a width 2β, such that $2\alpha >> 2\beta$ (Fig. 2.1b). An IKB consists of multiple parallel dislocation loops. As a first approximation, each dislocation loop can be assumed to be comprised of two edge and two screw dislocation segments with lengths, $2\beta_x$ and $2\beta_y$, respectively as shown in the bottom of Fig. 2.1c. The dislocations segments have opposite polarities and are thus attracted to each other. It is this force that causes the dislocation loops to shrink.

In an IKB, each dislocation segment is attracted to all other dislocation segments in the IKB with opposite polarity. For an IKB with length 2α, the dislocation segments form two dislocation walls with opposite polarity as shown in Fig. 2.1c top. The attractive force between the two dislocations walls is given by [27]:

$$F = \frac{Gb^2(2\beta)\ln(\alpha/\beta)}{\pi(1-\nu)D^2} \tag{2.3}$$

where D is the distance between dislocation loops along 2α (Fig. 2.1c); ν is Poisson's ratio; G is the shear modulus and b is the Burgers vector. As noted above, this attractive force is the driving force for the reversibility of the IKBs.

Frank and Stroh (F&S) also gave the remote shear stress, τ, needed to render such a subcritical KB stable as [27]:

$$\tau > \tau_c \approx \frac{\sigma_c}{2} \approx \sqrt{\frac{4G^2 b\gamma_c}{2\alpha\pi^2}\ln(\frac{b}{\gamma_c w})} \tag{2.4}$$

where τ_c and σ_c are the remote critical shear and axial stresses; *w* is related to the dislocation core width. The critical kinking angle, γ_c, is given by [27]:

$$\gamma_c = \frac{b}{D} \approx \frac{3\sqrt{3}(1-\nu)\tau_{loc}}{2G} \tag{2.5}$$

The local shear stress, τ_{loc}, needed to form a dislocation loop, is assumed to be given by [51]:

$$\tau_{loc} = \frac{G}{4\pi e}(\frac{b}{w}) \tag{2.6}$$

where e ≈ 2.718. Eq. 2.6 is effective only at an ideal condition, 0K. At room temperature, this equation is only roughly correct. Therefore the dislocation width w is changeable due to the test conditions, such as temperature. For most metals, $\tau_{loc} \approx G/20$ [51].

From the experiments in following chapters, we model the IKB formation as be in two stages: nucleation and growth. At this time the nucleation process is not well understood; in some cases it requires some plastic deformation; in others, not. In this

thesis we deal exclusively with IKB growth. It is thus assumed that for $0 \leq \sigma \leq \sigma_t$, IKB nuclei with dimensions 2α, $2\beta_{x,c}$ and $2\beta_{y,c}$ given by:

$$2\beta_{x,c} \approx k_1 \frac{2\alpha(1-\nu)}{2G\gamma_c}\sigma_t \qquad 2\beta_{y,c} \approx k_1 \frac{2\alpha}{2G\gamma_c}\sigma_t \tag{2.7}$$

are stable and exist. k_1 is a parameter that relates the remote shear stress with the axial stress. For a polycrystalline sample, k_1 is related to the texture of this sample. In this thesis it is assumed to be 2.

2.3 IKBs nucleation and growth

Based on previous F&S work, we developed our dislocation model to explain the incipient kink bands. In the F&S model, once a subcritical KB became critical (i.e. $\sigma > \sigma_t$), it grew rapidly and autocatalytically – to the ends of the 2-dimensional crystal modeled. More recently we have shown that in most KNE solids, these subcritical KBs grow *only* to the ends of the grains in which they originate [6, 25]. Since at that point their shape is such that a large attractive force is present at their tips [27], removal of the load results in their shrinkage. We define such *fully reversible* KBs as incipient kink bands or IKBs [6]. At higher stresses or temperatures, the IKBs are divided resulting in mobile dislocation walls (MDW), that in turn lead to kink bands [4, 6, 52] as shown in Fig. 1.3.

At $\sigma > \sigma_t$ three simplified scenarios are possible: the IKBs can either rotate by decreasing D; increase their radius β according to Eq. 2.8 below; or remain unchanged, with the strain accommodation occurring by an increase in N_k, the number of IKB per unit volume. Decreasing D results in dependencies of U_{IKB} and W_d that are *not* in accord

with our experimental results and was shown by F&S [27] to be unlikely and is not considered further. Also most of our results indicate that N_k for fine-grained solids and the MAX phases is almost a constant as σ increases. In large-grained hexagonal metals that may not be the case at high stresses (see Ch. 6). Therefore, we believe that increasing of β is the main way that KNE solids accommodate the nonlinear strain.

It follows that for $\sigma > \sigma_t$, the IKB nuclei are assumed to grow, according to:

$$\beta_x - \beta_{c,x} = k_1 \frac{\alpha(1-\nu)}{2G\gamma_c}(\sigma - \sigma_t) \qquad \beta_y - \beta_{c,y} \approx k_1 \frac{\alpha}{2G\gamma_c}(\sigma - \sigma_t) \tag{2.8}$$

2.4 Relationships between parameters

The growth and shrinkage of an IKB results in a nonlinear elastic strain ε_{IKB}. The dissipated energy W_d and stored nonlinear energy U_{IKB} due to this nonlinear strain can be calculated based on dislocation motion. The IKBs induce axial strains resulting from their growth assumed by us to be:

$$\varepsilon_{IKB} = \frac{\Delta V N_k \gamma_c}{k_2} \tag{2.9}$$

where ΔV and N_k represent the changes in volume of an IKB and the number of IKBs per unit volume, respectively; k_2 is a factor that relates the local IKB shear strain at the grain level to the macroscale uniaxial strain of the sample – assumed to be 2 in all cases. For polycrystalline solids, k_2 is related to sample texture. In the metallurgical literature it is known as the Taylor factor [53]. For an IKB with dimensions of 2α, $2\beta_x$ and $2\beta_y$, the change of volume ΔV (Fig. 2.2) can be calculated assuming:

$$\Delta V = \frac{4}{3}\pi\alpha(\beta_x\beta_y - \beta_{x,c}\beta_{y,c}) \tag{2.10}$$

which combined with Eqs. 2.9 and 2.10 yields:

$$\varepsilon_{IKB} = \frac{k_1^2 \pi (1-\nu) N_k \alpha^3}{3 k_2 G^2 \gamma_c} (\sigma^2 - \sigma_t^2) = m_1 (\sigma^2 - \sigma_t^2) \tag{2.11}$$

where m_1 is the term before σ^2.

The reversible dislocation density due to these IKBs, ρ, is given as:

$$\rho = N_k \cdot \pi (\beta_x + \beta_y) \cdot \frac{2\alpha}{D} \tag{2.12}$$

At this given stress σ, U_{IKB}, (Fig. 2.1a) due to the formation of the IKBs is given by $U_{IKB} = 1/2 \cdot \sigma \cdot \varepsilon_{IKB}$. Combining this relation with Eq. 2.11 yields:

$$U_{IKB} = \sqrt{\frac{3 k_2 G^2 \gamma_c}{4 k_1^2 \pi (1-\nu) N_k \alpha^3} \cdot \varepsilon_{IKB}^3 + \frac{1}{4} \sigma_t^2 \varepsilon_{IKB}^2} = \sqrt{m_2^2 \cdot \varepsilon_{IKB}^3 + \frac{1}{4} \sigma_t^2 \varepsilon_{IKB}^2} \approx m_2 \varepsilon_{IKB}^{1.5} \tag{2.13}$$

m_2^2 is the coefficient before ε_{IKB}^3. The last term is approximate as long as ¼ $\sigma_t^2 <<$ $m_2^2 \varepsilon_{IKB}$, which is true from our experimental results as shown in later chapters. In terms of σ:

$$\frac{U_{IKB}}{\sigma} = \frac{1}{2} \cdot \frac{k_1^2 \pi (1-\nu) N_k \alpha^3}{3 k_2 G^2 \gamma_c} (\sigma^2 - \sigma_t^2) \tag{2.14}$$

The energy dissipated per unit volume per cycle, W_d, resulting from the growth and shrinkage of the IKBs from β_{ic} to β_i, is given by:

$$W_d = N_k \frac{2\alpha}{D} \cdot 2\pi (\beta_x \beta_y - \beta_{xc} \beta_{yc}) \cdot \Omega = \frac{\Omega}{b} \pi N_k \alpha^3 \frac{(1-\nu) k_1^2}{G^2 \gamma_c} (\sigma^2 - \sigma_t^2) = m_3 (\sigma^2 - \sigma_t^2) \tag{2.15}$$

where Ω is the energy dissipated by a dislocation loop sweeping a unit area. In this equation, $N_k \frac{2\alpha}{D}$ is the number of dislocation loops per unit volume; D = b/γ_c and is replaced by b/γ_c in the third term of Eq. 2.15; $2\pi(\beta_x\beta_y - \beta_{xc}\beta_{yc})$ is the area swept by one dislocation loop, including growth and shrinkage. From the definition of Ω, Ω/b is proportional to, if not equal to, the critical resolved shear stress, CRSS, of an IKB dislocation loop. For 100% pure sample, the friction force for dislocation gliding in a basal plane is zero. Therefore Ω=0. However, all true materials have some defects. The defects increase the stress to move dislocations. Therefore, CRSS of materials depends on the pureness. In this these, we tested the commercial pure samples. The calculated CRSS is higher than that of 100% samples.

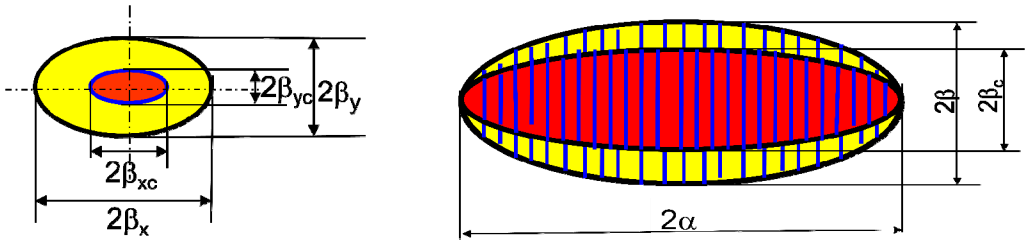

Figure 2.2: Growth of an IKB. The length 2α is assumed constant. Dislocation loops increase their area. Edge dislocation segments grow from $2\beta_{xc}$ to $2\beta_x$ and screw dislocation segments grow from $2\beta_{yc}$ to $2\beta_y$.

Combining Eqs. 2.11 and 2.15 yields:

$$W_d = 3k_2 \frac{\Omega}{b} \varepsilon_{IKB} = m_4 \varepsilon_{IKB} \tag{2.16}$$

In subsequent chapters will show that $N_k\alpha^3$ is not a strong function of σ, mainly because plots of ε_{IKB} vs. σ^2, U_{IKB} vs. $\varepsilon_{IKB}^{1.5}$, W_d vs. σ^2 or W_d vs. ε_{IKB} result in straight lines according to Eqs. 2.11, 2.13, 2.15 and 2.16, respectively. It is important to note here that $N_k\alpha^3$ should be of the order of unity, especially for fine-grained solids where it is unlikely to have more than one IKB per grain.

Furthermore, once m_1 to m_4 are determined from the slopes of these lines, $N_k\alpha^3$ and Ω/b can be calculated if k_1, k_2 and γ_c are known since:

$$N_k\alpha^3 = \frac{3k_2G^2\gamma_c}{\pi k_1^2(1-\nu)}m_1 = \frac{3k_2G^2\gamma_c}{4k_1^2\pi(1-\nu)m_2^2} \tag{2.17}$$

and

$$\frac{\Omega}{b} = \frac{m_3}{6k_2m_1} = \frac{4}{3k_2}m_2^2m_3 = \frac{m_4}{3k_2} \tag{2.18}$$

The calculated values of $N_k\alpha^3$ depend on k_1, k_2 and γ_c. From Eq. 2.5 and 2.6, the only variable to determined γ_c is w. Therefore the value of $N_k\alpha^3$ give us a criterion to choose the values of k_1, k_2 and w, which are difficult to obtain from experiments. The criterion is that N_k cannot be much greater than the number of grains per unit volume, i.e. $N_k\alpha^3 < 1$, the logic being that it is unlikely that many more than one IKB would form in a single grain, especially if $\alpha \approx \beta$. It is crucial to note the values of w, k_1 and k_2 chosen do *not* affect any of the conclusions of this work; they only affect whether ε_{IKB} is distributed amongst a large number of IKBs with small β values, or fewer ones, with larger β's. In this thesis, the assumption that $k_1=k_2=2$ and $w=5b$ is a good and reasonable choice.

2.5 Summary

In conclusion, four parameters, σ, ε_{NL}, W_d, U_{NL}, can be obtained from the stress-strain curves of KNE solids. Based on our dislocation model, if $N_k\alpha^3$ is not a strong function of stress, then plots of σ vs. ε_{NL}^2, U vs. $\varepsilon_{NL}^{1.5}$, W_d vs. σ^2 and W_d vs. ε_{NL} should result in straight lines, with slopes of m_1, m_2, m_3 and m_4, respectively. From the 4 slopes, we can calculate two micro dislocation parameters: the number of IKBs (N_k) from Eq. 2.17 and the critical resolved shear stress (CRSS, $\frac{\Omega}{b}$) from Eq. 2.18.

The validity of this model can be checked by the linear relations of the four plots and the calculated values of N_k and $\frac{\Omega}{b}$. In subsequent chapters will check the validity of this model by experiments on different materials and apply this model to calculate micro-dislocation parameter from stress-strain curves.

3. Kinking Nonlinear Elastic Deformation of Ti_2AlC

3.1 Introduction

In this thesis, Ti_2AlC is the first material selected to study kinking nonlinear elasticity and verify and apply the dislocation model presented in Ch. 2. Like other MAX phases, Ti_2AlC is damage tolerant, readily machinable and thermal shock resistant [1, 2, 54, 55]. Furthermore, its resistance to oxidation and thermal cycling is exceptional [54, 55]. The prospect of using Ti_2AlC for structural applications at room and elevated temperatures is quite promising.

Since kinking is somewhat similar to a buckling phenomenon, i.e. it should be enhanced when the grains are not constrained or confined as shown by previous work on porous Ti_3SiC_2 [56] and to further explore this intriguing phenomenon, this chapter compares the behavior of ≈ 10 vol. % porous and fully dense Ti_2AlC samples with comparable grain sizes. For the porous sample, the measured stress reported here is not the true stress and the shear modulus, G, is changed due to porosity. In order to focus the discussion on our dislocation model, we simply assume the measured stress to be the real stress and the dense Ti_2AlC's modulus for the porous sample's modulus. In the Ch. 4, the influence of different porosities on stress, G and kinking will be discussed in detail.

To verify and apply our dislocation-based model to this material, this chapter's work reports on the mechanical response of polycrystalline Ti_2AlC to compressive stresses, both uniform and highly localized. The latter is achieved by indenting the

surface with a 13.5 μm radius hemi-spherical indenter and converting the nanoindentation load-displacement results to nanoindentation stress-strain curves.

3.2 Experimental Details

Two sets of polycrystalline Ti_2AlC samples were used; one set was fully dense; the second set was comprised of 10 % porous samples. The fully dense samples were prepared by cold isostatic pressing of Ti_2AlC powder (d_{50} = 8 μm, Kanthal, AB, Sweden), followed by pressureless sintering at 1500 °C for 1 hr under flowing Ar. The 10 vol.% porous samples were prepared by cold isostatic pressing of Ti_2AlC powder (d_{50} = 20 μm, Kanthal, Sweden) followed by pressureless sintering at 1500 °C for 1 hr under flowing Ar.

The densities were calculated by dividing a regular shaped sample's mass over its volume. The microstructures shown here were observed using a scanning electron microscope, SEM, (FEI/Phillips XL30). The grain size was measured using an optical microscope, OM, (Olympus PMG-3 Optical Metallograph). From optical images, the thicknesses and diameters of more than fifty plate-like grains were acquired. Image analysis of polished and etched OM micrographs was used to quantify the volume fraction of TiC – an almost unavoidable impurity - in the microstructure.

Uniaxial compression tests were performed on cylindrical shaped specimens (9.7 mm in diameter and 31 mm high); the gauge length was 25 mm. Samples were electro-discharge machined and tested with no further surface preparation. The compression tests were performed using a hydraulic testing machine (MTS 810, Minneapolis, MN), supplied with a controller (Microconsoler 458.20, MTS), and a 100 kN capacity load cell.

In all tests, a preload, that corresponded to a stress of about 1 ~ 2 MPa, was applied to keep the samples aligned. All the cyclic loading-unloading tests were performed in load-control mode at a loading rate of 2 kN/s. The strains were measured by an extensometer (MTS, Minneapolis, MN) with a gauge length of 25 mm attached directly to the samples.

Nanoindentation tests were carried out using a nanoindenter (MTS XP System, MTS Corp., Oak Ridge, TN) with a 13.5 μm-radius spherical diamond tip. The tip was calibrated with a standard amorphous silica sample. The tests were carried out — using a Continuous Stiffness Measurement (CSM) option — to peak loads of 50 mN at several locations of the fully dense sample. Repeated indentations, up to 5 times typically, on the same location were carried out. The load-displacement curves were converted to indentation stress-strain curves by a method described in Appendix A. Furthermore, W_d for the nanoindentation tests was estimated by dividing the area of the load/depth of penetration cycles by πa^3, where a is the contact radius. In doing so it is implicitly assumed that the volume affected under the indenter is approximately a cylinder with height *a* and radius *a* [30].

3.3 Results

SEM and OM micrographs of both dense and porous fractured surfaces are shown in Figs. 3.1a and b, Figs. 3.2a and b, respectively. In both cases the microstructure is comprised of randomly aligned plate-like grains. The average grain diameter in the dense samples is ~ 113±60 μm; its thickness is ~ 14±7 μm. For the porous sample, the respective dimensions are ≈ 133±70 μm and ~ 16±7 μm.

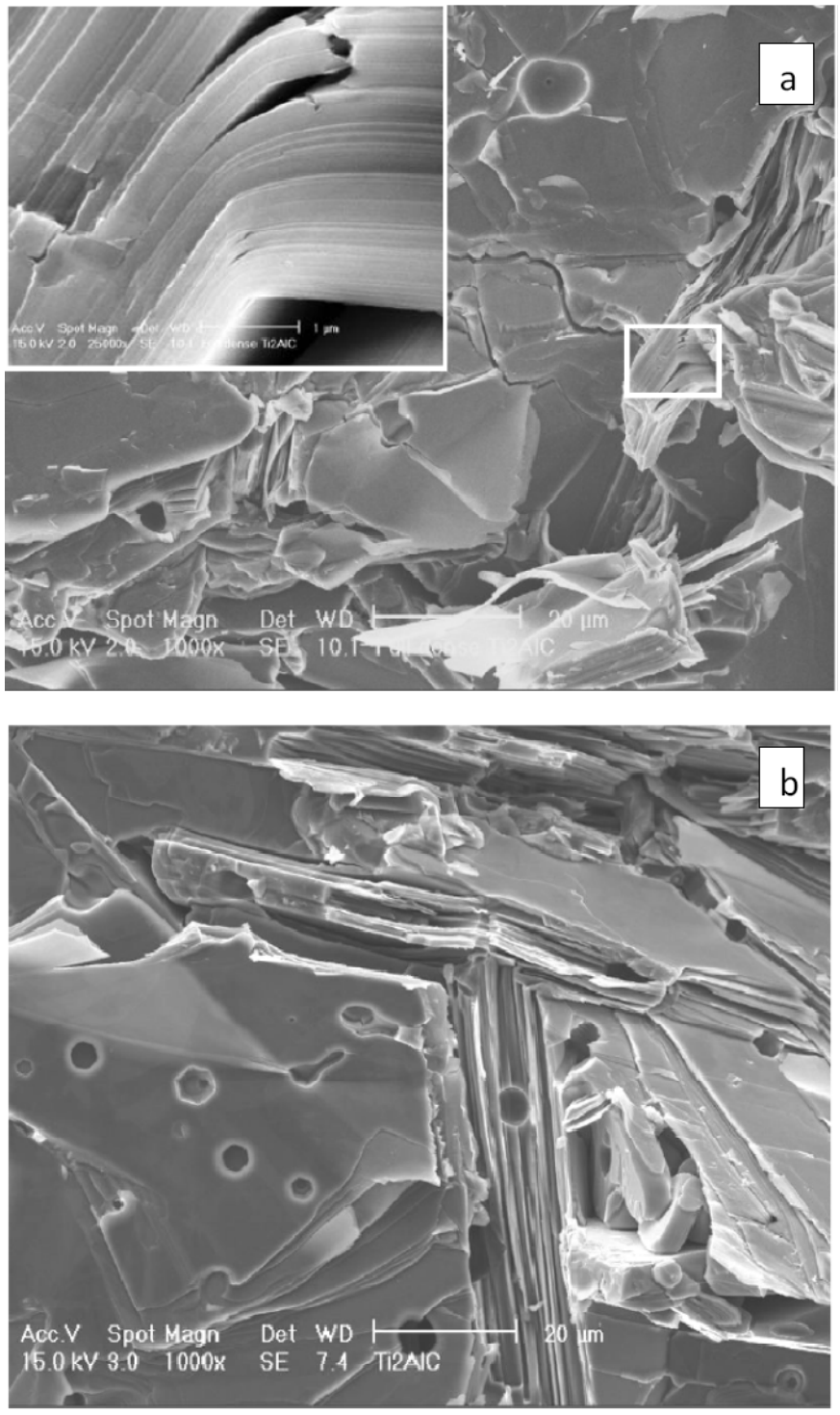

Figure 3.1: Fractured SEM micrographs of a, (a) dense Ti_2AlC sample. The inset in left corner is a kink band in high magnification; (b) porous Ti_2AlC sample. Note the pores are located within the grains.

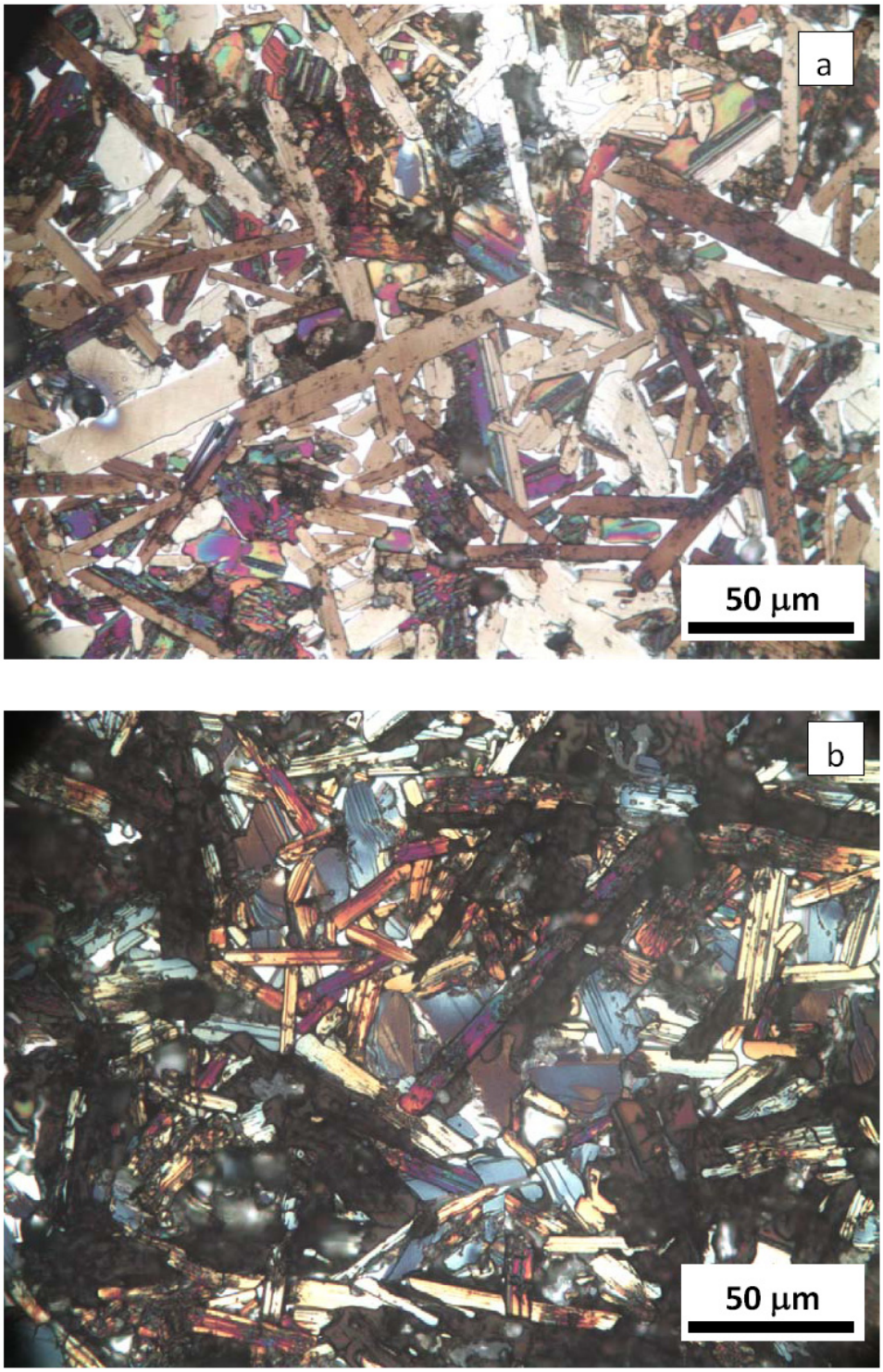

Figure 3.2: Optical micrograph of, (a) dense Ti_2AlC, (b) porous Ti_2AlC. The white areas in these micrographs are TiC.

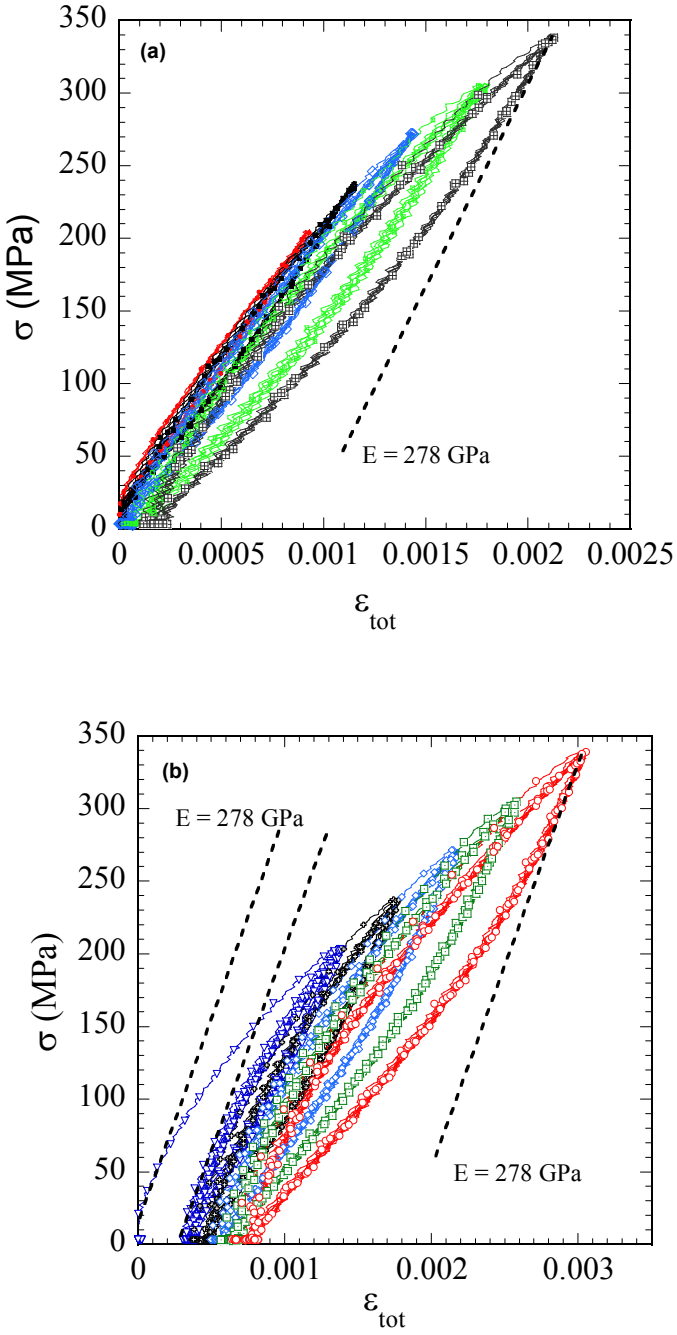

Figure 3.3: Uniaxial cyclic compression stress-strain curves of (a) dense Ti_2AlC and (b) porous Ti_2AlC cylinders, loaded to progressively higher stresses. The dotted lines are theoretic modulus of dense Ti_2AlC, 278 GPa [57].

From the measured density, the porous sample was calculated to be ~ 10 vol.% porous. As clearly seen in Fig. 3.1b, the porosity is in the form of ~ 3 μm diameter pores located within the plate-like grains. The formation of these pores may be because of decomposition of the Ti_2AlC at high temperature. Image analysis of OM micrographs showed that the TiC volume fraction is ≈ 6 vol. % for the dense samples, and ≈ 3 vol. % for the porous samples.

Typical cyclic stress-strain curves for uniaxial compression of a virgin dense and porous sample obtained by the progressive increasing stress are shown in Figs. 3.3a and Fig. 3.3b respectively. In the first cycle the sample was loaded to a stress of 200 MPa; in each successive cycle the stress was increased up to the maximum of ~ 340 MPa. Both samples show hysteretic loops. The first cycles to any stress levels have some plastic deformation. All subsequent cycles to same stress are fully closed. The porous samples had the larger plastic deformation at each cycle (compare Figs. 3.3a and 3.3b). In another set of experiments, the cylinders – dense (Fig. 3.4a) and porous (Fig. 3.4b) – were loaded to 340 MPa during the first cycle and unloaded. Subsequent cycles were loaded to progressively lower stresses. In the third set of experiments, a porous sample was loaded to 340 MPa and progressively unloaded to lower stresses and reloaded to the maximum stress, before total unloading (Fig. 3.5). This procedure results in a single unloading curve.

The fully reversible nature of the deformation in Figs. 3.4a and b are to be compared with the slightly open cycles shown in Fig. 3.3a and b. It is important to note that repeat cycles, to the same stress in Fig. 3.3a and b, are always fully reversible.

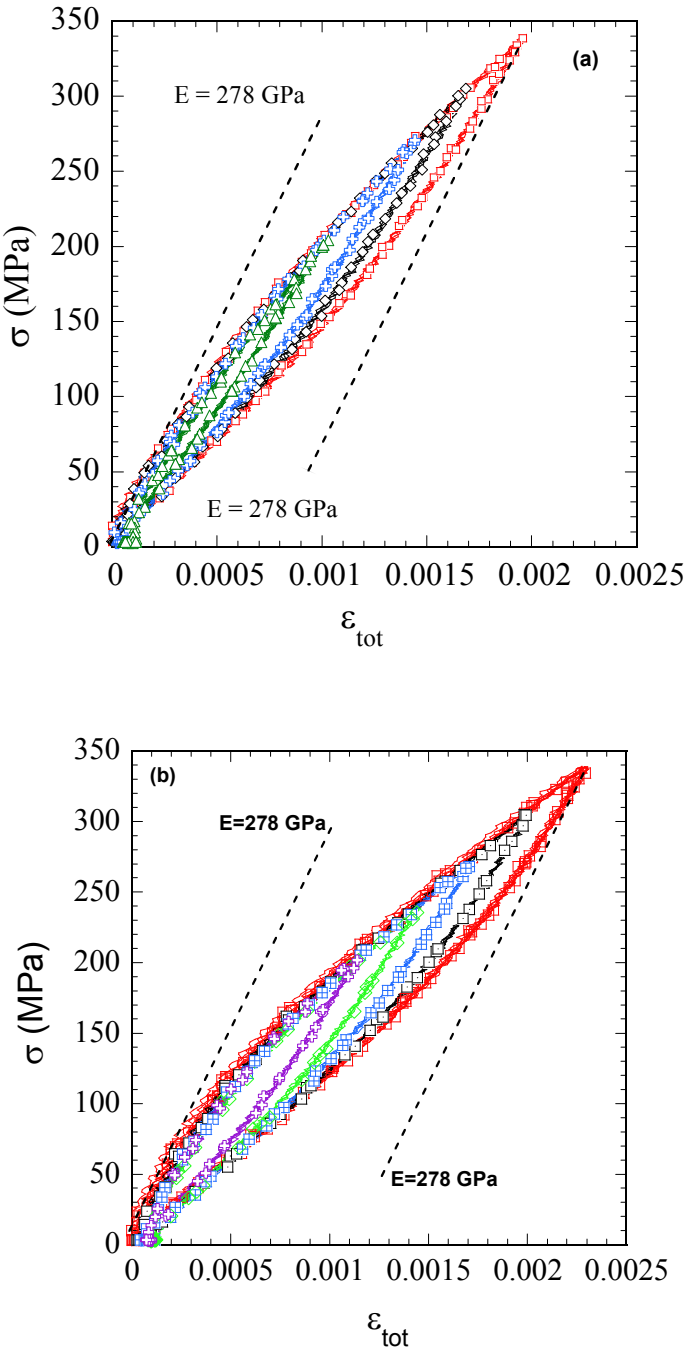

Figure 3.4: Stress-strain curves of uniaxial cyclic compression result of, (a) dense, and, (b) porous Ti_2AlC samples. The samples were first stressed to 350 MPa, unloaded and then reloaded to progressive lower stresses.

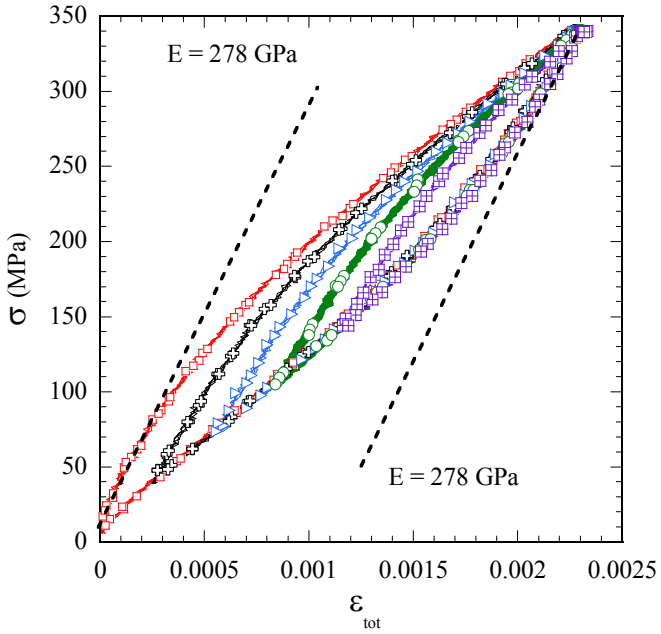

Figure 3.5: Stress-strain uniaxial cyclic compression result of 10 vol.% porous Ti_2AlC samples. The sample was loaded to 340 MPa and progressively unloaded to lower stresses and reloaded to the 340MPa, before total unloading.

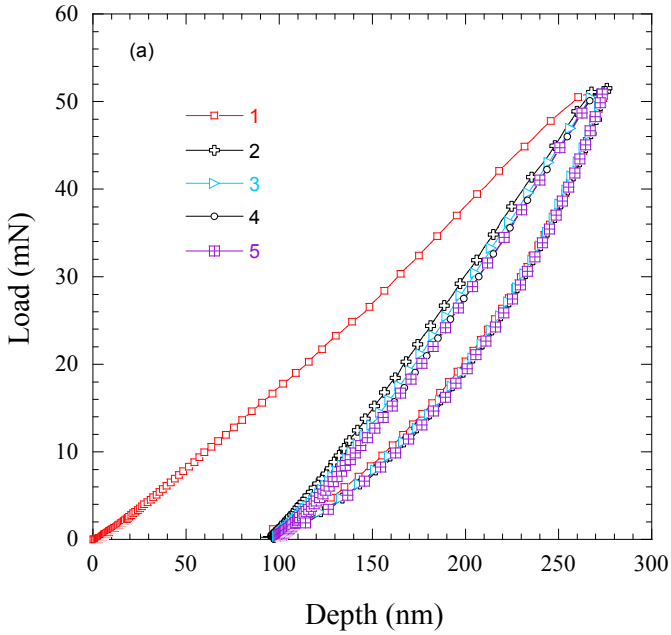

Figure 3.6 (*continued*)

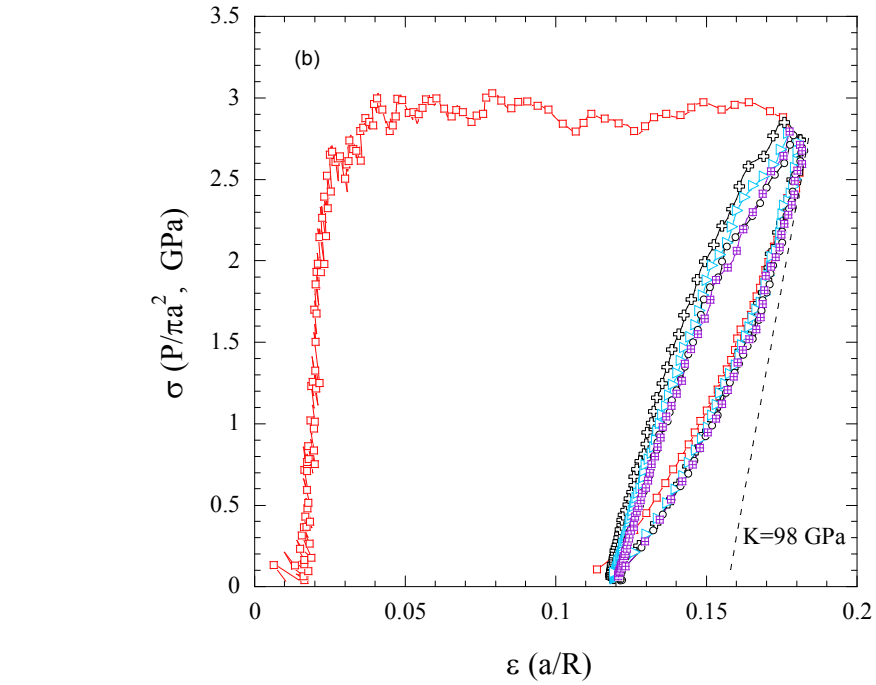

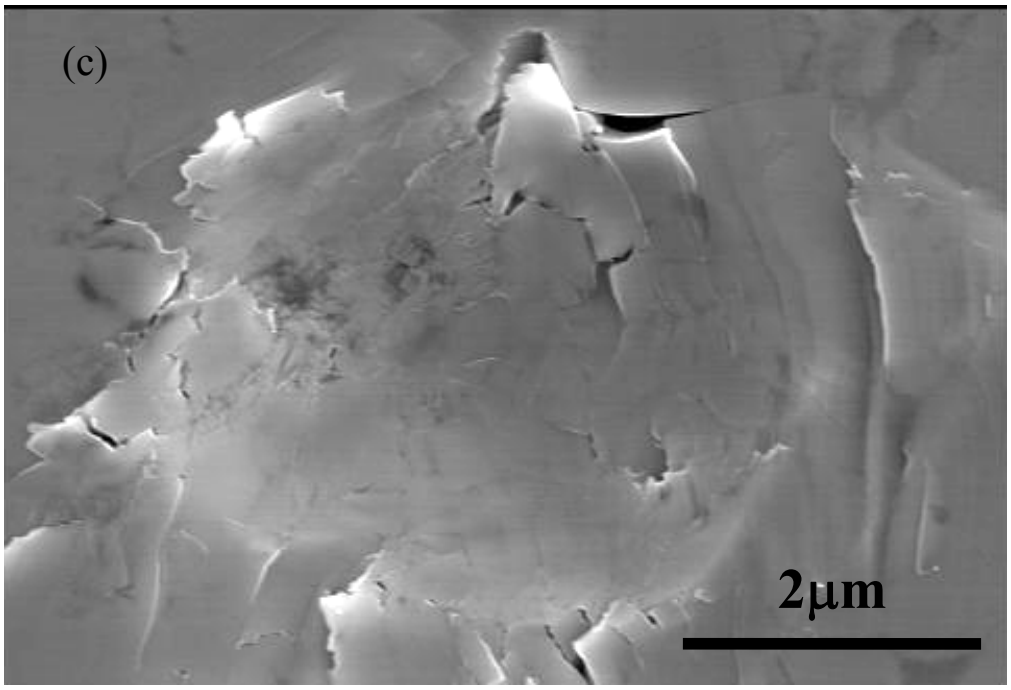

Figure 3.6: (a) Typical load-depth of penetration nanoindentation. (b) Corresponding P/πa2 vs. a/R curve. (c) SEM image of an indented location by 400 N. Delamination can be seen.

A comparison of Figs. 3.4a and b makes it clear that the loops obtained for the porous samples are larger – on an absolute scale, i.e. without normalizing the stress to account for porosity - than those for the dense samples. If normalization were to be carried out the differences in loop areas would be even higher than those reported herein.

Typical load vs. indentation depths results obtained by repeatedly indenting the same location of a Ti_2AlC dense sample to a load of 50 mN, are shown in Fig. 3.6a. The corresponding stress-strain curves are shown in Fig. 3.6b (see Appendix A for procedure). In both figures it is clear that while the first loop is open, the second and subsequent cycles are nearly fully reversible.

The last loop in Fig. 3.6b was the one used to determine W_d, U_{NL} and ε_{NL}. Given the polycrystalline nature of the solid, not surprisingly, the shapes of the first loops were quite stochastic with the amount of plastic deformation varying significantly from location to location. The variations in the second and subsequent loops, however, from location to location were much less.

Figure. 3.6c is a SEM image of an indented location that was loaded to ≈ 400 mN. Delamination and kinking can be observed. In general, after loading to only 50 mN, it was difficult to find the indentation marks and observe the deformation structure.

According to Eq.2.13, plots of U_{NL} vs $\varepsilon_{NL}^{1.5}$ should result in a straight line, as observed (Fig. 3.7). Figure 3.7a plots U_{NL} vs. $\varepsilon_{NL}^{1.5}$ obtained from the uniaxial compression stress-strain curves. For both dense and porous samples, least squares fits yield R values of > 0.999. Figure 3.7b combines the uniaxial compression and

nanoindentation results in a log-log plot where U_{NL} varies in a range from 0.02 to 80 MJ/m^3. The linear relation in Fig. 3.7b is still acceptable.

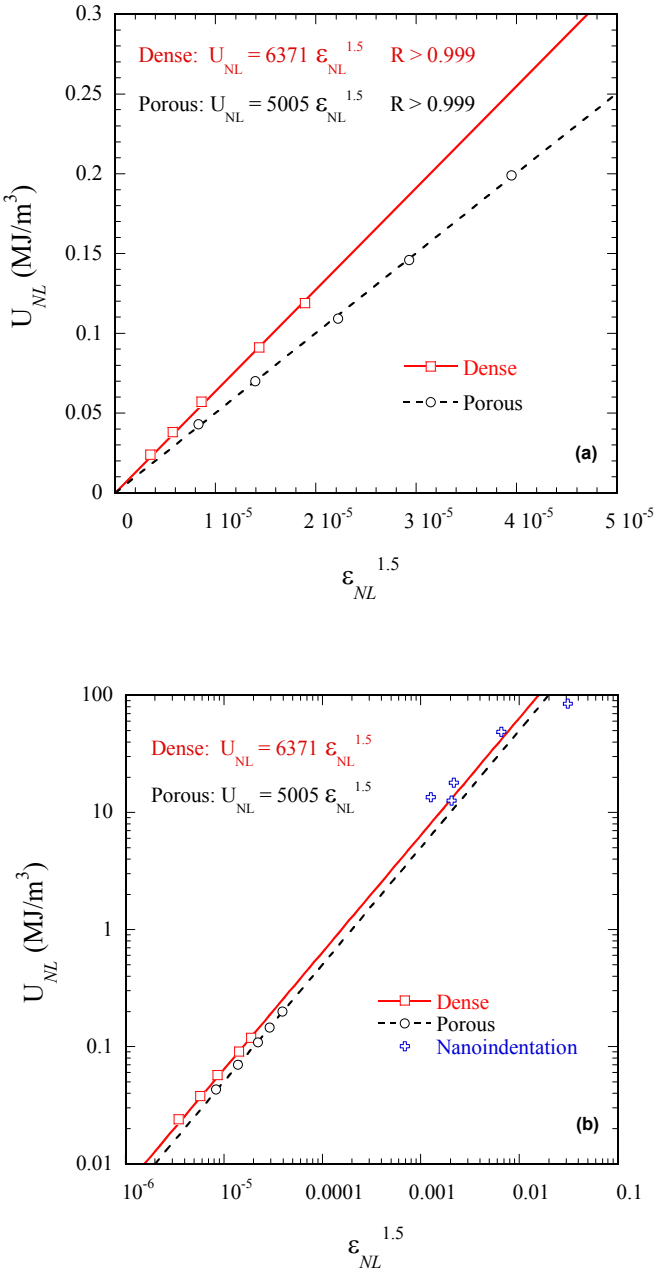

Figure 3.7: (a) Plots of U_{NL} vs. $\varepsilon_{NL}^{1.5}$ obtained from uniaxial compression stress-strain curves; (b) Log-log plot of same results, together with those obtained from nanoindentation stress-strain curves.

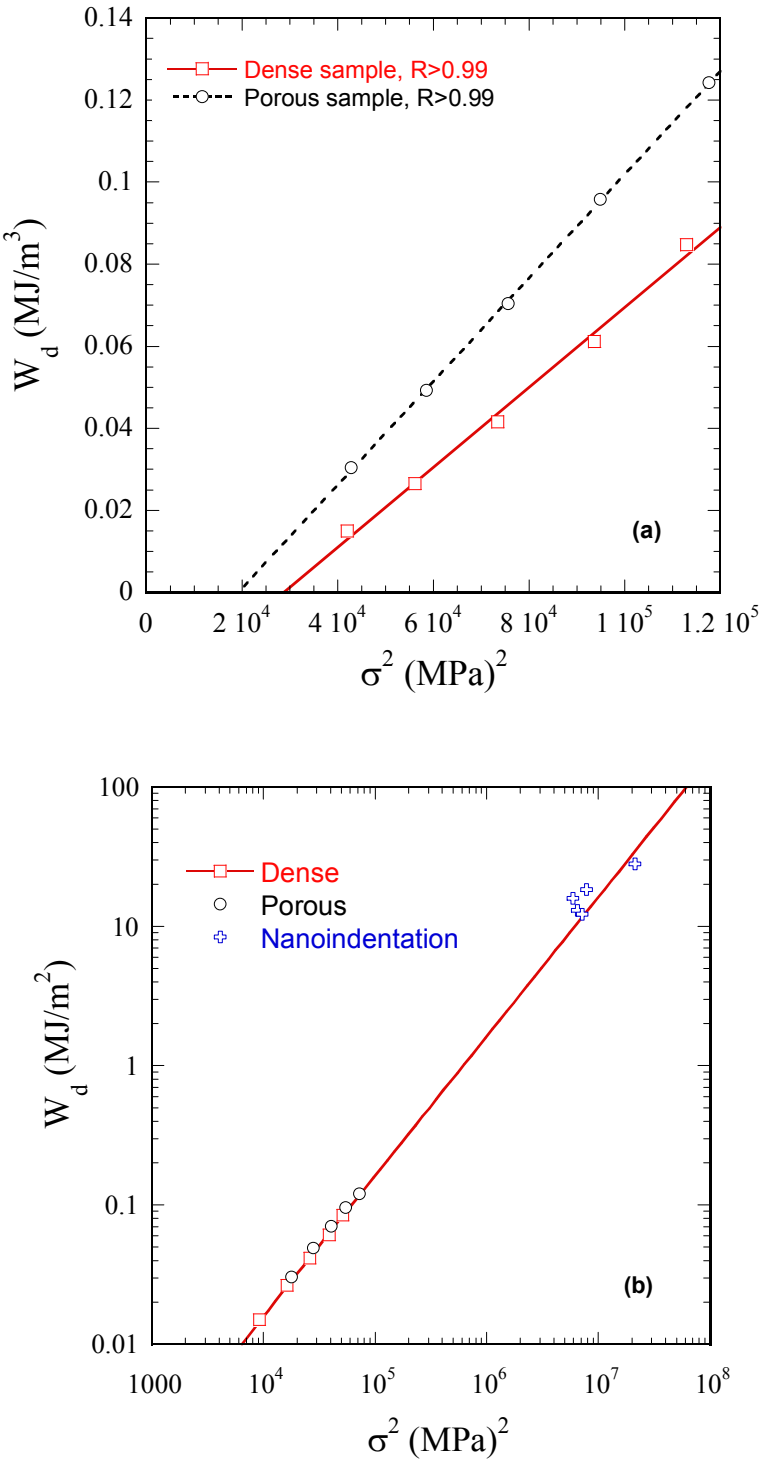

Figure 3.8: (a) Plot of W_d vs. σ^2 obtained from uniaxial compression stress-strain curves (b) Log-log plot of same results, together with those obtained from the load/depth-of-penetration nanoindentation curves.

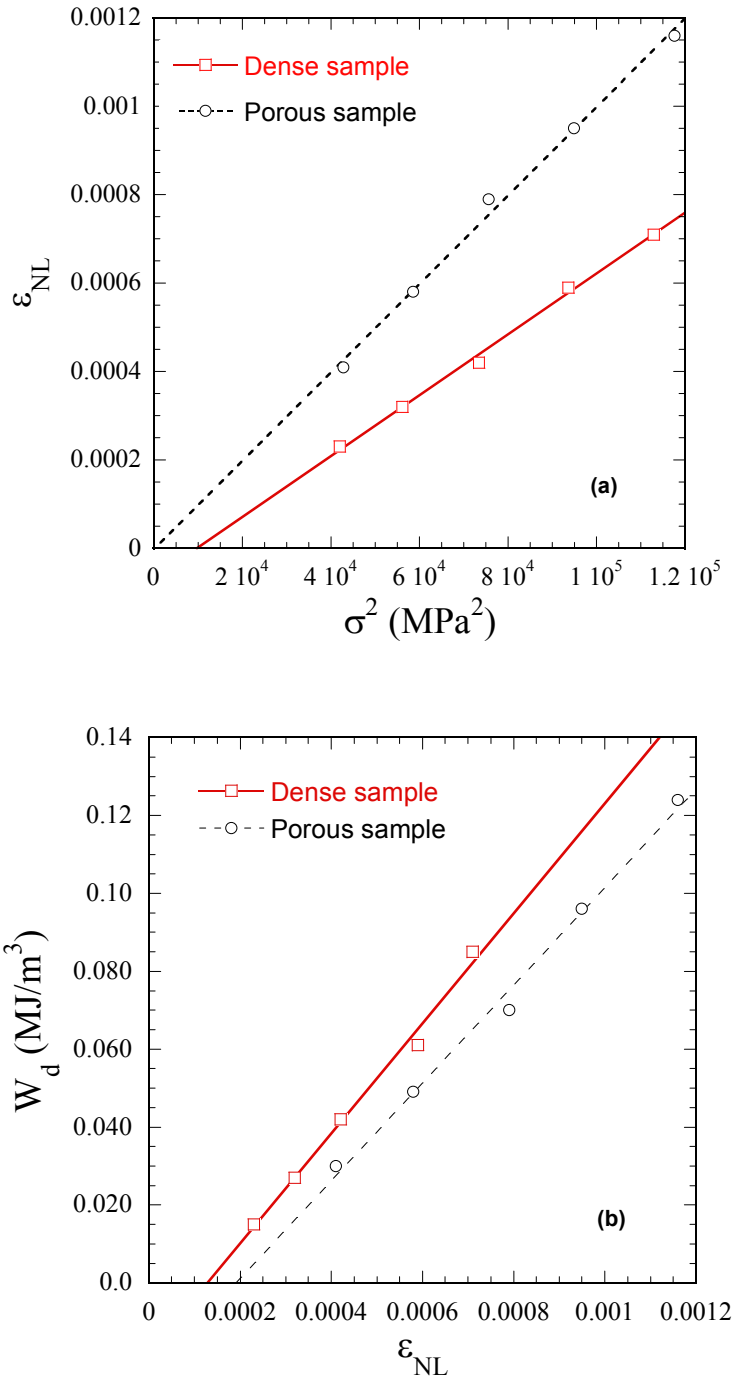

Figure 3.9: (a) Plot of W_d vs. σ^2 for uniaxial compression, (b) Plot of W_d vs. ε_{NL} for uniaxial compression.

If $N_k\alpha^3$ is not a strong function of stress, then, according to Eq. 2.15, plots of W_d versus σ^2, should yield straight lines with x-axis intercepts that correspond to the threshold stresses. That such plots are indeed linear, for both microstructures, is evident from Fig. 3.8a. In both cases, least squares fits yield R values > 0.99. Furthermore, for the dense sample, σ_t = 171 MPa; for the porous sample, σ_t = 140 MPa. Log-log plots of W_d vs. σ^2 obtained from uniaxial compression (lower left) and those obtained from the nanoindentation results are shown in Fig. 3.8b. Again, the linear relation is acceptable as W_d ranges from 0.015 to 28 MJ/m^3.

According to Eq. 2.11 and Eq. 2.16, plots of ε_{NL} vs. σ^2 and plots W_d vs. ε_{NL} should result in straight lines also as observed (Fig. 3.9a and 3.9b). For both microstructures, least squares fits result in straight lines with R values > 0.99.Table 3.1 lists material constants for Ti_2AlC. γ_c was calculated from Eq. 2.5. The Burgers vector, b, of the MAX phases is equal to the a-lattice parameter [33, 58]. 2α is taken to equal to the average grain *thickness*, determined from the microstructure. r is dislocation core width and assumed to be 5b (see Ch. 2).

Table 3.2 lists the measured values of σ, ε_{NL}, U_{NL} and W_d.

Table 3.3 lists the calculated Ω/b, σ_t, $N_k\alpha^3$, N_k and the reversible dislocation density, ρ, at the highest test stress σ_{max} from the dislocation model outlined in Ch. 2.

Table 3.1: Materials constants and calculated values.

Sample	G (GPa)	ν	b (Å)	r	γ_c (rad)	Grain thickness 2α (μm)
Dense	119	0.17	3.04	5b	0.072	14±7
10% porous	119	0.17	3.04	5b	0.072	16±7

Table 3.2: Experiment values in these experiments (σ, ε_{NL}, U_{NL}, Wd)

Sample	σ MPa	ε_{NL}	U_{NL} MJ/m^3	W_d MJ/m^3
Dense: Uniaxial Compression	205	0.00023	0.02	0.015
	237	0.00032	0.04	0.03
	271	0.00042	0.06	0.04
	306	0.00059	0.09	0.06
	336	0.00071	0.12	0.08
Porous: Uniaxial Compression	207	0.00041	0.04	0.03
	242	0.00058	0.07	0.05
	275	0.00079	0.11	0.07
	308	0.00095	0.15	0.10
	343	0.00116	0.20	0.12
Nanoindentation	2439	0.017	17.9	15.9
	2549	0.016	12.6	13.1
	2669	0.012	13.5	12.2
	2802	0.035	48.9	18.4
	4624	0.099	85.3	28.2

Table 3.3: Calculated values from dislocation model (Ω/b from Eq. 2.18, σ_t from the W_d vs. σ^2 plots in Fig. 3.8a, $2\beta_{xc}$ from Eq. 2.7, $2\beta_x$ from Eq. 2.8, $N_k\alpha^3$ from Eq. 2.17, N_k from $N_k\alpha^3$. Reversible dislocation density, ρ, at highest test stress σ_{max} from Eq. 2.12)

Sampe	Ω/b (MPa) Eq. 2.18			σ_t	$2\beta_{xc}$	$2\beta_x$	$N_k\alpha^3$ Eq. 2.17		N_k	ρ	σ_{max}
	2nd term	3rd term	4th term	MPa	μm	μm	2nd term	3rd term	μm^{-3}	cm^{-2}	MPa
Dense:	23.6	24.5	23.5	171	1	2.6	0.7	0.7	0.002	1.4x10^9	336
Porous	21.0	21.0	20.9	140	1	3.3	0.8	0.8	0.002	1.7 x10^9	343

3.4 Discussion

The results shown herein provide compelling evidence that our dislocation IKB microscale model, developed in Ch. 2 to explain the non-linear hysteretic response of KNE solids, is valid and applicable to Ti_2AlC. The reasons are several and include:

a) Fully reversible hysteresis loops are a signature of IKBs. Direct evidence for kinking is shown in inset of Fig. 3.1a. As noted in a previous paper [56], the fact that a 10 % porous sample dissipated more energy on an absolute scale (compare Figs. 3.4a and 3.4b) is compelling evidence that we are dealing with a kink-based phenomenon as opposed to one that is dependent on the volume of the material, such as simple glide or dislocation pileups for example.

b) According to Eq. 2.13, plots of U_{NL} vs. $\varepsilon_{NL}^{1.5}$ should result in straight lines. The actual plots (Fig. 3.7a) are quite gratifying and bear this relationship out. Even when the nanoindentation results are included, the relationship is borne out (Fig. 3.7b). In addition to validating the model, the results shown in Fig. 3.7b are important because they indirectly confirm, what was concluded for other KNE solids [25], that $N_k\alpha^3$ must be a weak function of σ.

c) That Eq. 2.15 is valid is clear from Fig. 3.8a. Here again the relationship appears to extend to quite high stresses (Fig. 3.8b). It is important to note here that W_d and U_{NL} are two totally *independent* measurements.

d) Figure 3.9a and b show that Eq. 2. 11 and Eq. 2.16 are also valid for both samples.

e) The measured values of σ_t are also quite reasonable. According to Eq. 2.15, the critical kinking stress, σ_c, of an average grain - with an average thickness, $2\alpha \approx 14$ μm (Table 3.1) and assuming w = 5b - is 191 MPa for dense samples. Given that it is not the average grains, but rather the largest grains, that determine the threshold stress of a polycrystal, the agreement between σ_c and the actual measured σ_t of 170 MPa has to be considered good. Interestingly, the main effect of the porosity is to reduce σ_t (Table 3.3); a result that is not too surprising given that porosity promotes kinking. This comes about because kinking as noted above is a form of buckling, which is easier in a porous solid than in a denser one.

Interestingly, and according to Eq. 2.15, the higher values of W_d of the porous samples derive mostly from a reduction in σ_t. In Ch. 4 we show that the main effect of porosity is to reduce G.

f) Based on the definition of Ω it is reasonable to expect that Ω/b to be closely related to, if not identical to, the critical resolved shear stress (CRSS) of dislocations gliding along the basal planes. The values calculated using three different terms of Eq. 2.18 are listed in Table 3.3. These values obtained from 3 different equations and four independent slopes are pretty close. This is strong evidence that our dislocation model is correct. These values are quite reasonable and comparable to the only reported value of a CRSS in a MAX phase, viz. 36 MPa for Ti_3SiC_2 [4].

Because of the complicated state of stress under the indenter and the several approximations made to convert the load/depth of indentation curves to indentation stress/strain curves (Fig. 3.6b) these results were not used to calculate Ω/b. This comment

notwithstanding, the plots shown in Fig. 3.6b are quite reasonable. This is especially true considering that the measured Vickers microhardness of the same sample was ≈ 2.8 GPa. The excellent agreement between the nanoindentation and microhardness results lends credence to the methodology described in Appendix A and in Refs. [19-22]. Lastly it is noted that the main benefit of the nanoindentation results is that they confirm that $N_k\alpha^3$ is indeed a weak function of stress up to quite high stresses.

The straight lines in Fig. 3.9b do not go through the origin; the small offset is not understood but could be related to dislocation pileups [25]. Both U_{NL} and W_d of dislocations associated with dislocation pileups are significantly smaller than those due to IKBs [25]. The fact that the intercept is slightly larger for porous samples is consistent with this conjecture.

Lastly, it is important to place the values calculated in Table 3.3 in perspective. First, it is gratifying that the values of N_k (≈ 0.002 μm^{-3}) calculated for both the dense and porous samples are almost identical. The total reversible dislocation density due to the IKBs at the maximum load of ~340 MPa is of the order of 1×10^9 cm^{-2}. These values are quite reasonable and fall in between those of well-annealed metal crystals and heavily cold-rolled ones [51].

3.5 Conclusions

The uniaxial compression and nanoindentation results on dense and porous samples unequivocally show that, like Ti_3SiC_2 [6, 25], Ti_2AlC is a KNE solid. The excellent agreement between experiment and theory, over quite an extended stress regime, lend strong support for our dislocation model for KNE solids in Ch. 2.

4. Effect of Porosity on the Kinking Nonlinear Elastic Deformation of Ti_3SiC_2

4.1 Introduction

Ti_3SiC_2 is the first reported kinking nonlinear elastic solid [59]. It has been shown that polycrystalline Ti_3SiC_2 samples can be cyclically loaded in compression at room temperature to stresses up to 1 GPa, fully recover on the removal of the load, while dissipating about 25 % (0.7 MJm^{-3}) of the mechanical energy [59].

It is believed that the high damping capability of KNE solids in general, and MAX phases, in particular is related to the formation of IKBs and KBs. Since KB formation is essentially a buckling phenomenon, it, in turn, is dependent on the constraints placed on the material. For example, when highly oriented Ti_3SiC_2 cubes were loaded parallel to the basal planes, they buckled at the unconstrained corners first [60]. Along the same lines, the thresholds for the formation of IKBs and KBs in nanoindentation experiments [61] are at least one order of magnitude higher than the same thresholds for their formation in macroscopic experiments [3, 20].

Based on this picture, we postulated that porous Ti_3SiC_2 samples should - as the result of facilitating the formation of IKBs and KBs - have higher damping capacity than fully dense samples. Our group have shown that to be the case in one paper by comparing 43 vol.% Ti_3SiC_2 with fully dense Ti_2SiC_2 [62]. In Ch. 3, it was shown that at comparable grain sizes and stresses, 10 vol.% porous Ti_2AlC dissipated more energy per cycle on an *absolute* scale than its fully dense counterparts. Actually, porosity may change many mechanical properties besides kinking, such as the shear modulus, G. The purpose of this chapter is to systematically research the effect of different porosity levels on the kinking

nonlinear elastic deformation of Ti_3SiC_2 samples. Before doing so it is useful to briefly describe our understanding of how porous solids respond to stress.

4.2 Effect of Porosity

The analysis in Ch. 2 is valid for fully dense solids with a density ρ_s. To take porosity into account we need to understand how it affects G. For open cell foams, it is well established that [63]:

$$\frac{E^*}{E_s} = C_1 (\frac{\rho^*}{\rho_s})^2 \tag{4.1}$$

where E* and E_s are the Young's moduli of the porous and dense solids, respectively; ρ^* is the density of the porous solid, and C_1 is ≈ 1. Furthermore, the shear modulus of a porous solid, G*, is given by [63]:

$$\frac{G^*}{E_s} \approx \frac{1}{2\,(1+\nu)} (\frac{\rho^*}{\rho_s})^2 \tag{4.2}$$

Foams are defined as solids with relative densities < 0.3, thus, strictly speaking, the microstructures tested herein - with relative densities between 0.95 and 0.45 - are not foams. Nevertheless, most pores of 55% and 40% porous samples are open, and in the remainder of this chapter we show that the major effect of porosity can be taken fully into account in our KNE model by simply replacing G in the various Ch. 2 equations by G* given by Eq. 4.2. For fully dense Ti_3SiC_2, E = 325 GPa, G = 135 GPa, ρ_s = 4.5 Mg/m^3 and ν = 0.2 [25].

Before proceeding further, it is important to note that for a porous solid it is more realistic to work with an effective stress, σ_{eff}, defined as

$$\sigma_{eff} = \frac{\sigma}{(\rho^*/\rho_s)} \tag{4.3}$$

where σ is the nominal stress, viz. load/cross-sectional area. It follows that in the remainder of this chapter, we use the effective values of U and W_d, viz. $U_{NL,eff}$ and $W_{d,eff}$ that are obtained from the σ_{eff} vs. ε curves (e.g. Fig. 4.3d below). Note ε_{NL} here is defined to be:

$$\varepsilon_{NL} = \varepsilon_{tot} - \frac{\sigma}{E^*} = \varepsilon_{tot} - \frac{\sigma_{eff}}{E^*_{eff}} \tag{4.4}$$

In the remainder of this chapter, we will use the σ_{eff} vs. ε curves and the effective moduli, E^*_{eff}, for all calculations. However, whenever G* is used it is estimated from Eq. 4.2, because that expression already takes into account the effect of porosity on the local stresses [64].

4.3 Experimental Details

Fully dense (100% dense), fine-grained Ti_3SiC_2, was made by reactive hot isostatic pressing (HIPing) a stoichiometric powder mixture of titanium (-325 mesh, 99.5%, Alfa Aesar, Ward Hill, MA), silicon carbide (-400 mesh, 99.5%, Atlantic Engineering Equipment, Bergenfield, NJ) and graphite (-300 mesh, 99%, Alfa Aesar, Ward Hill, MA). The sintering temperature was 1400 °C; the sintering time was 8 h.

The 5 vol. % porous sample was fabricated by HIPing at 1600 °C for 8 h. The aim was to fabricate a fully dense sample, but for reasons that are not clear, but most probably involved the exposure of the sample to the Ar atmosphere before complete densification

(i.e. a breach or de-wetting of the glass used for encapsulation), the sample was not fully densified.

The 18 vol.% porous sample also resulted from a HIP run that did not yield a fully dense sample. Additionally, to investigate the influence of microstructure on damping properties, after testing its mechanical properties, this sample was annealed in a tube furnace at 1600 °C in flowing Ar for 24 h, before subjecting it to compression testing. The same sample was also annealed for a further 24 h at 1600 °C, before a third round of testing.

The 40 vol. % porous sample was fabricated in a tube furnace. Proper stoichiometric ratios of Ti, SiC and graphite powders were mixed and cold isostatic pressed (CIPed) using a pressure of 300 MPa, then sintered in flowing Ar at 1600 °C for 4 h. To prevent oxidation or dissociation the Ar was passed over a boat containing Ti powder upstream of the sample. The 55 vol.% porous sample was made in a graphite heated vacuum furnace. Stoichiometric powder mixtures were placed in the furnace ($\approx 5 \times 10^{-2}$ torr), heated to 400 °C and held for 4 h; to 800 °C and held for 4 h and finally at 1500 °C and held for 4 h. All the heating rates were 2 °C/min.

The porosity was calculated from the density. The latter was measured by dividing the mass of the machined cylindrical samples by their volume. The apparent volume was measured by Archimedes' method from samples soaked in boiling water for two hours then room temperature water for 12 additional hr. Then the volume fraction of open pores and closed pores can be calculated. The composition of the samples (mainly Ti_3SiC_2 and some impurity TiC) was determined by X-ray diffraction, XRD, (Siemens D-500). Grains

and pores sizes were evaluated by scanning electron microscope, SEM, (FEI/Phillips XL30) on fracture surfaces, and optical microscopy, OM, (Olympus PMG-3 Optical Metallograph) on polished and etched surfaces. The etchant was $HF:HNO_3:H_2O$ = 1:1:1 by volume [65].

Cylinders (diameter = 9.7 mm, length =31 mm) were electro-discharge machined and cyclically compressed to different stress levels using a hydraulic testing machine (MTS 810, Minneapolis, MN), supplied with a controller (Microconsoler 458.20, MTS). The strain was measured using an extensometer. In most KNE solids, a small plastic deformation is usually recorded during the first cycle; all other subsequent cycles to the same stress are fully reversible and fully reproducible. The analysis was carried out on the latter.

4.4 Results

4.4.1 Microstructural Characterization

Typical SEM micrographs of the 40 and 55 vol. % porous samples are shown in Figs. 4.1a and b, respectively. All samples tested herein had similar plate-like grains. Table 4.1 summarizes the microstructural characteristics of the samples tested in this work. As discussed in previous chapters, the important microstructural dimension, 2α, is the width of the grains along the c-axis. However, since it was difficult to measure the grain thicknesses from micrographs of the porous samples, Table 4.1 lists the average grain sizes instead. Given that grain growth in Ti_3SiC_2 is faster along the a-direction, these values probably overestimate the grain thicknesses [66].

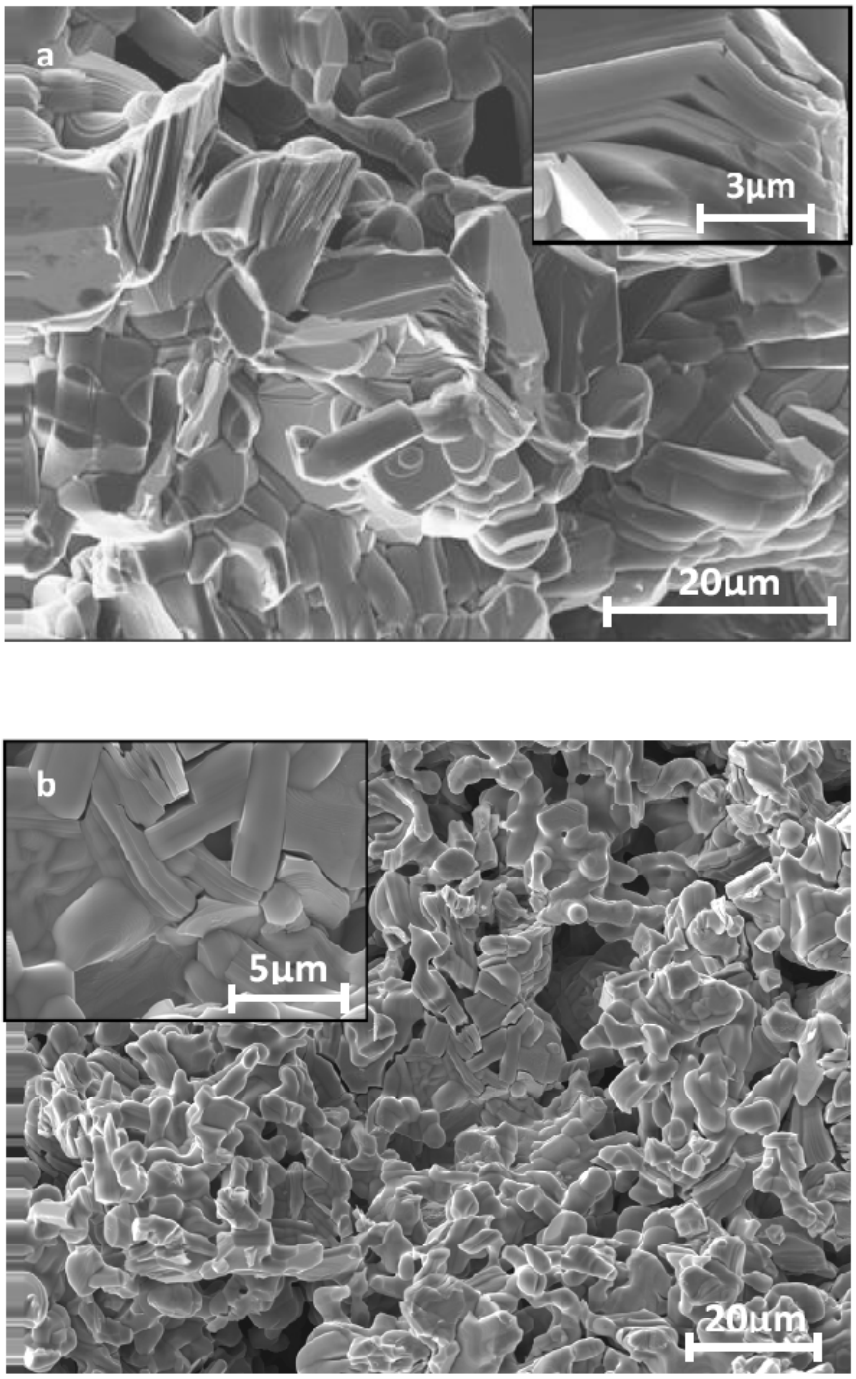

Figure 4.1 (*continued*)

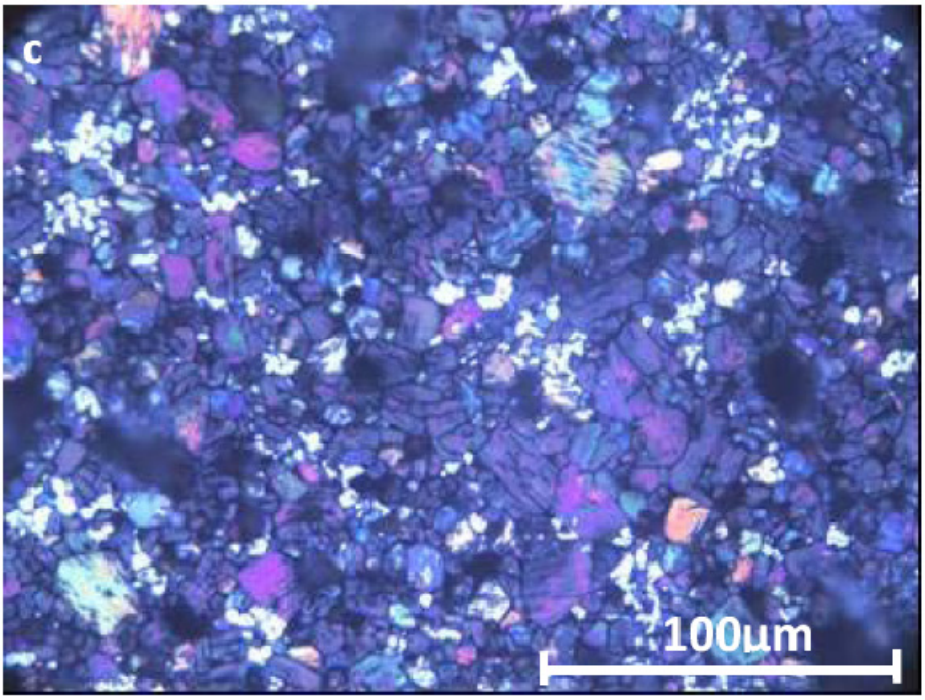

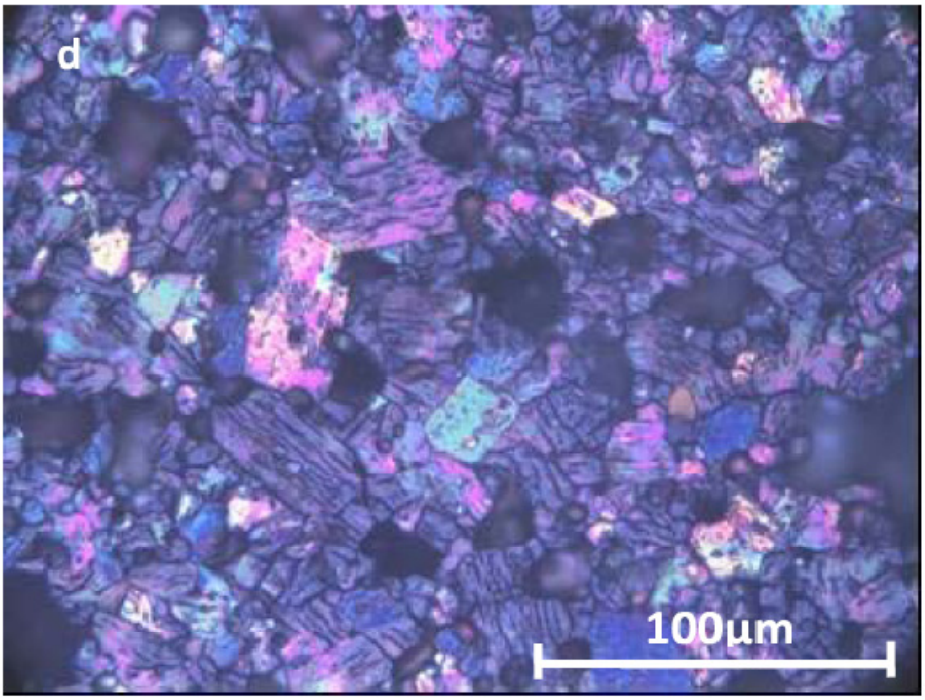

Figure 4.1 (*continued*)

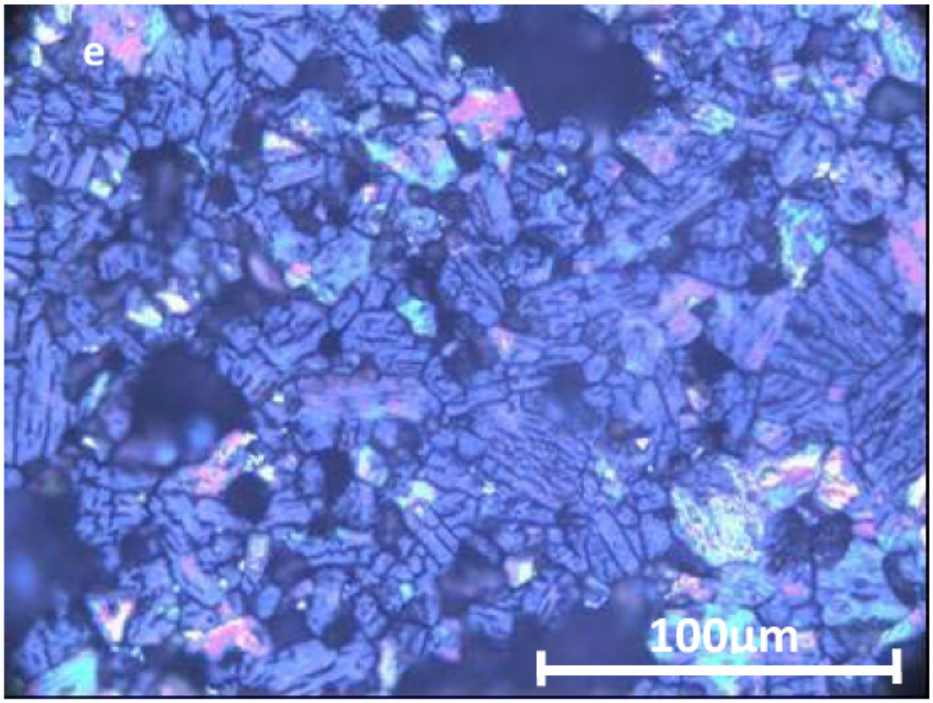

Figure 4.1: (a) SEM micrograph of 40 vol. % porous sample. The inset magnifies a kink band. (b) SEM micrograph of 55 vol. % porous sample. The inset magnifies the layered nature of the structure. (c) OM image of polished and etched surface of annealed 18 vol.% porous sample. (d) OM image of same sample after annealing for 24 h at 1600 °C, (e) OM image of same sample after a further 24 h (total 48 h) anneal at same temperature.

Table 4.1: Summary of porous Ti_3SiC_2 samples' properties (porosity, fraction of open pores, ultimate compressive strengths and average grain and pore sizes)

Porosity (vol. %)	Fraction of open pores vol. %	Ultimate compressive stress (MPa)	Average grain size (µm)	Average pore size (µm)
0	-	1300	8±4	0
5	10	820	8±3	15
18	30	290	7±3	7
40	70	100	13±5	60
55	90	60	7±4	20

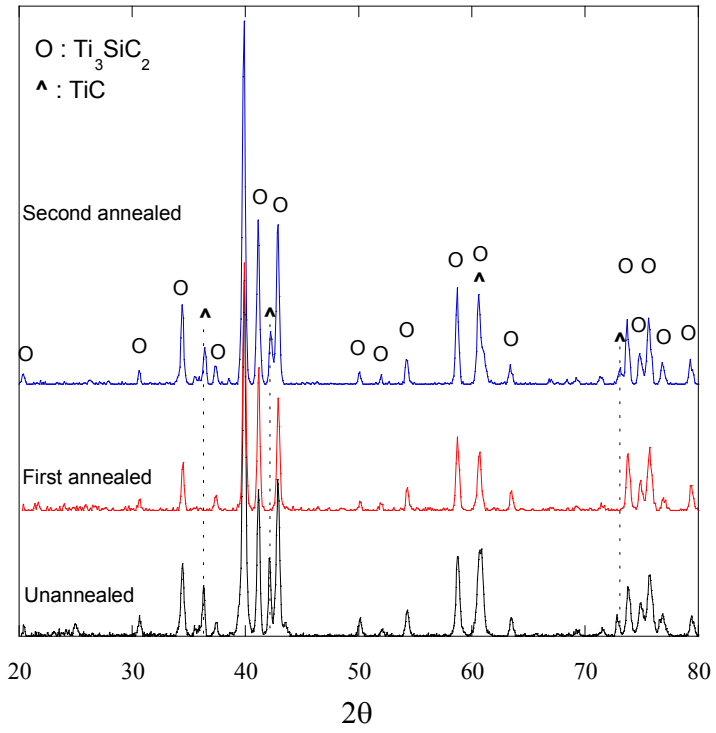

Figure 4.2: Typical XRD spectra of 18 vol. % sample, a) as-fabricated, b) after 24 h and, c) a further 24 h (48 h total) anneal in Ar at 1600 °C. Note disappearance and re-appearance of TiCx peaks, marked by vertical dotted lines.

The XRD patterns of the 18 vol.% sample - before and after annealing, twice at 1600 °C - are shown in Fig. 4.2. OM images of their polished and etched surfaces are shown in Figs. 4.1c, d and e. The changes in composition and microstructure of the 18 vol.% porous sample as a result of annealing can be summarized as follows:

a) The as-HIPed sample (Fig. 4.2a) contained unreacted TiC_x (white areas in Fig. 4.1c), and probably some $Ti_5Si_3C_x$ [66].

b) Annealing for 24 h at 1600 °C resulted in the disappearance of the TiC_x peaks (Fig. 4.2b) and a growth in grain and pore size (Fig. 4.1d). The porosity of the sample also increases from 18 vol.% to ~ 25 vol. %.

c) Annealing for another 24 h at 1600 °C did not change the porosity, but resulted in the re-emergence of TiC_x peaks (Fig. 4.2c). This TiC_x results from the dissociation of Ti_3SiC_2 when heated for extended periods in low Si partial pressure atmospheres and/or vacuum [67, 68]. The full-widths at half maximum of the TiC_x peaks after the second anneal were wider than for the as-received samples (compare Fig. 4.2a and c). Using the Scherer equation we estimated the size of the TiC_x particles to be ~ 0.08±0.01 μm. In other words, the TiC_x formed from the dissociation of Ti_3SiC_2 is in the form of a very fine dispersion; a fact confirmed that there is little difference between Figs 4.1d and e.

4.4.2 Uniaxial Compression Results:

Figure 4.3a shows the entire stress-strain curve of the 55 vol.% porous sample. The first cycle to a given stress-level has some plastic deformation. But all subsequent cycles to the same stress level are fully closed and without plastic deformation, which is very similar with those of Ti_2AlC shown in Ch.3. All other samples in this chapter show similar stress-strain curves. The hysteretic stress-strain loops at maximum stress of fully dense samples, 5 vol.% porous and 18 vol.% porous samples are compared in Fig. 4.3b. Those of 40 vol.% porous and 55 vol.% porous samples are shown in Fig. 4.3c. Typical σ_{eff} vs. ε hysteretic loops for all five samples tested herein are shown in Fig. 4.3d. Not surprisingly, increasing the porosity results in a reduction in stiffness, as well as an increase in W_d at any given σ.

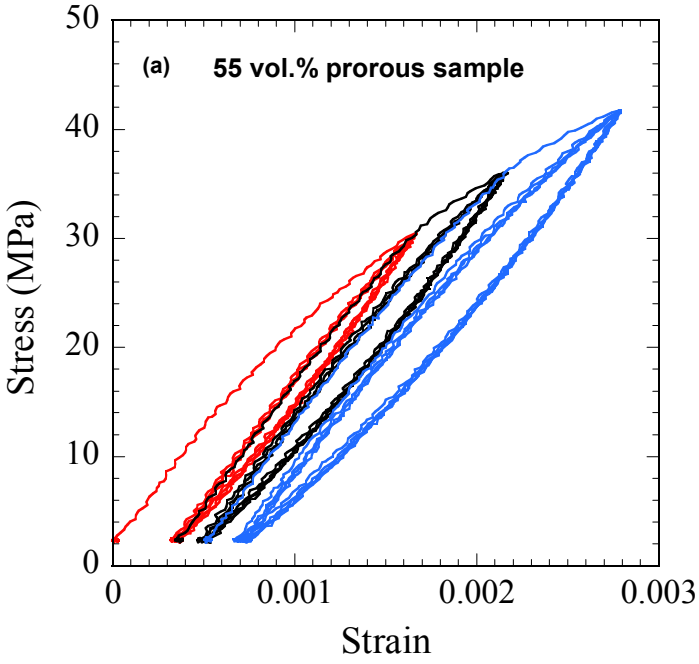

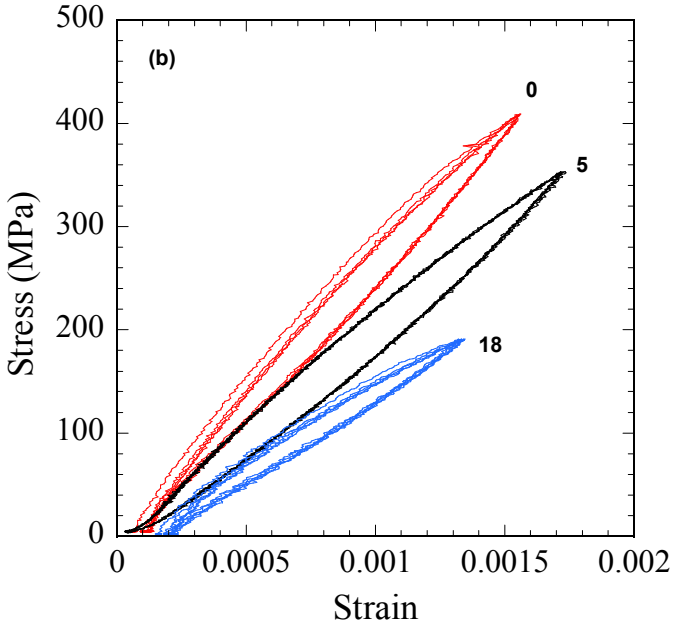

Figure 4.3 (*continued*)

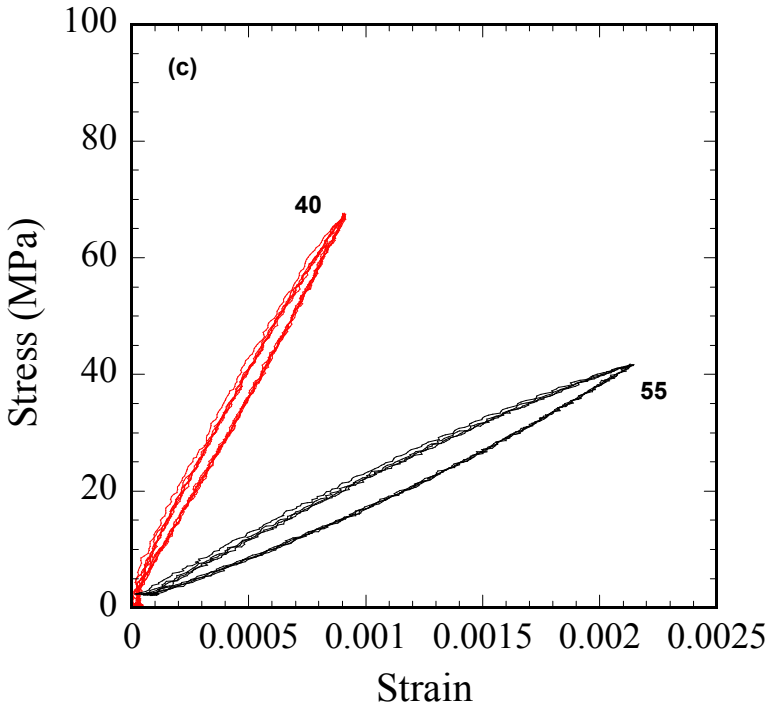

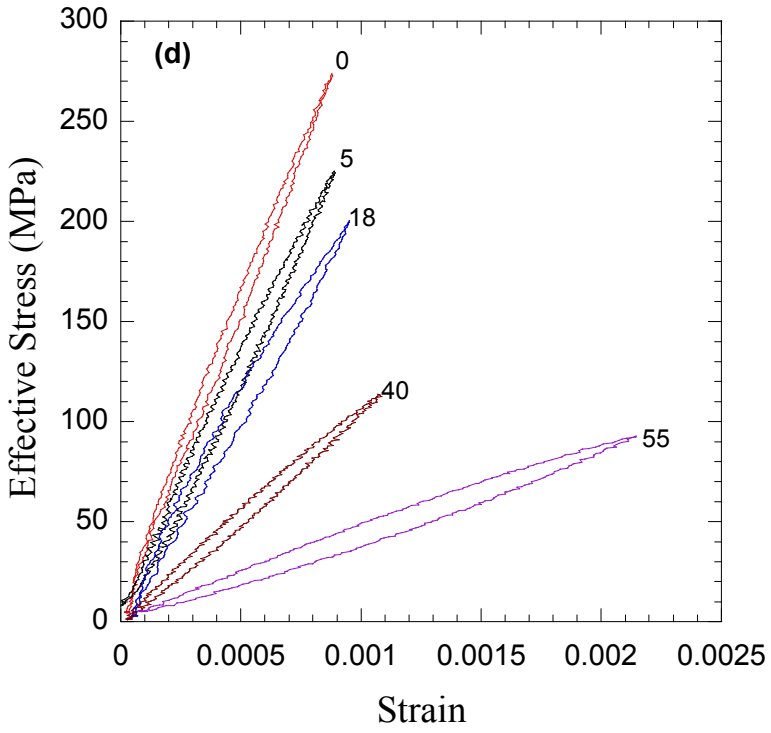

Figure 4.3 (*continued*)

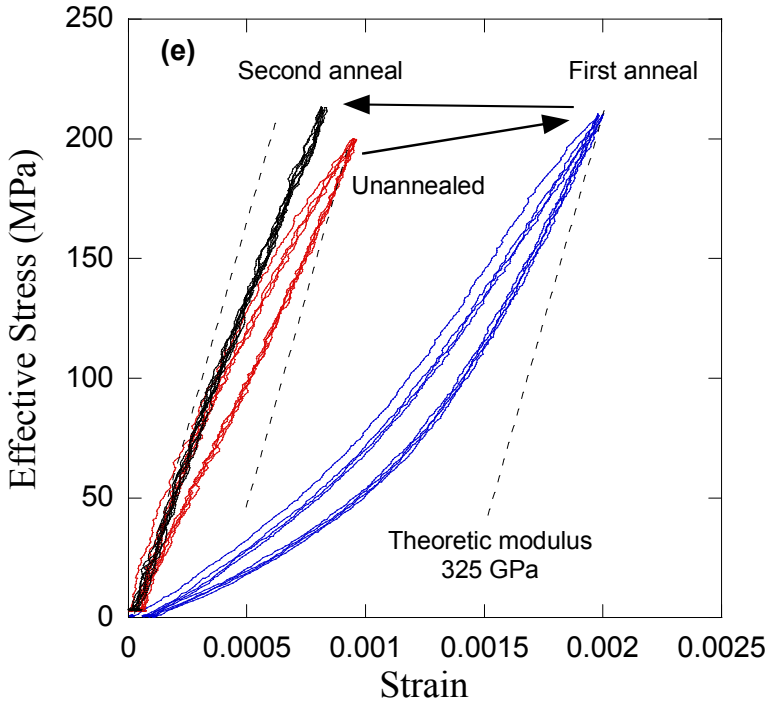

Figure 4.3: (a) The entire stress-strain curve of 55vol.% porous sample (b) Stress-strain loops at the maximum test stress of fully dense, 5% porous and 18% porous samples. In this, and most other graphs, the numbers shown represent the vol. % porosity (c) Stress-strain loops of 40% porous and 55% porous samples. (d) Typical effective stress-strain loops for samples with 5 different porosities. e) Typical effective stress-strain loops 18 vol. % porous sample as a function of annealing time at 1600 °C.

The effect of annealing on the σ_{eff} vs. ε curves for the 18 vol. % porous samples is shown in Fig. 4.3e. After the first 24 h anneal, the shape of the stress-strain curves changes from symmetrical and lenticular to an irregular shape (Fig. 4.3e). The shape of the latter is more reminiscent of cellular solids, in that a large deformation is observed at low stresses, before gradual stiffening [63]. Surprisingly, after the second 24 h anneal, the response of the sample is almost perfectly linear elastic. The slopes of the straight

inclined lines drawn in Fig. 4.3e are equal to the Young's modulus of Ti_3SiC_2 determined from ultrasound measurements [11, 69].

Figure 4.4 plots Eq. 4.1, viz. E^*/E_s vs. $(\rho^*/\rho_s)^2$. E^* was measured from the slopes of the initial unloading portions of the σ vs. ε curves (Fig. 4.3b and c). Least squares of these results yields a slope of 1.17 with a correlation coefficient, $R^2 > 0.99$.

Table 4.2: KNE parameters (σ_{eff}, ε_{NL}, $U_{NL, eff}$ and $W_{d,eff}$) of porous Ti_3SiC_2

Porosity, vol. %	σ_{eff} (MPa)	ε_{NL}	$U_{NL, eff}$ (MJ/m^3)	$W_{d, eff}$ (MJ/m^3)
55	67	0.000272	0.0086	0.0044
	80	0.000377	0.0145	0.0085
	93	0.000521	0.0237	0.0162
40	80	0.000070	0.0013	0.0019
	91	0.000109	0.0038	0.0029
	102	0.000127	0.0067	0.0044
	114	0.000166	0.0101	0.0070
18	134	0.000110	0.0052	0.0040
	167	0.000167	0.0160	0.0077
	200	0.000225	0.0235	0.0125
	233	0.000313	0.0420	0.0218
5	224	0.000178	0.0228	0.0118
	298	0.000287	0.0347	0.0272
	371	0.000421	0.0656	0.0551
	444	0.000645	0.1447	0.0950
0	207	0.000034	0.0024	0.0024
	274	0.000052	0.0094	0.0083
	342	0.000097	0.0237	0.0185
	409	0.000170	0.0517	0.0374

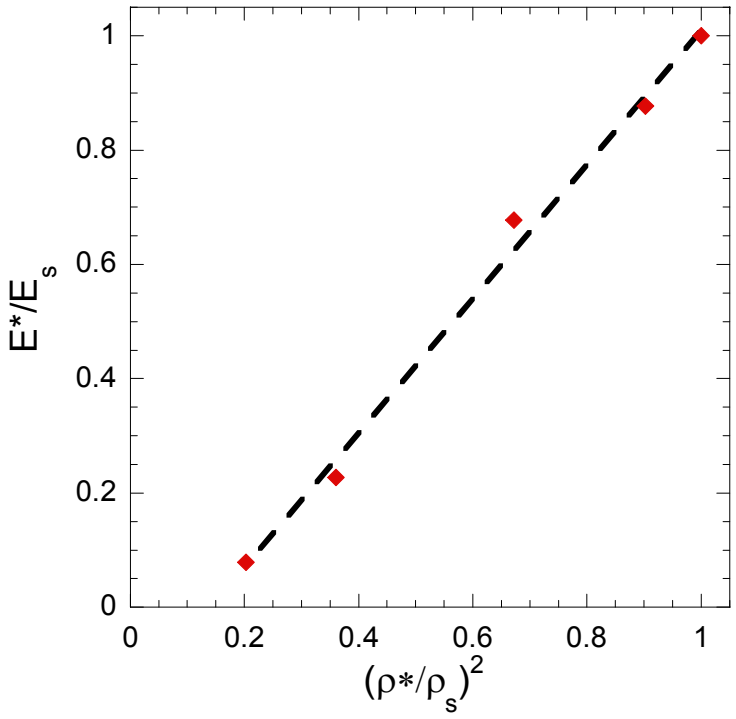

Figure 4.4: Effect of vol. % porosity on effective stiffness.

From the stress-strain curve, the KNE parameters (σ_{eff}, ε_{NL}, $U_{NL,eff}$ and $W_{d,eff}$) are obtained, and listed in Table 4.2. From our model in Ch. 2, the plots of ε_{NL} vs σ_{eff}^2, $U_{NL,eff}$ vs. $\varepsilon_{NL}^{1.5}$, $W_{d,eff}$ vs. σ_{eff}^2 and $W_{d,eff}$ vs. ε_{NL} should yield straight lines. Figure 4.5 show that, indeed, to be the case. Least squares analysis of the various lines shows that all R^2 values are > 0.98. The slopes of the lines shown in Fig. 4.5 are used to calculate the values of Ω/b and $N_k\alpha^3$, which, in turn are listed in Table 4.3.

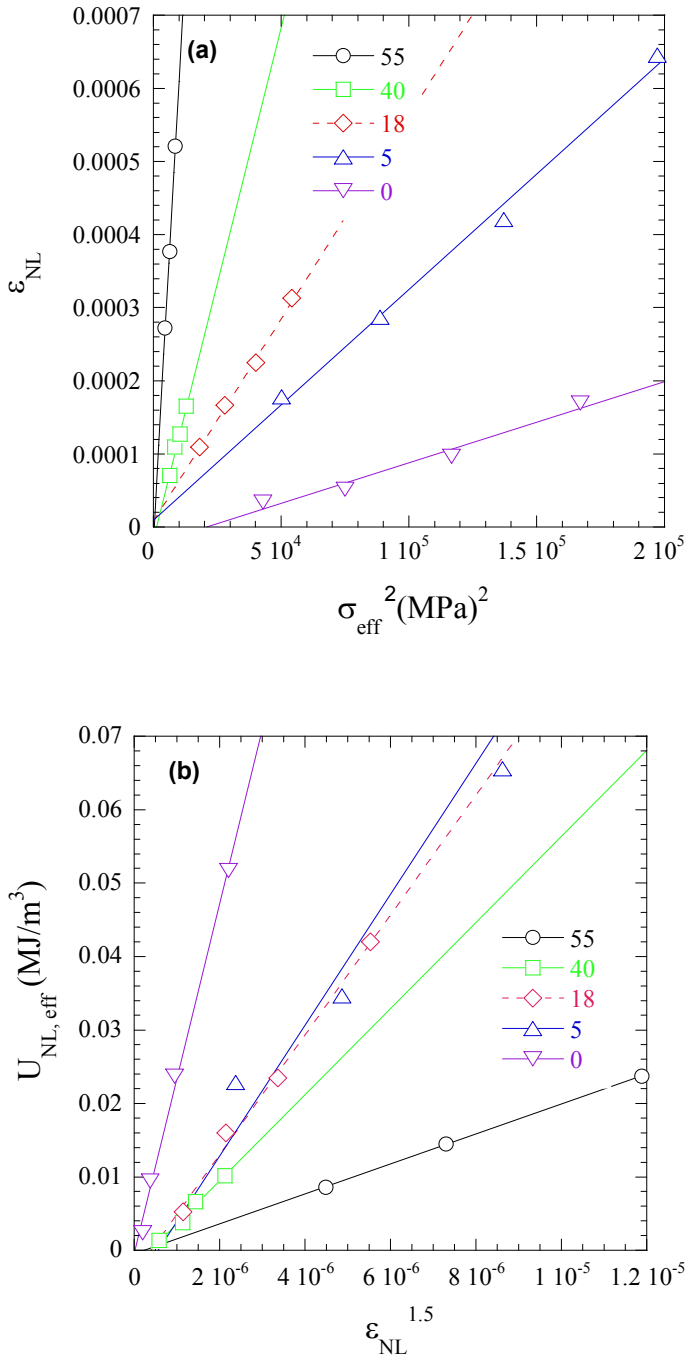

Figure 4.5 (*continued*)

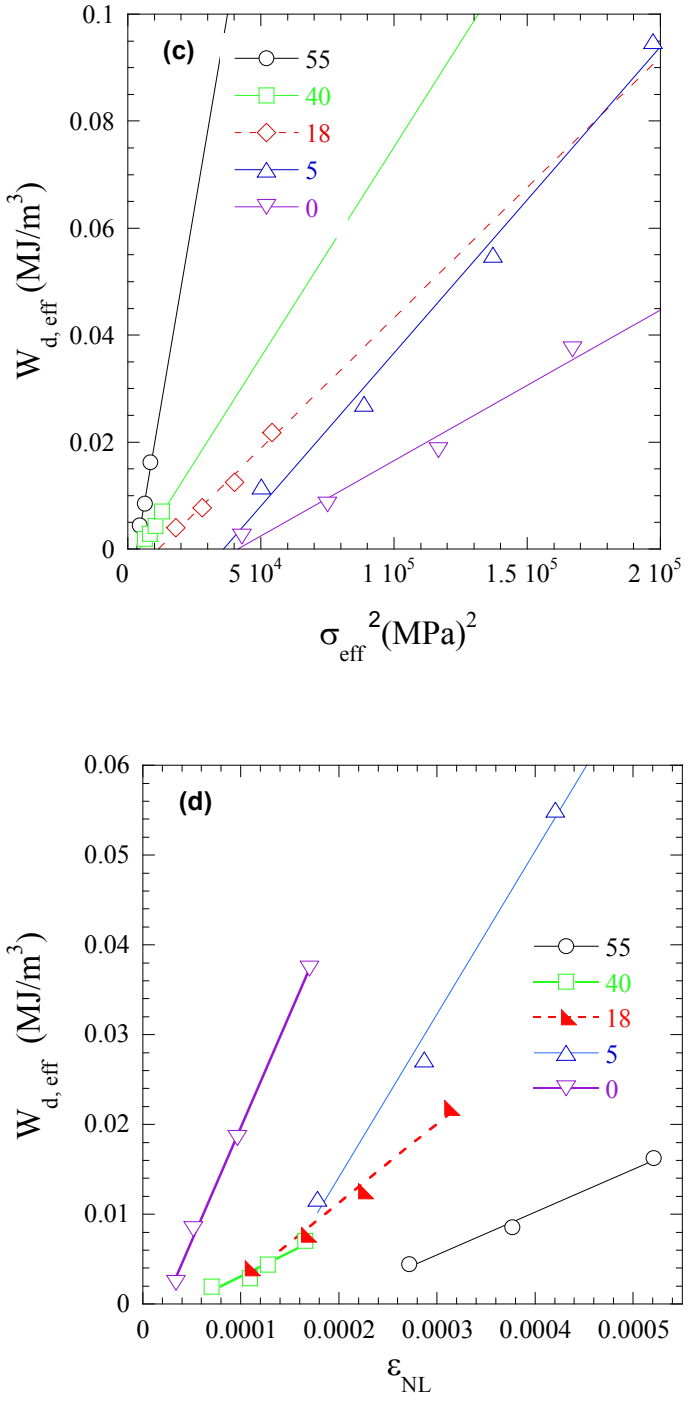

Figure 4.5: (a) Plots of ε_{NL} vs. σ_{eff}^2 (b) Plots of $U_{NL,eff}$ vs. $\varepsilon_{NL}^{1.5}$ (c) Plots of $W_{d,eff}$ on σ_{eff}^2 (d) Plots of $W_{d,eff}$ vs. ε_{NL} for the different porosity levels.

Table 4.3: Calculated values of Ti_3SiC_2 with different porosity. E^* is measured from initial unloading portions of σ vs. ε plots (Fig. 4.3b and c). G^* is from Eq. 4.2. σ_c is from Eq. 2.4 assuming $2\alpha = 4\mu m$. $N_k\alpha^3$ is from the first term of Eq. 2.17. Ω/b is from 2nd and 4th terms of Eq. 2.18.Reversible dislocation density ρ is from Eq. 2.12. ψ is from Eq. 4.5; η and E" are from Eq. 4.6.

Porosity (Vol.%)	E* GPa	G* GPa	σ_c	$\sigma_{t,eff}$ MPa	$N_k\alpha^3$	N_k μm^{-3}	Ω/b (MPa) 2nd term	Ω/b (MPa) 4th term	ρ(cm^{-2})	σ (MPa)	ψ	η	E" (GPa)
0	325	135	275	204	0.1	0.02	43	42	1×10^9	409	0.15	0.02	5.9
5	285	119	242	189	0.3	0.04	30	30	3×10^9	354	0.18	0.03	8.0
18	220	92	187	108	0.3	0.04	15	14	2×10^9	191	0.14	0.02	5.0
40	74	31	63	67	0.1	0.01	9.4	9.1	0.9×10^9	68	0.12	0.02	1.3
55	26	11	22	58	0.05	0.01	7.9	8.0	1×10^9	42	0.15	0.02	0.6

4.5 Discussion:

4.5.1 Validity of KNE Model

The results shown herein provide compelling evidence that our IKB-based dislocation model outlined in Ch. 2 is valid and applicable to porous Ti_3SiC_2 as well. The reasons are several and include:

a) By now it is fairly well established that fully reversible hysteresis loops are a signature of IKBs [15, 59, 62, 70]. The loops obtained in this work are indeed fully reversible (Fig. 4.3).

b) The results shown in Fig. 4.5 are gratifying and strongly suggest that the results can be analyzed in terms of our IKB-based model. The excellent agreement implies that indeed $U_{DP} << U_{IKB} \approx U_{NL}$, and that – for a given microstructure - $N_k\alpha^3$ is not a strong function of stress. It also implies that the procedure for extracting ε_{NL} from the stress-strain curves of porous solids (i.e. Eq. 4.4) is valid.

c) The intercepts in Fig. 4.5b and d - modeled to be the strain due to dislocation pileups – appear to increase with increasing porosity. It is worth noting that the uncertainty in measuring ε_{NL} is high, especially at low stresses.

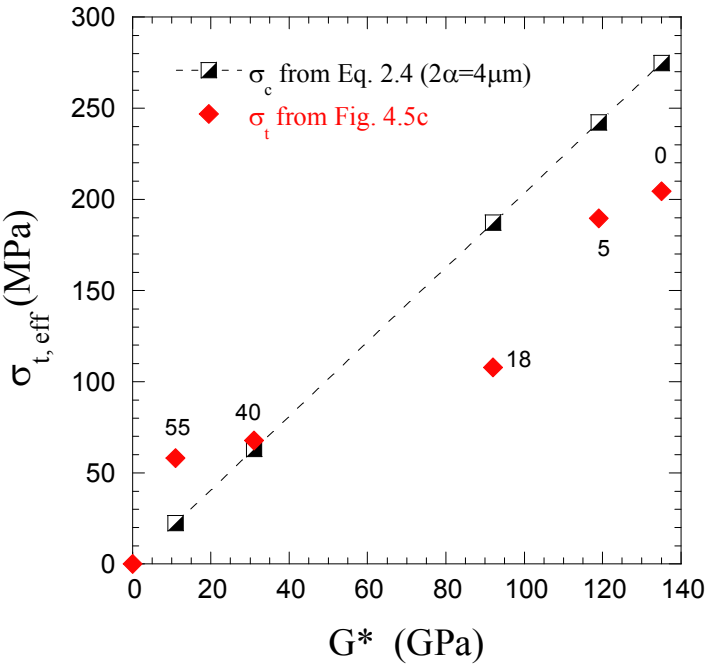

Figure 4.6: Plot of threshold stress $\sigma_{t,\,eff}$ vs. shear modulus, G* and calculated σ_c form Eq. 2.4 vs. G^*. Numbers represent vol. % porosity.

d) According to Eq. 2.15, the x-axes intercepts in Fig. 4.5c represent $\sigma_{t,eff}^2$. It is thus logical for this value to decrease with increasing porosity, as observed. Furthermore, if $\sigma_{t,eff} \approx \sigma_c$, then according to Eq. 2.4, a plot of $\sigma_{t,\,eff}$ vs. G* should yield a straight line that goes through the origin, as observed in Fig. 4.6. This figure plots measured $\sigma_{t,eff}$ and calculated G* values. The σ_c and $\sigma_{t,eff}$ for samples with different porosities are close. σ_c was calculated from Eq. 2.4, assuming a grain thickness, 2α of 4 μm, a value that is well

within the range of grain sizes measured from SEM and OM micrographs (see Table 4.1: Summary of porous Ti3SiC2 samples' properties (porosity, fraction of open pores, ultimate compressive strengths and average grain and pore sizes). For fully dense, 5 vol.% and 18 vol.% porous samples, σ_c is a little larger than $\sigma_{t,eff}$. This is because presumably σ_c is the threshold for an average grain to kink while $\sigma_{t,eff}$ is the threshold for the larger grains to kink. Here again the agreement is quite gratifying and implies that one major role of the pores is to reduce σ_t by decreasing G. Figure 4.6 also suggests that Eq. 4.1, and by extension Eq. 4.2, are good descriptors of how the moduli change with porosity.

A second important effect is a reduction in Ω/b (Table 4.3). In the porous samples, the Ω/b values range from 43 MPa to 8 MPa. These values are in excellent agreement with the 39 MPa determined previously for dense, fine-grained Ti_3SiC_2 and the 9.3 MPa obtained for coarse-grained Ti_3SiC_2 [15]. These values are also in agreement with the only measured value of CRSS on Ti_3SiC_2, viz. 41 MPa [60]. The effect of porosity is thus similar to that of increasing the grain size. The exact reason for this state of affairs is not understood at this time. Strictly speaking Ω/b should be independent of porosity level.

The values of $N_k\alpha^3$ in Table 4.3 (0.1-0.4) are a little lower than the previous values for Ti_2AlC in Ch. 3 (Table 3.3, 0.7-0.8). This is because effective values of σ and G were used in this chapter's calculation. From Eq. 2.11, the higher σ and lower G, because of porosity, both result in smaller $N_k\alpha^3$. From Table 4.1, it is obvious that, with the exception of the 40 vol.% sample, the α values are comparable, which implies that the changes observed in the $N_k\alpha^3$ values in Table 4.3 are due to changes in N_k in the range from 0.01 μm^{-3} to 0.04 μm^{-3}. And the reversible dislocation densities ρ at maximum test

stress calculated from these N_k and 2α are 1~3 x 10^9 cm^{-2} for all the samples with different porosities. This value is reasonable and comparable with the values obtained for Ti_2AlC in Ch. 3 (1~2 x 10^9 cm^{-2}).

4.5.2 Influence of Microstructure on Stress-Strain Curves

Before this work, the only microstructural KNE variable systematically studied had been grain size [15, 70]. It follows that the results shown in Fig. 4.3e are quite informative. When these results are combined with those shown in Fig. 4.2, it is apparent that the critical variable is the volume fraction of the TiC_x phase. In the as-fabricated samples, the TiC_x is present as an unreacted phase, with most probably some $Ti_5Si_3C_x$ [71]. After the first 24 h anneal, the reaction goes to completion and the volume fraction of TiC_x is reduced significantly (Fig. 4.2b). There was also some grain growth and a slight increase in volume fraction porosity from ≈ 0.18 to 0.25. All these factors enhanced the formation of IKBs and resulted in two consequences. The first is a ≈ 10 % increase in W_d. Second, and more important, a radical change in the shape of the stress-strain curves (Fig. 4.3e) from regular lenticular to bending lenticular shape. It is more characteristic of foams from some points of view [63]. This is an important result which suggests that highly porous MAX phase foams can be produced. Given that the energy dissipated by IKBs is at least an order of magnitude higher than in metals, the prospect of producing ultra-high energy absorbing MAX-based foams is an intriguing possibility.

The purpose of the second 24 h anneal at 1600 °C was to try and further enhance the damping capability. It thus was a surprise when the results shown in Fig. 4.3e were obtained; after the second anneal, the damping was almost totally quenched, a quenching

that correlated with the re-emergence of the TiC_x peaks. However, given that the TiC_x peak intensities in Figs. 4.2a and c are comparable, it follows that it is not the presence of TiC_x *per se* that is crucial, but its distribution. Clearly the TiC_x that forms upon the dissociation of Ti_3SiC_2 is much finer and more uniformly distributed than the unreacted TiC. How the former prevent the formation of IKBs is unclear at this time. The simplest explanation is that they effectively reduce the grain size to an extent that σ_c in Eq. 2.4 (or the threshold stress) is greater than the compressive strength of the material.

4.5.3 Technological Implications

There are several metrics by which damping capacity has been characterized. One is the specific damping capacity, ψ, defined as:

$$\psi = W_d/W \tag{4.5}$$

Another is η defined as:

$$\eta = \psi/(2\pi) \approx E''/E \tag{4.6}$$

where E" is the imaginary component of the modulus.

Table 4.3 summarizes the results obtained in this work. Interestingly, ψ appears to be a weak function of porosity level, which, at first blush, is somewhat surprising, until it is recognized that these ψ values are obtainable at quite different stresses (column 11 in Table 4.3). The potential of porosity in enhancing W_d is best appreciated by referring to Fig. 4.5c. If the effective compressive stress of the 55 vol.% porous samples could be doubled, the energy dissipated would be $\approx$ 0.16 MJ/m^3, a value that is approximately twice the highest value recorded in this work (see Table 4.2).

Besides the high ψ values, other important attributes to the damping described in this work are, high compressive strengths, high specific stiffnesses and, if required, low threshold stresses. It follows that porosity level, like grain size [59], becomes a useful microstructural variable that can be used to tune the stress level over which the damping is required.

Lastly it is important to note that the hysteretic stress-strain loops observed here is fully reversible, occurs without a reversal of stress, and is not susceptible to strain hardening, all important considerations from an applications point of view.

4.6 Conclusions

Based on the aforementioned results the role of porosity on the compressive response of KNE solids in general, and Ti_3SiC_2 in particular, can be summarized as follows:

Increasing the porosity levels reduces the strengths, stiffness values and threshold stresses needed for the formation of IKBs.

The nonlinear elastic response of the porous samples can be adequately described by the dislocation model outlined in Ch. 2, provided that the effective stress is plotted. The pores reduce the threshold stresses, a reduction that can be mostly accounted for by the concomitant reduction in shear moduli.

Extended heating at 1600 °C, resulted in a partial dissociation of the matrix, which in turn resulted in a fine distribution of TiC_x particles that totally quenched the formation of the IKBs.

5. Kinking nonlinear elastic deformation of Ti_3AlC_2, Ti_2AlC, $Ti_3Al(_{C0.5},N_{0.5})_2$ and $Ti_2Al(C_{0.5},N_{0.5})$

5.1 Introduction

The KNE behavior of the MAX phases is affected by several factors. In previous work, the effects of two microstructure variables, grain size [6] and porosity (Chs. 2 and 3) [15, 72], were explored and are reasonably well understood. At the same stress levels, coarse-grained samples have larger hysteretic loops than their fine-grained counterparts; porous samples have larger loops than their dense counterparts.

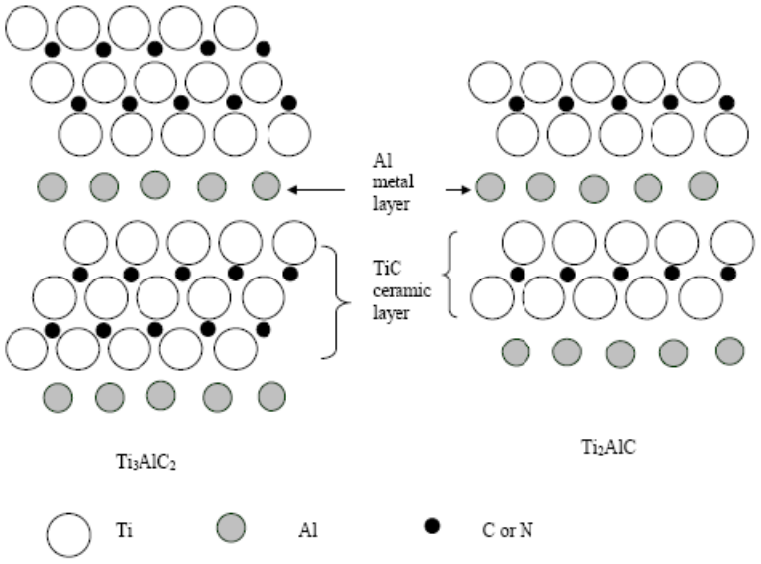

Figure 5.1: Unit cell structure of Ti_3AlC_2 and Ti_2AlC

The purpose of this chapter is to examine the effects of two other variables, namely, *solid solutions* and *unit cell structures* on the kinking nonlinear response of select MAX phases. Ti_3AlC_2 and Ti_2AlC and their solid solutions, $Ti_2Al(C_{0.5}N_{0.5})$ and $Ti_3Al(C_{0.5}N_{0.5})_2$ were made and cyclically tested in compression. The only difference between Ti_3AlC_2 and Ti_2AlC is the number of TiC_x layers separating the Al layers: in Ti_3AlC_2 there are

two, in Ti_2AlC, one (Fig. 5.1) [10]. The solid solutions, $Ti_2Al(C_{0.5}N_{0.5})$ and $Ti_3Al(C_{0.5}N_{0.5})_2$, henceforth denoted as Ti_3AlCN, have identical unit cells as their corresponding end members, except that half the C atoms are replaced by N atoms.

5.2 Experimental Details

The Ti_3AlC_2 sample was made from stoichiometric mixtures of Ti powder (-325 mesh, 99.5%, Alfa Aesar, MA), Al powder (-325 mesh, 99.5%, Alfa Aesar, MA) and graphite powers (-300 mesh, 99%, Alfa Aesar, MA). After 4 h mixing by ball milling, the powders were annealed at 625 °C for 3 h in a vacuum hot press following by a sintering at 1400 °C for 1 h with the pressure of ~ 45 MPa.

Same as in Ch. 2, the Ti_2AlC samples were prepared by cold isostatic pressing Ti_2AlC powders with an average particle size, d_{50} = 8 μm (Kanthal, AB, Sweden), followed by pressureless sintering at 1500 °C for 1 h in flowing Ar [15].

The Ti_3AlCN and $Ti_2AlC_{0.5}N_{0.5}$ samples are made from stoichiometric mixtures of Ti, Al, AlN (-200 mesh, 99.0% Cerac Inc., WI) and graphite powders after overnight ball milling and cold pressing to ≈ 600 MPa. The green bodies were pre-sintered in a vacuum furnace at 525 ºC for 2 h then at 625 ºC and for 10 h. The pre-sintered pellets were then sintered in a hot isostatic press (HIP) at temperature of 1400 ºC and pressure of 100 MPa for 10 hr [73, 74].

To grow the grains of the solid solution samples, they were annealed at 1400 ºC for 48 h in flowing Ar gas.

5.3 Results

5.3.1 Microstructural characterization

OM micrographs of two solid solutions and Ti_3AlC_2 are shown in Fig. 5.2 and SEM micrographs are shown in Fig. 5.3. Those of Ti_2AlC are shown in Ch. 3 (see Figs. 3.1a and 3.2a).

OM micrographs of the as-fabricated Ti_3AlCN and $Ti_2Al(C_{0.5},N_{0.5})$ samples, shown respectively in Fig. 5.2a and b, were comprised of two grains sizes; large plate-like grains, and smaller equiaxed grains. The stark difference in the grain sizes is more clearly shown in the SEM micrograph shown in Fig. 5.3a. This duplex microstructure is similar to that of Ti_3SiC_2 and occurs when the holding time at high temperatures is insufficient for the growth of the large grains [66]. Because grain growth is much faster along the a-than the c-direction, the latter grow as hexagonal plates with their large dimension along the a-direction [66].

As noted above, to rid the solid solutions of the fine grains, they were annealed at 1400°C for 48 h. The resulting microstructures of Ti_3AlCN (Figs. 5.2c and 5.3b) clearly indicate that the sample remained fully dense and that most of the small grains disappeared, with little growth in the size of the coarse grains. In the case of $Ti_2Al(C_{0.5}N_{0.5})$, in addition to the disappearance of many of the smaller grains, a multitude of pores appeared (Fig. 5.3c). The reason(s) for their formation is not understood at this time, but may be due to an incipient dissociation and the formation of nitrogen gas.

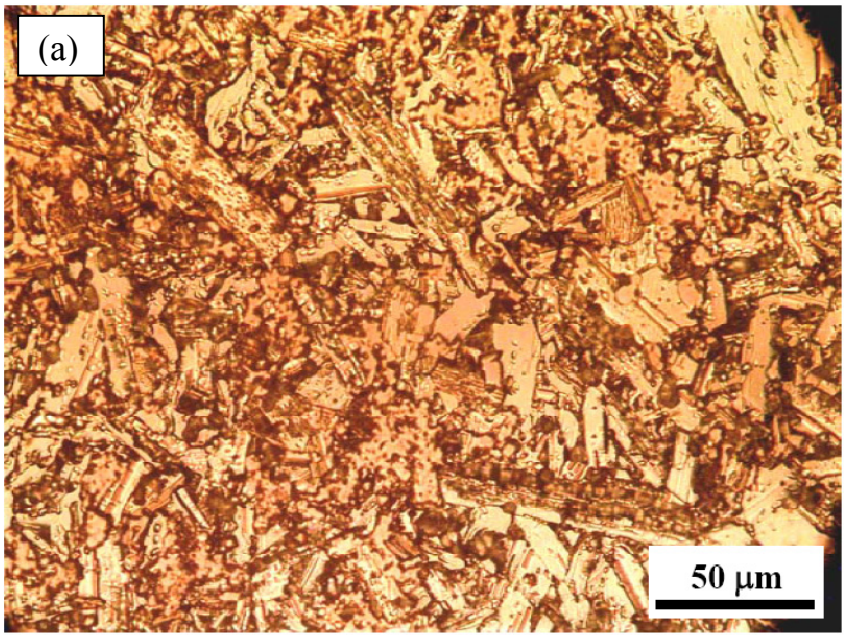

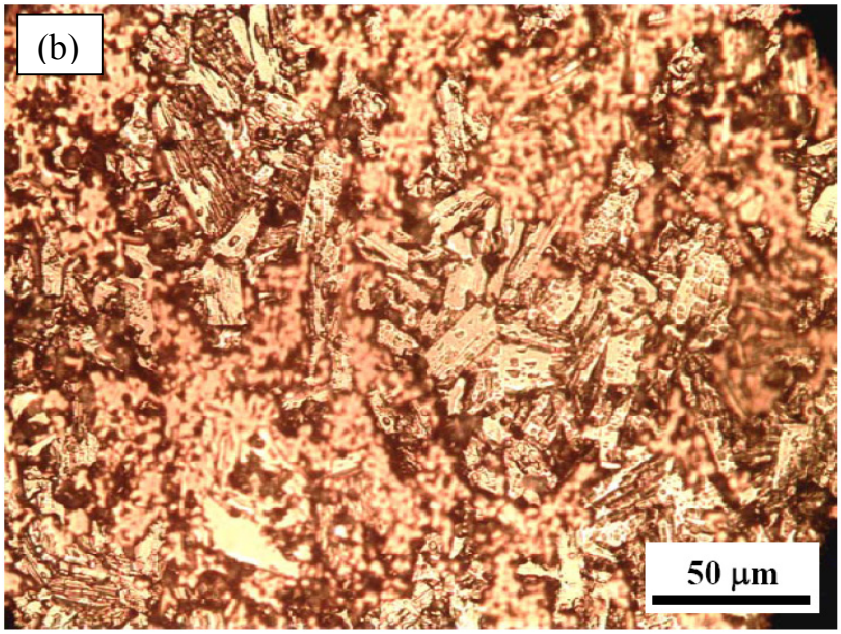

Figure 5.2: (*continued*)

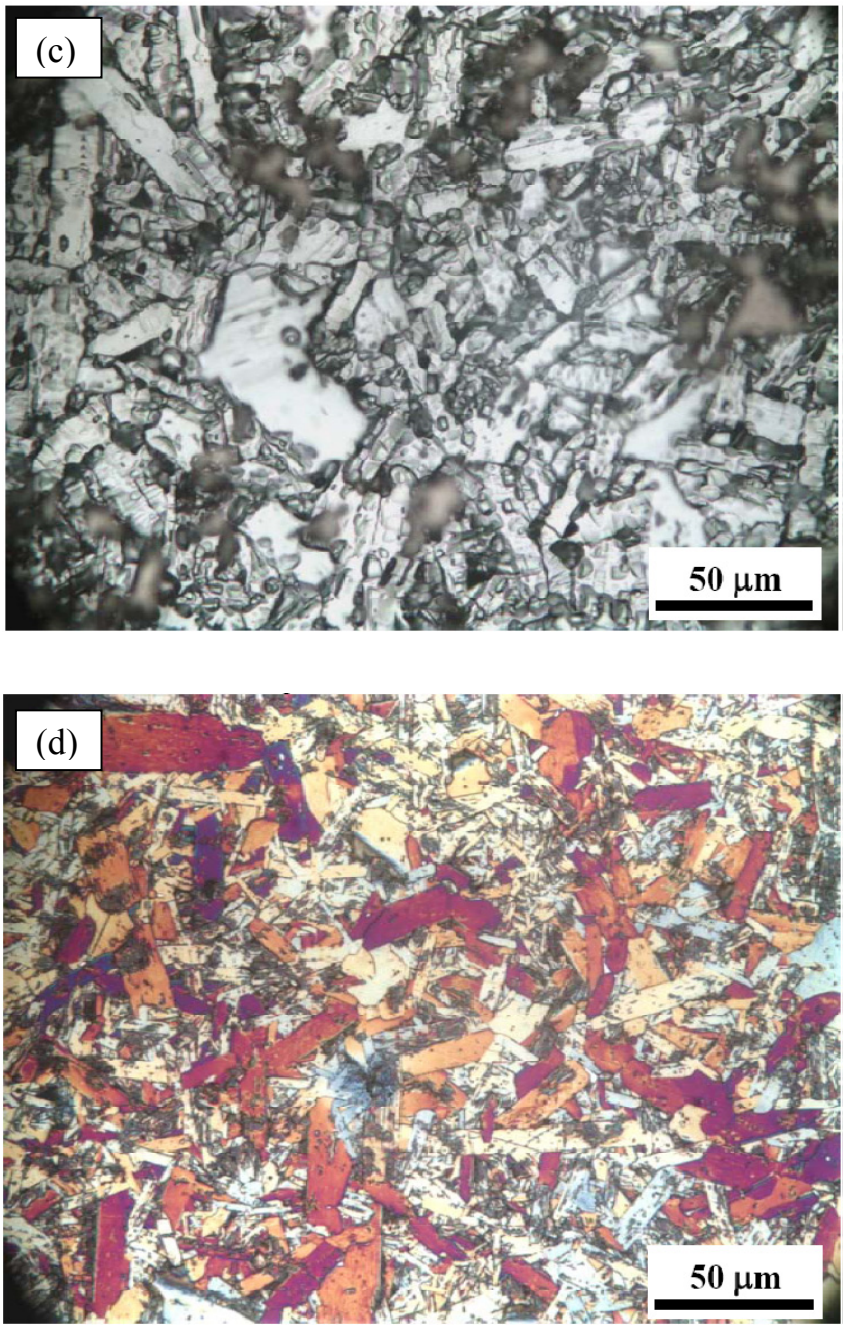

Figure 5.2: Optical micrograph of (a) Ti_3AlCN before annealing (b) $Ti_2Al(C_{0.5}N_{0.5})$ before annealing (c) Ti_3AlCN after annealing (d) Ti_3AlC_2

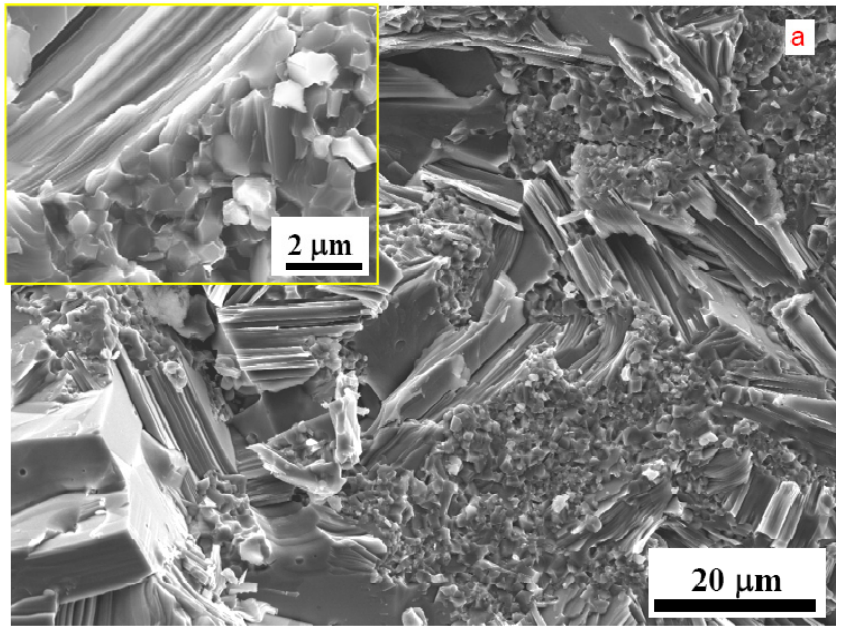

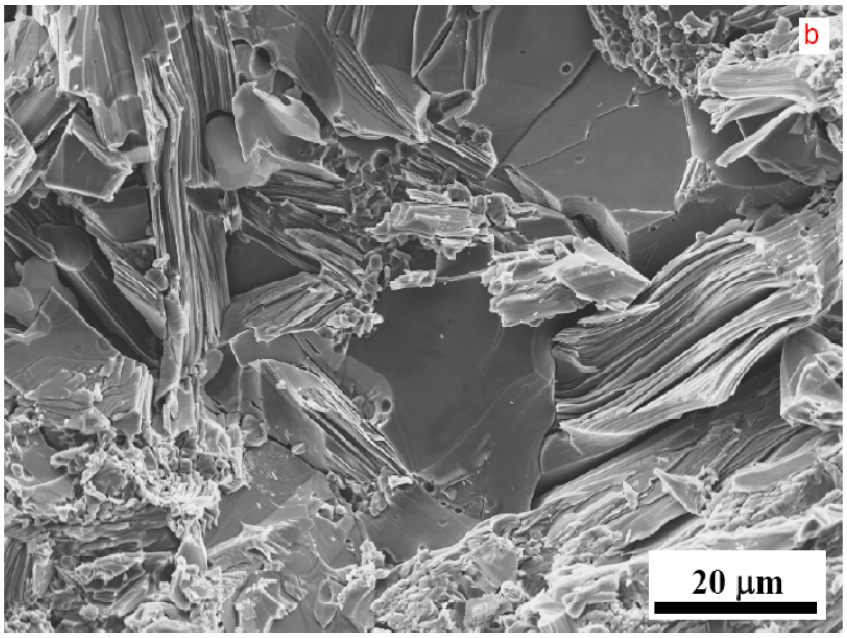

Figure 5.3: (*continued*)

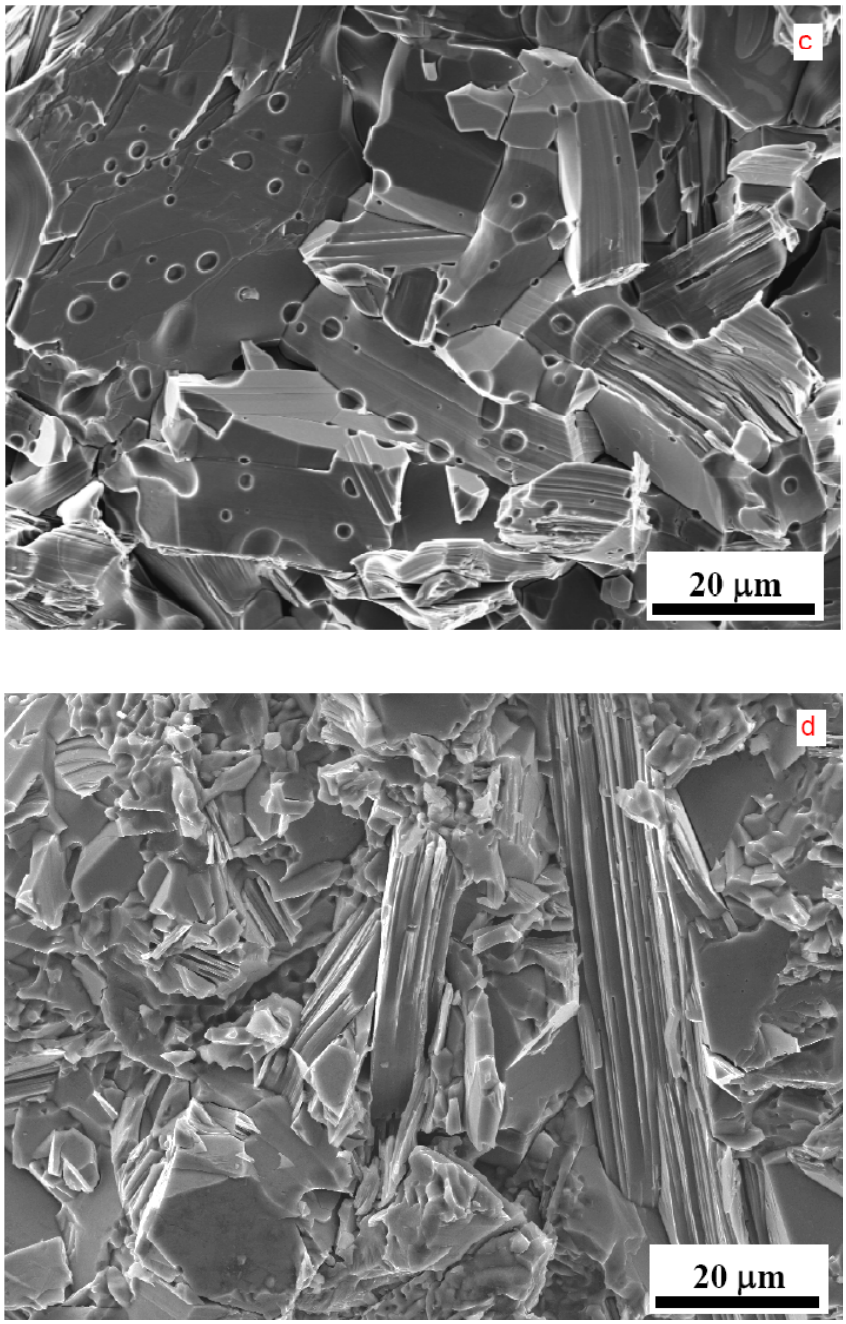

Figure 5.3: (*continued*)

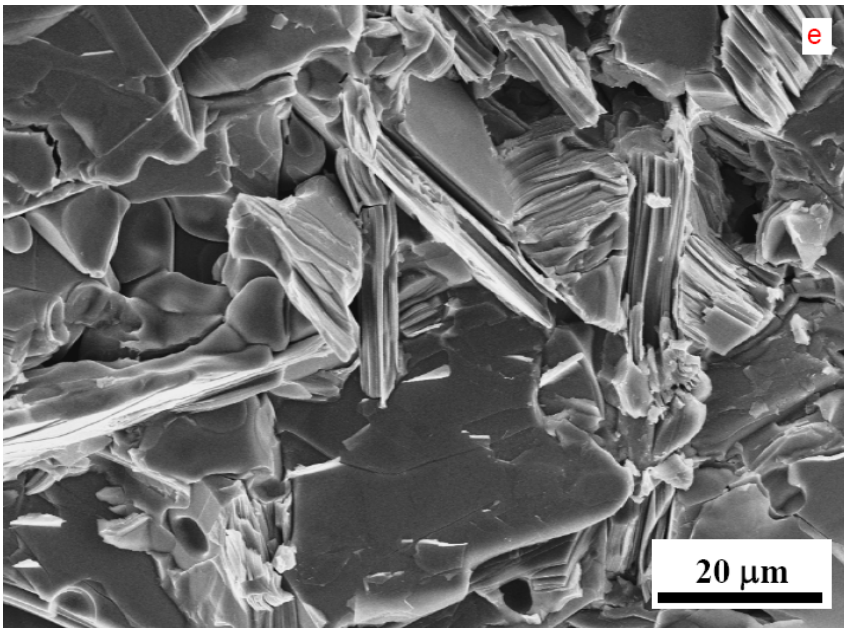

Figure 5.3: SEM micrographs (a) Ti_3AlCN before annealing (b) Ti_3AlCN after annealing (c) $Ti_2Al(C_{0.5}N_{0.5})$ after annealing (d) Ti_3AlC_2 (e) Ti_2AlC

Figures 5.2d and Fig. 5.3d show the microstructure of Ti_3AlC_2. When these micrographs are compared to those of the annealed Ti_3AlCN, it is reasonable to assume that all samples used in this work had comparable plate-like grains with diameters of 70 ~ 130 μm and thicknesses, viz. 2α values, that varied between 7 and 14 μm. In later calculation, we assume all $2\alpha = 10$ μm.

5.3.2 Cyclic Compression Results

Typical stress-strain curves – progressively shifted to the right for clarity - for the $Ti_2Al(C_{0.5}N_{0.5})$ sample are shown in Fig. 5.4a. At stress levels below 400 MPa, the response of the virgin sample, curve A, was linear elastic. At 620 MPa, obvious fully

reversible hysteretic loops are present, curve B. At 720 MPa, the hysteretic loops are larger, curve C, but they are not fully reversible. In other words, a very small plastic deformation is recorded at this stress. It is important to emphasize that the extent of the plastic deformation is quite small. When the sample was then unloaded, and reloaded to 620 MPa, curve D, the loops were slightly larger than upon loading the first time, curve B. When the sample was reloaded to a stress of 400 MPa, a small loop is observed where none was present for the virgin sample (compare red loop in D, with A).

Compared with this fully dense sample, the annealed $Ti_2Al(C_{0.5}N_{0.5})$ porous sample, curve E, shows a lower modulus and large loops at low stress level (250 MPa). A not too surprising result given the results shown in Chs. 3 and 4. The Young's moduli are determined from the slopes of lines - dashed lines in Fig. 5.4a and 5.4b – that are tangent to the loops during initial unloading.

Fully reversible hysteretic stress-strain loops were also recorded for Ti_3AlCN, Ti_3AlC_2 and Ti_2AlC (Fig. 5.4b). At ~ 300 MPa - horizontal line in Fig. 5.4b – the response of un-annealed Ti_3AlCN is linear elastic. Annealing reduces the threshold stress and fully reversible loops are observed at stresses of < 300 MPa (Fig. 5.4b). Note that the Young's moduli for Ti_3AlCN do not change upon annealing; those for $Ti_2Al(C_{0.5}N_{0.5})$ did, presumably as a result of the porosity.

Both Ti_3AlC_2 and Ti_2AlC samples show similar hysteretic loops also in stress-strain curves as shown in Fig. 5.4b. Compared with Ti_3AlC_2, Ti_2AlC has lower Young's modulus, and larger hysteretic loop at ~ 300 MPa.

The Young's moduli measured here from stress-strain curves are close to those measured by ultrasound [57, 74, 75]and listed in Table 5.2.

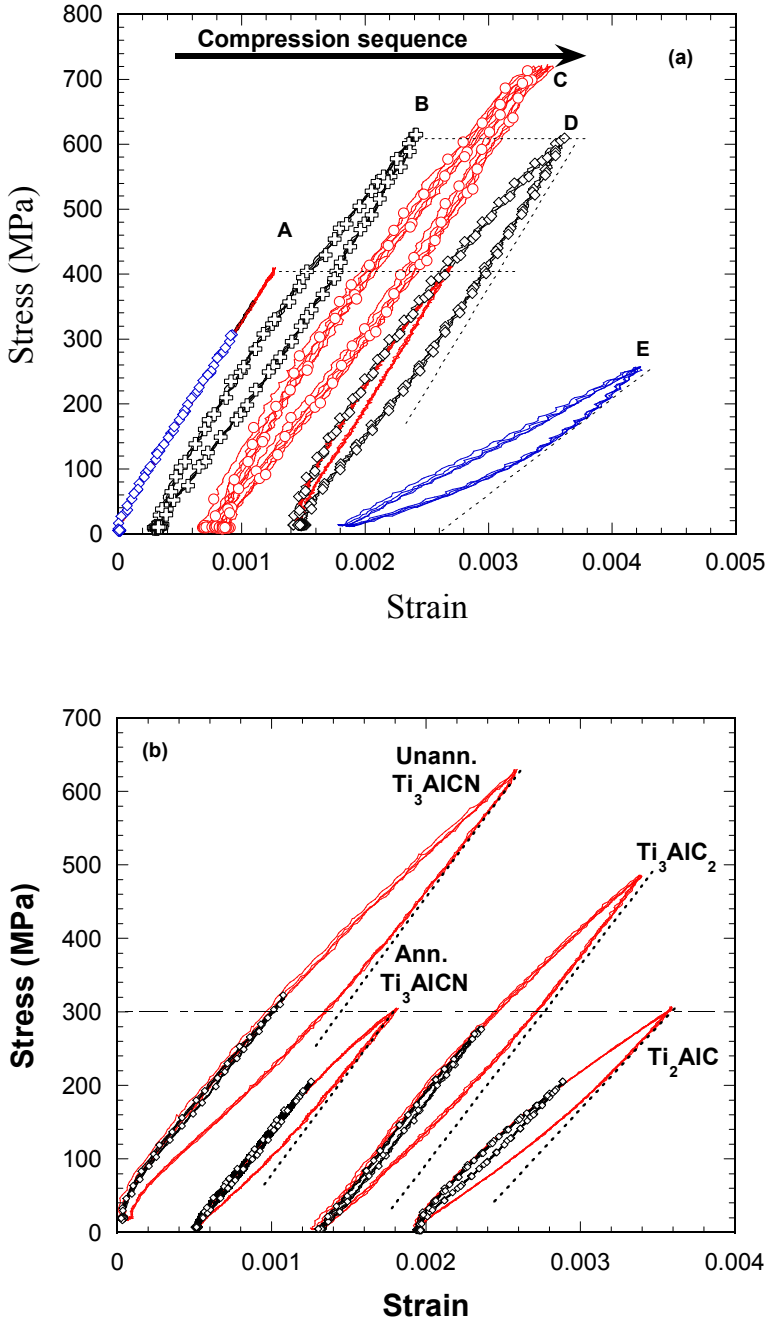

Figure 5.4: Test stress-strain curve of of (a) $Ti_2Al(C_{0.5}N_{0.5})$ and (b) Ti_3AlCN, Ti_3AlC_2 and Ti_2AlC

5.3.3 Application of KNE model

Table 5.1 lists the four parameters, σ, ε_{NL}, U_{NL} and W_d, used to characterize the KNE deformation tested in this chapter. The linear plots of ε_{NL} vs. σ^2, U_{NL} vs. $\varepsilon_{NL}^{1.5}$, W_d vs. σ^2 and W_d vs. ε_{NL} according to Eqs. in Ch. 2 are shown in Fig. 5.5a, b, c and d, respectively. The lowest correlation coefficient, R^2, is > 0.98 for all plots except one, the U_{NL} vs. $\varepsilon_{NL}^{1.5}$ plots of Ti_3AlC_2, which is > 0.97.

Table 5.1: List of stress σ, nonlinear strain ε_{NL}, stored nonlinear energy U_{NL} and dissipated energy W_d for Ti_3AlC_2, Ti_2AlC, $Ti_2Al(C_{0.5}N_{0.5})$ and Ti_3AlCN samples.

	σ MPa	ε_{NL}	U_{NL} MJ/m^3	W_d MJ/m^3
Ti_3AlC_2	280	0.00017	0.020	0.011
	349	0.00025	0.035	0.029
	417	0.00038	0.063	0.054
	486	0.00051	0.122	0.087
Ti_2AlC	205	0.00023	0.024	0.015
	237	0.00032	0.038	0.027
	271	0.00042	0.057	0.042
	306	0.00059	0.091	0.061
	336	0.00071	0.119	0.085
$Ti_2Al(C_{0.5}N_{0.5})$	462	0.00018	0.048	0.048
	511	0.00024	0.082	0.073
	561	0.00034	0.116	0.102
	610	0.00044	0.160	0.146
Ti_3AlCN Un-annealed	321	0.00010	0.018	0.009
	426	0.00017	0.044	0.028
	526	0.00033	0.096	0.074
	629	0.00050	0.154	0.136
Ti_3AlCN annealed	156	0.00008	0.002	0.001
	206	0.00009	0.008	0.006
	255	0.00014	0.018	0.015
	305	0.00023	0.041	0.031

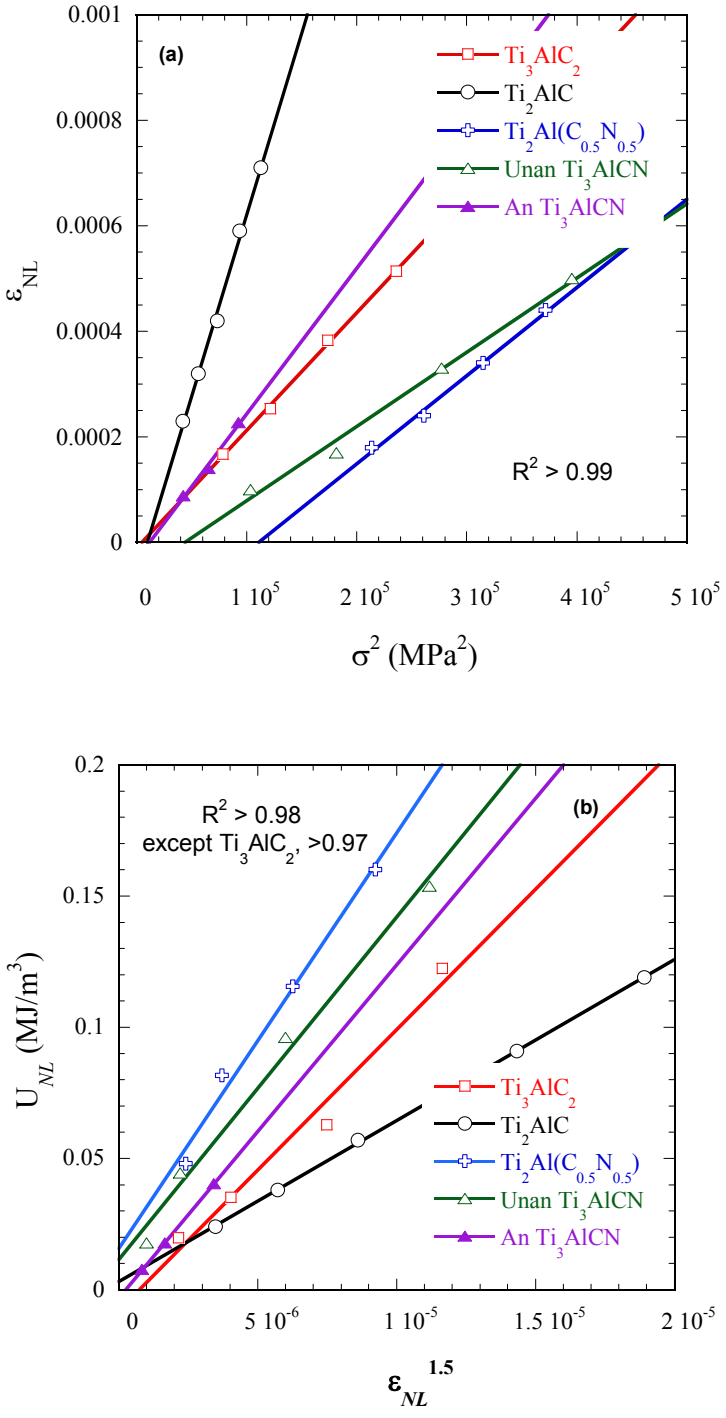

Figure 5.5: (*continued*)

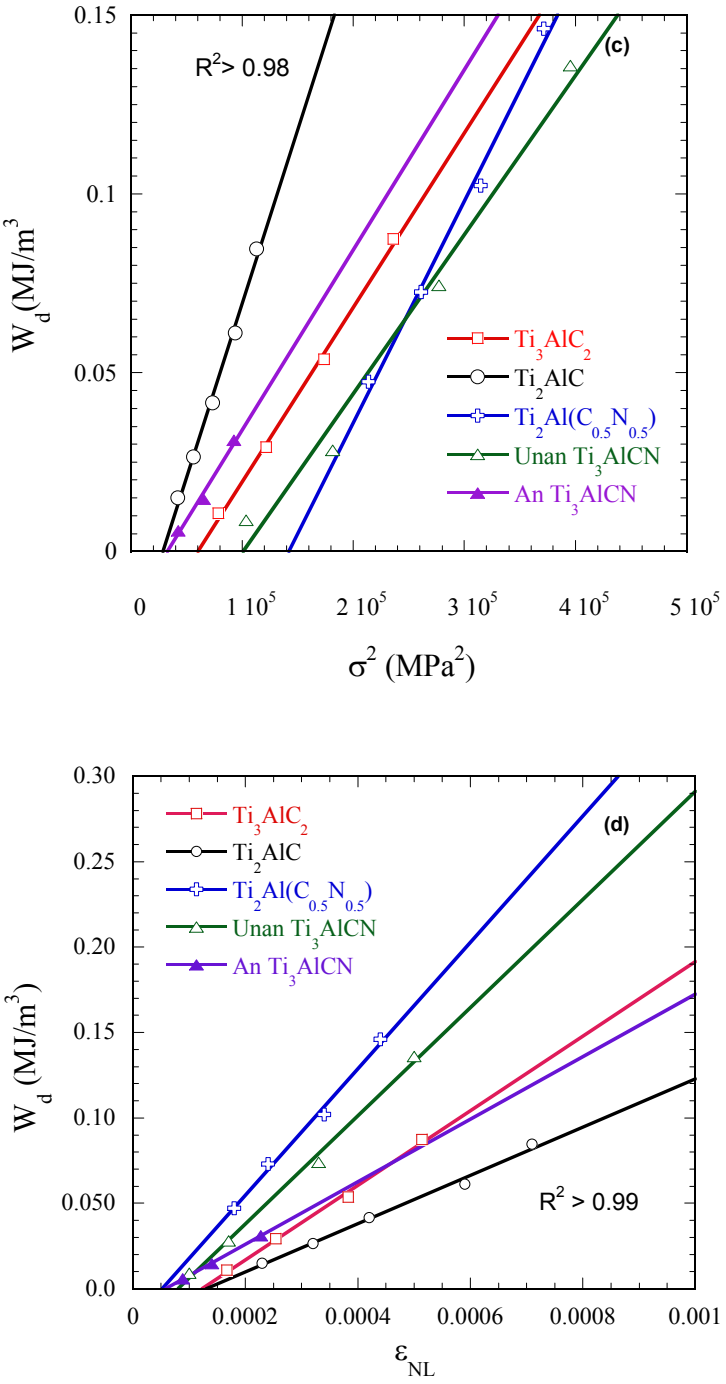

Figure 5.5: Model plots (a) σ vs. ε_{NL}^2 (b) U_{NL} vs. $\varepsilon_{NL}^{1.5}$ (c) W_d vs. σ^2 (d) W_d vs. ε_{NL}

Table 5.2: List of physical constants, E, G, ν and b, and calculated values of γ_c, σ_c and σ_t (see text). For all cases, we assumed, $2\alpha = 10$ μm, b = 3Å, w = 5b and $\nu = 0.2$.

	E GPa	G GPa	σ_c MPa	σ_t* MPa	σ_t‡ MPa	γ_c (rad)
Ti_3AlC_2	298[75]	124[75]	160	244	205	0.01
Ti_2AlC	277[57]	119[57]	153	170	98	0.01
Un-ann. $Ti_2Al(C_{0.5},N_{0.5})$	290[74]	123[74]	158	376	295	0.01
Un-ann. Ti_3AlCN	330[74]	137[74]	176	317	286	0.01
Ann. Ti_3AlCN			176	180	160	0.01

* From W_d vs. σ^2 plots (Fig. 5.5c)
‡ From stress-strain curves (Fig. 5.4a and b).

Table 5.2 lists the physical constants needed for the calculation and the calculated values of σ_c and γ_c. σ_c was calculated from Eq. 2.4 and γ_c was calculated from Eq. 2.5. For all calculations, w = 5b, $2\alpha = 10$ μm, b = 3Å, and $\nu = 0.2$. The threshold stress, σ_t, was obtained by two different methods. The first is from plots of W_d vs σ^2 (Fig. 5.5c). According to Eq. 2.15, the x-intercept is σ_t^2 and σ_t can be calculated, referred to as σ_t* (column 5 in Table 5.2). The second method is from the point at which the stress-strain curves deviate from linearity, henceforth referred to as σ_t‡ (column 6 in Table 5.2). Based on these two method, it is reasonable to assume that σ_t* is the threshold for grains with average thickness while, σ‡ is the threshold for grains with the largest thickness. So normally as observed, $\sigma‡ < \sigma_t$*.

Based on the results shown in Figs. 5.5, the model presented in Ch. 2, and the physical constants listed in Table 5.2, the values of Ω/b, $N_k\alpha^3$, N_k, $2\beta_{xc}$ and $2\beta_x$ were calculated and are listed in Table 5.3. The agreement of Ω/b calculated using three different experimental slopes, especially the first and third, are reasonable.

Table 5.3 Calculated values of Ω/b, $N_k\alpha^3$, N_k, $2\beta_{xc}$ and $2\beta_x$. For all cases, we assumed, $2\alpha = 10$ μm and $w = 5b$.

	Ω/b (MPa) from Eq. 2.18			$N_k\alpha^3$	N_k (μm^{-3})	$2\beta_{xc}$ (μm)	σ (MPa)	$2\beta_x$ (μm)	ρ (cm^{-2}) x 10^9
	2^{nd} term	3^{rd} term	4^{th} term						
Ti_2AlC	24	24	22	0.7	0.006	0.8	336	1.9	2
$Ti_2Al(C_{0.5},N_{0.5})$	62	84	62	0.7	0.001	0.8	610	3.3	1
Ti_3AlC_2	36	37	36	0.4	0.003	0.8	486	2.5	2
Un-ann. Ti_3AlCN	53	50	53	0.2	0.002	0.8	629	3	1
Ann. Ti_3AlCN	30	54	31	0.4	0.003	0.8	305	1.5	1

5.4 Discussion

Clearly all solids tested herein are KNE solids, with the unit cell structure, solid-solution, grain-size distributions and preload history all influencing the threshold stresses and the shapes and extent of hysteresis observed.

In previous studies on the MAX phases, it was assumed that σ_t is independent of deformation history [6, 15, 25]. It is now becoming apparent that this is not always the case. For example, during the nanoindentations of single crystals of ZnO [76], GaN [21], $LiNbO_3$ [77], and sapphire [19] pop-ins result in the formation of multiple domains that rotate basal planes into directions of shear, greatly enhancing IKB activity. The same is true of Mg polycrystalline samples; a small deformation is sometimes needed to activate IKB activity [78]. The results shown in Fig. 5.4a, confirm this notion: it was only after the sample was loaded to 700 MPa that loops were seen at 400 MPa. The mechanism by which this occurs is unclear, but the formation of dislocation pileups, microcracking and grain boundary sliding are distinct possibilities. Better understanding of what is occurring here is important because it suggests a method by which otherwise brittle solids could be endowed with limited ductility.

The fact that porous sample can dissipate more energy at same stress level (comparing curve E with other curves in Fig. 5.4a) is predictable and agrees well with previous results [15, 72].

The plots in Fig. 5.4b show the influence of grain size distribution. Clearly, annealing changes the grain size distribution of Ti_3AlCN (compare Figs. 5.2a, c and 5.3a, b), but does not affect the linear elastic properties. The two samples have nearly identical Young's moduli. However, the kinking nonlinear response is changed. In the un-annealed sample, the small grains presumably resist "kinking" of the larger layered grains. This would explain why the nonlinear deformation is only observed at higher stress levels (>300 MPa, Fig. 5.4b).

As shown in Fig. 5.4b, Ti_2AlC is a less stiff than Ti_3AlC_2, which ultimately results in the larger hysteretic loops at a given stress level. The difference between the two materials can be explained from their unit cell structure. From Fig. 5.1, Ti_3AlC_2 has a sandwich structure with two TiC layers and one Al layer; Ti_2AlC has a similar structure but with one TiC layer and one Al layer. Thus Ti_3AlC_2 has a higher fraction of the stronger TiC bonds, which results in higher values of G. Ti_2AlC is more layered, which enables it to kink more easy.

From Table 5.2, the calculated σ_c values are in good agreement with the experimental $\sigma‡$ and σ_t* values for Ti_2AlC, Ti_3AlC_2 and annealed Ti_3AlCN. The agreement for the other two samples, un-annealed Ti_3AlCN and un-annealed $Ti_2Al(C_{0.5}N_{0.5})$, do not agree well. The main reason for this phenomenon is believed to be the presence of the small grains in the two solid solution composition samples (Fig. 5.2a,

b and Fig. 5.3a). These small grains resist the kinking of large grains and result in the increase of the measured threshold stresses observed.

A clear result shown in Table 5.3 is the effect of n in $M_{n+1}AlX_n$ on the CRSS; increasing n from 1 to 2 increases the latter by 50 %, from ≈ 22 MPa to 36 MPa. Note that a some part of that increase is probably related to the increase in G (Table 5.2).

All materials have CRSSs or Ω/b values, in the range of 22 to 62 MPa as shown in Table 5.3. Clearly and consistent with its definition, the composition affects this value. For example, Ti_2AlC in this chapter shows the largest hysteretic loops (Fig 5.4b). It has the smallest CRSS. And this results in the largest N_k the number of IKBs per unit volume, at a relatively low stress (336 MPa). A similar effect was seen for Mg and its alloys.

It is interesting to see from Table 5.3 that the reversible dislocation density ρ related with the formation of IKBs for all MAX phases is at the range of 1~3 x 10^9 cm^{-2}. This agrees with the results in Ch. 3 and Ch. 4. Therefore, it can concluded that all MAX phases, no matter their composition, grain size, porosity and strengths, have comparable reversible dislocation densities if they are tested by a stress near their ultimate compressive strengths.

This is the first study on solid solutions' kinking nonlinear elastic deformation. Solid solution, replacement of half C atoms with N atoms makes Ti_2AlC or Ti_3AlC_2 harder. As shown in Table 5.2, solid solutions have higher shear moduli than their end members. Therefore, solid solution can definitely change the linear elasticity of solids. Additionally, it is also change the kinking nonlinear elastic deformation by changing grain size distribution, shear modulus and finally, the critical resolved shear stress Ω/b.

5.5 Conclusion

Not surprisingly, Ti_3AlC_2, Ti_2AlC and their solid solutions Ti_3AlCN, $Ti_2Al(C_{0.5}N_{0.5})$ are KNE solids. In this chapter and for the first time it is obvious that some plastic deformation is sometimes needed to nucleate IKBs. Grain size distribution of $Ti_3Al(C_{0.5}N_{0.5})_2$ can't influence linear elastic deformation of this sample. However, it can strongly change the samples' KNE deformation. Because the difference of unit cell structure, Ti_2AlC is less stiff and has more nonlinear deformation than Ti_3AlC_2. Solid solutions can definitely change the linear elastic deformation and can also influence mechanical hysteresis by change shear modulus, grain size distribution and critical resolved shear stress.

6. Kinking Nonlinear Elasticity, Damping and Microyielding of Hexagonal Close-Packed Metals

6.1 Introduction

In previous chapters (Chs. 3-5), we reported on the KNE deformation of the MAX phases. Actually, besides MAX phases, many other materials are also KNE solids as shown in Fig. 1.4a. A *sufficient* condition for belonging to KNE solids is plastic anisotropy. The fact that hexagonal metals, HM, are plastically anisotropic [79, 80], led directly to this work where we show that the HM can be classified as KNE, thus explaining their damping and microyielding.

Because of their crucial technological role, HM such as Ti, Zr, Mg, Zn, Co, among others, have been intensively studied over the past 70 years. Zr alloys used as cladding for nuclear reactor fuels, Ti alloys for aerospace and the aircraft industry, and Mg alloys for automobile and computer, communication and consumer electronic applications, are but a few examples. Consequently, the deformation mechanisms of these solids and their alloys to high strains are reasonably well understood. However, how these solids deform at low strains, defined herein as strains, $\varepsilon < 1$ % is much less understood and, as shown here, cannot be understood until the crucial role KBs play in that deformation is appreciated. Before discussing the latter, however, it is useful to briefly summarize what is known about the initial deformation of HMs.

Several decades of work on the *initial* deformation of hexagonal metals have resulted in the following understanding. Following elastic deformation, the stress-strain curves for fine-grained, FG, and coarse-grained, CG, materials have quite different microyielding stresses and hardening rates. In FG samples, microyielding is taken to

indicate the activation of primary slip (basal in Mg, Zn and Co [81], and prismatic in Ti [82], Hf and Zr [37]) which is quickly restricted by anisotropy. Microyielding is followed by a macroscopic yield point, σ_y, the nature of which is not entirely clear. In coarse-grained samples of Mg, Zr and Hf, wide $\{10\bar{1}2\}$ twins - which are believed to occur more readily than prismatic slip - are invoked to explain the lower hardening rates [37, 38]. And, while this explanation may be valid at higher strains, it does not apply in the regime of interest to this work because specimens loaded to strains < 1 % usually do not form twins, or if they do, their volume fraction is too small to account for the strain [83].

It is also fairly well established that below a critical strain level, ε_{cr}, the damping of Mg and Zn is independent of strain amplitude; above ε_{cr} the damping increases *linearly* with increasing strain amplitude [84-86]. This response has ostensibly been ascribed to the bowing of dislocations pinned between defects or solutes [36, 85, 86].

Herein we show that the origins of the microyielding *and* damping, in *both* FG and CG Mg, Ti, Co, Zn and Zr are *identical* and attributable to the same micromechanism: the formation of incipient kink bands, IKBs.

6.2 Experiment Details

Rods of Mg (99.8 %) and Zn (99.9%) were from Alfa Aesar, Ward Hill, MA. Rods of Co (99.97%) were from ESPI metals, Ashland, Oregon. High purity α-Ti (99.998%) plates were obtained from Alta Group of Johnson Matthey, Inc. Spokane, WA.

In order to obtain coarse-grained, CG, samples, the Ti was annealed in a tube furnace at 800 °C in a flowing Ar atmosphere for 2 h; the Co was annealed at 1000 °C for

12 h (only annealed Co samples were used in this chapter). In both cases, the samples were furnace cooled. Their grain sizes - measured by an optical microscope, OM, (Olympus PMG-3) - are listed in Table 6.1 and designated as 2α.

Cylindrically shaped specimens of Ti and Mg (31 mm high and 9.7 mm in diameter) were electro-discharge machined. The 12.7 mm diameter Co rods were cut to a length of 31 mm. A hydraulic testing machine (MTS 810, Minneapolis, MN), supplied with a controller (Microconsoler 458.20, MTS, Minneapolis, MN) was used for the compression experiments. An extensometer (MTS 632.59C-01) with gauge length of 25 mm was used to measure the strains. The compression direction for Mg and Co was parallel to the original rods' axis with a mild fiber texture (see Chs. 7 and 8); that of Ti was normal to the basal planes with a strong fiber texture [87].

Most loading and unloading tests were performed 4 times to the same stress using a load-control mode with load rate of ≈ 13 MPa/s. This translates to a maximum strain rate of ~ 0.0003 s^{-1} for Mg, and a minimum ~ 0.00007 s^{-1} for Co. The differences reflect the different Young's moduli, E.

6.3 Results

The stress-strain curves for Mg, Co and Ti (Fig. 6.1a-d), exhibited three regimes: At the lowest stresses the response was linear elastic, LE, with a slope that corresponded to the Young's modulus, E, of each metal. The values of Young's modulus E for Mg and Ti measured herein (Table 6.1) are in excellent agreement with published values. The slope of the stress-strain curves at the lowest loads for Co (130 GPa) is smaller than the literature value (209 GPa) [88]. As discussed in more detail in Ch. 8, we believe that Co

kinks at quite low stresses, which results in the lower value of the apparent modulus. It is important to note that in our model calculations we use the literature E value of 209 GPa. (see Ch. 8 for more details).

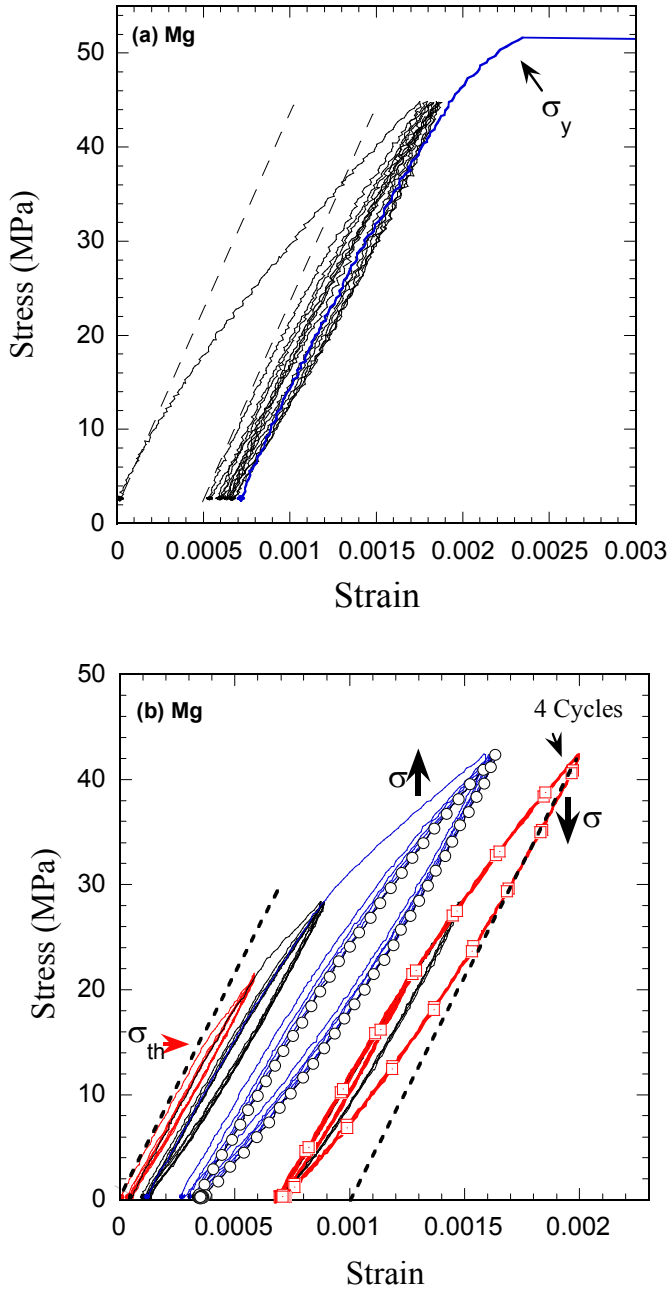

Figure 6.1 (*continued*)

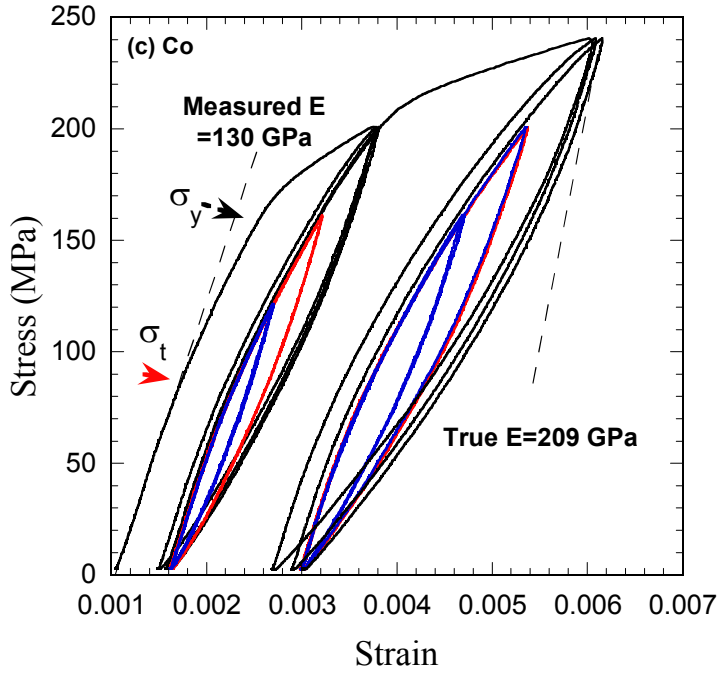

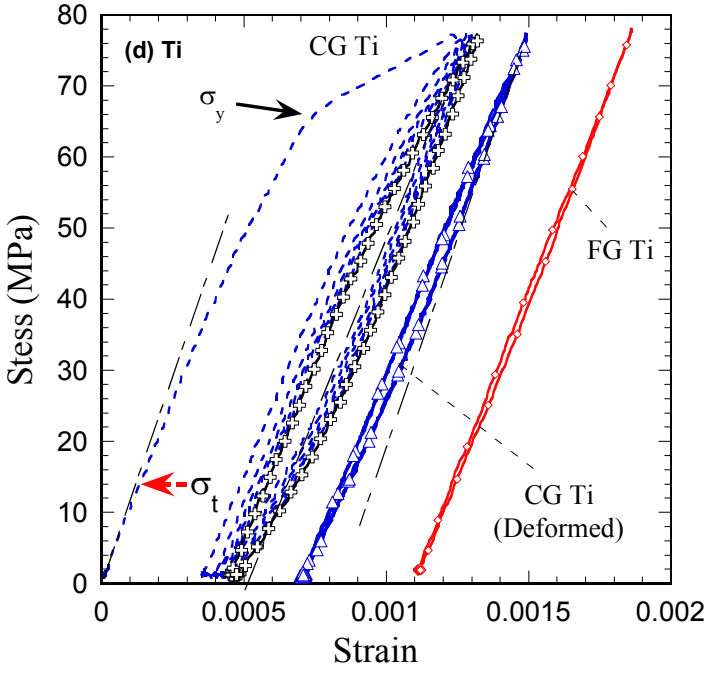

Figure 6.1 (*continued*)

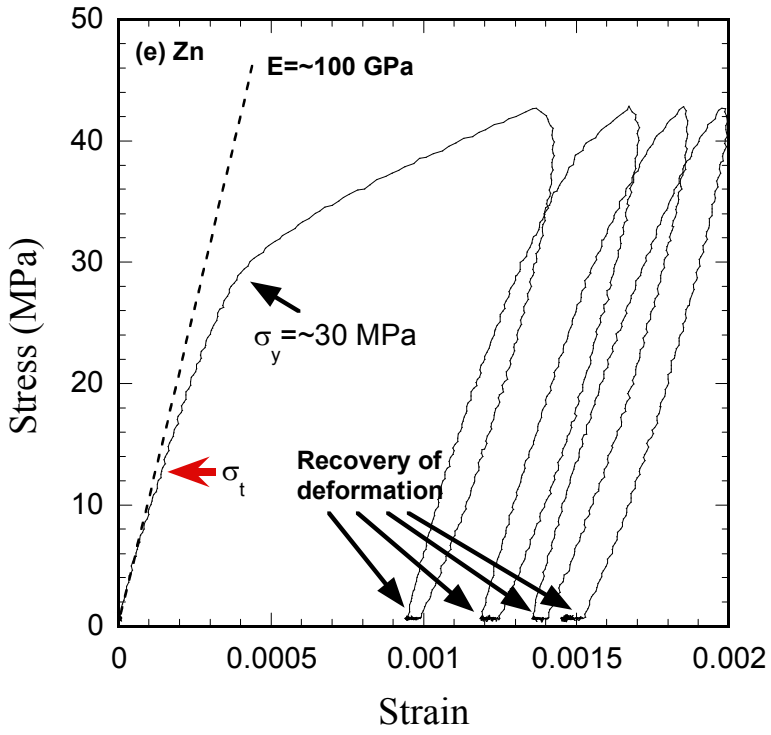

Figure 6.1: (a) Stress-strain curvev of Mg with a yield point σ_y, 52MPa. Below σ_y, there are hysteretic loops. (b) Stress-strain curves of Mg show some hysteretic loops below σ_y. The left one was obtained from a progressively-increasing-stress test (↑). The right one was obtained from a progressively –decreasing-stress test (↓). (c) Stress-strain curves of Co (d) Stress-strain curves of coarse grained Ti (CG) and fine grained Ti (CG). (e) Stress-strain curves of Zn

Table 6.1: Summary of Young's modulus, E, shear modulus, G, Poisson's ratio, ν, critical kinking angle, γ_c, grain size, 2α, yield points σ_y, calculated σ_c and measured σ_t's. Also listed are literature results on Zr.

	E (GPa)	G (GPa)	ν	γ_c (rad)	2α (μm)	σ_y (MPa)	σ_c (MPa)	σ_t‡ (MPa)	σ_t* (MPa)	Ref.
Mg	42*	19	0.35	0.01	35±20	52	11	19	14	This work
Ti(FG)	110*	44	0.32	0.01	10±4	130	53	75	40	
Ti(CG)					100±30	62	17	47	14	
Co	209	75	0.31	0.01	110±30	103	21	84	78	
Zr	95	36	0.34	0.01	40 [83]					Reed-Hill et al [89]

‡ From Figs. 6.2e and f and Eq. 2.15 * From stress-strain curves (Fig. 6.1).

At the threshold stress, σ_t (columns 9 & 10 of Table 6.1 and denoted in Fig. 6.1 by short horizontal red arrows) – referred to as the microyielding stress in the literature - the response was no longer LE (Fig. 6.1). In between σ_t and the yield point, σ_y (column 7 in Table 6.1) fully reversible hysteresis loops were observed. In other words, the loops occurred with little, if any, plastic deformation. Fully reversible loops were also obtained when a metal was loaded to a higher σ, unloaded, and then reloaded to a lower σ (e.g. loops labeled $\sigma\downarrow$ in Fig. 6. 1b).

At $\sigma > \sigma_y$, plastic deformation was observed, with σ_y's that are a function of grain size, GS (Table 6.1). σ_y of Mg was obtained from Fig. 6.1a. Other values of Mg were obtained of Fig. 6.1b, which are testes below σ_y and show clear hysteretic loops. When reloaded to the *same* σ, the extent of plastic deformation is significantly reduced, the yield point *vanishes* (Fig. 6.1b-d). As the number of cycles to a given σ increase, the loops become more fully reversible (Fig. 6.1b-d).

Increasing the GS reduces both σ_t and σ_y (Table 6.1). It also dramatically increases W_d at any given σ (compare fine-grained, FG and coarse-grained, CG, plots in Fig. 6.1d). Typically a small pre-deformation (i.e. excursion slightly beyond σ_y) first increases, but ultimately decreases W_d (see Chs. 7 and 8).

The stress-strain curve of Zn (Fig. 6.1e) shows similar results. The plastic deformation of Zn is so large, however, because of creep that all hysteretic loops are open. We therefore did not apply our model to Zn, but there is no reason to believe that if work

at lower stresses and/or lower temperatures is carried out on Zn, where creep can be minimized, then it is reasonable to assume that Zn is also a KNE solid.

6.4 Discussion

6.4.1 Application of model

Based on this, previous chapters and other work [6, 15, 16, 25, 29, 90], it is possible to account for all our results, and many in the literature, by postulating that the non-linear response is due to the formation of IKBs on the primary slip system, viz. prismatic for Ti and basal for Mg and Co. As noted above, however, the conclusions reached herein could apply to Zn as well.

At this time it is fairly well established that the signature of IKBs is the formation of fully reversible stress-strain loops, wherein W_d is a strong function of grain size [6, 15, 16, 25, 29, 90]. Based on this criterion alone, it is reasonable to conclude that Mg, Ti, Co, Zn, and, under the right circumstances (see below) Zr, are KNE solids. Evidence for the existence of KBs in Mg, Ti, Zr, Zn and Co in the literature is also presented.

Figure 6.2a-h plots the linear relation of ε_{NL} vs. σ^2, U_{NL} vs. $\varepsilon_{NL}^{1.5}$, W_d vs. σ^2 and W_d vs. ε_{NL} for Ti, Mg and Co, respectively. Based on these figures, it is obvious that our results are consistent with the equations derived in Ch. 2. This is quite gratifying considering that σ, ε_{NL}, U_{NL}, W_d are *independent* parameters and the factor of almost 5 in the values of E, and the factor of 10 in Ti grain size, are explored.

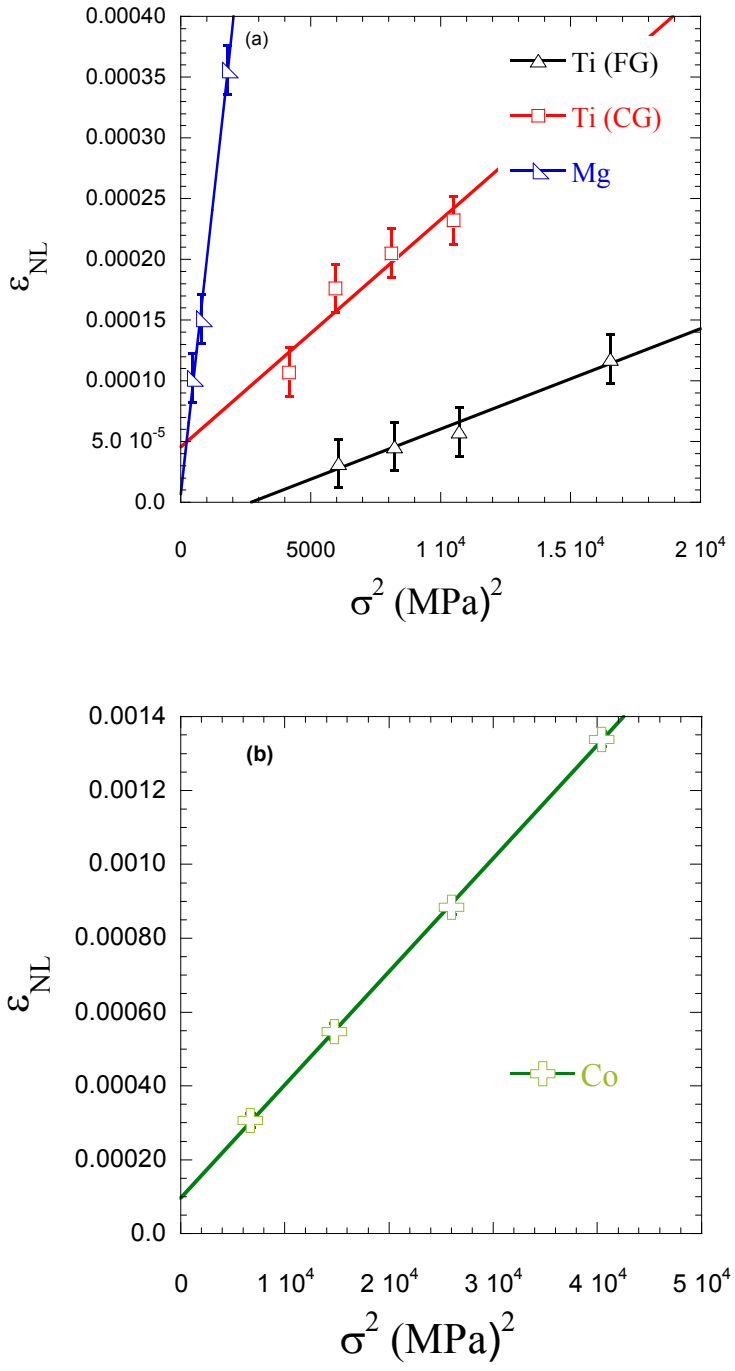

Figure 6.2 (*continued*)

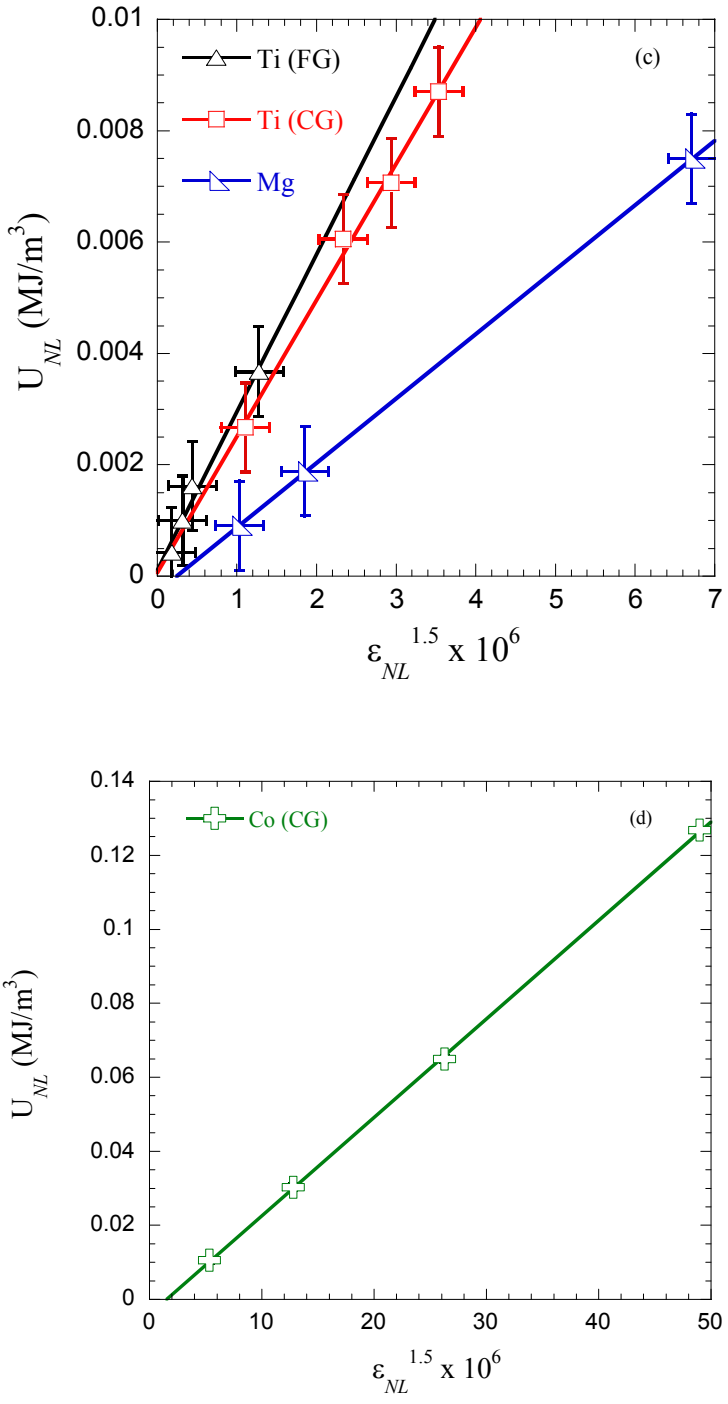

Figure 6.2 (*continued*)

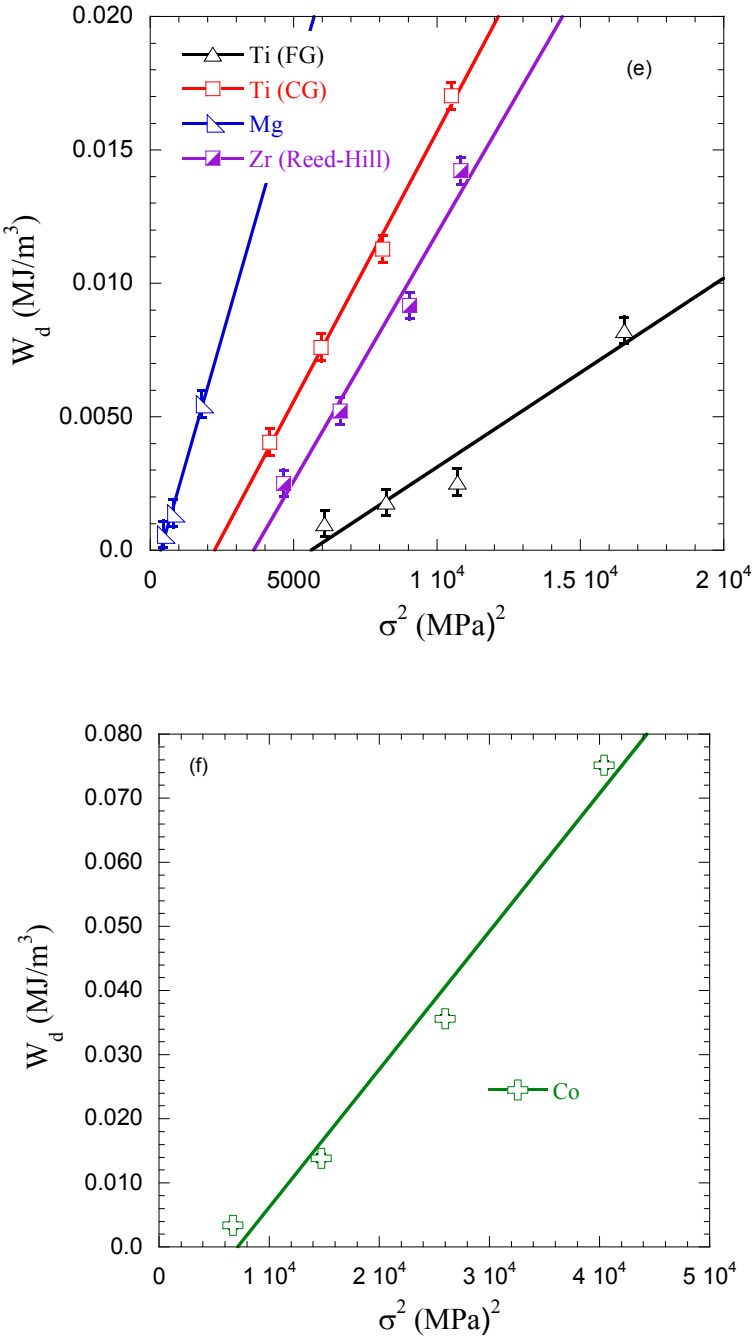

Figure 6.2 (*continued*)

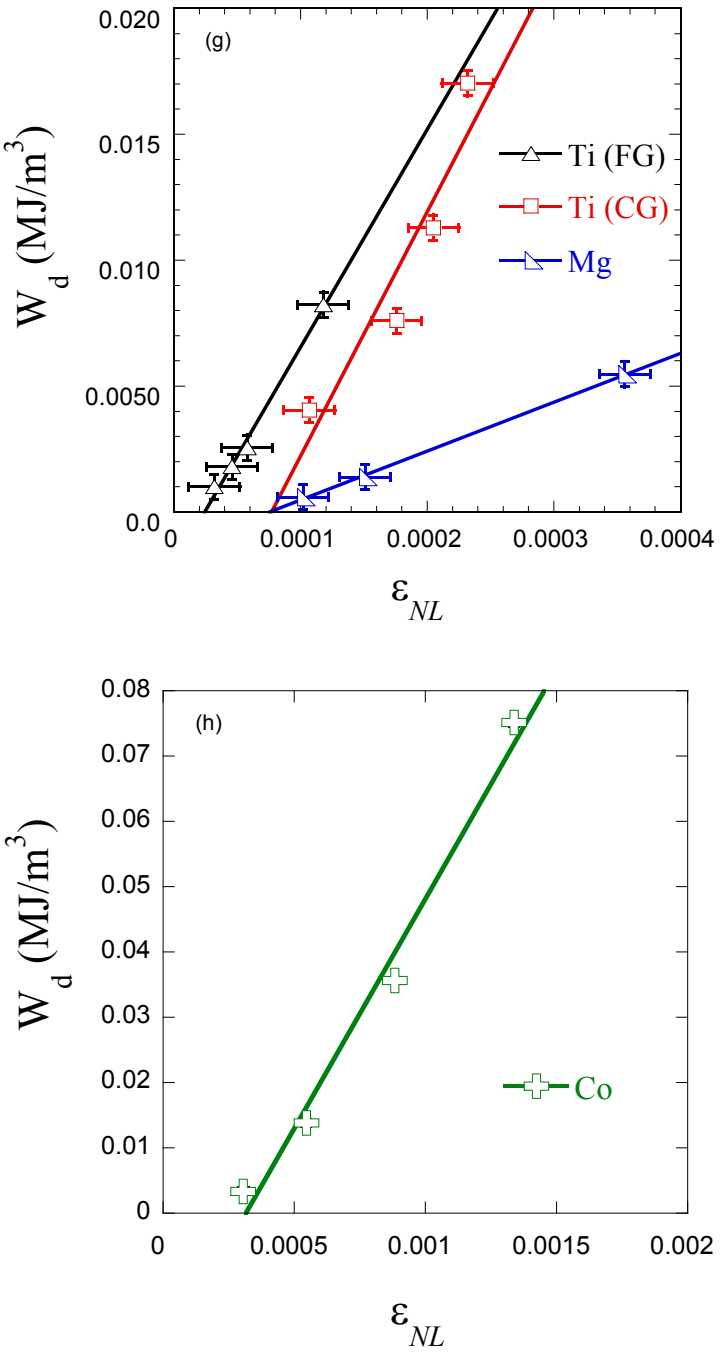

Figure 6.2: Model plots (a) ε_{NL} vs σ^2 for Ti and Mg (b) ε_{NL} vs. σ^2 for Co (c) U_{NL} vs. $\varepsilon_{NL}^{1.5}$ for Ti and Mg (d) U_{NL} vs. $\varepsilon_{NL}^{1.5}$ for Co (e) W_d vs. σ^2 for Ti and Mg. Results for Zr [89] is also shown, (f) W_d vs. σ^2 for Co, (g) W_d vs. ε_{NL} for Ti and Mg, (h) W_d vs. ε_{NL} for Co.

Table 6.2 lists the values of Ω/b, $N_k\alpha^3$, N_k, β_{xc}, β_x and ρ calculated from our model. The agreement between the 3 values of Ω/b calculated using the various expressions in Eq. 2.18, for Mg and Co (columns 2-4 in Table 6.2, respectively) is *excellent* and indirectly confirms the model and assumptions. This is especially true given the independence of U_{NL} and W_d. The situation for Ti is not as good, but again given all the assumptions made, it is acceptable. It should be noted that the most direct measure of Ω/b is that obtained from the 4th term in Eq. 2.18 because it does only depends on m_4.

Table 6.2: Summary of calculated values of Ω/b, $N_k\alpha^3$, N_k, $2\beta_{xc}$, β_x and ρ at the maximum stress, σ_{max}. The CRSS values are taken from the literature. In all cases, w = 5b.

	Ω/b (MPa) from Eq. 2.18			CRSS (MPa)	$N_k\alpha^3$	N_k μm^{-3}	$2\beta_{xc}$ μm	σ_{max} MPa	ρ cm^{-2}	$2\beta_x$ μm
	2nd term	3rd term	4th term							
Mg	3	4	3	0.6-5.0 [91]	0.5	0.0001	1.3	42	4×10^8	5
Ti (FG)	27	4	14	20 [92, 93]	0.06	0.0005	0.8	129	2×10^8	2
Ti (CG)	18	8	16		0.3	0.000002	2.5	102	0.6×10^8	15
Co	6	10	12	6.6-13[88, 94-96]	2	0.00002	2.8	201	5×10^8	19

Furthermore when the Ω/b values are compared with published single crystal CRSS values (column 5, Table 6.2), the agreement has to be considered excellent considering the assumptions made in deriving the equations, the sensitivity of the CRSS to impurities and the fact that our values were obtained from polycrystalline samples. In the case of Mg and Co, we compare Ω/b with basal slip; in Ti, with prismatic slip. This agreement is of paramount importance because it indirectly confirms that Ω/b is, if not identical to, then proportional to the CRSS of the primary slip dislocations and that W_d is due to the to-and-fro motion of these dislocations. Furthermore, that this value can now be

estimated from a compression test provides a simple technique to measure a value that, in general, is nontrivial to measure.

Remarkably, given the very different HM explored and the sensitivity of N_k to the value of 2α, the resulting reversible dislocation densities, ρ values, all fall in the range of 0.6 to 5 x 10^8 cm^{-2}. These values are smaller than those of the MAX phases, that ranged from 1 to 2 x 10^9 cm^{-2}, in Ch. 3-5. One possible reason is that we used the grain size as 2α to make the calculation for these metals. For the MAX phase, we used grain thicknesses as 2α. Grain thickness is a more correct measurement of 2α but is not easily determined for the metals. Therefore, it is reasonable to assume that the true 2α of metals is smaller than the grain size listed in Table 6.1. This is especially true for the coarse-grained metals. Thus, the low ρ for CG Ti is probably a lower bound. In the subsequent chapters, 2α was calculated from Eq. 2.4 instead of the measured grain size. But in this chapter, we assume the measured grain size to be 2α to be consistent with previous chapters on the MAX phases. Anyway, all values fall between those of heavily deformed and annealed metals [51].

6.4.2 Evidence for kink band formation in HM

It is well established that Zn [39] and Mg [40] form basal plane KBs upon deformation. Vaidya et al. [41] not only observed kink bands in Co, but as important, also $\{11\bar{2}1\}$ twins. We note that the microstructure of Ti_3SiC_2 – in which only basal slip is activated - after compression at 1300 °C, is quite similar to that of coarse-grained Mg deformed at room temperature (compare Fig. 7b in Ref. [52] to Fig. 6 in Ref. [97]). The situation for Ti is different in that the easy slip system is not basal, but prismatic. Thus if

KBs were to form in Ti, they would be normal to the prismatic slip lines. Direct unambiguous evidence for such kink boundaries in CG Ti deformed at room temperature exists as shown by Rosi at 1954 [42]. Figure 6.3 is the Fig. 10 of Rosi's paper and show kink bands of Ti.

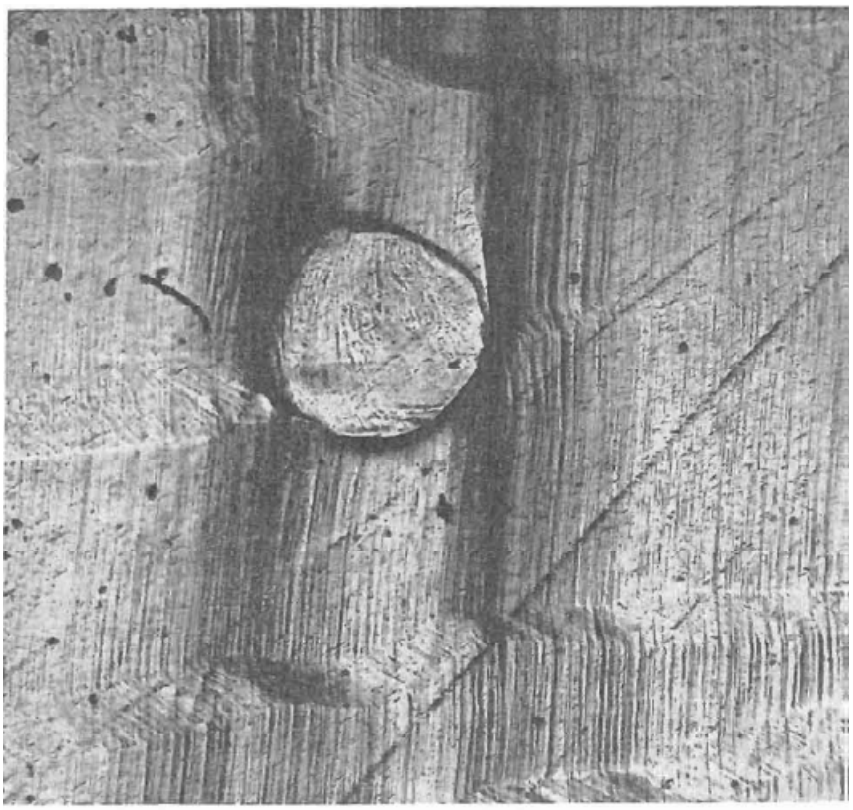

Figure 6.3: Kink bands of Ti (Fig. 10 of Ref. [42])

We also did a test on Zr cylinders (99%, Alfa Aesar, Ward Hill, MA). As shown in Fig. 6.4a, the results for Zr is a classic elastic/plastic response, viz. *no* microyielding or loops were observed, which as first blush implies that it is not a KNE metal. Like Ti, the

primary slip system of Zr is believed to be prismatic [81]. However, basal plane KBs have been observed [98]. Furthermore, as shown in Fig. 6.4b, a large room-temperature mechanical hysteretic effect, under room temperature cyclic tensile loading, was observed by Reed-Hill et al., but only after pre-straining at 77 K [89]. Reed-Hill et al. concluded that the large hysteretic loops observed were due to the formation of $\{11\bar{2}1\}$ twins [89]. Given that the latter are nothing but KBs - where a basal-plane dislocation is nucleated every c-lattice parameter [99, 100] - these results are again in agreement with our model.

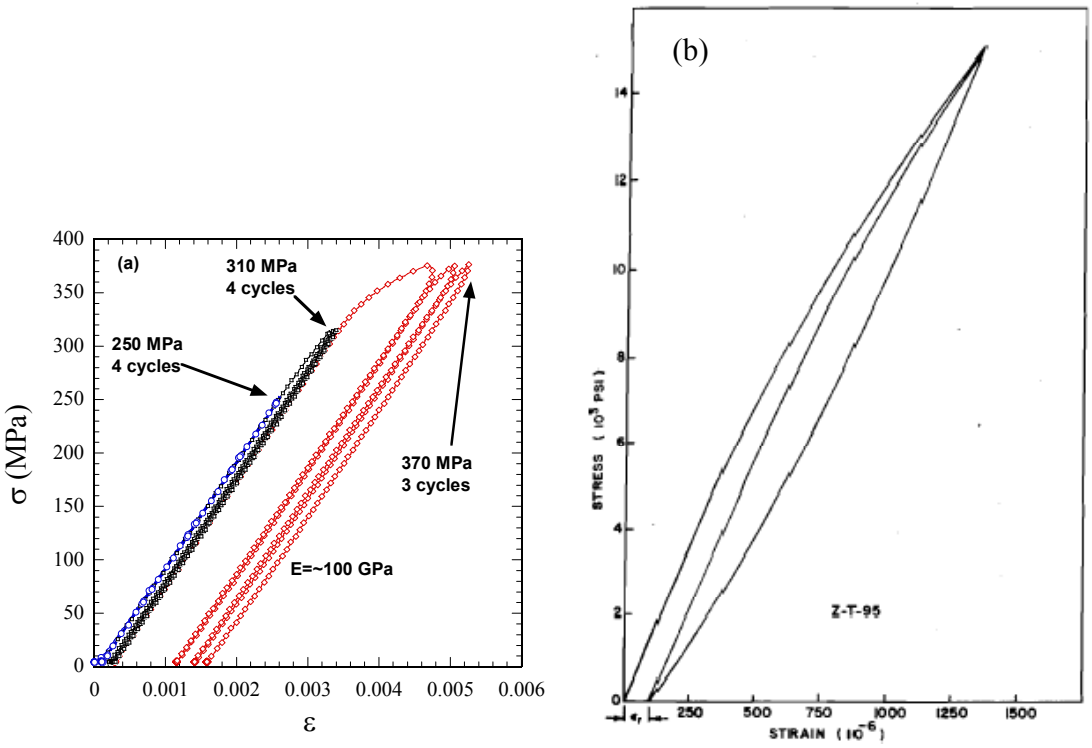

Figure 6.4: Classic linear elastic responds of Zr in this thesis (b) Reed-Hill's work on77k prestrained Zr (Fig. 1 of Ref. [89]).

Reed-Hill et al. [89] also reported that beyond a certain pre-strain, W_d decreased once more. The reduction in W_d with further deformation is understood and results from a reduction in domain size as a result of the breakup of large grains into smaller domains, viz. a reduction in 2α. [6, 52, 90] Why pre-straining at 77 K is required to observe the hysteresis is not understood, but must be related to IKB nucleation. A similar effect was observed in Mg: loops for annealed virgin samples W_d was almost imperceptible; a 2 % pre-deformation increased $W_d \approx 2.5$ times. This observation will be discussed in details in Ch. 7.

6.4.3 Damping in HM

As noted above, in several HM, the damping response is similar to that shown in Fig. 6.2g and h. The threshold strain in a Mg sample with a grain size ≈ 120 μm has recently been reported to be ≈ 0.0001 [86]. The ε_{th} measured herein – 0.00008 - for a Mg with half the grain size is of the same order of magnitude. Part of the difference may be due to the different grain sizes, part to the different purity levels and part to the very different methods by which the measurements were made. These differences notwithstanding, what is crucial and consistent with our model is that beyond ε_{th}, W_d increases linearly with strain, for reasons that are now more transparent. It is important to note that most of the current damping models - based on the classic work of Granato and Lucke [36], G&L, who postulated that the damping was due to the bowing out of dislocations - are, at the very least, incomplete. For example, the G&L model neither explains why Mg is such a good damping element, while Al and Cu are not, nor does it explain why a threshold exists. More importantly the G&L model cannot account for the strong effect of grain size on damping and/or strain thresholds (Fig. 6.2g and h). Our IKB

model not only explains all of these observations, but quantifies the damping and elucidates the important variables.

6.5 Summary and Conclusions

Because the HM metals are plastically anisotropic, their initial deformation results in the formation of fully reversible, dislocation-based IKBs. Both σ_t and W_d are a strong function of grain sizes, with larger grains resulting in lower σ_t's, but higher W_d's.

As important by making use of our microscale model, we show how, from a single compression experiment, to obtain a decent picture of the distribution and density of dislocations at any stress, as well as extract the CRSS, of the dislocations comprising the IKBs.

Lastly we note that IKBs are nature's solution to plastic anisotropy because their formation results in the dissipation or storage of substantial amounts of energy at low strains. Based on this and previous work, it is fair to conclude that IKBs constitute the last piece in the deformation-of-solids puzzle for strain <5%, without which it is not possible to understand the early deformation of plastically anisotropic solids, be they held together by covalent, ionic, metallic, or even secondary, bonds like in graphite [16].

7. Kinking Nonlinear Elasticity and the Deformation of Mg

7.1 Introduction

In Ch. 6, the hexagonal metals (Ti, Mg, Zn, Co and Zr etc.) were classified as KNE solids in that their mechanical hysteresis can be explained by the dislocation model outlined in Ch. 2. In this chapter, we focus on the deformation of Mg. Mg is an extensively used structure metal and a well-know high damping metal. After several decades of work on the deformation of single[101-107] and polycrystalline Mg[43-50] at *small* (< 5 %) plastic strains, the following picture has emerged: a) Deformation occurs mostly by basal slip, for which the critical resolved shear stresses, CRSSs, fall in the range of 0.6 to 5.0 MPa [91]. b) In modeling the deformation of polycrystalline Mg, all authors assume (and concede) that the activation of non-basal slip (viz. prism and <c+a>) occurs at CRSS's that are significantly – in some cases by more than one order of magnitude - smaller than those measured on single crystals [43-50]. That despite the fact that neither Roberts and Partridge [108], nor Hauser et al. [109] report the activation of pyramidal slip in their single crystal work. c) In fine-grained samples, grain boundary sliding is observed [110]. d) In coarse-grained Mg, $\{10\bar{1}2\}$ twins also play a role, but only in highly oriented microstructures, loaded parallel to their basal planes [38, 50, 91, 101, 102, 111-114].

Early work on twinning of Mg and Zn single crystals established that, in most cases, twinning is associated with bend planes and kink bands, KBs [38, 108, 115, 116]. For reasons that are not entirely clear, however, the role of kinking and KB formation in the deformation of coarse-grained Mg - clearly demonstrated by Hauser et al. [109] several decades ago – has, for the most part, been ignored in more recent work. Furthermore,

Burke and Hibbard [102] have shown that bending results in $\{10\bar{1}2\}$ twins. Interestingly, and probably not coincidentally, more recently Mann et al. [117] made use of bend specimens to observe twinning in Mg (see below). As discussed herein we believe kinking plays a key, but hitherto unappreciated role, without which full understanding of the deformation of Mg remains elusive.

Arguably, the two most vexing, and unsatisfactorily explained, observations concerning the deformation of Mg have to be the fact that in *both* tension and compression only $\{10\bar{1}2\}$ tensile twins have ever been observed [118]. To quote Agnew et al. [118] "There is only one major twinning mode in Mg, the $\{10\bar{1}2\}$ tension twin; hence, *the crux of the problem is c-axis compression.* If a grain is forced to deform under c-axis compression, a large plastic incompatibility will develop between neighboring grains, and plastic instability and/or fracture will ensue". Even if basal, prismatic <a> and/or pyramidal <a> slip occur, there is still <u>no</u> mechanism to accommodate strains along the c-axis [50]. As noted above, to solve this serious problem, modelers of Mg deformation have had to invoke sudden bursts of <c+a> slip [50] to explain something as fundamental as yielding, while simultaneously conceding that this conjecture does *not* agree with prior understanding of Mg deformation [119].

The situation gets even more intriguing when it is appreciated that the strain associated with twinning can sometimes be *opposite* of what one would expect. For example, Hauser et al. [109] conclude, "… the overall strain due to twinning in this specimen is actually *negative*, a fact *not* easily reconciled with strain energy considerations." Quite recently [120], we observed a similar effect in coarse-grained

Ti_3SiC_2 that was crept in tension. Using orientation image microscopy, OIM, we observed a grain - with its basal planes *parallel* to the loading axis - kink in such as way as to actually *shrink* along the loading direction, despite the fact that it was being pulled in *tension* [120]. This observation was explained by invoking that dislocation pileups from neighboring grains caused the hard grain to deform like an accordion (Fig. 7.1a).

In cast Mg alloys, with random texture, the differences between stress-strain curves obtained in compression or tension are small [45, 121]. In contradistinction, large anisotropies are observed when highly oriented microstructures are tested [44, 49, 50, 111, 112, 122, 123]. Along the same lines, Mg and its alloys are characterized by high damping and the related phenomenon of pseudo-elasticity [44, 45, 117, 124-126]. For example, Caceres et al. [45] - working with an AZ91 cast Mg alloy with a grain size of ≈ 130 μm - observed large stress-strain hysteresis loops under both compressive and tensile cyclic loading after small (≈ 0.001 % - 0.01 %) pre-strains. These results, and others, are discussed below.

In Ch. 6, the focus was on the KNE deformation of an as-received Mg with a grain size of ≈ 35 μm. Given that Mg can deform prior to failure, its deformation history, as well as, its grain size and preferred orientations, as shown here, are important. The purpose of this chapter, therefore, is to better understand the deformation of Mg by systematically varying the grain size and amounts of pre-strain. We also make the case that a major hurdle with understanding Mg deformation to date has been the fact that the role bending/kinking – which can result in some strain along the c-axis – can play has not

been taken into account. Before doing so, we briefly present a simple KB-based model for the deformation of Mg.

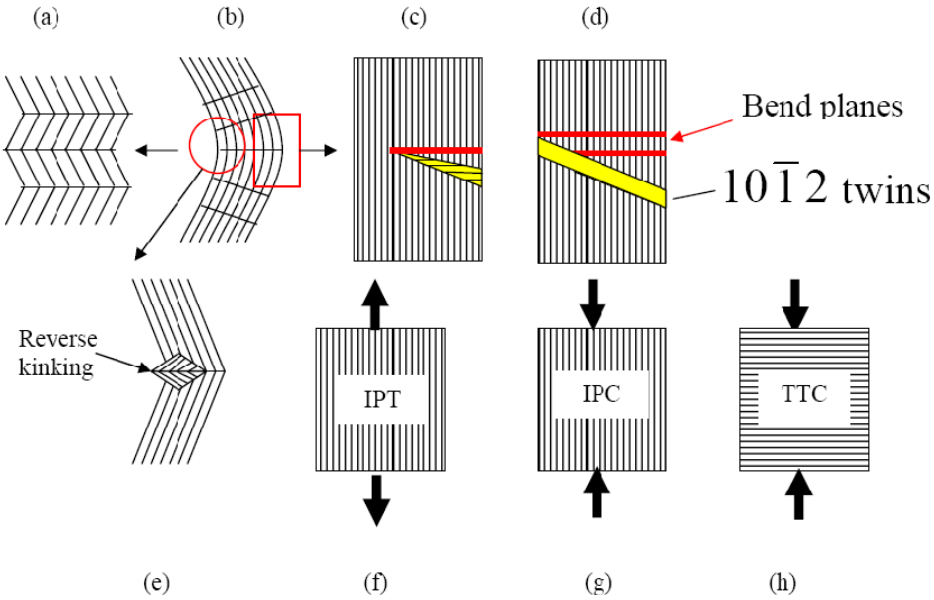

Figure 7.1: Schematic of relationship between bending and twining in oriented microstructures. In all sketches the lines represent basal planes and vertical arrows the direction of the applied load. a) Buckling of a grain by the formation of kink boundaries, b) bending of grain showing tensile and compressive regions, c) formation of a tensile twin in the tensile region of the bent grain. In such a situation, the twin is always associated with a kink boundary (horizontal line), d) same as c, except here the twin is assumed to have traversed the entire grain. e) reverse buckling to accommodate compressive stresses in bent grain; f) In-plane tension, g) in-plane compression; h) through thickness compression.

7.2 Kinking-Based Model for the Deformation of Mg

Given that bending favors twin formation [102], in Figs. 7.1b to 7.1d, we schematically show how a hard grain - subjected to a compressive load parallel to the basal planes - can, in principle, deform without the activation of other than basal slip. The

initial response of such a grain (Fig. 7.1b) is to bend, not unlike when single crystals with the same orientation are loaded parallel to their basal planes [28, 101, 127]. If, however, the stress is increased further, the fraction of the grain above the neutral axis would be subjected to high tensile stresses (Fig. 7.1b), that in turn, can be partially, or totally, relieved by the formation of tensile twins (Fig. 7.1c). The formation of the latter is always associated with bend planes [128], referred to here as MDWs in this thesis (Fig. 7.1c and 7.1d). If the grain is small enough, or the stress conditions favorable, the twin can, in principle, cross the entire grain (Fig. 7.1d). The rest of the grain, below the neutral axis can deform by the formation of "reverse" kink-bands (Fig. 7.1d), observed when Mg single crystals are deformed [104, 108]. Another possible mechanism for deformation is grain buckling – accordion-like, viz. Fig. 7.1a, as observed in Ti_3SiC_2 [120].

Agnew et al. have shown that the twins that form in Mg are in a tensile stress state parallel to the compression direction, relative to the surrounding grains [50]. Why that is the case is obvious from Fig. 7.1c; if the twin that forms does not relieve all the strain, it will remain in a state of tension along the compression axis. Note that such twins, when they form, end up being more or less *parallel* to the basal planes, and hence roughly at 90° to the kink boundaries. Figures 13 and 14 of Ref. [102] are examples of such configurations.

Figures 7.1f, g and h are schematics of three orientations, in plane tension (IPT) and compression (IPC) in which the applied load is parallel to the basal planes, and a through thickness compression (TTC) in which the applied load is normal to the basal planes, respectively, that have been studied in some detail by others (see below) [112, 129]. At

this juncture we simply note that if indeed, as we claim, bending is key to twinning then the propensity for the latter must be highest in the IPC configuration (Fig. 7.1g) as observed (see below).

7.3 Experimental Details

Rods of Mg (Alfa Aesar, Ward Hill, MA, 99.8 % pure per metal basis) 3.3 cm in diameter, were electro-discharge machined into 31 mm long cylinders with 9.7 mm diameters. Some samples were tested as received; others were annealed in flowing Ar gas at 500 °C for 4 h or 12 h to grow their grains. These will henceforth be referred to as AN4 and AN12, respectively.

In order to obtain a fine-grained (FG) Mg, a $45\times30\times30$ mm^3 cube from as-received rod was uniaxially compressed 20 % at 120 °C. This sample - henceforth referred to as the *DEF* - was then rotated 90^o and compressed another 20 % in each of the other two orthogonal directions. This sample was then annealed in flowing Ar at 200 °C, one for 2 h; the other for 8 h. These will henceforth be referred to as AN2 and AN8.

Prior to testing the samples were polished (down to 0.25 μm) and etched ($HCl:H_2O$ = 1:3 by volume) to reveal their microstructure, observed using an optical microscope, OM, (Olympus PMG-3, Tokyo, Japan). The grain size was estimated by Heyn's intercept approach [130]. XRD diffraction was used to estimate the degree of preferred orientation.

A hydraulic testing machine (MTS 810, Minneapolis, MN), supplied with a controller (Microconsoler 458.20, MTS, Minneapolis, MN) was used for all compression tests. An extensometer (MTS 632.59C-01), with gauge length of 25 mm, attached directly

to the sample was used to measure the strains. The loading direction was always coincident with the original rod axis.

Most samples were loaded and unloaded to a given stress level 4 times using a load-control mode. With one exception – where the loading rate was ≈ 0.13 MPa/s - the load was programmed to increase and decrease at a rate corresponding to ≈ 13 MPa/s, which translates to a strain rate of ~ 0.0003 s^{-1}.

7.4 Results

Table 7.1 summarizes the thermo-mechanical treatments, resulting grains sizes and textures. Typical OM micrographs of select samples are shown in Fig. 7.2. The multitude of small pits observed in the deformed sample (Fig. 7.2c) are most probably dislocations pits [51]. Annealing this sample at 200 ^{o}C for 2 h (Fig. 7.2d) reduces the number of such pits but does not change the grain size. Annealing for 8 h removes all pits and results in grain growth (Fig. 7.2e).

According to XRD diffraction, the as-received, AN4 and AN12 samples have mild fiber texture with the basal planes parallel to the compression axis. The DEF, AN2 and AN8 samples have similar, but stronger textures. The texture intensity is qualitatively shown in Table 7.1.

When the as-received Mg was cyclically, and uniaxially, compressed, below its yield stress, σ_y, of 50 MPa, hysteresis loops were observed as shown in Fig. 7.3a. The first loops, to any stress, were slightly open; all subsequent loops to the same stress were, for the most part, closed, provided the testing was carried out relatively rapidly (13 MPa/s). At significantly slower rates (0.13 MPa/s) the loops are open (Fig. 7.3a, open loop on

right) as a result of creep. All the results in this paper were obtained at the faster strain rates.

Table 7.1: Summary of samples' annealing conditions, resulting grain sizes, and the KNE parameters (σ, ε_{NL}, W_d and U_{NL}) obtained from the stress-strain curves. Also listed in the first row are the same results in Ch. 6. It is listed here for comparison. The 2α is the grain size as measured in the OM.

Sample	Annealing conditions	Prestrain	Grain size (2α μm)	Fiber texture	σ MPa	ε_{NL}	W_d MPa	U_{NL} MPa
As-received [Ch. 6]	None	0	35 ± 20	Medium	21	0.00011	0.0006	0.0009
					28	0.00016	0.0014	0.0019
					42	0.00037	0.0055	0.0075
AN2	Deformed + 200 °C 2 h	0	20±10	Strong	21	0.00022	0.0010	0.0015
					28	0.00029	0.0019	0.0030
					35	0.00039	0.0032	0.0052
					42	0.00047	0.0048	0.0076
AN4	500 °C 4 hr	4 %	170 ±100	Medium	14	0.00008	0.0006	0.0001
					21	0.00017	0.0019	0.0010
					28	0.00031	0.0046	0.0033
AN12	500 °C 12 hr	4 %	600 ±400	Medium	14	0.00008	0.0008	0.0004
					21	0.00021	0.0026	0.0016
					27	0.00047	0.0064	0.0052
AN8	Deformed + 200 °C 8 h	0	40 ± 25	Strong	28	0.00016	0.0026	0.0017
					35	0.00028	0.0050	0.0029
					42	0.00039	0.0084	0.0047
		1 %			21	0.00035	0.0033	0.0015
					28	0.00054	0.0071	0.0036
					35	0.00079	0.0128	0.0072
					42	0.00111	0.0223	0.0142
		2 %			35	0.00096	0.0162	0.0076
					42	0.00133	0.0266	0.0163
		3%			28	0.00037	0.0051	0.0017
					35	0.00055	0.0089	0.0042
					42	0.00086	0.0175	0.0095
		5%			36	0.00039	0.0067	0.0026
					42	0.00055	0.0111	0.0052

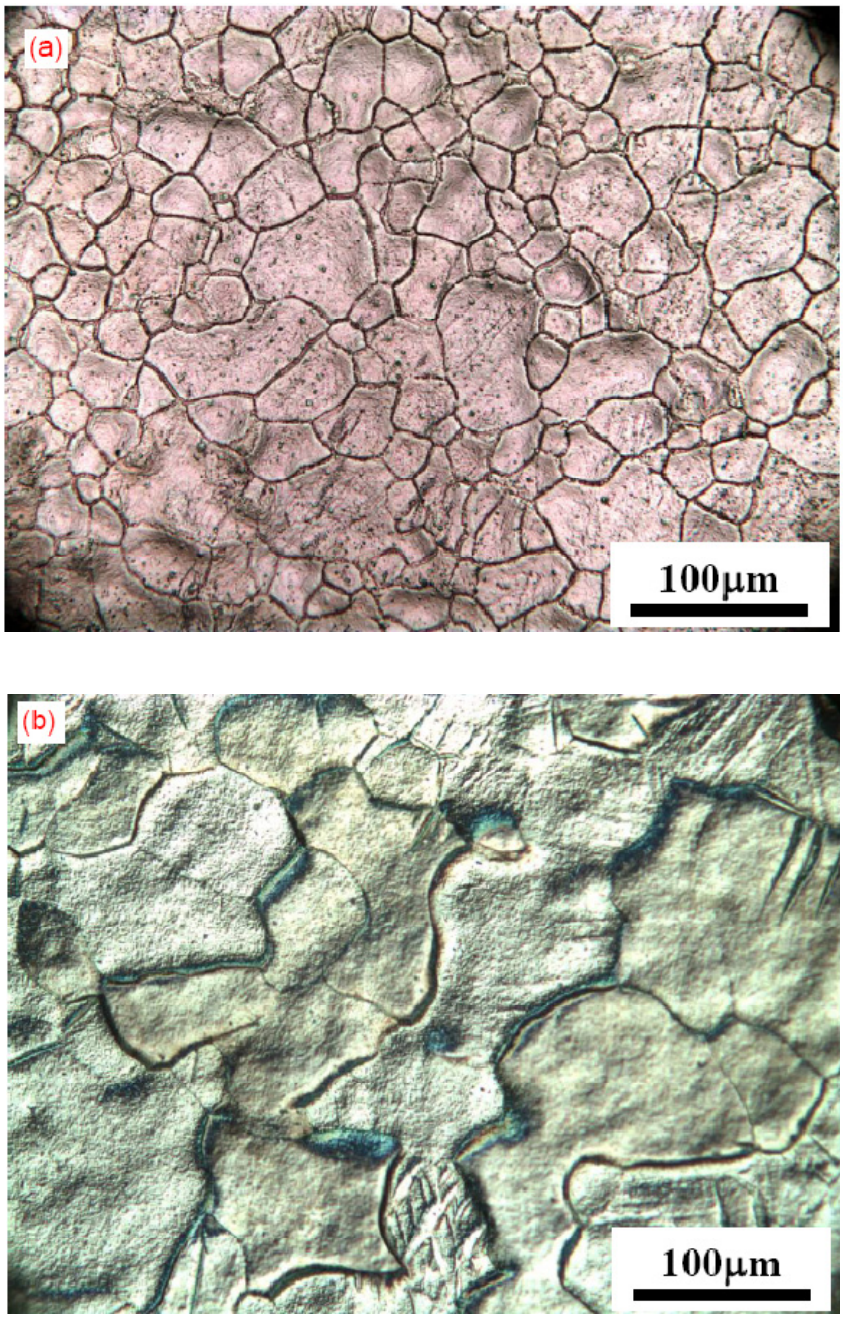

Figure 7.2 (*continued*)

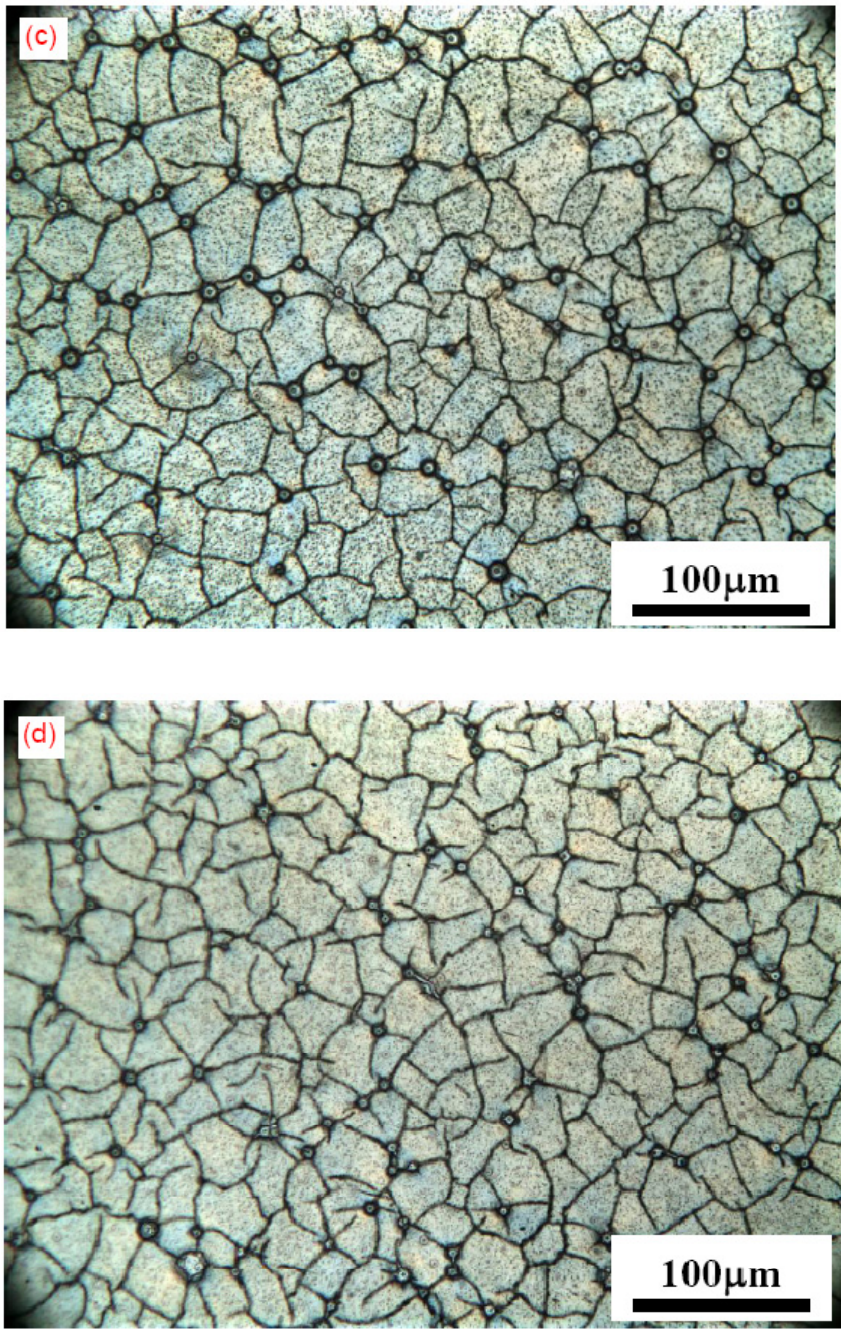

Figure 7.2 (*continued*)

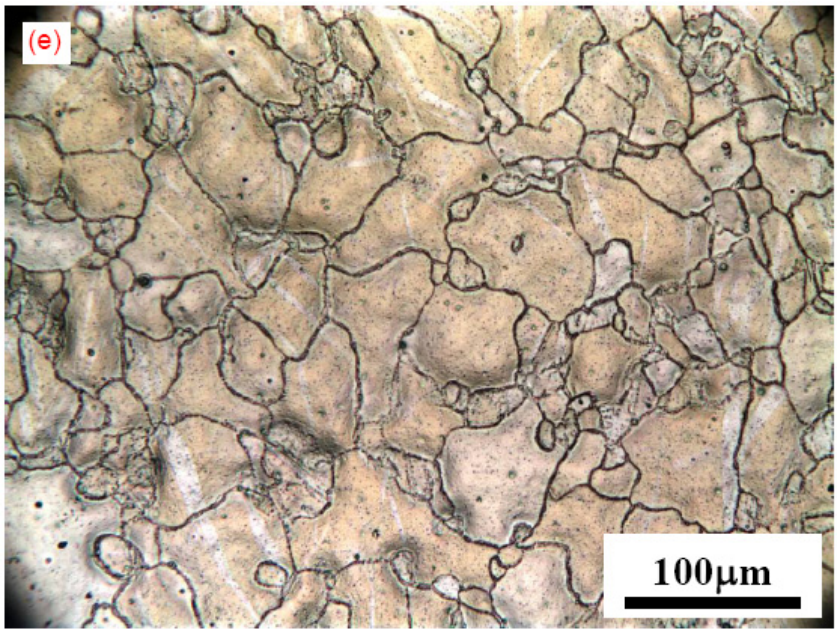

Figure 7.2: Optical micrograph of (a) As-received sample (b) AN4 (c) DEF (d) AN2 (e) AN8 samples

When the AN4 sample was compressed (Fig. 7.3b), a clear yield point is observed at ≈ 10 MPa; at 7 MPa, the response was linear elastic. At σ_y, plastic deformation up to a strain of 0.0022 (dashed vertical line in Fig. 7.3b) is observed, with *no* strain hardening; beyond that, strain hardening is observed. After every ~ 1 % permanent deformation, the sample was cyclically loaded-unloaded to obtain the closed hysteretic loops. The loop obtained at 14 MPa for sample with prestrain of 1, 2, 3 and 3.7 % are shown in Fig. 7.3c. The loop areas clearly decrease with increasing permanent strain. The clear yield point at 10 MPa and linear deformation at 7 MPa for 0% prestrained samples are also shown in Fig. 7.3c.

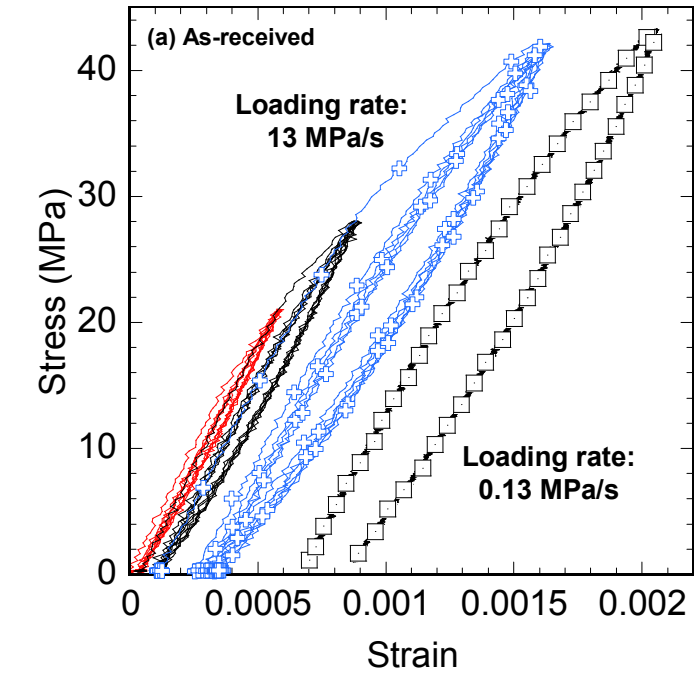

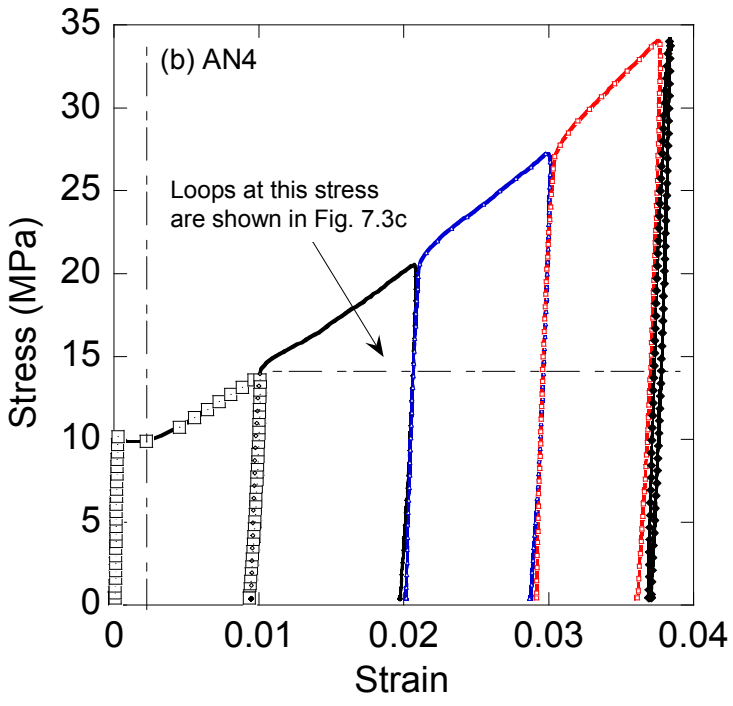

Figure 7.3 (*continued*)

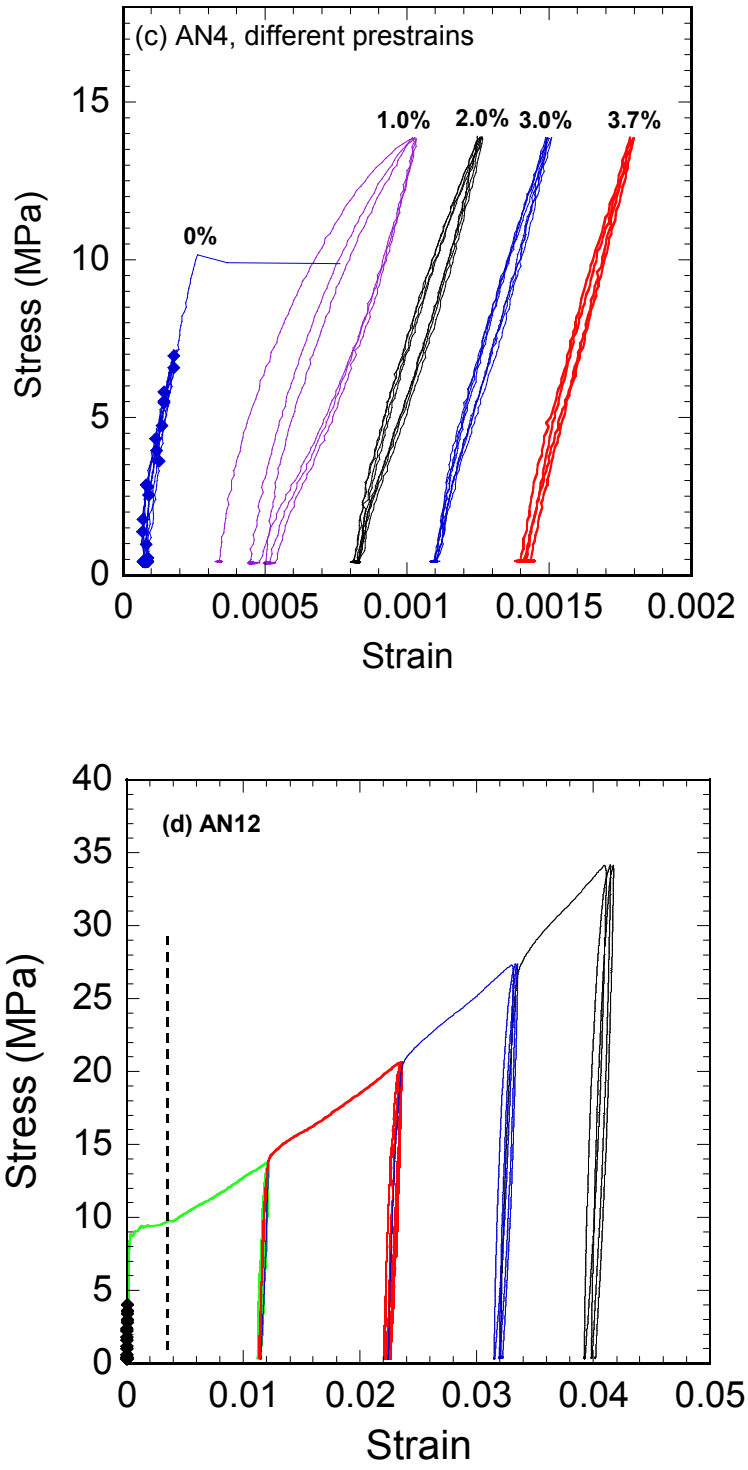

Figure 7.3 (*continued*)

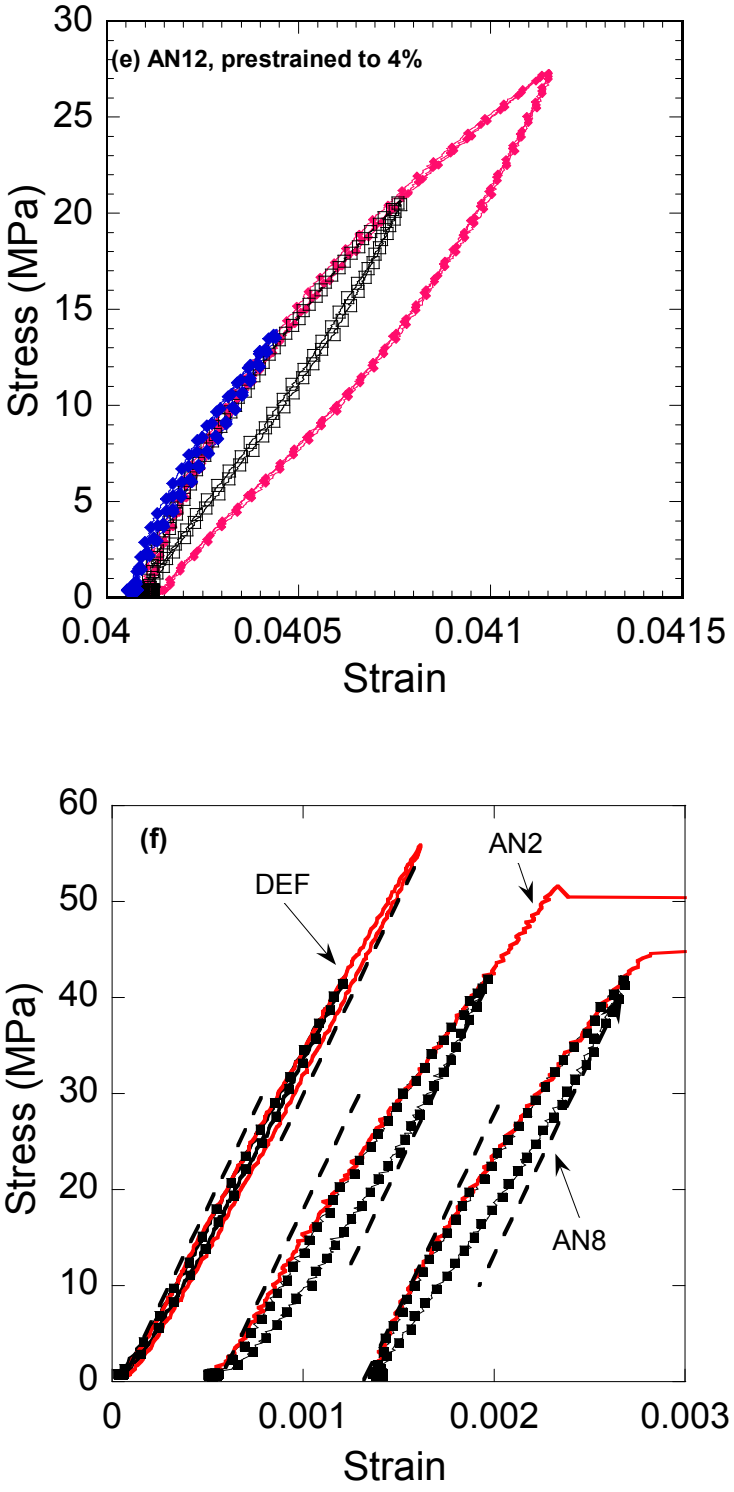

Figure 7.3 (*continued*)

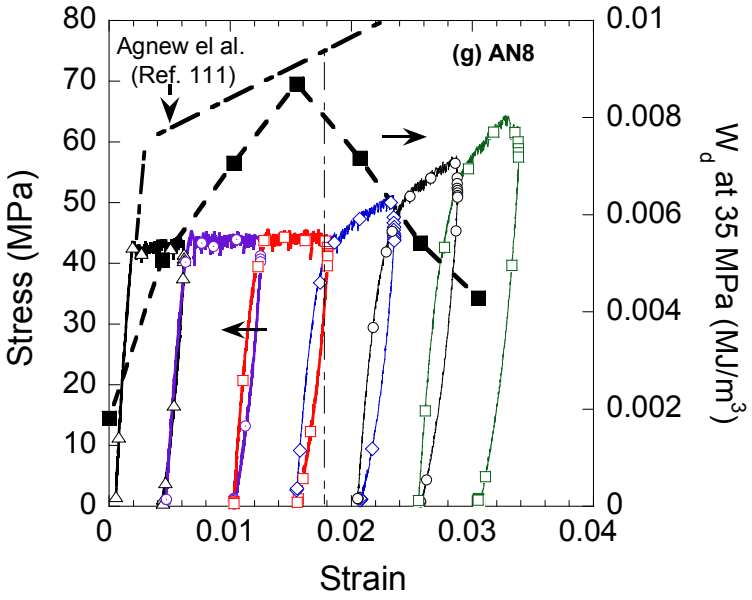

Figure 7.3: Typical stress-strain curves, including repeat loading-unloading cycles of, (a) as-received Mg at two different loading rates; (b) AN4, deformation history; (c) AN4, compares the hysteretic loops with different prestrain; (d) AN 12, deformation history; (e) AN12, nested hysteretic loops with prestrain 4%; (f) deformed, AN2 and AN8 and; g) AN8 sample deformation history. Also plotted on the same curves are the results of Agnew et al. [111]. The W_d values at 35 MPa – which peak at ≈ 2 % - are plotted as a function of pre-strain on the left-hand side y-axis.

The stress-strain curves of the AN12 sample (Fig. 7.3d) were quite similar to those of AN4 shown in Fig. 7.3b, in spite of the large differences in grain sizes - 170 μm vs 600 μm – between the two samples. The nested hysteretic loops of AN 12 with prestrain 0.04 are shown in Fig. 7.3e.

Up to a stress of 54 MPa, the stress-strain curves of the DEF sample were characterized by small loops and the absence of a yield point (Fig. 7.3f). The yield point of this sample was > 60 MPa. Annealing for 2 or 8 h, restores the σ_y's to ≈ 50 and ≈ 43 MPa, respectively, and enlarges the hysteretic loops (Fig. 7.3f). Not surprisingly, σ_y is lower for the AN8 sample than for AN2. To further explore the effect of deformation on the size of the loops, sample AN8 was compressed beyond its σ_y of 43 MPa (Fig. 7.3g). Three regimes are observed: At strains < 0.1 %, the response is almost linear elastic and W_d (plotted on the right y-axis) at 35 MPa is quite small. At ≈ 0.2 %, the sample yields, without strain hardening, up to a strain of ≈ 1.8 %, at which point W_d is at, or near, its maximum value (Fig. 7.3g). Beyond 1.8 %, strain hardening occurs and W_d decreases again. For the coarse-grained samples (Fig. 7.3b and d), only a decrease in W_d is observed, because the strain hardening starts at strains - ≈ 0.22 % - that are quite small. Note that to be comparable, the W_d's were all measured at the *same* stress of 35 MPa.

According to our model and as long as $N_k\alpha^3$ is not a strong function of deformation, then plots of ε_{NL} vs. $(\sigma^2-\sigma_t^2)$, U_{NL} vs. $\varepsilon_{NL}^{1.5}$, W_d vs. σ^2 or W_d vs. ε_{NL} should all yield straight lines, as observed in Figs. 7.4a-d, respectively. Similar linear plots were obtained for the AN8 sample after the various prestrains. Fig. 7.4e shows W_d vs. σ^2 plots. From the resulting plots and the values of σ, ε_{NL}, W_d and U_{NL} listed in Table 7.1, some important parameters concerning dislocations and their characteristics were calculated (Table 7.2). As is clear in Table 7.2, Ω/b calculated from the three terms of Eq. 2.18 are comparable, and independent of grain size and/or prestrain. To calculate N_k, $2\beta_x$, $2\beta_{xc}$ and ρ the value of 2α is required. In previous chapters, 2α was taken to be equal to the grain

size. As discussed below, the actual 2α is smaller than the grain size, especially for samples with grain sizes larger than 100 μm. Another way to obtain 2α is to calculate it from by Eq. 2.4 assuming $\sigma_c = \sigma_t^*$. Table 7.3 compares the parameters calculated by using both assumptions for the value of 2α.

Note that the linear relationships between ε_{NL} vs. $(\sigma^2 - \sigma_t^2)$ (Fig. 7.4a) or W_d vs. ε_{NL} (Fig. 7.4d) break down at higher strains for samples with grain sizes > 100 μm. This is shown in Figs. 7.4a-d by short vertical arrows that highlight the deviation from linearity at the highest stresses or strains.

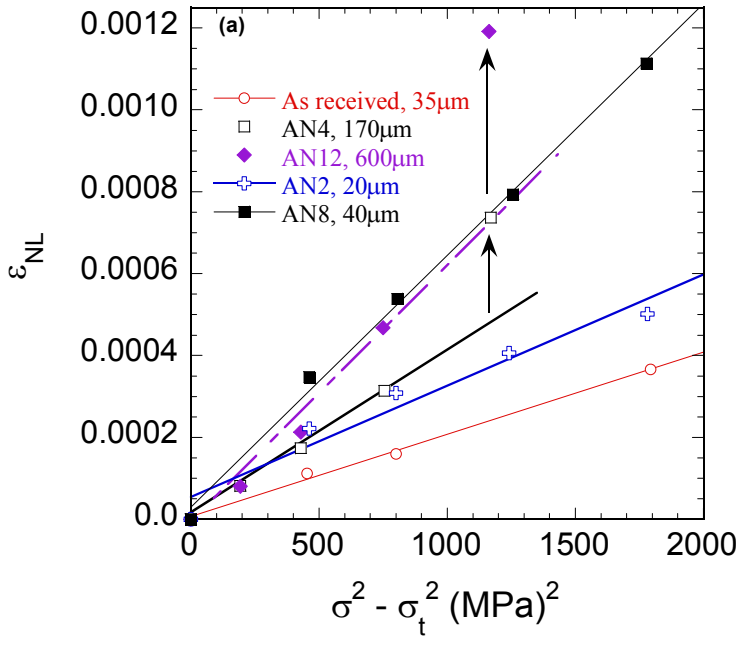

Fig. 7.4 (*continued*)

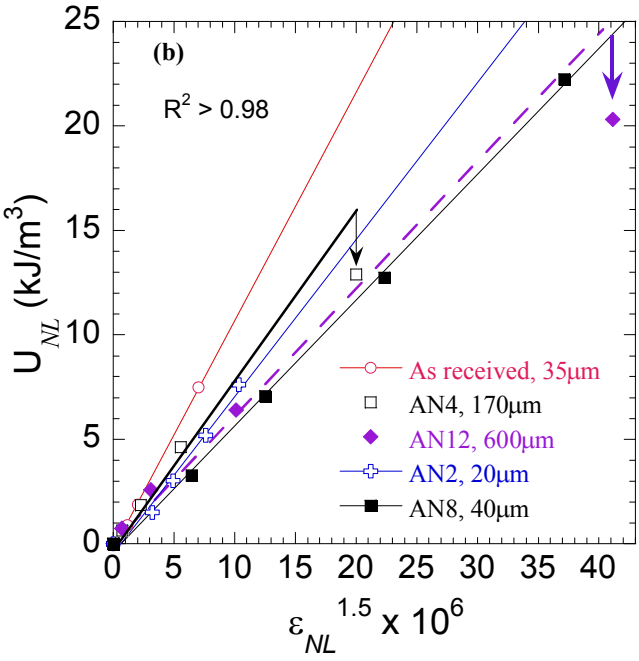

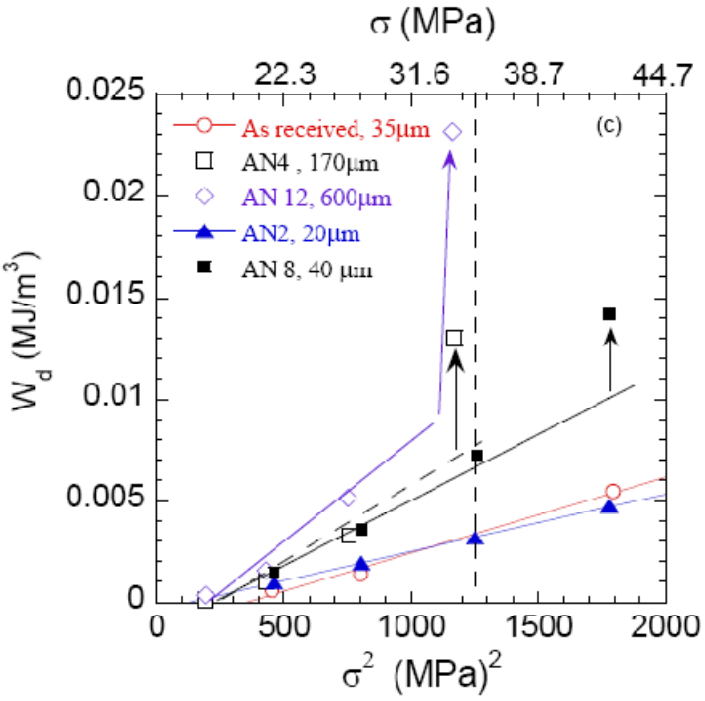

Figure 7.4 (*continued*)

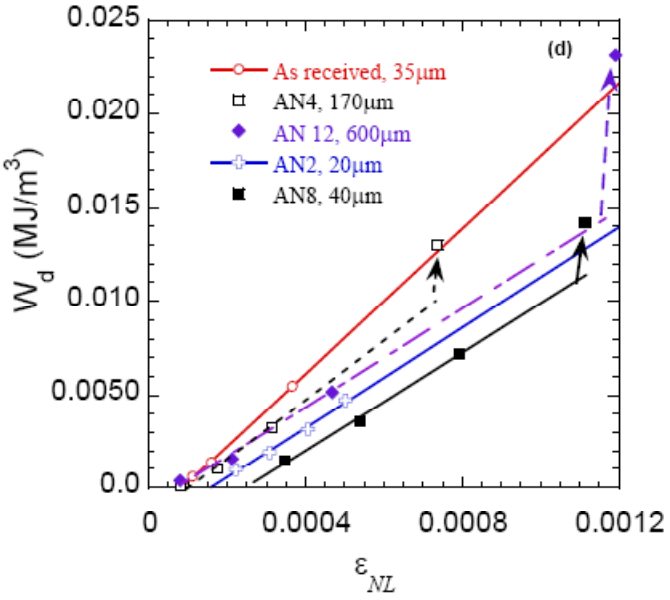

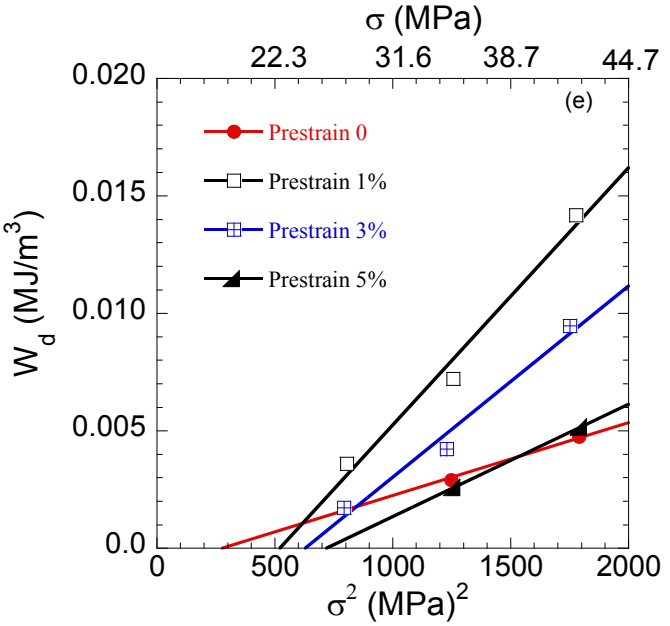

Figure 7.4: Plots of, Plots of, a) ε_{NL} vs. $\sigma^2 - \sigma_t^2$; b) U_{NL} vs. $\varepsilon_{NL}^{1.5}$; c) W_d vs. ε_{NL} and, d) W_d vs. σ^2 of various samples; (e) W_d vs. σ^2 of AN8 samples with different prestrains

Table 7.2: Summary of yield points, σ_y, threshold stresses, σ_t, determined directly from the stress-strain curves and from Fig. 7.4c; calculated values of Ω/b using Eq. 2.18; $N_k\alpha^3$ from m_1 term of 2.17. Results of as-received sample were taken from Ch. 6.

Sample	σ_y MPa	σ_t‡ MPa	σ_t* MPa	Prestrain	Ω/b (MPa) Eq. 2.18			$N_k\alpha^3$
					2nd term	3rd term	4th term	
As-received	50	19	14	0	3.2	3.2	3.2	0.5
AN2	51	11	12	0	2.3	1.4	2.2	0.5
AN4	10	14	6	4%	2.3	2.6	2.3	1.2
AN12	9	14	8	4%	2.1	2.0	2.1	1.7
AN8	45	17	20	0	2.2	2.2	2.2	0.6
		23	11	1%	3.1	2.8	2.8	1.5
		28	18	2%	3.9	3.4	3.9	1.8
		25	17	3%	2.6	2.6	2.7	1.3
		27	15	5%	2.6	2.2	2.6	0.7

‡ Determined from the W_d vs σ^2 plot in Fig. 7.4c and Fig. 7.4e
* Determined from deviation of stress-strain curves (Fig. 7.3) from linear elastic slopes.

Table 7.3: Comparison of using the measured grain size (column 3) as 2α or calculating 2α from Eq. 2.4 (column 8) assuming $\sigma_c = \sigma_t^*$ on N_k, the critical IKB diameter, $2\beta_{xc}$, from Eq. 2.7 and maximum IKB diameter, $2\beta_x$ from Eq. 2.8 and reversible dislocation densities ρ from Eq. 2.12.

Sample	Pre-strain	Grain size as 2α μm	N_k (μm^{-3})	$2\beta_{xc}$ μm	$2\beta_x$ μm	ρ (cm^{-2})	Cal. 2α μm	N_k (μm^{-3})	$2\beta_{xc}$ μm	$2\beta_x$ μm	ρ (cm^{-2})	σ_{max} (MPa)
As-received	0	35	0.0001	0.8	5	$3x10^8$	15	0.001	0.5	2	$6x10^8$	42
AN2	0	20	0.0005	0.6	3	$5x10^8$	20	0.0005	0.6	3	$5x10^8$	42
AN4	4%	170	$2x10^{-6}$	1.7	20	$9x10^7$	30	0.0003	0.7	3	$5x10^8$	34
AN12	4%	600	$7x10^{-8}$	3	71	$5x10^7$	30	0.0005	0.7	3	$9x10^8$	34
AN8	0	40	0.00007	0.8	5	$3x10^8$	20	0.0006	0.6	3	$5x10^8$	42
	1%		0.0002	0.8	5	$7x10^8$	11	0.01	0.4	2	$3x10^9$	42
	2%			0.8	5	$8x10^8$	8	0.03	0.4	1	$4x10^9$	42
	3%		0.0002	0.8	5	$7x10^8$	8	0.02	0.4	1	$3x10^9$	42
	5%			0.7	4	$5x10^8$	8	0.01	0.4	1	$2x10^9$	42

Table 7.4: Summary of KNE analysis of Mg and Mg alloys reported in the literature. Table also lists annealing conditions, reference (including the figure numbers in the original papers analyzed), grain size, test direction, pre-strain and the flow stress results. The letters in column 1 are the same as those in Fig. 7.5 and Fig. 7.6.

No.	Alloy Composition and annealing conditions	Ref.*	Grain size μm	Test direction‡	Pre-strain %	σ_f MPa	Ω/b (MPa) Eq. 2.18			$N_k\alpha_3$
							2nd term	3rd term	4th term	
A	Mg-7.7 at.% Al alloy, melted at 650°C, cast, extruded at 250°C; annealed at 400 °C for 24 h; solution treated for 8h at 415 °C, quenched in water. Aged 330 °C for 600 s. This sample has 10±1 vol. % β precipitates ($Mg_{17}Al_{12}$) dispersed within the grains	[44] Fig. 4	60	C	0.8	150	8.9	8.8	8.8	0.4
B	Extruded pure Mg (99.9%), annealed 8 h at 415 °C	[44] Fig. 4	60	C	1.05	50	3.1	3.1	3.1	2.2
C	Mg 6Zn alloy (Zn: 5.6 mass %), cast at 780 °C; solution treated at 450 °C for 9 h and quenched in water.	[117] Fig. 2	81	T	1.2	127	6.8	7.2	10.2	0.3
D	Commercial purity Mg (Zn contain < 0.005 mass %, Zr 0.64 mass %), Cast and stress relieved at 250 °C and air cooled.	[117] Fig. 2	91	T	1.25	70	3.5	3.4	3.6	1.5
E	Commercial purity Mg (Zn contain < 0.005 mass %, Zr 0.64 mass %), Cast and stress relieved at 250 °C and air cooled.	[117] Fig. 3a	91	C	1.2	50	3.5	3.6	3.9	3.0
F	Mg 6Zn alloy (Zn: 5.6 mass %), cast at 780 °C; solution treated at 450 °C for 9 h and quenched in water.	[117] Fig. 3b	81	C	1.3	100	8.4	10.3	8.7	0.6
G	Commercial purity Mg (Zn contain < 0.005 mass %, Zr 0.64 mass %), Cast and stress relieved at 250 °C and air cooled.	[117] Fig. 4a	91	T	1.2	70	8.4	12.3	12.2	1.8
H	Commercial purity Mg (Zn contain < 0.005 mass %, Zr 0.64 mass %), Cast and stress relieved at 250 °C and air cooled.	[117] Fig. 4a	670	T	1.2	52	11.5	7.8	7.8	2.7
I	Mg 6Zn alloy (Zn: 5.6 mass %), cast at 780 °C; solution treated at 450 °C for 9 h and quenched in water.	[117] Fig. 4b	48	C	1.1	153	15.5	17.4	12.6	0.2
J	Mg 6Zn alloy (Zn: 5.6 mass %), cast at 780 °C, solution treated at 450 °C for 9 h and quenched in water.	[117] Fig. 4b	344	C	1.3	80	5.9	6.5	8.2	0.6
K	Commercial AZ91, HPDC, casted by 250 ton cold chamber machine	[45] Fig. 1	10	T	1.1	180	9.9	9.7	9.7	0.3
L	Commercial AZ91, sand cast T4, solution treated 24 h at 413°C; water quenched.	[45] Fig. 2	130	T	3.1	170	14.2	14.4	14.4	0.2
M	Commercial AZ91, sand cast T6, solution heat treat 24 h at 413°C, water quenched, aged 16 h at 165°C	[45] Fig. 2	130	T	2	230	18.1	17.1	17.3	0.2
N	Commercial AZ91, sand cast 120, solution treated 24 h at 413°C, and water quenched; aged 120 h at 165°C	[45] Fig. 3	130	T	3.5	270	22.1	20.9	21.0	0.1
O			130	C	3.3	268	24.1	24.7	24.9	0.1

*: Figure numbers in this column refers to figures numbers in original paper. ‡ T: Tension, C: Compression.

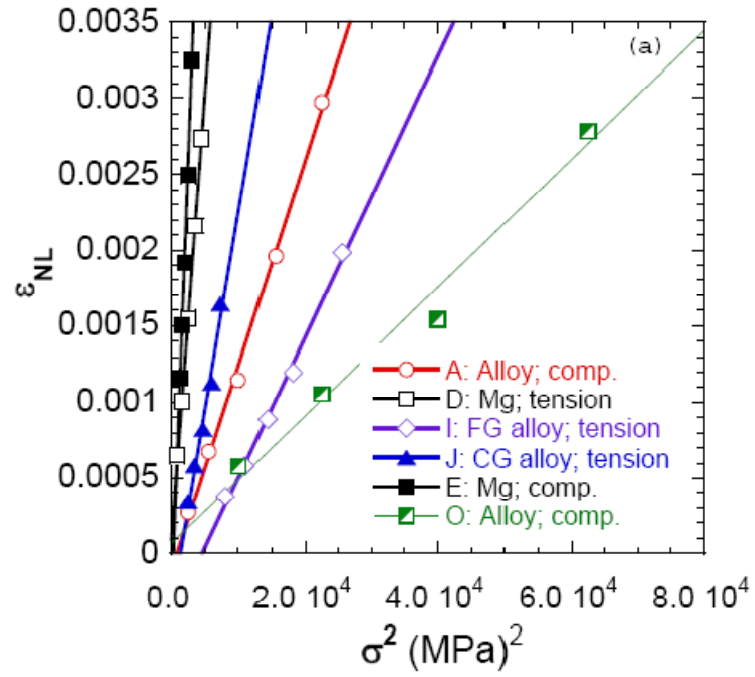

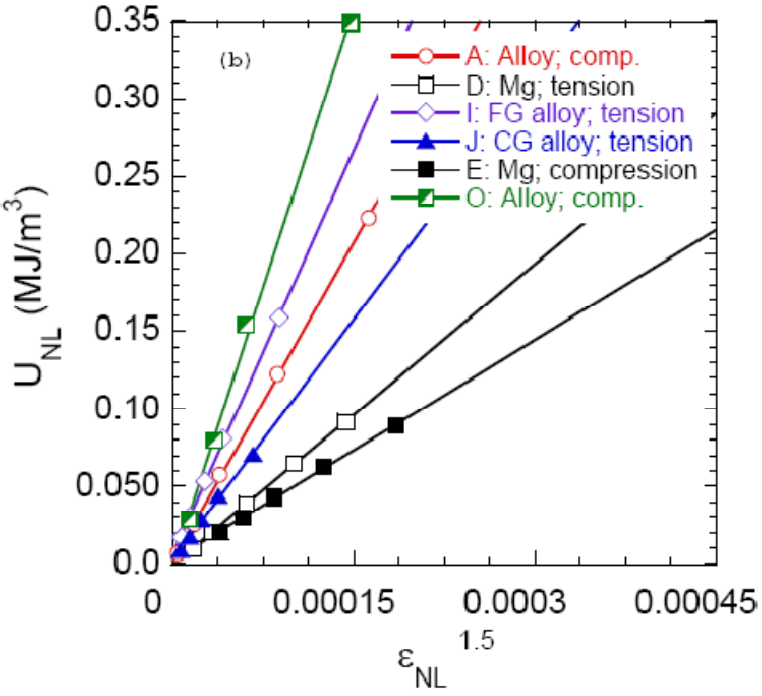

Figure 7.5 (*continued*)

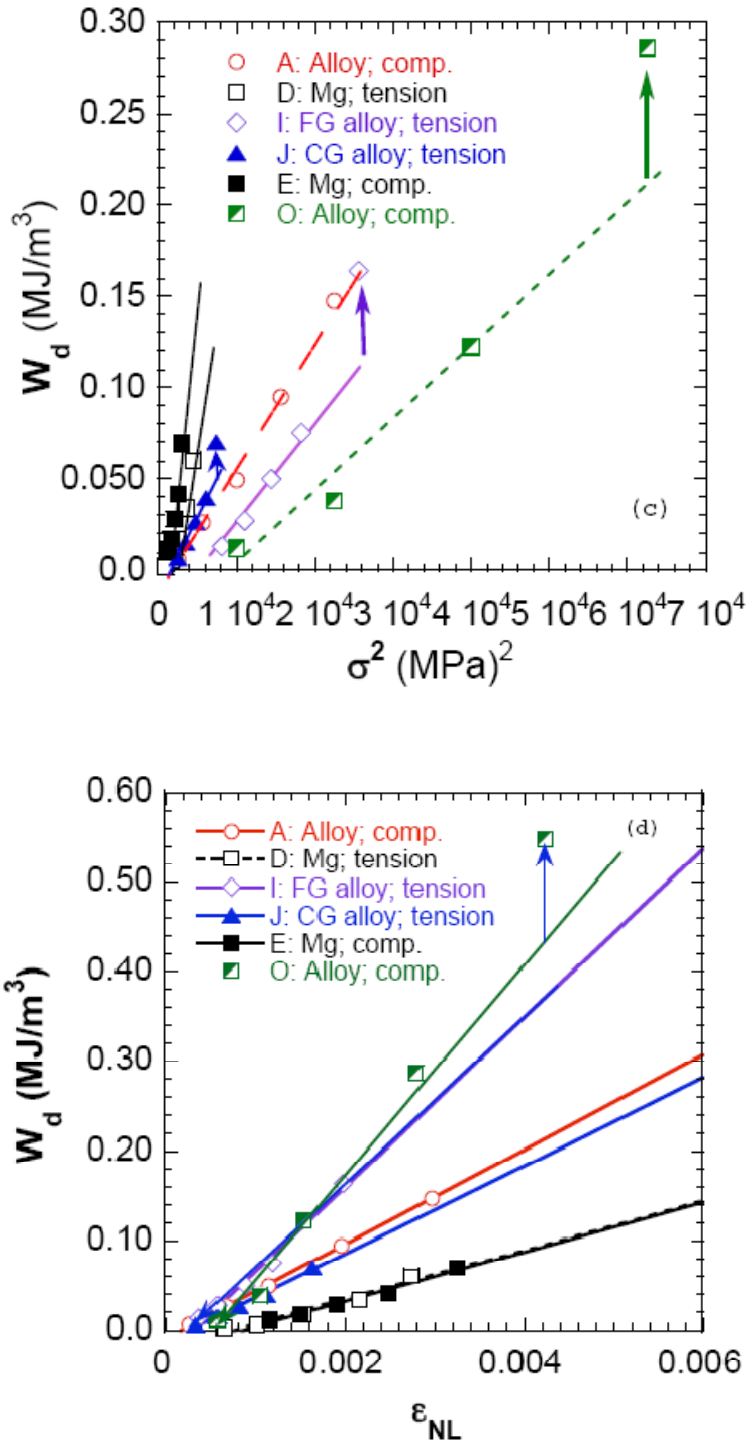

Figure 7.5: Plots of, a) ε_{NL} vs. σ^2; b) U_{NL} vs. $\varepsilon_{NL}^{1.5}$; c) W_d vs. σ^2 and, d) W_d vs. ε_{NL} for select results from Refs.[44, 45, 117]. For details see Table 7.4.

To further test the applicability of our model we applied it to the results obtained by Mann et al. [117], Caceres et al. [45] and Gharghouri et al. [44]. In Figs. 7.5a-d we plot ε_{NL} vs. σ^2, U vs. $\varepsilon_{NL}^{1.5}$, W_d vs. σ^2 and W_d vs. ε_{NL}, for some of their results, respectively. In all cases, agreement between theory and model is excellent. Table 7.4 summarizes the various experiments and the resulting Ω/b values obtained from our model again using Eq. 2.18. The calculation details can also be found in Appendix B.

7.5 Discussion

7.5.1 Kinking Nonlinear Elasticity

The results presented herein, especially those shown in Figs. 7.4 and 7.5, not only confirm our recent conclusion that Mg is a KNE solid [131], but also shed important light on IKB nucleation and growth. From the totality of the results the following observations are noteworthy and support our model:

i) Some small plastic deformation – most likely in the form of dislocation pileups - is needed for the nucleation of IKBs. This is best seen in Fig. 7.3g: W_d for the virgin sample is small, reaches a maximum at a strain of ≈ 1.5 %, before decreasing again. Others also reported that pre-deformation increased the W_d values [45, 117].

Presumably, during the deformation plateau (Fig. 7.3g) more IKBs are nucleated, which increases both W_d and U_{NL} (Table 7.1). The plateau has been associated with the twining of easy to twin grains [112, 132]. Such twins presumably rotate grains such that their basal planes are in a better position to form IKBs and increase W_d. As more twins form, they result in the work

hardening observed at the end of the plateau, which results in a reduction in domain size and thus W_d. The relationship between twinning and work hardening is made clear when these results are compared with Ti_3SiC_2 that does not twin. In the latter case, W_d scales with σ^2 until the sample fails. In other words, no decrease in W_d is observed.

Consistent with this conclusion is the monotonic increase in σ_t – from ≈ 16 MPa for the virgin sample, to 26 MPa for the sample deformed 5 % - with increased deformation (Fig. 7.4e and Table 7.2). The relationship between σ_t and domain size, or 2α, is given in Eq. 2.4. That twins result in significant strain hardening is well established in the metallurgical literature, in general [132, 133], and in Mg, in particular [46, 111, 112, 123, 134]. The relationship between the plateau and twinning is further enhanced by noting that neither Co nor Ti_3SiC_2 twin; neither exhibit a plateau.

ii) From Table 7.2, the average CRSS of the basal plane dislocations is 2.7±0.6 MPa. As noted above, this value is in good agreement with literature results obtained from the deformation of Mg single crystals that fall in the range of 0.5-3 MPa [114, 135, 136]. The importance of this result cannot be overemphasized, since it indirectly confirms one of the basic tenets of our model namely, that U_{NL} and W_d are due to basal plane dislocations. The three columns labeled Ω/b in Tables 7.2 and 7.4 are obtained from Eq. 2.18. The fact that we obtain essentially the same values of Ω/b from two totally

independent variables, U_{NL} and W_d, is noteworthy and lends significant credence to our model.

The fact that Ω/b remains constant, and essentially a weak function of grain size and/or deformation history (Table 7.2) is also consistent with its definition. Our values are also in excellent agreement with those obtained from the pure Mg stress-strain results – both in tension and compression - of Gharghouri et al. [44] and Mann et al. [117] (entries B, D and G in Table 7.4).

iii) The validity of our Ω/b results and their relationship to the flow stress, σ_f – defined here as the maximum stress at which a series of nested loops was obtained – is best seen in Fig. 7.6, where Ω/b is plotted vs. σ_f. Despite some scatter, the R^2 correlation coefficient value of 0.87 indicates a strong correlation, nevertheless. This is especially significant given that the Ω/b values were calculated from the *reversible* loops obtained in both *compression and tension*, the large range in flow stresses - over a factor of 5 - and alloy compositions covered. These results also include extruded sample with strong textured, as well as cast samples with weak texture (Table 7.4). Note that in all cases k_1 and k_2 were assumed to be 2; values that are reasonable for non-textured samples, but become less so for highly textured samples, which probably contributes to some of the scatter seen. The importance of these results, again, cannot be overemphasized.

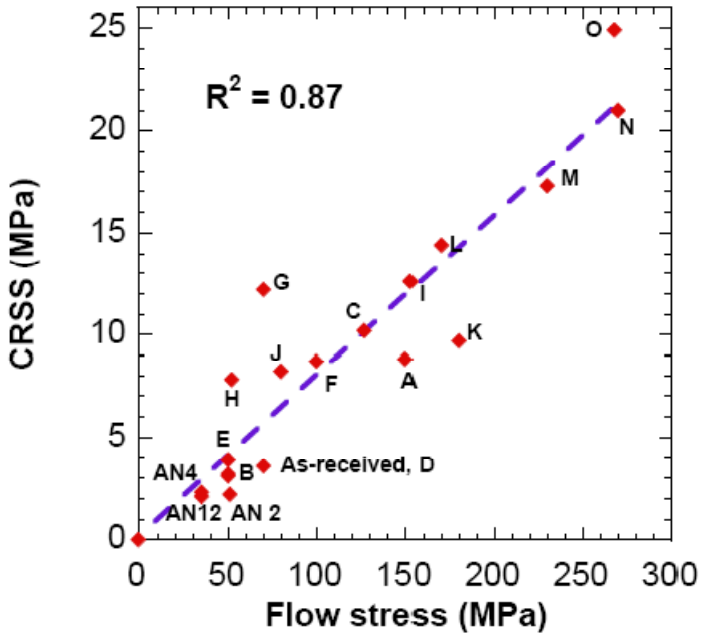

Figure 7.6: Plots of Ω/b versus flow stress – defined as the maximum stress at which a loop is obtained - for our and literature results. See Tables 7.2 and 7.4 for details.

iv) As we have repeatedly shown, coarse-grained samples dissipate substantially more energy per cycle than their fine-grained counterparts [6, 25]. This is best seen in Fig. 7.4c: at ≈ 35 MPa (dashed vertical line), W_d for the samples with the largest grain size, AN12, is roughly 3 times larger than the as-received or AN2 samples, with the finest microstructures. Note that since the governing equations are *identical*, it is unlikely that different mechanisms are occurring in fine- and coarse-grained Mg as has been suggested by some. The same conclusion is valid for the results of Mann et al. [117]; at a *given* stress level, their coarse-grained Mg dissipates *more* energy than their finer-grained counterpart (compare open diamonds with solid triangles in Fig. 7.5c).

v) The product $N_k\alpha^3$ is roughly equal to the number of IKBs per grain, or domain, and thus should be of the order of unity as observed (Tables 7.2 and 7.4). Note these values are obtained *directly* from the experimental results, the only assumptions being the values of k_1, k_2 and w chosen. So it is reasonable that $N_k\alpha^3$ increases with grain size. and pre-strain as observed (Table 7.2). It is thus not coincidental that a 2 % pre-strain, that results in the largest loops, also results in the largest value of $N_k\alpha^3$ (Table 7.2).

vi) In previous chapters, we assumed the grain size to be 2α. The results of this chapter clearly show (see below) that beyond a certain grain size, here is little effect on the shapes of the stress-strain curves (compare Fig. 7.3b and 3d) and as important the threshold stresses (Fig. 7.4c). There is thus an effective domain size 2α that must be smaller than the grain size. As shown in Table 7.3, if the grain size is used as 2α, some calculated values for coarse-grained Mg (170 μm and 600 μm) are obviously wrong (An IKB with diameter 70 μm is too large to reverse and/or would have been observed). The other method to obtain 2α is calculated from Eq. 2.4. The calculated values listed in Table 7.3 are more reasonable. For example, ρ based on the calculated 2α are in the range of 0.5-4 x 10^9 cm^{-2}. This value is in much better agreement with the values reported for the MAX phases in Ch. 3-5, viz. 1-2 x 10^9 cm^{-2}. Therefore, it is reasonable to conclude that the calculated 2α values from Eq. 2.4 is correct. It follows then that ρ due to IKBs is always in the range of 1-3 x 10^9 cm^{-2} before IKBs transform to KBs.

vii) From the comparison of N_k and ρ in Table 7.3, it is clear that ρ is more a function of stress than microstructure. In the coarse-grained samples, relatively few, large diameter, IKBs form; in the fine-grained samples, many more, smaller, IKBs form.

7.5.2 Limitations of model

In the remainder of this paper we discuss some limitations of our model and point out a few remaining aspects that are not totally understood. We subsequently evaluate the literature results in light of our hypotheses to try to shed some more light on the problem.

Based on our model, σ_t should decrease with increasing grain size. The results shown in Table 7.2, however, clearly show that not to be the case; beyond a certain grain size, σ_t does not decrease further. There appears to be a limiting size to 2α, that for Mg is of the order of ≈ 50 μm. The same is true for Co in Ch. 8. In other words, there is a limit, beyond which the effective domain size is limited by something other than grain boundaries. The reason for this state of affairs is not understood at this time.

To better understand the role of grain size on the deformation behaviour of Mg it is useful to compare Figs. 7.3b, d and g, for which the grain sizes are 170 μm, 600 μm and 40 μm, respectively. Qualitatively, the curves are identical; a linear regime, followed by a yield point, a plateau, followed by a regime of substantial strain hardening. The major differences between the three curves lie in the values of the yield points and, as important, the widths of the stress plateaus. In the finer-grained samples, where grain bending is more difficult, the propensity for twinning is also reduced and vice versa for the coarse-

grained samples. Thus, in the coarser-grained sample, twinning is induced at lower stresses than in the finer-grained sample (10 MPa vs. 43 MPa).

7.5.3 Relationship between Kinking, Bending and Twinning

As noted above previous work had shown a strong relationship between kinking, bending and twinning [38, 102, 108, 115, 116]. It thus follows that microstructures that favor the former two, should also favor the latter. In this section we present some evidence for the mechanism we propose in Fig. 7.1 for the formation of tensile $\{10\bar{1}2\}$ twins that form under compression.

We start with highly oriented microstructures. Using *in situ* neutron diffraction, Agnew et al. [111, 122, 137, 138] carefully studied the deformation of a highly oriented commercial Mg alloy (AZ31B) with a grain size of 55 μm. And while the stress-strain curves for the IPT and TTC microstructures (Figs. 7.1f and h) were almost superimposable, the response of the IPC microstructure was quite different. (The results for the latter are plotted in Fig. 7.3g in top left). The *in situ* work showed that in the latter case, the yield point coincided with the formation of $\{10\bar{1}2\}$ twins and the deformation of soft grains by the formation of dislocation pileups. Given that the hardening rate observed by Agnew et al. [111] is similar to the one we report (compare the hardening rates of curve labeled Agnew et al. and our results in Fig. 7.3g), and since their grain size is comparable to ours, it is reasonable to conclude that the hardening we observe is also due to twin formation. As noted above, the role of twinning in hardening is well appreciated in the metallurgical literature [46, 111, 112, 123, 132-134]. When Agnew et al. [122] studied the two other orientations, viz. IPT and TTC (Figs. 7.1f and h), they found that twinning played a more modest role in the deformation.

When the basal planes were compressed edge on (Fig. 7.1g), the stress-strain curves of Barnett et al. [139] – who tested AZ31 plates with a grain size of 9 μm - are qualitatively similar to the ones shown in Fig. 7.3g. They were characterized by a yield point, followed by a *plateau* at ≈ 80 MPa to about a strain of ≈ 2 %, followed by a region of work hardening, again, with a hardening rate, again, comparable to that shown in Fig. 7.3g. Conversely, when the basal planes were pulled in tension (Fig. 7.1f), or compressed along the c-axis (Fig. 7.1h), here again, the propensity for bending was reduced and twinning played a much more modest role.

Gharghouri et al. [44] – working with a grain size of ≈ 60 μm - also reported large anisotropies in tension and compression in their oriented microstructures, as well as nonlinear deformation. As importantly, their stress-strain compression curve - after the nonlinear deformation - was remarkably flat at about 50 MPa, up to a strain of ≈ 0.015 at which point the sample was unloaded. In other words, their work was confined to the plateau region shown in Fig. 7.3g. A similar plateau was observed more recently by Agnew et al. [50]. To explain the nonlinear deformation, Gharghouri et al. [44] invoked the formation of a fully reversible $\{10\bar{1}1\}$ twins. As discussed below, this interpretation is most likely incorrect.

The totality of the aforementioned results can be explained qualitatively by the schematic presented in Fig. 7.1. Kinking is a “buckling” instability that leads to bending, and therefore it is not surprising that the samples loaded in IPC (Fig. 7.1h), would result in the highest density of IKBs, and consequently twins. In the IPT and TTC cases, the propensity for grain bending is reduced, which in turn explains the more modest role played by twinning in those microstructures [122]. In other words, the microstructures

that enhance KB formation should be the ones that enhance twinning, as observed. Such a view would also explain the close relationship between twinning and kinking that is especially strong in single crystal work and coarse-grained samples [38, 108, 115, 116]. It is vital to note, however that the opposite is not true, i.e. lack of twinning does *not* reduce the propensity for IKB formation (see below).

In contradistinction, when cast AZ91 Mg – with a 130 μm grain size - was tested [45, 117] there was very little *asymmetry* between compression and tension. This observation is also consistent with our conjecture. When a KNE solid, with no preferred orientation, is loaded the propensity for grain bending, IKB, KBs, etc. formation should not depend on the loading direction, as observed. Said otherwise, whatever phenomenon results in the reversible loops is independent of the state of stress, but only in a non-oriented microstructure.

To date, we have not presented direct evidence for the existence of IKBs. The circumstantial evidence presented here, and in previous work is quite strong, however [6, 15, 16, 19, 23, 25, 29-31, 72, 140]. Recently we attempted to observe IKBs in lightly textured Co by neutron diffraction [141], and while we were not able to see their effects, most probably because of the small values of γ_c, we did *not* see evidence for twins and/or dislocation pileups either. And since the measured neutron diffraction strain, could only account for the elastic part, it follows, by a process of elimination, that the only remaining plausible mechanism is the one we propose.

7.5.4 Damping and the Case Against Reversible Twinning

Ever since Reed-Hill et al. [89] proposed the idea of reversible twinning to explain

the room temperature hysteresis in Zr alloys - that were pre-deformed at 77 K - others have invoked it to explain hysteresis in other hexagonal metals including Mg alloys [44, 45, 117, 142]. And while this explanation maybe valid in Zr where $\{11\bar{2}1\}$ twins – that are nothing but *special cases of KBs* [100, 143] and thus *mobile* and reversible – formed, we do not believe reversible twinning can explain the results obtained in this and previous work [44, 45, 117] for a number of reasons:

i) As far as we are aware, and in sharp contrast to IKBs, it is not clear to us what the driving force for spontaneous reversible twinning is. Twinning in Mg is indeed reversible, but *only* if the stress is *reversed* [123, 138, 144].

ii) In the early work on twinning in Mg single crystals [101-106, 108] there is no mention of reversible twinning. Also if the reversibility is due to the formation of twins then it is not clear why W_d decreases with increasing deformation, rather than increase. This is especially true given the modest strains explored herein (Fig. 7.3c and g).

iii) There is a fundamental difference between twinning and KB formation: the former leads to hardening (as seen here and previously), the latter to *softening*, because it rotates the basal planes into a direction more suitable for slip. This was best exemplified in our work on Ti_3SiC_2 loaded in IPC (Fig. 7.1g). The stress increased until the corners buckled - by kink band formation - which in turn rotated basal planes into a direction in which basal slip could now occur, leading to shear banding and strain, or geometric softening [5]. Yang et al. [145] studied the dynamic recrystallization of a Mg alloy deformed at 673 K and, using OIM, presented compelling evidence for the idea that KBs lead to softening. There is no reason why

such a process – without the formation of shear bands – could not be operative here at a lesser scale at room temperature.

iv) Agnew et al. [50] reported a strong Bauschinger effect upon unloading from tensile experiments. Given that IKBs are due to the reversible motion of dislocations, they are most likely the origin of that Bauschinger effect. A similar Bauschinger effect is observed in compression experiments of equal channel angular extrusion Mg [49]. Here again there is no evidence for twinning. It follows that no correlation exists between twinning and the Bauschinger effects.

v) There is another fundamental problem with attributing the strains observed to twins. In Ref. [44], the strains associated with $\{10\bar{1}2\}$ twins are relatively large and therefore their concentration would have to be quite low and, consequently, highly non-homogeneous. In contrast our IKB model is one in which a large number of IKBs, of the order of one per grain (see Table 7.2), each contributing a very small ≈ 1.5°, rotation to the overall strain. In other words, IKB strains are small and homogeneously distributed.

vi) KNE elasticity in the ternary carbides, Ti_3SiC_2 [6, 25] (Ch.4), Ti_2AlC [15] (Ch.3), $Ti_2AlC_{0.5}N_{0.5}$, Ti_3AlC_2, Ti_3AlCN (Ch. 5) and Cr_2GeC [146] among others, that do *not* twin, are subject to the *same* relationships derived herein. The same is true for Co, which at low strains does not twin and for which we saw no evidence of twinning in neutron diffraction, despite the presence of robust loops [141]. In other words, our model works equally well for solids that do not twin in which case it is impossible that the latter are causing the loops.

We are not advocating that there is *no* correlation between twinning and KNE behavior. For example, a recent paper on $LiNbO_3$ [22] we showed that twining that rotated basal planes - that prior to the deformation could not contribute to W_d – in such a way as to increase the shear stress acting on them greatly enhancing W_d. We propose a similar relationship here. The formation of twins can rotate the lattice and form new domains in which IKBs can nucleate, which is what we believe may be happening during the plateau region. However, as we show herein that the effect can be tempered by a concomitant reduction in domain size and the ultimate reduction in W_d (Fig. 7.3g).

The role of IKBs has to date not been appreciated is first and foremost because they are fully reversible and their effect is quite subtle and thus easy to overlook. The subtle derives mostly from the fact that the misorientations are typically small (≈ 1.5°). It is much more prevalent at higher temperatures as several groups have shown. For example, even after a 10 % deformation the misorientations are typically in the 2-3° range, and these are apparent only when large grains are scanned over their entire lengths [120, 145]. There is no compelling reason for these mechanisms *not* to be occurring during the room temperature deformation of Mg. These comments notwithstanding, the excellent and meticulous work of Hauser et al. [8, 18] clearly and unambiguously demonstrated the importance of kink bands and bend planes, referred to here as MDWs – and shown by Hauser et al. to be indeed mobile under load - in the deformation of coarse-grained Mg. In that paper they also showed that in one specimen 10 twins caused extension and 23 caused contraction in the stress direction rendering the strain due to twinning in that specimen negative, a fact, as noted above, not easily reconciled with strain energy consideration. It follows that the twins are not a direct reaction to the compressive

stresses, but most probably a response to bending strains as postulated herein. No evidence for pyramidal slip was found.

In random texture, TTC and IPT Mg samples a well-defined yield point does not exist; rather microyielding is followed by a gradual softening with increased deformation [112, 129, 147]. The response of Ti_3SiC_2 at room temperature is fully reversible till failure, i.e. there is no plastic deformation. The latter is only observed at temperatures higher than the brittle-to-plastic transition, at which point the fracture toughness drops, but the strain to failure – due to cavitation and microcracking is greatly enhanced [52]. In other words, the response of Mg at room temperature is closer to that of Ti_3SiC_2 at higher temperatures than at room temperature. Given that both Mg and Ti_3SiC_2 are plastically anisotropic - with basal slip being the preferred system – it is reasonable to ascribe the difference between them to the interaction of the dislocation pileups with the grain boundaries: In Mg, the grain boundary decohesion strength must be lower, which, in turn, would allow the dislocation pileups to cause GB decohesion. Such a mechanism would explain the creep observed at the lower strain rates (Fig. 7.3a). Another implication of weaker grain boundaries is that the IKBs can devolve into mobile dislocation walls, MDW, as a result of the tensile stresses at their tips. Such MDW have been observed in post-creep examination of coarse-grained Mg subjected to tensile creep at higher temperatures [47]. This indirectly confirming that the response of Mg at room temperature is comparable to that of Ti_3SiC_2 at elevated temperatures. Along those lines it is worth noting that in our high temperature work on the tensile creep deformation of Ti_3SiC_2 strains of up to 4 % were recorded without cavitations [148]. In other words, the combination of dislocation pileups and kinking are sufficient to impart the solid with

cavitation-free deformation; at strains greater than 4 % cavitation was observed [148]. It is therefore reasonable to conclude that Mg - that can also twin – can deform, to at least 4 % strain - by the activation of basal slip *alone,* provided MDW and KBs form. The Ti_3SiC_2 results cannot be overstated, since non-basal slip and/or twins have *never* been observed in deformed samples; the c/a ratio of ≈ 5 renders non-basal slip prohibitively expensive [33, 120]. Incidentally a very similar situation is encountered in ice, where only basal slip is observed [149, 150].

We submit that the answer lies in the formation of, first and foremost, dislocation pileups and then a combination of grain boundary sliding and/or decohesion, together with twinning, IKBs, MDWs and KBs. It is quite likely, that when the latter three are accounted for in the various models, the need to invoke non-basal slip can be avoided, or at least minimized. This is especially true given that the evidence of non-basal slip remains weak; evidence for its absence is much stronger. For example, Partridge and Roberts [108] compared the impressions formed on two different planes of single crystals of Mg and Zn that were indented with Vickers and Knoop indenters. Their major conclusions was, " deformation mode…. in the basal planes is pyramidal slip (in Zn) and twinning (in Mg), and in the prism planes it is basal slip". Thus evidence for pyramidal slip was *only* found for Zn, but *not* Mg; if sharp indenters do not activate pyramidal slip in Mg, it is unlikely that it would be activated in a uniaxially loaded polycrystal. In contradistinction, these authors invoke the presence of KBs to explain some of their anisotropic effects. They also noted that stresses are transmitted over large (sometimes as large as 10X) distances, when the indenter is loaded parallel to the c-axis by a mechanism involving KB formation. It is important to note a very similar conclusion was recently

reached by analysis of indentation marks in sapphire [19] and ZnO single crystals [20] also in two orientations. When loaded parallel to the c-axis, KBs were invoked to explain the large distances over which the deformation was observed [20]. There is no reason to believe such a mechanism is not operative here.

7.6 Summary and Conclusions

Herein we show that the microyielding and the fully reversible stress-strain loops of Mg and some of its alloys, in both tension and compression – in this and previous work [44, 45, 117] - can be explained by invoking the formation of fully reversible, dislocation-based IKBs. We also propose that twins initially enhance the size of the loops, before ultimately suppressing their formation. We further make the case that reversible twinning cannot be the source of the reversible loops. Lastly we make the case that our understanding of the deformation of polycrystalline Mg could be better modeled by invoking the formation of MDW's walls and KBs, as opposed to <c+a> slip for which the evidence is weak. The combination of IKBs, MDW and KBs, can, in principal, account for at least some of the elusive slip in the c-direction that is so sorely needed.

Based on this chapter's results, the damping capacity or elastic hysteresis of Mg can now be explained and controlled. First, it is strongly dependent on grain size. Coarse-grained samples dissipate more energy than their fine-grained counterparts. This enhancement is only good, however, to a grain size ≈ 100 μm, beyond that size the further increases in grain size are do not further enhance damping. Additionally, preexisting IKB nuclei play an important role. A well annealed sample with no IKB nuclei does not show much elastic hysteresis. A small plastic deformation before strain hardening can induce some IKB nuclei in the sample and improve the sample's damping

capacity. However, further plastic deformation that causes strain hardening will reduce the damping capacity because of a reduction of domain size, which results from the formation of twins in the sample.

8. Kinking Nonlinear Elastic Deformation of Cobalt

8.1 Introduction

Cobalt (Co) is an important magnetic metal that is applied in many fields. In Chapter 6, Co was classified as a kinking nonlinear elastic (KNE) solid [131] because of its large fully reversible hysteretic stress-strain curves. Generally, basal slip, kink bands and twins are formed during the plastic deformation of Co [41, 88, 151, 152]. Two types of twins were observed in the deformation of Co: normal lenticular twins and some very narrow twins $\{11\bar{2}1\}$ [151]. Vaidya et al. [41] also observed kink bands and $\{11\bar{2}1\}$ twins in Co. It is important to note that $\{11\bar{2}1\}$ twins are nothing but KBs - where a basal-plane dislocation is nucleated every c-lattice parameter [99, 100]. Yoo et al showed that the prevailing slip systems in Co are $(0001)[11\bar{2}0]$ basal slip [81]. The CRSS of Co for this slip was reported to be 6.4-6.9 MPa [95, 96] or ~13MPa [94].

Besides its technological importance, Co has some unique properties, as compared with other KNE solids, that render it almost a perfect model material to study kinking non-linear elasticity in metals. First, it has a higher yield point than other KNE metals (Ti, Mg, Zn etc.) and thus can be loaded to higher stresses, which in turn, i) results in larger hysteretic loops and, ii) renders the transition from linear to nonlinear elastic deformation more easily observable. Co can also be plastically deformed and thus allow for a systematic exploration of such deformation on kinking. Third, Co is the only known KNE solid to date with magnetic properties. It shows both magnetic hysteresis as well as mechanical hysteresis and an intriguing possibility is the linkage between the two. For example, it is well known that the Young's modulus of Co varies with magnetization [153]. And while this facet is beyond the scope of this work and is a topic of ongoing

research, fully understanding its mechanical hysteresis is a first necessary step to explore such an intriguing interaction.

As noted above, a sufficient condition for a solid to be KNE is plastic anisotropy (Ch. 1) [25]. Co is hexagonal close-packed (HCP) at room temperature, and face center cubic (FCC) at temperatures > ~ 450 ^{o}C [88]. Given that the former is plastically anisotropic and the latter is not, a crucial test of this idea is to compare the mechanical hysteresis of both crystal structures. Therefore, the purpose of this chapter is to study the KNE deformation of Co as a function of grain size, prestrain and temperature.

8.2 Experimental Details

Rods and bars of Co (99.97 %, ESPI metals, Ashland, Oregon) were tested. Rods, 12.7 mm in diameter and 31 mm long, were used for the compression tests; a bar with dimension of 3x10x80 mm^3 was used for the tensile test. A hydraulic testing machine (MTS 810, Minneapolis, MN), supplied with a controller (Microconsoler 458.20, MTS, Minneapolis, MN) was used for the compression tests. Tensile grips (MTS 686) were used for the tensile tests. A 25 mm gauge length extensometer (MTS 632.59C-01) attached directly to the sample, was used to measure the strains. All tests were carried out in load control mode with a load rate of 10 MPa/s, which translates to a strain rate of ≈ 7x10^{-5} s^{-1}. At every test, the sample was loaded to one stress level and unloaded to almost zero. This procedure was repeated several cycles for every stress levels to obtain nested hysteretic loops.

In order to increase the grain size, some samples were annealed at 1000 °C in flowing Ar gas for 4, 12 or 48 h, before furnace cooling. The samples' microstructures

were revealed by polishing (to 0.25 μm by silica) and etching (HNO_3:H_2O=1:1 by volume). The samples were then observed using an optical microscope, OM (Olympus PMG-3), and a scanning electron microscope, SEM (FEI/Phillips XL30). The grain size was estimated by Heyn's intercept approach [130]. Several lines were superimposed over the OM micrographs at a known magnification. The true line lengths were divided by the number of grains intercepted by the lines to obtain the grain size.

The compression direction was parallel to the original rods' axis. According to neutron diffraction in Los Alamos National Lab, the Co samples had mild fiber texture with c-axes preferably oriented along original cylinder axis (thank Dr. S. Vogel for this texture information).

A high temperature furnace (MTS 657.01) was used for some of the compression tests at 300 ^{o}C and 500 ^{o}C. The temperature was measured by placing a B-type thermocouple near the sample. The thermal expansion of the same sample, in the temperature range from room temperature to 700 ^{o}C, was measured by a dilatometer (UNITHERM model 1161, Anter, Pittsburgh, PA). The heating rate was 5^{o}C/min.

In order to observe the microstructural changes that occur upon loading, a 48 h annealed Co sample was polished and etched. The surface marked by Vickers indentations was then observed in the OM, before and after, a 3 % deformation in compression.

8.3 Results:

From the OM micrographs, the grain size of as-received Co was measured to be ~30±15 μm. The grain size after annealing at 1000 °C for 4, 12 and 48 h was 80±20 μm, 110±30 μm and 130 ±40 μm, respectively.

Typical cyclic compressive stress-strain curves - to the same stress of 190 MPa, which resulted in a ≈ 0.002 plastic pre-strain - are shown in Fig. 8.1a, as a function of annealing time. The loops for the as-received sample are almost non-existent; those obtained after 4 h, or more, annealing are significantly larger. The differences in loop shape and areas were weak function of annealing times. In all cases, a clear yield point was ***not*** detected. The red dashed lines in Fig. 8.1a represent the theoretical Young's modulus of Co, viz. 209 GPa [88]. It is this value that is used in all calculations (see below).

Figure 8.1b compares typical cyclic stress-strain curves obtained in compression and tension of a sample that was annealed 4 h at 1000 °C. To obtain the nested loops, the sample was first loaded to 190 MPa, unloaded and progressively reloaded to higher stress levels. Interestingly the compression loops are more symmetrical - across a line joining the two ends of the loops - than the tensile ones. The differences in loop areas, however, are small between the two types of tests.

When the same sample (4 h @ 1000 °C) was tested at 300 °C, the results (Fig. 8.1c) were qualitatively similar to those measured at room temperature. One significant difference, however, was that the loops were not as closed and reproducible from cycle to cycle as those at room temperature. In other words, at 300 °C, the sample plastically

deformed ever so slightly every cycle. The results at 500 °C (Fig. 8.1d) were substantially different. Here an elastic region was followed by a plastic regime at a yield point of ≈ 45 MPa. Every subsequent repeat cycle to 60 MPa resulted in a little plastic deformation, but more importantly loops did not form. The *room temperature* stress-strain curves after the 500 °C excursion were stiffer than before the excursion (Fig. 8.1e); as importantly the values of W_d decreased.

In the 450-470 °C temperature regime, on heating a sudden increase in the thermal expansion was recorded (Fig. 8.1f) A similar discontinuity occurs in the 360-400 ^{o}C temperature range during cooling. This temperature corresponds to the phase transformation between HCP and FCC in Co [88]. The difference between HCP and FCC phases is stacking order. So this phase transformation can be deemed as stacking fault [154]. After cooling the sample was XRD and found to be composed of only the hexagonal phase. The presence of stacking faults, however, cannot be ruled out at this time.

Figure 8.1g plots the deformation history of a sample (4 h @ 1000 °C). The functional dependence of W_d on strain - measured at 120 MPa and plotted as red diamonds on right-hand side axis in Fig. 8.1g – initially increased before ultimately decreasing. The various loops at 120 MPa are shown in Fig. 8.1h. The pre-strain at which W_d is a maximum is ≈ 0.0048. At a pre-strain is 0.035, W_d is reduced by ≈ 75 % from its maximum value.

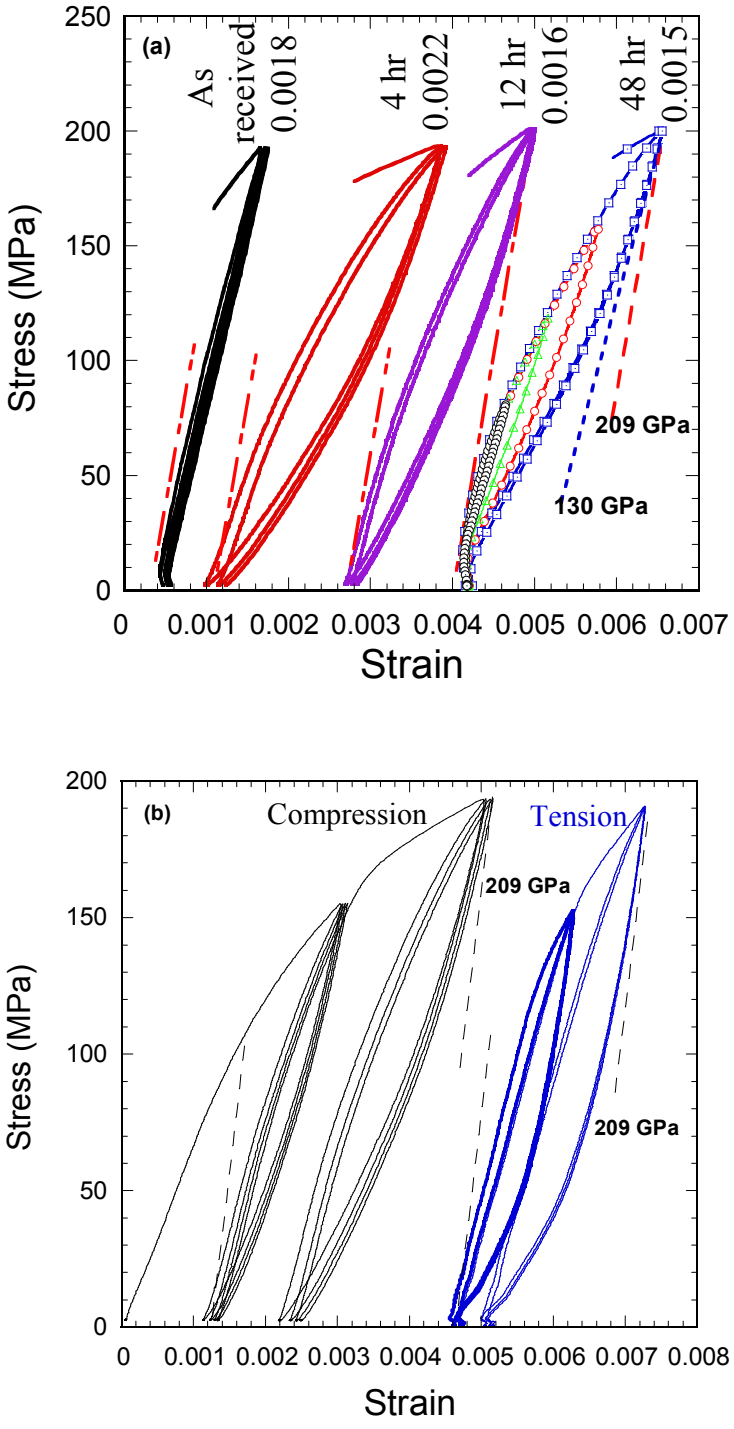

Figure 8.1 (*continued*)

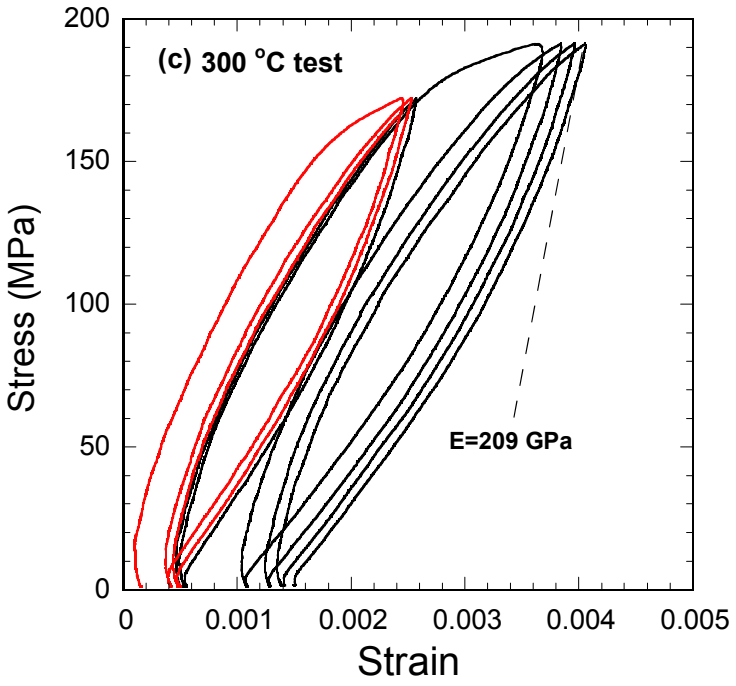

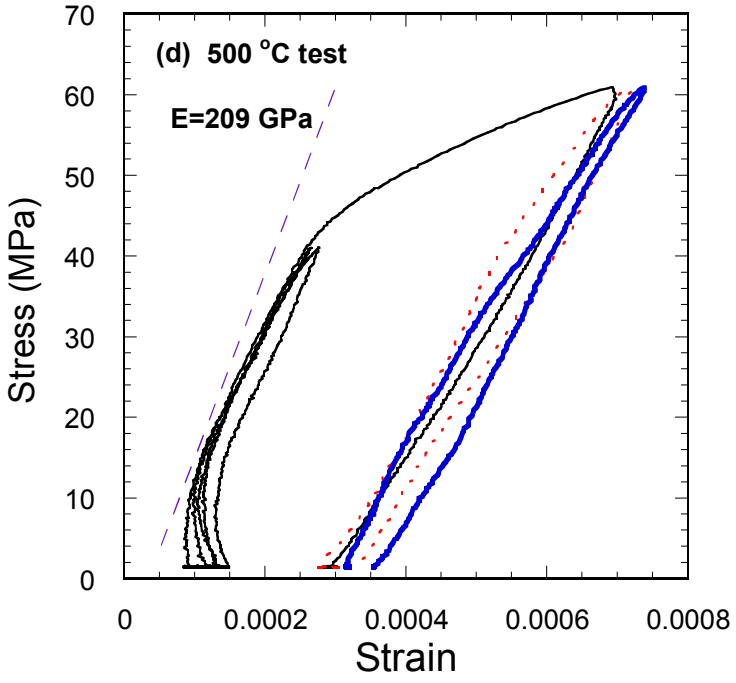

Figure 8.1 (*continued*)

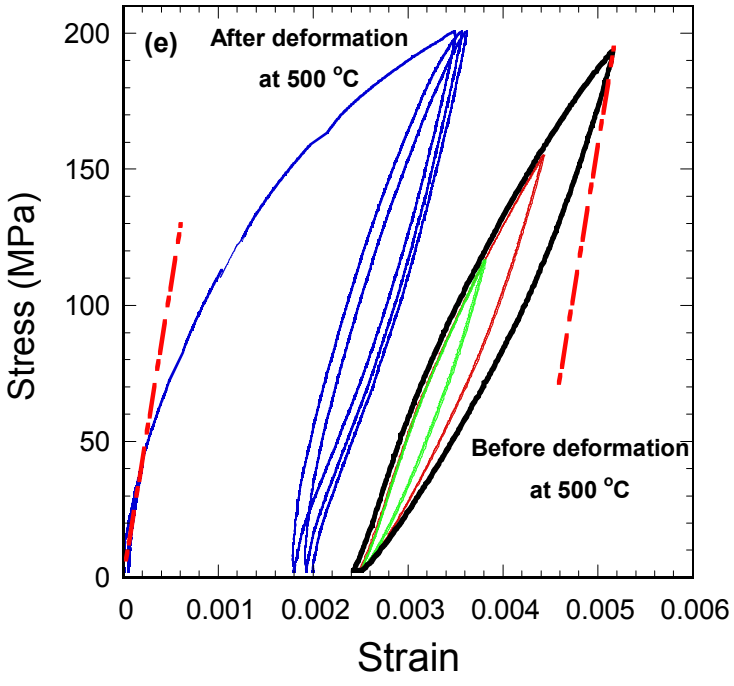

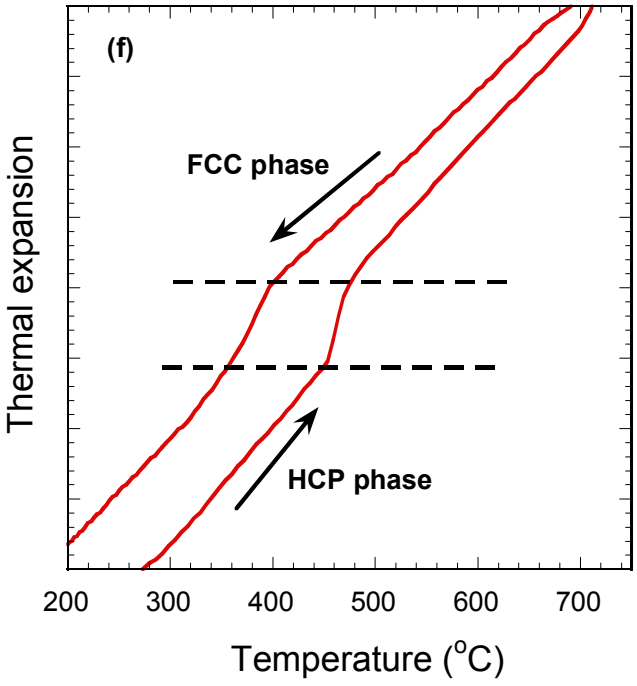

Figure 8.1 (*continued*)

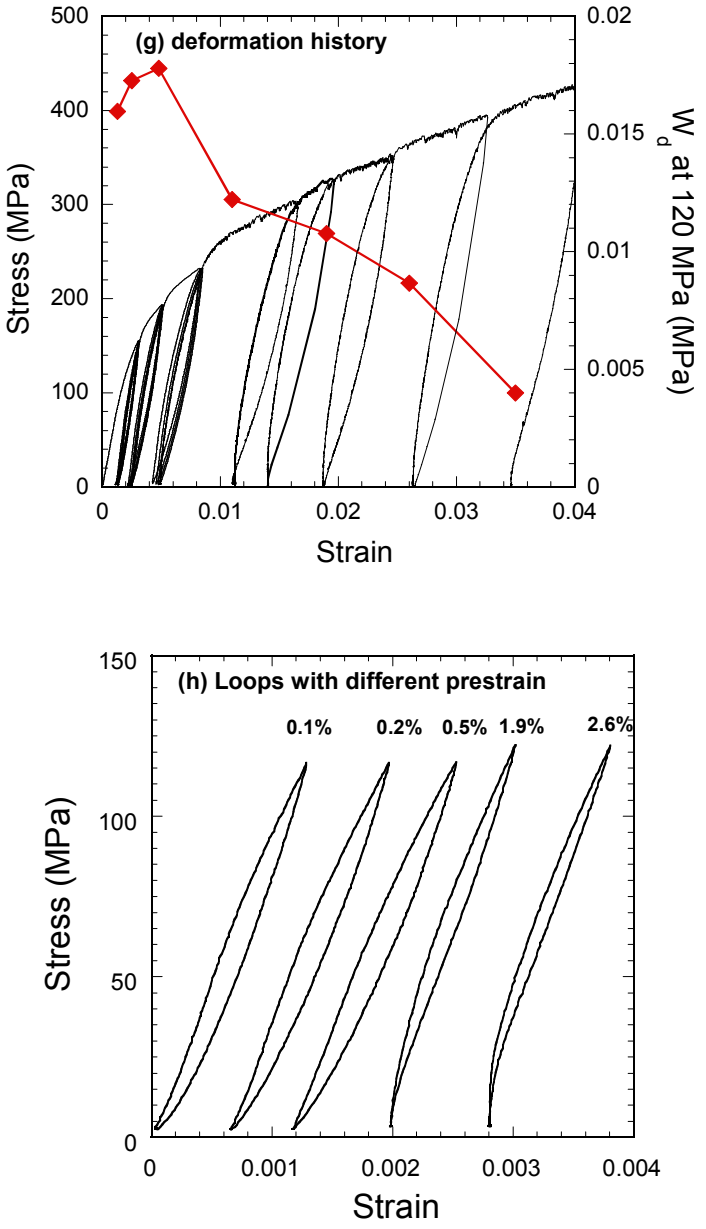

Figure 8.1: (a) Stress-strain curves of Co after different annealing times at 1000°C. (b) Compressive and tensile stress-strain curves of Co annealed 4 hr at 1000°C. (c) Stress-strain curves of Co (annealed 4hr at 1000 °C) tested at 300°C. (d) Stress-strain curves of Co (annealed 4hr at 1000 °C) tested at 500°C. (e) Stress-strain curve of Co before and after 500°C temperature test. (f) Thermal expansion test of Co from room temperature to 700°C. (g) Deformation history of Co (annealed 4hr at 1000 °C). The loop areas at 120 MPa of this sample after different prestrains are shown also (red diamond). (h) Loops of Co at 120 MPa after different deformation history.

Table 8.1 Calculated results from dislocation model of different Co samples. σ_t is from W_d vs σ^2 plots in Fig. 8.2c. Ω/b is from Eq. 2.18. $N_k\alpha^3$ is from the m_1 term of Eq. 2.17. 2α is from Eq. 2.4. $2\beta_{xc}$ is from Eq. 2.7 and $2\beta_{xc}$ from Eq. 2.8. ρ is from Eq. 2.12. In the last row, the new calculated results for Co sample in Ch.6 (1000°C @12 hr) is also listed.

Prestrain	σ_t MPa	Ω/b (MPa) from Eq. 2.18			$N_k\alpha^3$	2α μm	N_k (μm^{-3})	$2\beta_{xc}$ (μm)	$2\beta_x$ (μm)	ρ (cm^{-2})	σ_{max} (MPa)
		2nd term	3rd term	4th term							
0.002 (300 °C)	89	11	11	14	2.1	12	0.0001	0.9	1.9	3.9×10^9	191
0.002	99	13	13	11	1.7	9	0.0002	0.8	1.6	4.1×10^9	194
0.011	112	12	14	12	1.5	7	0.0003	0.7	1.5	5.9×10^9	241
0.035	134	11	12	11	0.9	5	0.0005	0.6	1.1	4.6×10^9	242
0.002 Ch.6 sample	116	6	10	12	2.5	7	0.06	0.7	1.2	8.0×10^9	201

According to our dislocation KNE model in Ch. 2, the mechanical hysteresis of a KNE solid can be characterized by four parameters, σ, ε_{NL}, U_{NL} and W_d. Plots of ε_{NL} vs. σ^2, U_{NL} vs. $\varepsilon_{NL}^{1.5}$, W_d vs. σ^2 and W_d vs. ε_{NL} should yield straight lines as observed in Figs. 8.2. All curves show good agreement with our model.

In order to test our KNE model, the following constants for Co were assumed: G = 75 GPa, b = 3.21 Å, w=5b, and γ_c=0.6° from Eq. 2.5. The threshold stresses, σ_t, were obtained from the x-intercepts of plots such as the ones shown in Fig. 8.2c. In previous chapters (Ch. 3, 4 and 5) on the MAX phases, 2α was measured from experiment as grain thickness or grain size. But for metals, as shown in Chs. 6 and 7, the calculated 2α values results in reasonable results. The rationale being that the IKB domain size is smaller than the grain size for coarse grained metals. So in this chapter, 2α was calculated from Eq. 2.4 assuming $\sigma_c = \sigma_t$ and w = 5b. Based on the slopes of the plots shown in Fig. 8.2, and

making use of Eqs. in Ch. 2, the values of Ω/b, $N_k\alpha^3$, N_k, $2\beta_{xc}$, $2\beta_x$ and ρ at σ_{max} (last column) for the Co annealed 4hr @1000°C were calculated and are listed in Table 8.1.

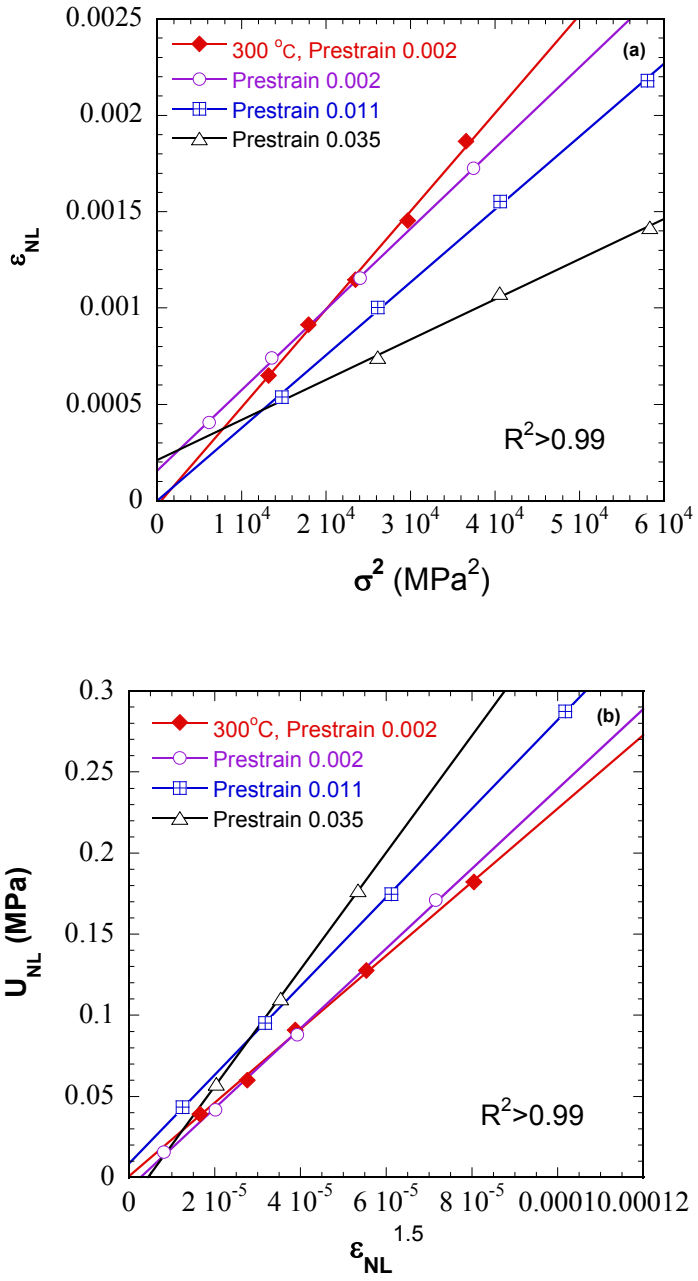

Figure 8.2 (*continued*)

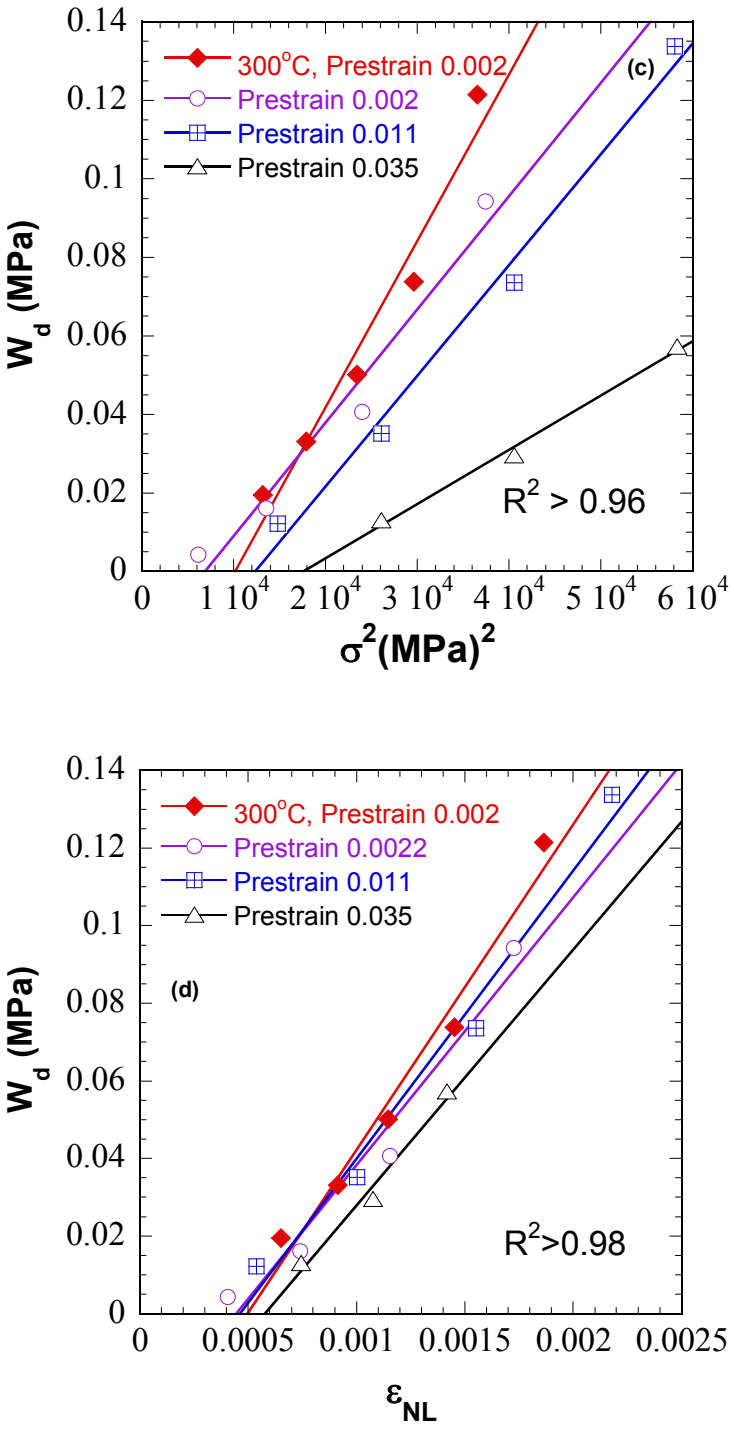

Figure 8.2: Model plots of Co samples (a) ε_{NL} vs. σ^2 (b) U_{NL} vs. $\varepsilon_{NL}^{1.5}$ (c) W_d vs. σ^2 (d) W_d vs. ε_{NL}

Figure 8.3, shows micrographs of Co before and after deformation. Figure 8.3a is the OM micrograph of Co before deformation. Figure 8.3b and 8.3c are the OM and SEM micrographs of Co at the same location after a 3 % deformation. Some cracks, kink bands and possible twins appear on the previous flat surface after this deformation.

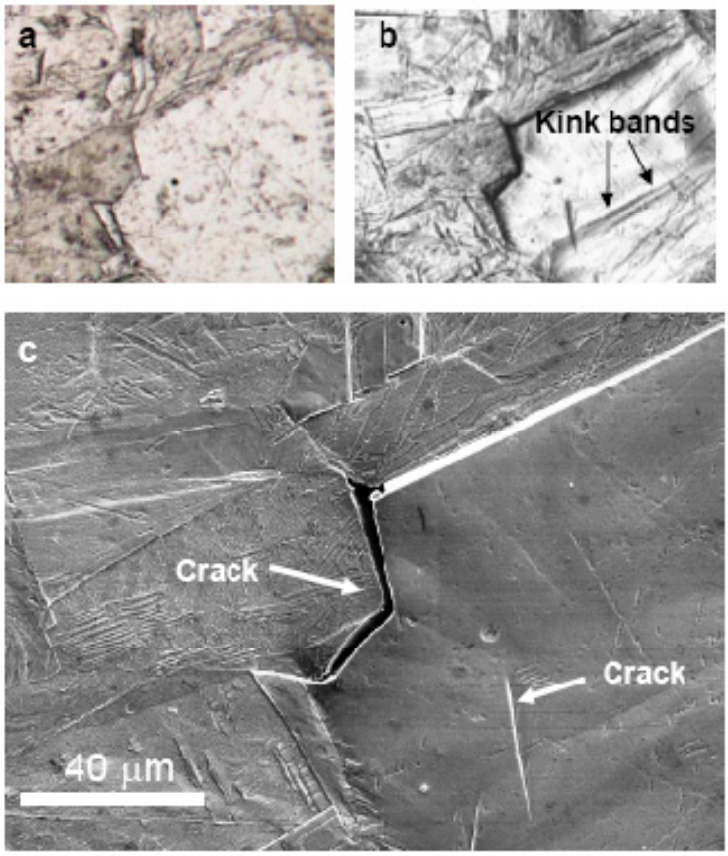

Figure 8.3: Micrographs of Co before and after deformation. (a) OM micrograph of Co before deformation. (b) OM micrograph of Co at same area after 3% deformation (c) SEM image of same area after 3 % deformation.

8.4 Discussion

Based on the excellent agreement of the experimental results with our model, the paucity of possible phenomena that can be used to explain such reversible hysteretic loops, and consistent with our previous work [Chapter 3-7], there is little doubt that Co is a KNE solid. The experimental result can be summarized as thus:

As-received samples show traditional linear elastic deformation. All annealed samples show hysteretic loops that are comparable (Fig. 8.1a).

The loops formed in the tensile tests (Fig. 8.1b) are also comparable to those formed under compression. The hysteretic loop areas first expand then shrink with prestain (Fig. 8.1g) as those of Mg in Ch.7 (Fig. 7.3g).

Cracks and kink bands appear on the originally flat surface after some plastic deformation (Fig. 8.3).

The test results fit our KNE model predictions quite well. More importantly, at ≈ 12 MPa, the values of the CRSS of basal plane dislocations calculated from our model (Table 8.1) are not only reasonable, but agree with values obtained from single crystal work for which the range is 6.4-6.9 MPa [95, 96] or 13MPa [94]. The agreement between the values of Ω/b calculated for the various microstructures and prestrains, etc. (Table 8.1) is also gratifying and consistent with our definition of Ω/b and previous result in Ch. 6 and [23].

The reversible dislocation density ρ in the order of 10^9 cm^{-2} agrees well with that at MAX phases and Mg (Ch. 3-5, 7).

In this section the deformation of Co is explained from the point of view of our KNE model. The as-received extruded Co rods have multiple defects (twins, kink bands, etc) during processing, which presumably prevent or interfere with the nucleation of IKBs and the as-received Co rods do not form IKBs and behave linearly elastically (Fig. 8.1a). It is reasonable to assume that annealing removes these defects, after which obvious mechanical hysteresis is observed (Fig. 8.1a). According to our model, the loop areas depend on the lengths of IKBs, 2α. For metals, 2α is normally smaller than the grain size. As shown in Table 8.1, it is less than 10 μm in the Co tested herein, which is smaller than their grain size. If w = b, the calculated 2α (< 60 μm) are still smaller than the sample's grain size. This would explain why increasing the grain size from 80 μm to 130 μm has little effect on the shape and size of the loops.

The motion of dislocations is a function of temperature. It is easier for dislocations to move at high temperature than at room temperature which probably explains why the 300^{o}C test loops are larger than those at room temperature tests (Compare Fig. 8.1b and 8.1c). Some creep appears at 190 MPa at 300 ^{o}C, which does not exist at the same stress at room temperature.

A sufficient condition to be KNE solid is plastic anisotropy. The FCC structure of Co is isotropic. So the mechanical hysteresis of Co disappeared at 500^{o}C test as shown in Fig. 8.1d because HCP structure converts to the FCC structure at ~420^{o}C (Fig. 8.1f).

Bending is needed to nucleate MDW, KBs and IKBs [4, 5, 28]. It is thus not surprising that prestrain is needed to nucleate IKBs. After annealing no IKBs form (Fig. 8.1g and h). A little plastic deformation helps the nucleation of the IKBs. So pre-strain

like in Mg can make the hysteretic loops larger. Plastic strain can obviously induce some flaws (twins, kink bands, cracks, etc) in the sample. Some of them are trans-grains; some are distributed within grains. Thus these flaws can decrease the IKB domain size (2α) even though 2α is smaller than the grain size. So further plastic deformation results in the shrinkage of the hysteretic loops (Fig. 8.1g and h).

The agreement between the values of Ω/b calculated for the various microstructures and prestrains, etc. (Table 8.1) is gratifying and consistent with our definition of Ω/b. The value is also in good agreement with the value of CRSS from literature6.4 - 6.9 MPa for high purity Co, and 9.5 MPa for 99.5% Co [88, 96] and 13 MPa for commercial pure Co[94].

8.5 Summary and Conclusions

As an important magnetic and structural material, the mechanical hysteresis of Co was researched in this paper. After annealing, Co sample show obvious mechanical hysteresis both in compressive and tensile tests. The hysteretic loops of Co are not dependent on grain size because the grain size is larger than the IKB domains. They are dependent on test temperature and prestrain of the sample. When Co transformed from HCP to FCC structure, the loops disappear. We believe that the mechanical hysteresis of Co fits the KNE model well and the phenomena in this chapter can be successfully explained by our model. The CRSS of the basal planes is estimated to be $\approx$ 12 MPa.

9. Kinking Nonlinear Elastic Solids and the Preisach-Mayergoyz Model

9.1 Introduction

In previous chapters, we proposed and applied a dislocation model to explain the deformation mechanisms of KNE solids. However, there is a more fundamental engineering question: how can we calculate strain of these solids from stress? This is easy for linear elastic deformation without hysteresis. But for deformation of KNE solids with hysteresis, it is impossible to calculate strain only from stress. Strain of a KNE solid can only be calculated from its stress history. Following the lead of the geologists' work on mechanical hysteresis [155-157], we tested the Preisach-Mayergoyz model.

Hysteresis is fairly common in Nature. In the mid 1930's Preisach [158] developed a powerful model wherein he assumed that any hysteresis can be modeled by invoking the presence of a large number of small independent hysteric units. This model was successfully used to describe ferromagnetic hysteresis. Mayergoyz [159, 160], recognizing that the Preisach model offered a general mathematical framework for the description of hysteresis of different physical origins, derived the necessary and sufficient conditions for representation of any given hysteresis by the Preisach model. This model is now renamed the Preisach-Mayergoyz model (P-M model).

Before the P-M model can be used, it is essential to establish that these two necessary and sufficient conditions are indeed valid for deformation of KNE solids. These conditions are: closure of any minor hysteresis loops and congruency of the minor hysteresis loops with the same end points of input, but different pre-histories. Mayergoyz called these two conditions wiping-out and congruency, respectively.

Guyers et al. [155, 161] and Ortin [162] successfully applied this model to describe nonlinear elastic response of granular geological materials and a shape memory alloy, respectively. And while these previous works have clearly shown wiping out, as far as we are aware, dislocation-based congruency has *never* been reported in mechanical systems. In this chapter we present the experimental evidence that verifies that the Preisach model can be used to describe the elastic response of kinking non-linear elastic solids and consequently illustrate the predictive power of the P-M model.

9.2 Simple P-M model and the calculation

Accoding to the P-M model, the hysteretic behavior of a KNE solids is due to many indepandent hysteretic units in the solid. In the simplest P-M model, every hysteretic unit has a operator $\hat{\gamma}_{\theta\omega}$ with a rectangular hysteresis loop. The output strain ε of all $\hat{\gamma}_{\theta\omega}$ can only be 0 or 1 as shown in Fig. 9.1a. Every $\hat{\gamma}_{\theta\omega}$ has one up-threshold stress, θ, and one down-threshold stress, ω, such that $\theta > \omega > 0$. For loading from 0, $\hat{\gamma}_{\theta\omega} = 0$ if input $\sigma < \theta$; $\hat{\gamma}_{\theta\omega} = 1$, if $\sigma \geq \theta$. During unloading, $\hat{\gamma}_{\theta\omega} = 1$ if $\sigma > \omega$ and $\hat{\gamma}_{\theta\omega} = 0$, if $\sigma \leq \omega$. Because of friction, $\theta > \omega$ and a rectangular hysteretic loop is formed (Fig. 9.1a). If the set of operators $\hat{\gamma}_{\theta\omega}$ has an arbitrary weight function, μ(θ, ω), defined as a P-M density, then the output of this systerm after a given load history is the sum of the outputs of all $\hat{\gamma}_{\theta\omega}$ or:[160]

$$\varepsilon(t) = \hat{\Gamma}\sigma(t) = \iint_{x \geq y} \mu(x, y)\hat{\gamma}_{\theta\omega}\sigma(t)dxdy \tag{9.1}$$

Note that because at any σ there can be multiple values of strain – and vice versa - the time, t, variable is introduced here only to indicate that both the stress and strain are measured at the same moment in time, *not* that they are time dependent.

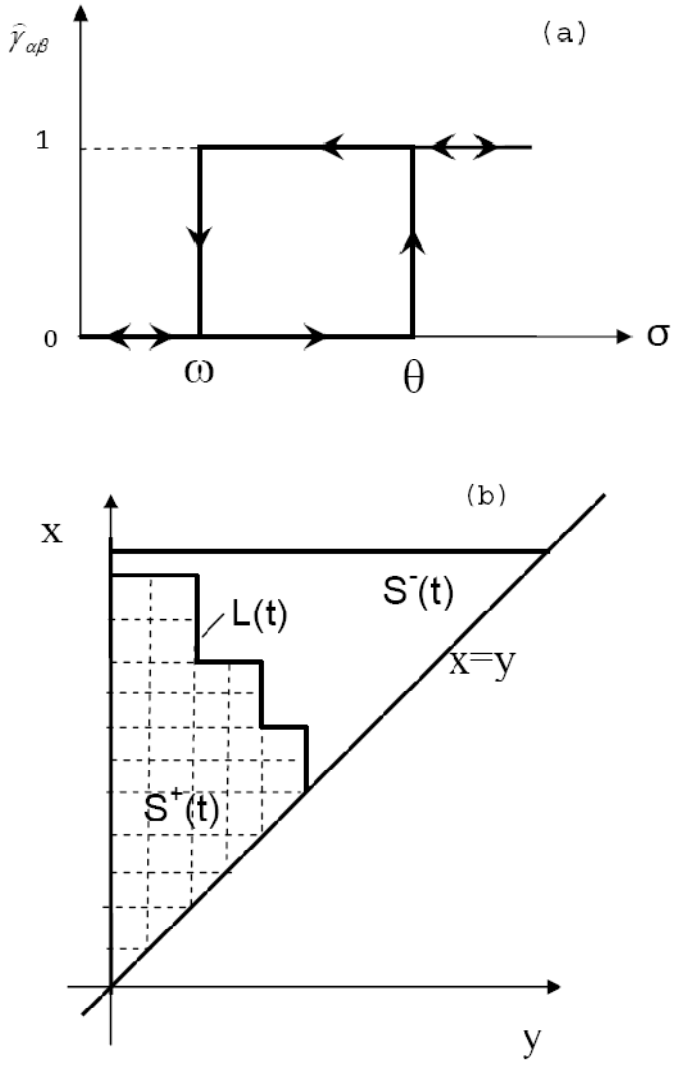

Figure 9.1: (a) The NL strain of one hysteresis unit changes with stress (σ) and forms a rectangular hysteretic loop. (b) P-M space μ(θ, ω) in a x-y plane. x means increasing stress. y means decreasing stress. μ(θ, ω) = 1 in S+ area and μ(θ, ω) = 0 in S- area.

In order to figure out the output of every $\hat{\gamma}_{\theta\omega}$, Mayergoyz gave a geometric interpretation (Fig. 9.1b) of this model based on the fact that there is a one-to-one correspondence between operator $\hat{\gamma}_{\theta\omega}$ and points (x, y) in the half plane x≥y. x axial in Fig. 9.1b means stress load to a value x. y axial means stress unload to a value y. At any instant of time, the triangle in Fig. 9.1b is subdivided into two sets: $S^+(t)$ consisting of points (x, y) for which $\hat{\gamma}_{\theta\omega}$=1, and $S^-(t)$ consisting of points (x, y) for which $\hat{\gamma}_{\theta\omega}$=0. The interface L(t) between $S^+(t)$ and $S^-(t)$ is a staircase line whose shape is determined by local maxima and minima of inputs at previous instants of time. ε(t) can be calculated by double integration if μ(θ,ω) is obtained by double differentiation of the test results from Fig. 9.3a (see below), which is a series of ε(t) at different strain and defined as Everett function.

A simple calcualtion can be obtained if one follows the algorithm proposed in Refs. [159, 162] which uses parametric fitting involving just summation and subtraction of Everett function. This approximate method permits a relatively simple graphical construction of the Preisach space distribution function (P-M density) and can be used for the simulation of any arbitrary stress-strain relationship.

This simple P-M model can then be used to similuate stress-strain curves. But the simple rectangual hysteretic unit is not the true hysteretic behavior of IKBs. In the next section, the true IKB behavior is described and modelled by a P-M model with real physical meanings.

9.3 Incipient Kink Bands and the PM model and their interrlationship

In this section we discuss a more complex and more real P-M hysteretic unit based on the dislocation model outlined in Ch. 2. To do so, we propose a friction stress, σ_f, which is related with Ω/b (see previous chapters). Due to this friction stress, mechanical energy is dissipated during dislocation motion. For an IKB (N_k=1) , during loading, if $\sigma > \sigma_t$, the IKB grows and Eq. 2.11 can be recast as:

$$\varepsilon_{IKB} = C_1 \frac{k_1^2}{k_2} \alpha^3 ((\sigma - \sigma_f)^2 - \sigma_t^2) = m_1 ((\sigma - \sigma_f)^2 - \sigma_t^2) \tag{9.2}$$

where C_1 equals to $\frac{\pi(1-\nu)}{3G^2\gamma_c}$. It is a constant for a given material. $\frac{k_1^2}{k_2}$ gives the orientation of this IKB. 2α is the length of this IKB.

During unloading, the same IKB shrinks and ε_{IKB} is given by:

$$\varepsilon_{IKB} = C_1 \frac{k_1^2}{k_2} \alpha^3 ((\sigma + \sigma_f)^2 - \sigma_t^2) = m_1 ((\sigma + \sigma_f)^2 - \sigma_t^2) \tag{9.3}$$

Based on Eqs. 9.2 and 9.3, the stress-strain response of a single IKB is shown in Fig. 9.2a. It follows that if this relationship between IKBs and the PM model exists then the response of a polycrystal should result from the collective response of a distribution of IKBs. Note that the latter are confined to single grains and each is characterized by distinct values of σ_t and σ_f. It is also important to note that the variations in σ_f are not due to variations in Ω/b - which is ideintical to the CRSS of the dislocations making up the IKBs and is thus a material property – but rather to variations of the orientation of the

basal planes to the direction of applied load. This is reflected in $\frac{k_1^2}{k_2}$ which is of a cos xx cos yy form.

In order to calculate the distributions of σ_t and σ_f, we start with the Everett function for a single isolated IKB given by:

$$\begin{aligned} &E(x-\sigma_f, y+\sigma_f, \sigma_t) = \\ &C\frac{k_1^2}{k_2} k\alpha^3 s(x-y-2\sigma_f) s\left(x-\left(\sigma_t+\sigma_f\right)\right)\left(\left(x-\sigma_f\right)^2-\sigma_t{}^2\right) \\ &-C_1\frac{k_1^2}{k_2}\alpha^3 s(x-y-2\sigma_f) s\left(y-\left(\sigma_t-\sigma_f\right)\right)\left(\left(y+\sigma_f\right)^2-\sigma_t{}^2\right) \end{aligned} \tag{9.4}$$

$s(x)$ is a unit step function (unity for positive arguments, zero for negative arguments). $C_1\frac{k_1^2}{k_2}\alpha^3$ can be viewed as the amplitude of the IKB.

The Preisach distribution for such an isolated IKB is calculated through double differentiation of the Everett function:

$$\begin{aligned} &\frac{\partial E(x-\sigma_f, y+\sigma_f, \sigma_t)}{\partial x} = C_1\frac{k_1^2}{k_2}\alpha^3\delta(x-y-2\sigma_f)s(y+2\sigma_f-\sigma_t-\sigma_f)((y+2\sigma_f-\sigma_f)^2-\sigma_t{}^2) \\ &+C_1\frac{k_1^2}{k_2}\alpha^3 s(\sigma_t+\sigma_f-y-2\sigma_f)\delta(x-\sigma_t+\sigma_f)((\sigma_t+\sigma_f-\sigma_f)^2-\sigma_t{}^2) \\ &+2C_1\frac{k_1^2}{k_2}\alpha^3 s\left(x-\left(\sigma_t+\sigma_f\right)\right)s(x-y-2\sigma_f)\left(x-\sigma_f\right)-C_1\frac{k_1^2}{k_2}\alpha^3\delta(x-y-2\sigma_f)s(y-(\sigma_t-\sigma_f))((y+\sigma_f)^2-\sigma_t{}^2) \\ &=2C_1\frac{k_1^2}{k_2}\alpha^3 s\left(x-\left(\sigma_t+\sigma_f\right)\right)s(x-y-2\sigma_f)\left(x-\sigma_f\right) \end{aligned} \tag{9.5}$$

From mathematics, when use the δ function, use the peak values replace all other value in the equation:

$$\mu(x,y,\sigma_t,\sigma_f) = \frac{\partial^2 E(x-\sigma_f, y+\sigma_f, \sigma_t)}{\partial x \partial y}$$
$$= -2C_1 \frac{k_1^2}{k_2} \alpha^3 s\left(x-\left(\sigma_t+\sigma_f\right)\right)\delta(x-y-2\sigma_f)\left(x-\sigma_f\right) \tag{9.6}$$

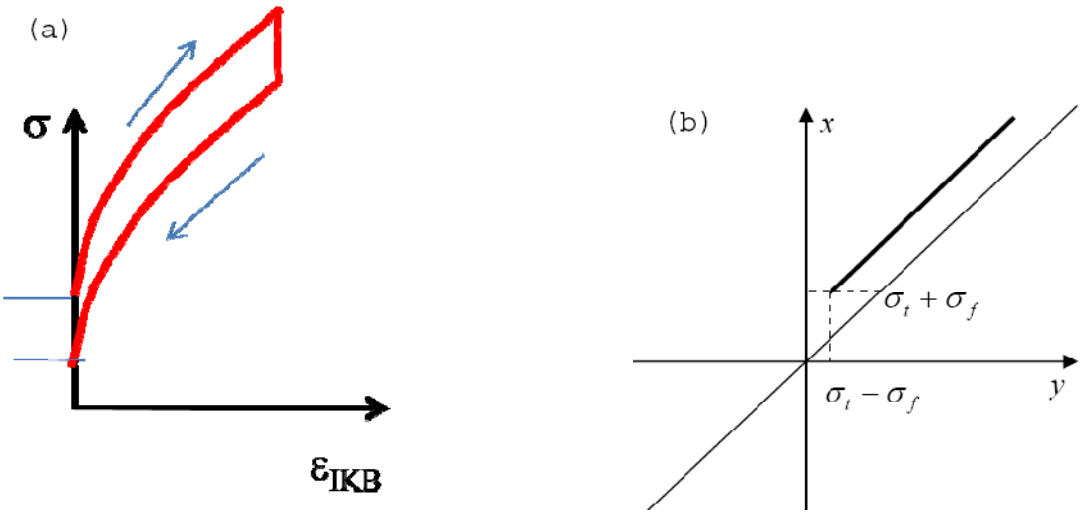

Figure 9.2 (a) Typical stress-strain curve of a single IKB (b) Preisach distribution corresponding to a single IKB. The distribution varies only along the two solid lines shown.

Graphically, the region of support of this distribution on the Preisach plane is shown in Fig. 9.2b. Note that this region of support is a line parallel to $x = y$ line in the Preisach plane. This suggests that more convenient variables than x and y, are:

$$\nu = \frac{x+y}{2} \qquad \text{and} \qquad \eta = \frac{x-y}{2} \tag{9.7}$$

Transforming Eq. 9.6 in terms of ν and η gives:

$$\tilde{\mu}(\nu,\eta,\sigma_t,\sigma_f) = -2C_1\frac{k_1^2}{k_2}\alpha^3(\sigma_t)s\left(\nu+\eta-(\sigma_t+\sigma_f)\right)\delta(2\theta-2\sigma_f)\left(\nu+\eta-\sigma_f\right)$$
$$= -C_1\frac{k_1^2}{k_2}\alpha^3(\sigma_t)\nu s(\nu-\sigma_t)\delta(\eta-\sigma_f) \tag{9.8}$$

It follows that, the Preisach function of the entire system, which consists of many IKBs with different values of σ_t and σ_f is given by:

$$\varphi(\nu,\eta) = \int_{-\infty}^{\infty}\int_{0}^{\infty}\rho(\sigma_t,\sigma_f)\tilde{\mu}(\nu,\eta,\sigma_t,\sigma_f)d\sigma_f d\sigma_t = -\int_{-\infty}^{\infty}\int_{0}^{\infty}\rho(\sigma_t,\sigma_f)C_1\frac{k_1^2}{k_2}\alpha^3\nu s(\nu-\sigma_t)\delta(\eta-\sigma_f)d\sigma_f d\sigma_t =$$
$$-\int_{-\infty}^{\infty}C_1\frac{k_1^2}{k_2}\alpha^3(\sigma_t)\nu s(\nu-\sigma_t)\int_{0}^{\infty}\rho(\sigma_t,\sigma_f)\delta(\eta-\sigma_f)d\sigma_f d\sigma_t = -\nu\int_{-\infty}^{\infty}C_1\frac{k_1^2}{k_2}\alpha^3(\sigma_t)\rho(\sigma_t,\eta)s(\nu-\sigma_t)d\sigma_t =$$
$$-\nu\int_{-\infty}^{\nu}C_1\frac{k_1^2}{k_2}\alpha^3(\sigma_t)\rho(\sigma_t,\eta)d\sigma_t \tag{9.9}$$

where $\rho(\sigma_t,\sigma_f)$ can be interpreted as the distribution of IKBs, each parameterized by different values of σ_t and σ_f. This distribution function can be computed from Eq. 9.9 since:

$$-\frac{1}{C_1\frac{k_1^2}{k_2}\alpha^3}\frac{\partial}{\partial\nu}\left(\frac{1}{\nu}\varphi(\nu,\eta)\right) = -\frac{1}{C_1\frac{k_1^2}{k_2}\alpha^3}\frac{\partial}{\partial\nu}\left(\frac{1}{\nu}\frac{\partial^2 E(\nu,\eta)}{\partial\nu\partial\eta}\right) = \rho(\nu,\eta) \tag{9.10}$$

α can be calculated from a simplified Eq. 2.4:

$$\sigma_t = \sigma_t = \sqrt{\frac{4G^2 b\gamma_c}{2\alpha\pi^2}\ln(\frac{b}{\gamma_c w})} = C_2\sqrt{1/\alpha}\,, \qquad \alpha = {C_2}^2/{\sigma_t}^2 \tag{9.11}$$

where C_2 is a constant. Therefore, the distribution $\rho(\sigma_t,\sigma_f)$ can be simply calculated from:

$$\rho(\nu,\eta) = -\frac{\sigma_t^6}{C_1C_2^6\frac{k_1^2}{k_2}}\frac{\partial}{\partial\nu}\left(\frac{1}{\nu}\frac{\partial^2 E(\nu,\eta)}{\partial\nu\partial\eta}\right) \tag{9.12}$$

We call the distribution $\rho(\sigma_t, \sigma_f)$ an IKB distribution. It is different than the distribution μ(θ, ω), or P-M density in section 9.2. P-M density is the distribution of a simple rectangle hysteretic unit. The calculation of P-M density is simple but the rectangle hysteretic units are not physically relevant. The true hysteretic units in KNE solids are IKBs.

9.4 Experimental Details

Herein five representative KNE solids, namely, cobalt (99.97%, ESPI metals, Ashland, OR) [163], Ti_3SiC_2 [25] and 10vol.% porous Ti_2AlC [15] and two Ti_2AlC samples with prefered orientation [164] were examined. A hydraulic testing machine (MTS 810, Minneapolis, MN), supplied with a controller (Microconsoler 458.20, MTS, Minneapolis, MN) was used for the compression experiments. A extensometer (MTS 632.59C-01) with 25 mm gauge length attached directly to the sample was used to measure the strains. The processing, microstructural and testing details can be found at previous chapter and elsewhere [15, 25, 163].

9.5 Results and Discussion

9.5.1 Wiping out and congruency

Same as in our previous work [25], when the Ti_3SiC_2 sample was loaded to progressively higher loads, reproducible, closed, strain rate invariant, hysteretic loops (Fig. 9.3a) are obtained. Note in this figure, the linear elastic strain, assuming a Young's modulus of 325 GPa, was removed from the total stain. Similar loops were obtained for textured Ti_2AlC (Fig. 9.3b), Ti_2AlC (Fig. 9.3c) (Ch.3) and Co (Fig. 9.3d) (Ch. 8). Note the unique loading, but multiple unloading trajectories. The latter depends on the

maximum stress from which the unloading occurs. The loops of two Ti_2AlC samples, with different prefered orientations, A and B, are shown in Fig. 9.3b. Insets A and B schematicaly show the orientation of the basal planes, on which slip is occuring, that were, respectively, parallel and normal to the vertically applied stress. In these figures, the elastic strain was again removed, assuming a Young's modulus of 340 GPa for both orientations.

Figures 9.3a and 9.3b clearly illustrate the wiping-out property of Ti_3SiC_2 and the two oriented Ti_2AlC samples, respectively. When a sample is loaded to a stress σ, all minor (intermediate) loops obtained below that stress are wiped out; i.e. there is complete loss of memory or load prehistory. The same is true for the 10 vol.% porous Ti_2AlC sample (Fig. 9.3c); during unloading, all the minor loops are closed and are wiped out by the larger unload.

Congruency is illustrated in Fig. 9.3d. Here the minor loops for Co, obtained when the stress is cycled between 100 and 170 MPa, are congruent, and independent of whether the loops were obtained on loading *or* unloading. Similar results were obtained for all compositions examined herein. Clearly, the results shown in Fig. 9.3 satisfy the two criteria needed for a hysteresis to be adequately described by the PM model.

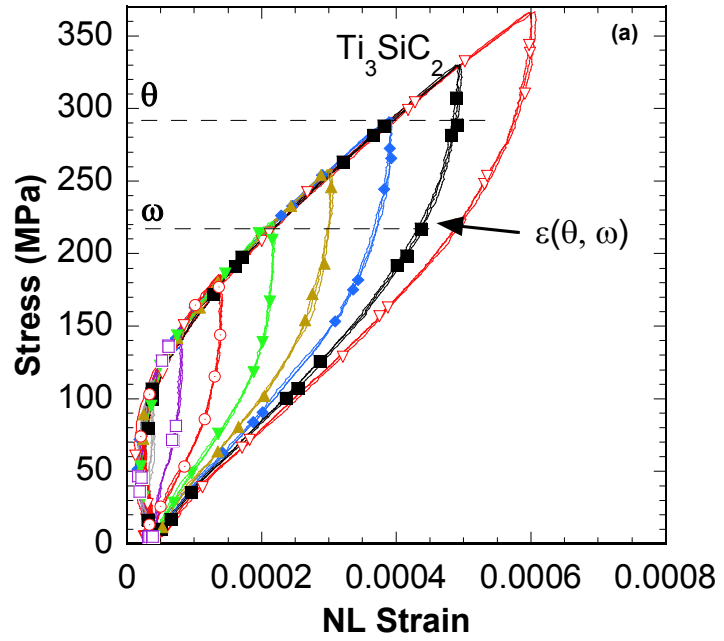

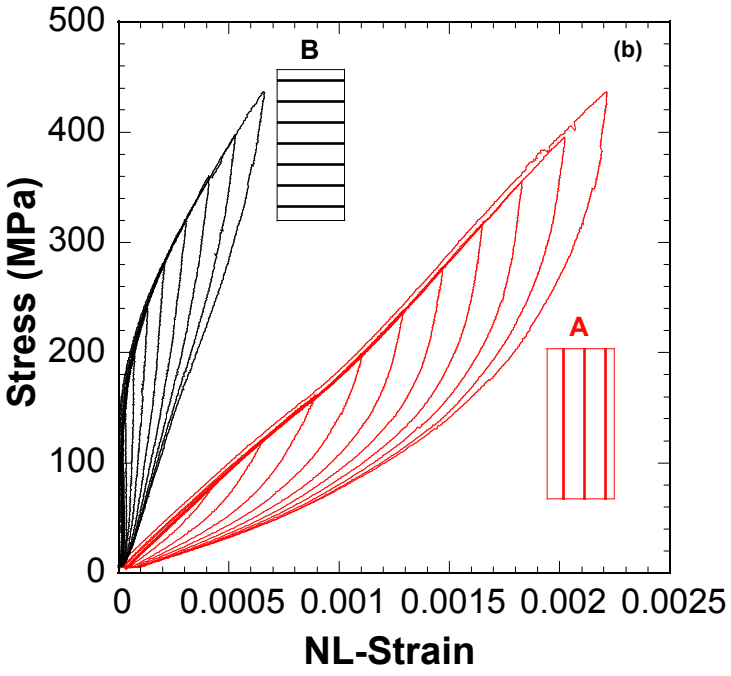

Figure 9.3 (*continued*)

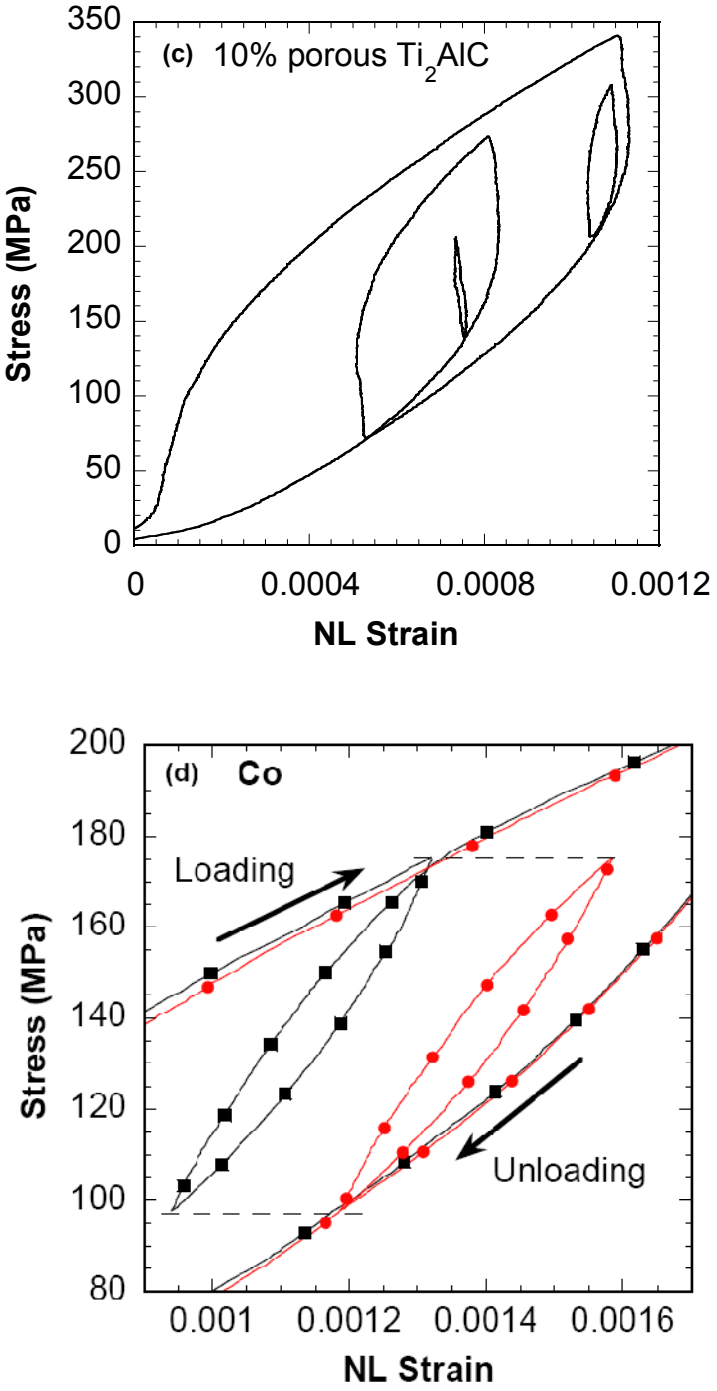

Figure 9.3: Stress-NL strain curves of (a) Ti_3SiC_2 (b) textured Ti_2AlC (c) 10% porous Ti_2AlC (d) Co

9.5.2 P-M density

The P-M density function for Ti_3SiC_2 is plotted in Fig. 9.4a, where the highest densities correspond to the darkest areas. For the sake of illustration, we schematically show, as insets in Fig. 9.4a, the relative shapes of the various rectangular hysteretic units represented by the various regions on the map. Similar maps (Fig. 9.4b and c) are obtained for 10 vol. % porous Ti_2AlC and Co. For both Ti_3SiC and Co, the highest densities fall on a 45° line. For 10% Ti_2AlC, the density peak is at high stress area (close to the test limit, 341 MPa). But there is also a high density ridge that fall on a 45° line.

The P-M density map of the two textured A and B samples - whose stress-strain curves are shown in Fig. 9.3b - are shown in Figs. 9.4d and 3e, respectively. Sample A - whose basal planes are parallel to the applied load and thus more likely to kink - has a peak distribution of hysteretic units at low θ and ω thresholds. For sample B, in which the basal planes are normal to the applied load, most of the nonlinear strain can be generated only at higher values of θ and ω.

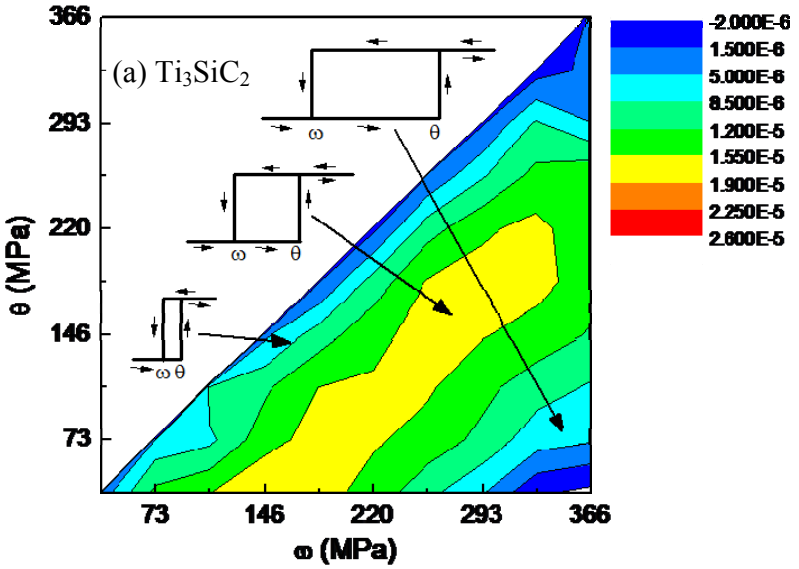

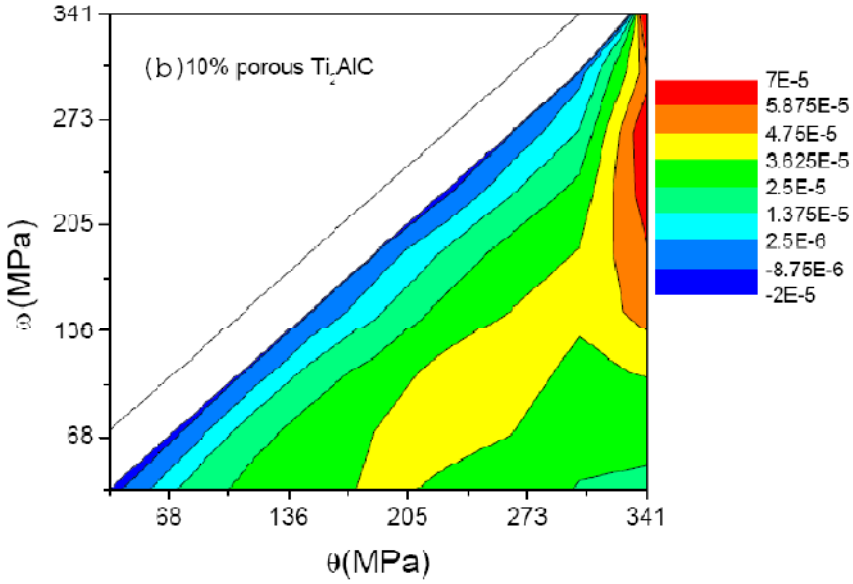

Figure 9.4 (*continued*)

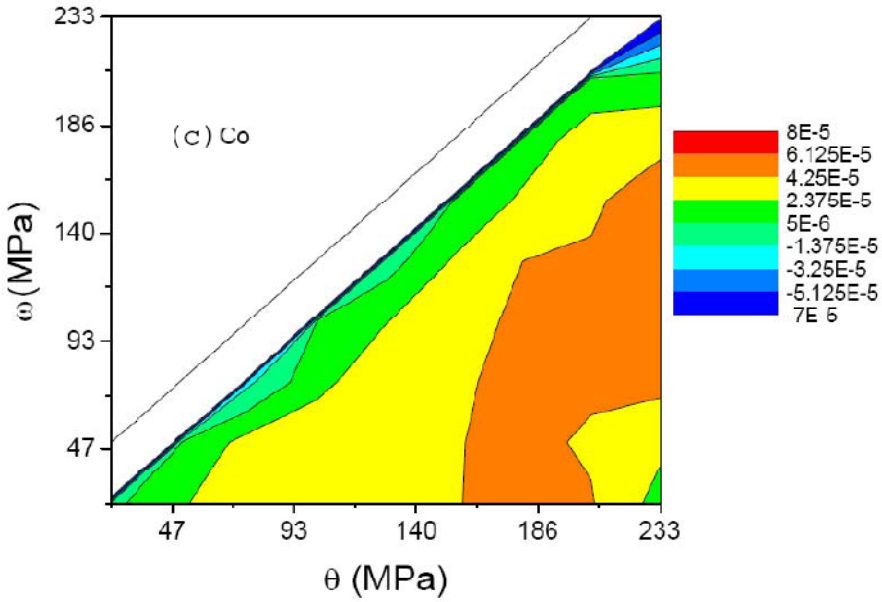

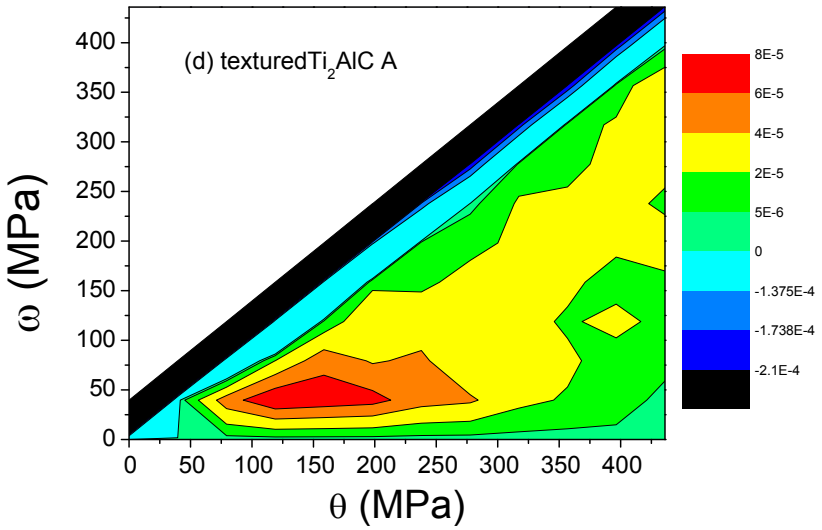

Figure 9.4 (*continued*)

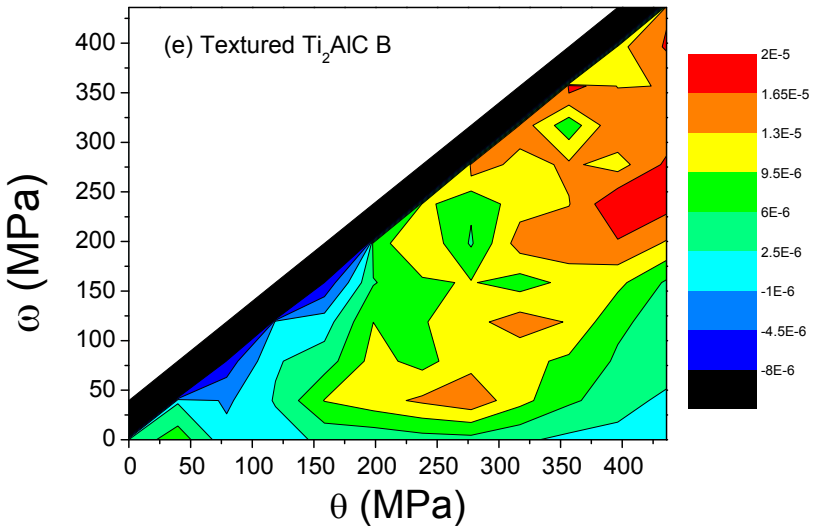

Figure 9.4: P-M density of samples tested in this chapter (a) Ti_3SiC_2 (b) porous Ti_2AlC (c) Co (d) Textured Ti_2AlC A (e) Textured Ti_2AlC B

9.5.3 IKB distributions

Figure 9.5 show the IKB distributions of Co, Ti_3SiC_2, 10% porous Ti_2AlC and the textured Ti_2AlC. All samples have similar IKB distributions. They have a very large distribution of IKBs in the high σ_t regions regardless of their microstructure, texture or shape of hysteretic loops. High σ_t implies small $2\alpha s$ or grain sizes. It is true that the number of fine grains is much larger than that of coarse grains in any polycrystalline sample. However some coarse grains with low σ_t can induce very large nonlinear strain. Therefore, the number distribution of IKB can NOT give us direct clue of this sample's hysteretic loops.

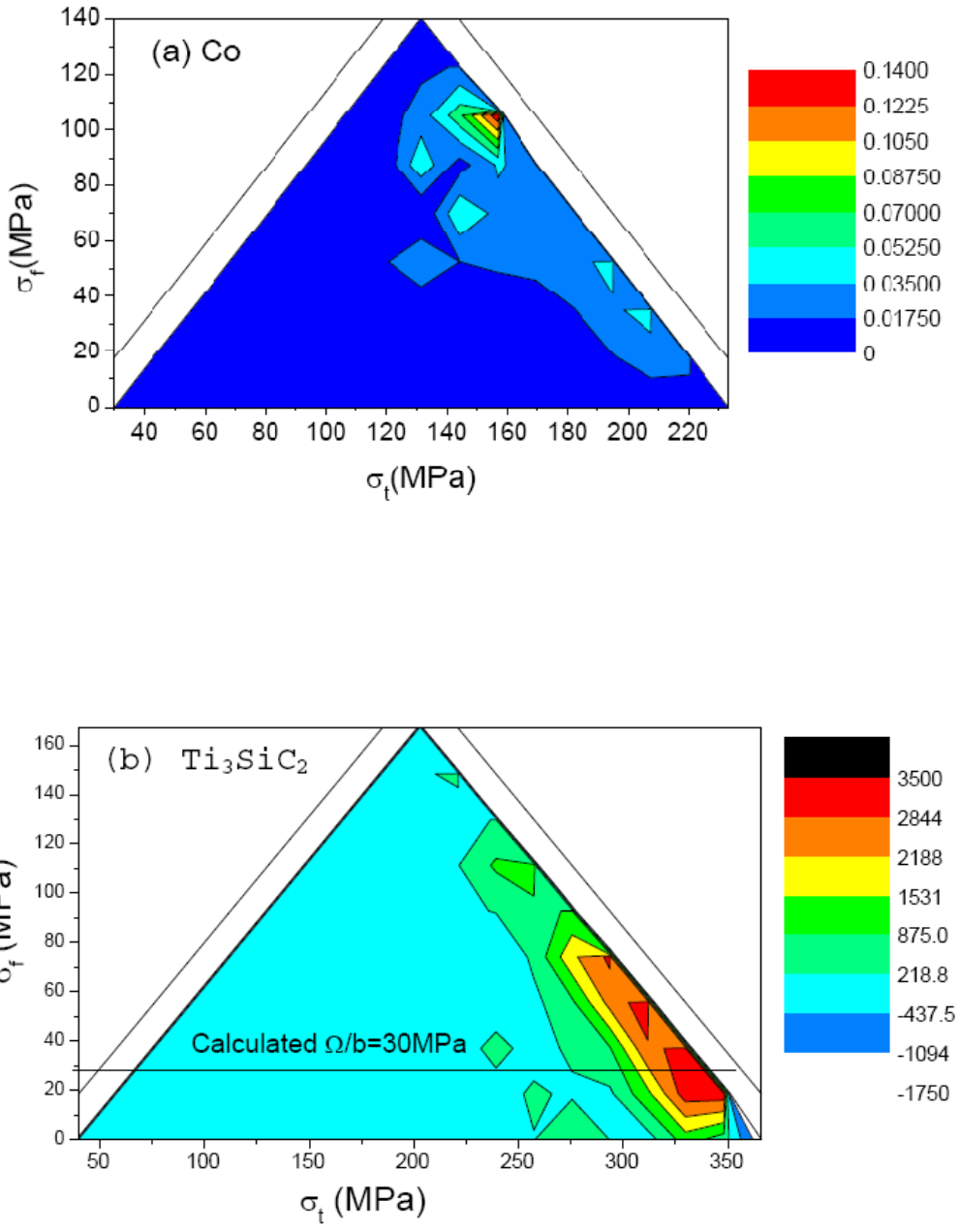

Figure 9.5 (*continued*)

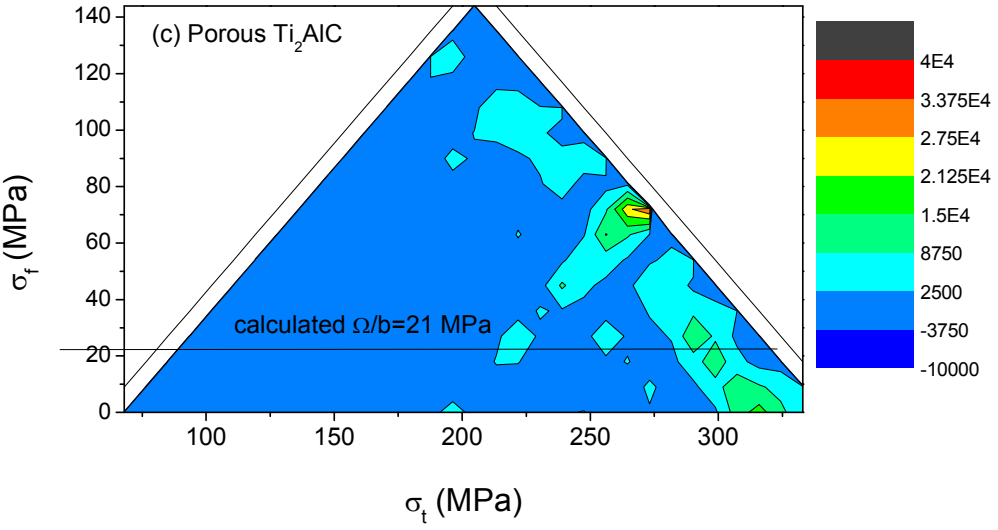

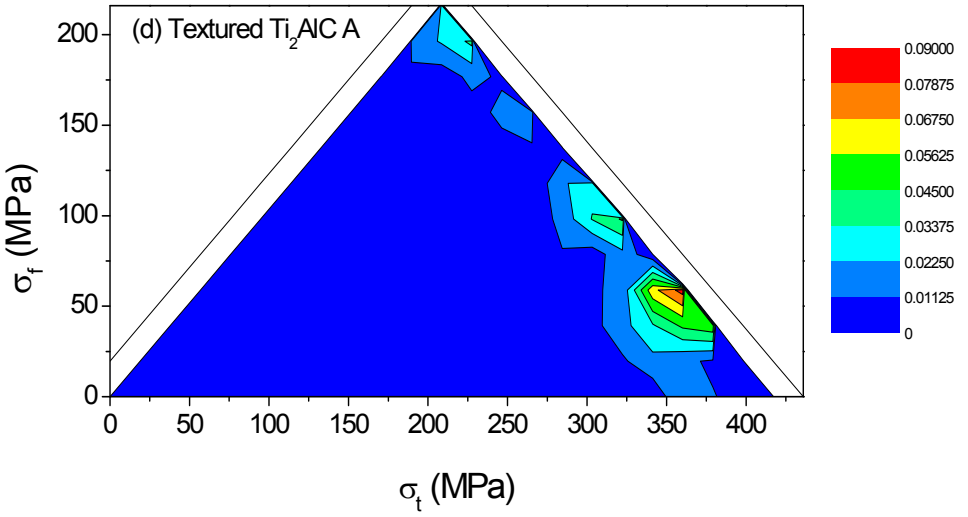

Figure 9.5 (*continued*)

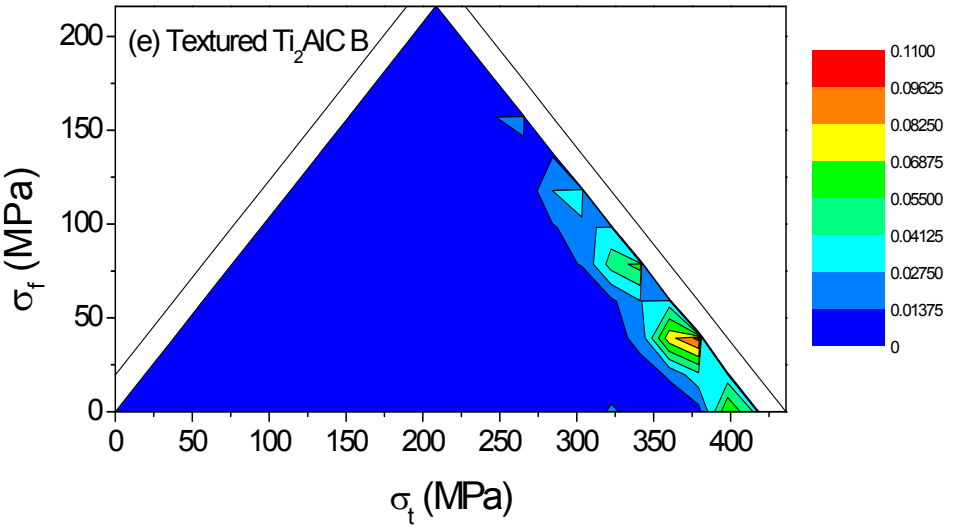

Figure 9.5: IKB distribution of (a) Co (b) Ti_3SiC_2 (c) Porous Ti_2AlC (d) Textured Ti_2AlC A (e) Textured Ti_2AlC B

However, two more useful distributions, the distributions of σ_t and σ_f, can be calculated from this IKB distribution by summarizing the columns or rows of the distribution matrix. The results are shown in Fig. 9.6. Because σ_t is related with grain size ($\alpha=C_2\sigma_t^{-2}$), the distribution of σ_t is actually a distribution of grain sizes, which is normally a Weibull distribution for most polycrystalline samples. This agrees with the plots in Fig. 9.6. The distribution of σ_f has a maximum values in some stress values as shown in Fig. 9.6. Both the distributions of σ_t and σ_f are not a strong function of texture. Because the numbers of fine grain in both textured Ti_2AlC are very high and the fine grains are not highly orientated.

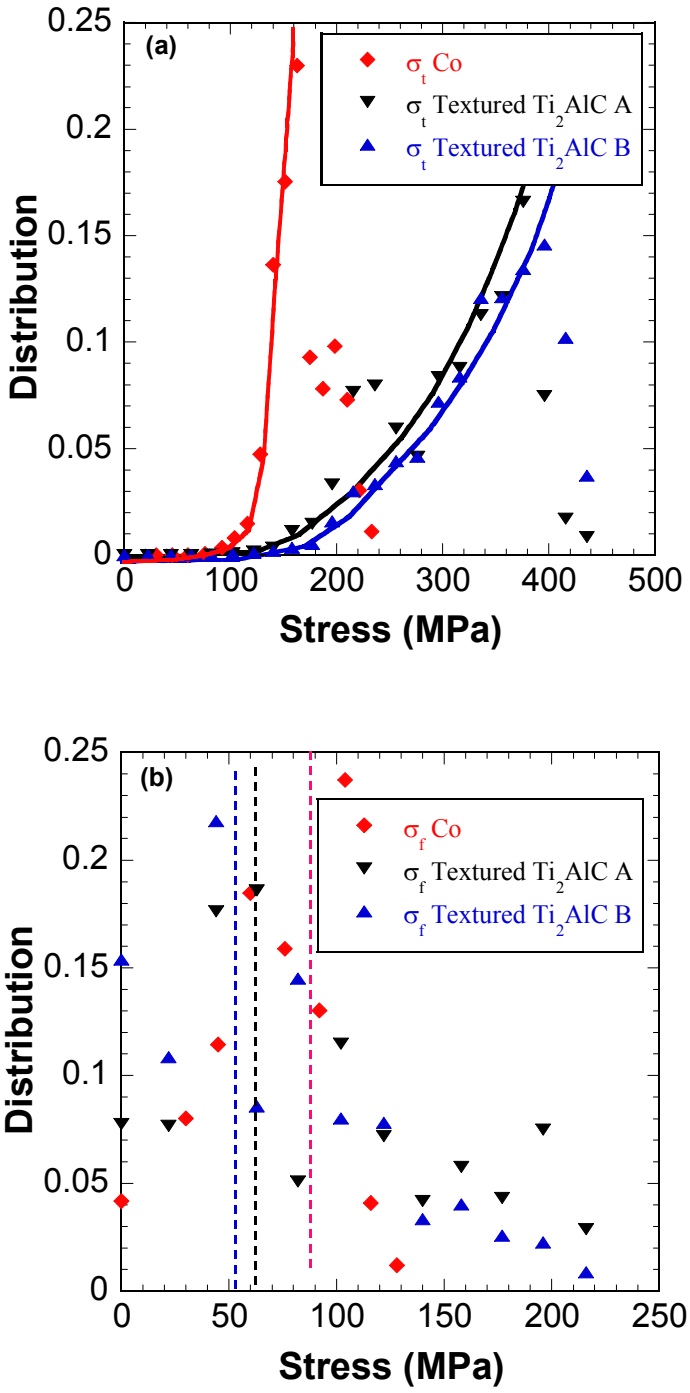

Figure 9.6: Calculated σ_t and σ_f of different KNE solids from P-M model

In a conclusion, the distribution of σ_t is highly related with the grain size distribution. The distribution of σ_t has a peak value at some stress. But both distributions reflect the fine grains' influence on the hysteresis. Coarse grains, despite the small number, play a more important role in the formation of the hysteretic loop. Therefore, P-M density of the simple hysteretic units is a better way to present the hysteretic properties of a KNE solids, though IKBs distribution are more accurate.

9.5.4 Strain from calculation of the P-M density

In this section, the strain of KNE solids after any stress history is calculated from P-M densities and compared with the experimental stress-strain curves. Figure 9.7 shows the results on 10% porous Ti_2AlC and Co. The agreement between the measured and predicted strains is excellent in both cases, further solidifying our important claim that all KNE solids can be described by the PM model. It follows that for any KNE solid, once a set of $\mu(\theta, \omega)$ is experimentally determined, the strain on this solid, for *any* deformation history, can be calculated from the P-M model. In other words, once the distribution of the hysteretic elements is known, one can determine any macroscopic stress-strain relationship.

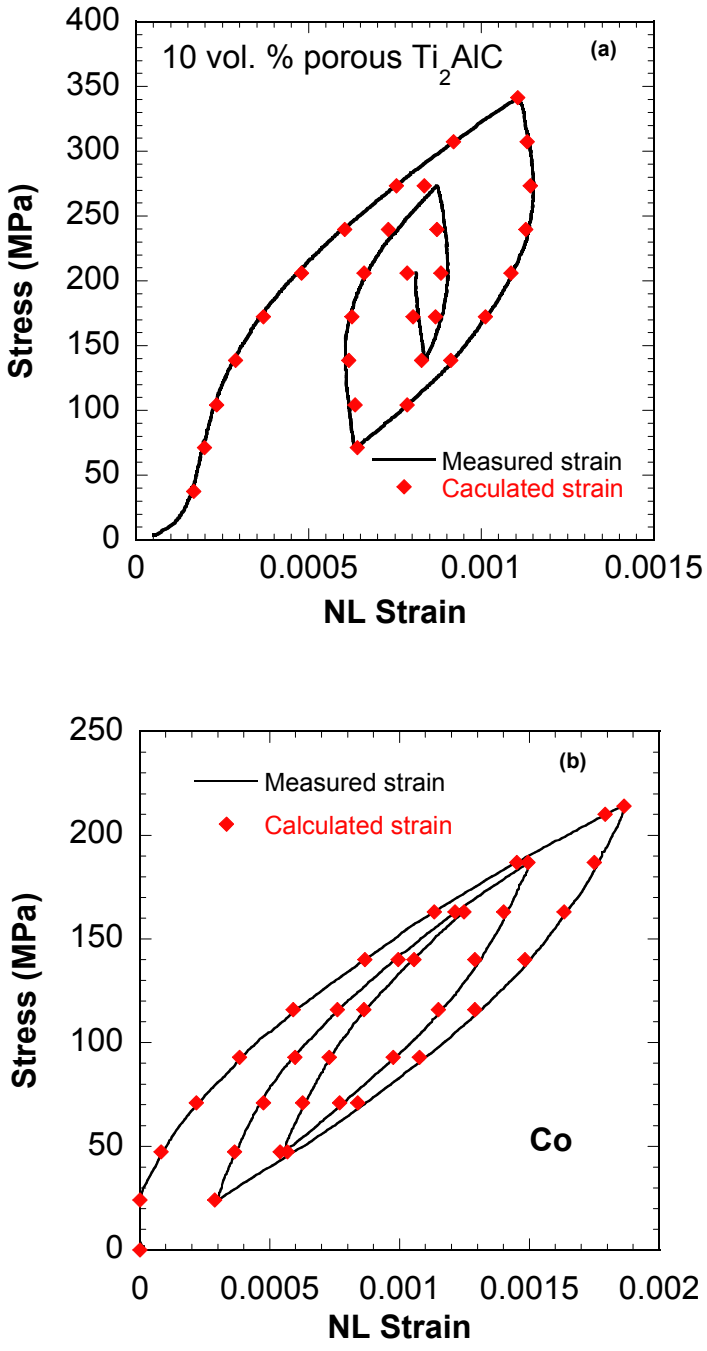

Figure 9.7: Calculated stress-strain curves from P-M density and experimental stress-strain curves for (a) 10% porous Ti_2AlC (b) Co

9.5.5 Impact

The conclusion that all KNE solids, in their ubiquity, can be described by the PM model has several important implications. First, one of the fundamental underlying assumptions of the PM model is that the behavior of the individual independent hysteretic units – IKBs in our case - is transferred to the behavior of the whole sample. It follows that despite the fact that many IKBs are expected to interact in various ways, one can conclude that they still behave as a collection of *independent* hysteretic units of the same type. Note this does not mean that the IKBs do not interact, instead it implies that whatever interactions, if any, occur, do not qualitatively change the behavior or shape of the underlying hysteretic units. Said otherwise, despite possible, but unlikely, interactions, each individual unit continues to display wiping-out and congruency which the entire system, therefore, inherits; a truly remarkable result.

The fact that key properties of the individual IKBs are preserved in the bulk polycrystalline KNE solids has several important practical implications. First, as we show, the constitutive equations are known and can be used to accurately predict the response of KNE solids to complicated stress histories. That this model can be used to describe the behavior of the over 50 MAX phases known, Co, Mg, Zr, and possibly their alloys - all technologically important solids - among many others is significant. At this junction it is important to point out that the PM model can only be used when the system is in a pure IKB regime. In some solids, at higher temperatures and/or stresses, the IKB's can be sundered and transform to mobile dislocation walls that in turn result in permanent deformation and creep. In those situations, the system can no longer be adequately described by the PM model since the response has an anelastic component [6, 52].

However, since in most cases, cycling to the same stress a few times, rids the system of non-IKB related dislocations [15, 163], the PM model would still be applicable as long as the maximum stress does not exceed the highest stress level experienced by the sample.

Second, the need to prove congruency and end-point memory for KNE solids, again in all their ubiquity, is no longer needed simplifying future experiments. This comment notwithstanding, it is hereby acknowledged that, we are just starting to understand KNE solids and it is possible, that further work shows a subcategory of KNE solids that may not exhibit congruency. We also acknowledge that while obtaining the distribution of hysteretic elements (Fig. 9.4 and Fig. 9.5) is straightforward, it is time consuming.

Third, we recently proposed to use KNE solids as stress/strain sensors where the stress history of the sample can be continually monitored [165]. Having a robust constitutive model for how these solids respond to stress is an important and necessary condition for implementation of this idea. The fact that in some cases, the response is a weak function of temperature – at least for Ti_3SiC_2 [6] – bodes well for the use of these solids as high temperature sensors. Along those lines it is important to note that for all materials tested there is a consistency in the form of the Preisach distribution function. Specifically, to a good approximation the curves of the Preisach function, over the plane of the upper and lower switching thresholds are nearly parallel to the $\theta = \omega$ line (Fig. 9.4a, b, c) for samples without texture. This implies that the Preisach distribution is mostly a function of the difference $\theta - \omega$, rather than on θ and ω separately, which in turn has important implications. Specifically, when the Preisach function depends only on $(\theta - \omega)$, it can shown that the inverse hysteresis operator - where stress is treated as the output and strain as the input - is also of the Preisach type. This is particularly convenient in some

potential applications, such as sensing or actuation, where both forward and inverse constitutive laws need to be computed quickly. This form of the Preisach function also demonstrates that parameterization of the model may be reduced ($\theta - \omega$ is a single parameter instead of two separate θ and ω parameters) suggesting that the irreversible behavior is dominated by frictional IKB growth and shrinkage processes, rather than their appearance and disappearance in agreement with our microscale modelling [163]. These comments notwithstanding, this hypothesis requires additional testing that we hope to perform in the near future.

Fourth, the results shown in Fig. 9.7, are invaluable to any modeling, especially finite element, of the deformation of the KNE solids. Our results can be used to either guide the modeling efforts or act as a check on their validity.

Fifth, based on our understanding of KNE solids they should not experience measurable fatigue. In fact, their behavior stabilizes in response to a cyclic load after a few cycles. This suggests that such materials are ideally suited for a situation where cyclic loading can affect longevity of engineering structures. Indeed preliminary results on Ti_3SiC_2 [6], and other KNE solids like C-plane sapphire [19], have been shown to produce the identical hysteretic stress-strain curves even when cycled under high stresses. For example we showed that sapphire single crystals can be repeatedly loaded, with a spherical indenter for up to 30 times to stresses greater than 20 GPa without evidence of creep or fatigue [8]. This distinction in important in differentiating between hysteresis that is not truly time or cycling invariant, such as microcracking for example, and what we are proposing here, where the cycles are truly repeatable and reproducible.

9.6 Summary

In summary, because the nonlinear hysteretic response of KNE solids exhibits wiping-out and congruency, the PM model is applicable. Once the distribution of independent hysteretic elements is determined, the model can be used to predict the response of these materials to complex stress histories remarkably well. Lastly we note that the conclusions of this work are valid *regardless* of the exact nature of the microscopic hysteretic units. Consequently, if further work, however unlikely, shows that the hysteretic units are *not* IKBs, but rather another micro-mechanism, the conclusions of this work do *not* change: KNE solids can be rigorously described by the PM model.

10. Summary, Conclusion and Future Work

10.1 Summary and conclusions

In this thesis, MAX phases and some hexagonal metals (Ti, Mg, Zn, Co etc) are classified as kinking nonlinear elastic solids. These solids exhibit large mechanical hysteresis due to the reproducible growth and shrinkage of incipient kink bands (IKBs). The sufficient condition to be a KNE solids is plastic anisotropy (c/a>1.4 for hexagonal structure). The stress-strain curves of KNE solids can be described by 4 parameters (stress σ, nonlinear strain ε_{NL}, stored nonlinear energy U_{NL} and dissipated energy W_d). A microscale model based on dislocation mechanisms is proposed to relate the four parameters. Based on the relations, some microscale parameters (IKB density, reversible dislocation density, IKB dimensions, critical resolved shear stress of dislocation gliding, etc.) can be calculated.

A number of solids are tested and their mechanical hysteresis is explained by this model. For Ti_2AlC, two samples (fully dense and 10% porous) with similar grain size are tested by uniaxial compression and nanoindentation. The dislocation model is effective for both these two methods and a wide stress range (200 MPa to 4GPa). For Ti_3SiC_2, five samples with different porosity (fully dense to 55% porous) and microstructure are tested. The nonlinear elastic response of the porous samples can be adequately described by dislocation model provided that the effective stress is plotted. The pores reduce the threshold stresses, a reduction that can be mostly accounted for by the concomitant reduction in shear moduli. The solid solutions Ti_3AlCN, $Ti_2Al(C_{0.5}N_{0.5})$ are tested also. The relation between KNE behavior and pre-strain history in KNE ceramic solids was observed and described. Solid solutions can definitely change the linear elastic

deformation and also can influence mechanical hysteresis by change shear modulus and grain size.

Metals with hexagonal structure (Mg, Ti, Zn, Co etc.) are KNE solids also. They show mechanical hysteresis. And the deformation can be explained by our dislocation model. In contrast to ceramics, predeformation history can seriously influence their mechanical hysteresis. For metals, grain size can influence their nonlinear deformation. However there is a grain size limit. Up this limit, grain size has little effect. The IKB mechanisms explained damping and micro-yielding of these metals also. IKBs constitute the last piece in the deformation-of-solids puzzle

A mathematic hysteretic model (P-M model) is used to calculate the strain of KNE solids from their stress history. Because the nonlinear hysteretic response of KNE solids exhibits wiping-out and congruency, the PM model is applicable. Once the distribution of independent hysteretic elements is determined, the model can be used to predict the response of these materials to complex stress histories remarkably well.

10.2 Future work

Based on the results at this thesis, we believe the following issues should be systematically investigated in order to supplement the understanding developed thus far on the mechanical hysteresis of KNE solids and the future application of this research.

1) Obtained the direct evidence that IKBs exist by neutron diffraction and/or in situ orientation image microscope (OIM). The neutron diffraction can measure any orientation changing in samples and OIM can measure the

orientation changing on the surface of samples. We hope can directly observe the grow and shrinkage of IKBs by these two methods.

2) Detect dislocations dynamics by mechanical deformation of KNE solids. Based on this research, dislocation density and critical resolved shear stress of dislocations on basal plane can be easily calculated from hysteretic loops of KNE solids. Further research can help us obtain more dislocation parameters more accurately from this simple method to better understand dislocations dynamics. The later is vital to fully understand the deformation of metals.

3) Continue working on KNE metals to research the influence of load rate on the value of Ω/b. And find the strain limit for transform IKBs to regular kink bands.

4) Develop high damping solids by controlling their microstructure. The research explained high damping capacity of some materials by kinking nonlinear elastic deformation and study the influence of microstructure parameters. Thereafter, it is promising to make materials with control damping capacity by changeing their microstructure.

5) Further research on the coupling of mechanical hysteresis with other hysteresis. For example, Co has mechanical hysteresis as a KNE solid. However, it is also has magnetic hysteresis. It is interesting to further research the mechanical hysteresis in magnetic environments and the coupling of these two hysteresis.

6) Research the mechanical hysteresis of KNE solid by acoustic emission (AE) and acoustic coupling test (ACT). AE and ACT are two methods to research dislocations. Combining these two methods with our previous work can help us better understand KNE solids.

7) Apply MAX phases as structure health sensors. This thesis explained the relation of dislocation density change of KNE solids with their strain. Combined other properties of MAX phases, it can detect and record the deformation history of large structures by recording MAX phases dislocation density changes.

List of References

[1] Barsoum MW, Ali M, El-Raghy T. Processing and Characterization of Ti_2AlC, Ti_2AlN, and$Ti_2AlC_{0.5}N_{0.5}$. Met. Mat. Trans. A 2000;31A:1857.

[2] Barsoum MW, Brodkin D, El-Raghy T. Layered Machinable Ceramics for High Temperature Applications. Scripta Materialia 1997;36:535.

[3] Barsoum MW, El-Raghy T. Synthesis and Characterization of a Remarkable Ceramic: Ti_3SiC_2. J. Amer. Cer. Soc 1996;79:1953.

[4] Barsoum MW, El-Raghy T. Room-Temperature Ductile Carbides. Met. Mat. Trans. A 1999;30A:363.

[5] Barsoum MW, Farber L, El-raghy T. Dislocations, Kink Bands, and Room-Temperature Plasticity of Ti_3SiC_2. Met. Mat. Trans. A 1999;30A:1727.

[6] Barsoum MW, Zhen T, Kalidindi SR, Radovic M, Murugaiah A. Fully reversible, dislocation-based compressive deformation of Ti_3SiC_2 to 1 GPa. Nat. Mate. 2003;2:107.

[7] Nickl JJ, Schweitzer KK, Luxenberg P. Gasphasenabscheidung im Systeme Ti-C-Si. J. Less Common Metals 1972;26:335?3.

[8] Goto T, Hirai T. CHEMICALLY VAPOR-DEPOSITED TI3SIC$_2$. Mater. Res. Bull. 1987;22:1195.

[9] Barsoum MW, El-Raghy T. The MAX phases: Unique new carbide and nitride materials - Ternary ceramics turn out to be surprisingly soft and machinable, yet also heat-tolerant, strong and lightweight. American Scientist 2001;89:334.

[10] Barsoum MW. The MN+1AXN Phases: a New Class of Solids; Thermodynamically Stable Nanolaminates. Prog. Solid State Chem. 2000;28:201.

[11] Pampuch P, Lis J, Stobierski L, Tymkiewicz M. Solid Combustion Synthesis of Ti_3SiC_2. J. Eur. Ceram. Soc. 1989;5:283.

[12] El-Raghy T, Barsoum MW, Zavaliangos A, Kalidindi SR. Processing and mechanical properties of Ti_3SiC_2: II, effect of grain size and deformation temperature. J. Amer. Cer. Soc 1999;82:2855.

[13] El-Raghy T, Zavaliangos A, Barsoum MW, Kalidindi SR. Damage Mechanisms Around Hardness Indentations in Ti_3SiC_2. J. Amer. Cer. Soc 1997;80:513.

[14] Zhou AG, Ganguly A, Barsoum MW. Kinking nonlinear elastic deformation of Ti_3AlC_2,Ti_2AlC, $Ti_3Al(C_{0.5},N_{0.5})_2$ and $Ti_2Al(C_{0.5},N_{0.5})$. In preparation.

[15] Zhou AG, Barsoum MW, Basu S, Kalidindi SR, El-Raghy T. Incipient and Regular Kink Bands in Dense and 10 vol.% Porous Ti2AlC. Acta Mat. 2006;54:1631.

[16] Barsoum MW, Murugaiah A, Kalidindi SR, Zhen T, Gogotsi Y. Kink bands, nonlinear elasticity and nanoindentations in graphite. Carbon 2004;42:1435.

[17] Zhen T. Compressive Behavior of Kinking Nonlinear Elastic Solids - Ti_3SiC_2, Graphite, Mica and BN. Department of Materials Science and Engineering, vol. PhD. Philadelphia, PA 19104: Drexel University, 2004.

[18] Basu S, Zhou A, Barsoum MW. On Nanoindentations, Kinking Nonlinear Elasticity of Mica Single Crystals and Their Geological Implications. Submitted.

[19] Basu S, Barsoum MW, Kalidindi SR. Sapphire: A kinking nonlinear elastic solid. J. App. Phys. 2006;99:063501.

[20] Basu S, Barsoum MW. Deformation micromechanisms of ZnO single crystals as determined from spherical nanoindentation stress-strain curves. Journal of Materials Research 2007;22:2470.

[21] Basu S, Barsoum MW, Williams AD, Moustakas TD. Spherical nanoindentation and deformation mechanisms in freestanding GaN films. Journal of Applied Physics 2007;101.

[22] Basu S, Zhou A, Barsoum MW. Reversible Dislocation Motion under Contact Loading in LiNbO3 Single Crystal. Journal of Materials Research Accepted.

[23] Zhou AG, Basu S, Barsoum MW. Kinking nonlinear elasticity, damping and microyielding of hexagonal close-packed metals. Acta Materialia 2008;56:60.

[24] Zhou AG, Barsoum MW, Basu S, Kalidindi SR, El-Raghy T. Incipient and Regular Kink Bands in Dense and 10 vol.% Porous Ti2AlC. Acta Mat. 2006;54:1631.

[25] Barsoum MW, Zhen T, Zhou A, Basu S, Kalidindi SR. Microscale modeling of kinking nonlinear elastic solids. Phys. Rev. B 2005;71:134101.

[26] Orowan E. A type of plastic deformation new in metals. Nature 1942;149:643.

[27] Frank FC, Stroh AN. On The Theory of Kinking. Proc. Phys. Soc., vol. 65. LONDON, 1952. p.811.

[28] Hess JB, Barrett CS. Structure and nature of kink bands in zinc. Trans. AIME 1949;185:599?05.

[29] Barsoum MW, Murugaiah A, Kalidindi SR, Zhen T. Kinking Nonlinear Elastic Solids, Nanoindentations, and Geology. Phys. Rev. Lett. 2004;92:255508.

[30] Murugaiah A, Barsoum MW, Kalidindi SR, Zhen T. Spherical nanoindentations and kink bands in Ti_3SiC_2. J. Mater. Res. 2004;19:1139.

[31] Barsoum MW, Radovic M, Zhen T, Finkel P, Kalidindi SR. Dynamic elastic hysteretic solids and dislocations. Phys. Rev. Lett. 2005;94:085501.

[32] Farber L, Barsoum MW, Zavaliangos A, El-Raghy T, Levin I. Dislocations and stacking faults in Ti3SiC2. J. Amer. Cer. Soc 1998;8:1677.

[33] Farber L, Levin I, Barsoum MW. High-resolution transmission electron microscopy study of a low-angle boundary in plastically deformed Ti_3SiC_2. Phil. Mag. Lett. 1999;79:163.

[34] Anderson TB. Kink-bands and related geological structures. Nature 1964;202:272.

[35] Paterson MS, Weiss LE. Experimental Folding in Rocks. Nature 1962;195:1046.

[36] Granato A, Lucke K. Theory of mechanical damping due to dislocations. J. App. Phys. 1956;27:583.

[37] Addessio LB, Cerreta EK, Gray GT. Mechanical behavior of zirconium and hafnium in tension and compression. Metallurgical and Materials Transactions a-Physical Metallurgy and Materials Science 2005;36A:2893.

[38] Roberts E, Partridge PG. The accommodation around {1012}<1011> twins in magnesium. Acta Met. 1966;14:513.

[39] Gilman JJ. Mechanism of ortho kink-band formation in compressed zinc monocrystals. Transactions AIME 1954;200.

[40] Burke EC, W. R. Hibbard J. Plastic deformation of magnesium single crystals. Tran. AIME 1952;194:295.

[41] Vaidya S, Mahajan S. Accommodation and formation of {112-1} twins in Co single crystals. Acta Metallurgica 1980;28:1123.

[42] Rosi FD. Mechanism of Plastic Flow in Ti: Manifestations and Dynamics of Glide. Trans. AIME 1954;200:58.

[43] Hauser FE, Landon PR, Dorn JE. Deformation and fracture mechanisms of polycrystalline magnesium at low temperatures. 1955. p.19.

[44] Gharghouri MA, Weatherly GC, Embury JD, Root J. Study of the mechanical properties of Mg-7.7at.% Al by in-situ neutron diffraction. Philosophical Magazine a-Physics of Condensed Matter Structure Defects and Mechanical Properties 1999;79:1671.

[45] Caceres CH, Sumitomo T, Veidt M. Presudoelastic behaviour of cast magnesium AZ91 alloy under cyclic loading-unloading. Acta Mat. 2003;51:6211.

[46] Barnett MR, Keshavarz Z, Beer AG, Atwell D. Influence of grain size on the compressive deformation of wrought Mg-3Al-1Zn. Acta Materialia 2004;52:5093.

[47] Chung SW, Watanabe H, Kim W-J, Higashi K. Creep deformation mechanisms in coarse-grained solid solution Mg alloys. Materials Transactions 2004;45:1266.

[48] Ono N, Nowak R, Miura S. Effect of deformation temperature on Hall-Petch relationship registered for polycrystalline magnesium. Materials Letters 2004;58:39.

[49] Agnew SR, Mehrotra P, Lillo TM, Stoica GM, Liaw PK. Texture evolution of five wrought magnesium alloys during route A equal channel angular extrusion: Experiments and simulations. Acta Materialia 2005;53:3135.

[50] Agnew SR, Brown DW, Tome CN. Validating a polycrystal model for the elastoplastic response of magnesium alloy AZ31 using in situ neutron diffraction. Acta Materialia 2006;54:4841.

[51] Hull D. Introduction to Dislocation. Oxford: Pergamon Press, 1965.

[52] Zhen T, Barsoum MW, Kalidindi SR, Radovic M, Sun ZM, El-Raghy T. Compressive creep of fine and coarse-grained T_3SiC_2 in air in the 1100-1300 degrees C temperature range. Acta Materialia 2005;53:4963.

[53] Taylor GI. Plastic strain in metals. J. Inst. Met. 1938;62:307.

[54] Wang XH, Zhou YC. High-temperature oxidation behavior of Ti_2AlC in air. Oxid. Met. 2003;59:303.

[55] Sundberg M, Malmqvist G, Magnusson A, El-Raghy T. Alumina forming high temperature silicides and carbides. Ceramics Intenational 2004;30:1899.

[56] Sun ZM, Murugaiah A, Zhen T, Zhou A, Barsoum MW. Microstructure and Mechanical Properties of Porous Ti_3SiC_2. Acta Mat. 2005;53:4359.

[57] Hettinger JD, Lofland SE, Finkel P, Meehan T, Palma J, Harrell K, Gupta S, Ganguly A, El-Raghy T, Barsoum MW. Electrical transport, thermal transport, and elastic properties of M_2AlC (M= Ti, Cr, Nb, and V). Physical Review B 2005;72:115120.

[58] Kooi BJ, Poppen RJ, Carvalho NJM, De Hosson JTM, Barsoum MW. Ti_3SiC_2: A damage tolerant ceramic studied with nanoindentations and transmission electron microscopy. Acta Mat. 2003;51:2895.

[59] Barsoum MW, Zhen T, Kalidindi SR, Radovic M, Murugahiah A. Fully Reversible, Dislocation-Based Compressive Deformation of Ti_3SiC_2 to 1 GPa. Nature Materials 2003;2:107.

[60] Barsoum MW, El-Raghy T. Room Temperature Ductile Carbides. Metallurgical and Materials Trans. 1999;30A:363.

[61] Murugaiah A, Barsoum MW, Kalidindi SR, Zhen T. Spherical Nanoindentations in Ti_3SiC_2. J. Mater. Res. 2004;19:1139.

[62] Sun Z-M, Murugaiah A, Zhen T, Zhou A, Barsoum MW. Microstructure and Mechanical Properties of Porous Ti_3SiC_2. Acta Mater. 2005;53:4359.

[63] Gibson LJ, Ashby MF. Cellular Solids, Structure and Properties. Oxford: Pregamon Press, 1988.

[64] Duval P, Ashby MF, Andermant I. Rate-Controlling Processes in the Creep of Polycrystalline Ice. J. Phys. Chem. 1983; **87**: 4066.

[65] Barsoum MW, El-Raghy T. Synthesis and Characterization of a Remarkable Ceramic: Ti_3SiC_2. J. Amer. Cer. Soc. 1996;79:1953.

[66] El-Raghy T, Barsoum MW. Processing and mechanical properties of Ti_3SiC_2: part I: reaction path and microstructure evolution. J. Amer. Cer. Soc 1999;82:2849.

[67] Murugaiah A, Souchet A, El-Raghy T, Radovic M, Barsoum MW. Tape Casting, Pressureless Sintering and Grain Growth in Ti_3SiC_2 Compacts. J. Amer. Cer. Soc. 2004;**87**:550.

[68] Ganguly A, Barsoum MW, Doherty RD. A Study of Ti_3SiC_2/Ti_3GeC_2 and Ti_2AlC/Nb_2AlC Diffusion Couples. Sub. for pub.

[69] Finkel P, Barsoum MW, El-Raghy T. Low Temperature Dependencies of the Elastic Properties of Ti_4AlN_3 and $Ti_3Al_{1.1}C_{1.8}$ and Ti_3SiC_2. J. Appl. Phys. 2000;87:1701.

[70] Barsoum MW, Zhen T, Zhou A, Basu S, Kalidindi SR. Microscale Modeling of Kinking Nonlinear Elastic Solids. Phys. Rev. B. 2005;71:134101.

[71] El-Raghy T, Barsoum MW. Processing and mechanical properties of Ti_3SiC_2: part I: reaction path and microstructure evolution. . J. Amer. Cer. Soc. 1999;82: 2849.

[72] Fraczkiewicz M, Zhou AG, Barsoum MW. Mechanical Damping in Porous Ti_3SiC_2. Acta Mat. 2006;54:5261.

[73] Manoun B, Saxena SK, Hug G, Ganguly A, Barsoum MW. Synthesis and compressibility of $Ti_3(Al,Sn)C_2$ and $Ti_3Al(C_{0.5}N_{0.5})_2$. Submitted.

[74] Ganguly A. Synthesis and Characterization of Solid Solutions of $M_{(N+1)}AX_N$ Phases. Department of Materials Science and Engineering, vol. PhD. Philadelphia: Drexel University, 2006.

[75] Finkel P, Barsoum MW, El-Raghy T. Low Temperature Dependencies of the Elastic Properties of Ti_4AlN_3 and $Ti_3Al_{1.1}C_{1.8}$ and Ti_3SiC_2. J. App. Phys. 2000;87:1701.

[76] Basu S, Barsoum MW. Deformation Micromechanisms of ZnO Single Crystals as Determined From Spherical Nanoindentation Stress-Strain Curves. J. Mater. Res. 2007;22:2470.

[77] Basu S, Zhou A, Barsoum MW. Reversible Dislocation Motion under Contact Loading in LiNbO3 Single Crystal. Submitted.

[78] Zhou AG, Barsoum MW. Nonlinear deformation of Mg. Acta Mat.;Under review.

[79] Yoo MH, Morris JR, Ho KM, Agnew SR. Nonbasal deformation modes of HCP metals and alloys: Role of dislocation source and mobility. Metallurgical And Materials Transactions A-Physical Metallurgy And Materials Science 2002;33:813.

[80] Yoo MH. Slip, Twinning, And Fracture In Hexagonal Close-Packed Metals. Metallurgical Transactions A-Physical Metallurgy And Materials Science 1981;12:409.

[81] Yoo MH, Wei CT. Slip modes of hexagonal-close-packed metals. J. App. Phys. 1967;38:4317.

[82] Rosi FD, Dube CA, Alexander BH. Mechanism of plastic flow in titanium - determination of slip and twinning elements. Trans. AIME 1953:257.

[83] Reed-Hill RE. Role of deformation twinning in the plastic deformation of a polycrystalline anisotropic metal. Met. Soc. AIME conf., vol. 25. Gainesville, FL: Gordon and breach science publishers, New York, 1964. p.295.

[84] Lazan B. Damping of materials and members in structural mechanics. Oxford, New York: Pergamon Press, 1968.

[85] Roberts JM, Brown N. Microstrain in zinc single crystals. Tran. Meta. Soc. AIME 1960;218:454.

[86] Hu XS, Wu K, Zheng MY. Effect of heat treatment on the stability of damping capacity in hypoeutectic Mg-Si alloy. Scri. Mater. 2006;54:1639.

[87] Salem AA, Kalidindi SR, Doherty RD. Strain hardening of titanium: role of deformation twinning. Acta Materialia 2003;51:4225.

[88] Betteridge W. The properties of metallic cobalt. Progress in Materials Science 1980;24:51.

[89] Reed-Hill RE, Dahlberg EP, W. A. Slippy J. Some anelastic effects in Zirconium at room temperature resulting from prestrain at 77^oK. Trans. AIME 1965;233:1766.

[90] Zhen T, Barsoum MW, Kalidindi SR. Effects of temperature, strain rate and grain size on the compressive properties of Ti_3SiC_2. Acta Mat. 2005;53:4163.

[91] Yoshinaga H, Obara T, Morozumi S. Twinning deformation in Magnesium compressed along the C-axis. Mater. Sci. Eng. 1973;12:255.

[92] Levine ED. Deformation mechanisms in titanium at low temperatures. Tran. Meta. Soc. AIME 1966;236:1558.

[93] Shechtman D, Brandon DG. Orientation dependent slip in polycrystalline titanium. J. Mat. Sci. 1973;8:1233.

[94] Seeger A, Kronmuller H, Boser O, Rapp M. Plastic deformation of Cobalt single crystals. Physica Status Solidi 1963;3:1107.

[95] Buckley DH, Johnson RL. Relation of lattice parameters to friction characteristics of Beryllium, Hafnium, Zirconium, and other hexagonal metals in vacuum. vol. TN D-2670: NASA tech. note, 1965. p.4.

[96] Davis KG, Teghtsoonian E. Plastic deformation in cobalt crystals. Transactions of the Metallurgical Society of AIME 1963;227:762.

[97] Hauser FE, Landon PR, Dorn JE. Deformation and Fracture Mechanisms of Polycrystalline Magnesium at Low Temperatures. Trans. AIME 1956;48:986.

[98] Martin JL, Reed-Hill RE. A study of basal slip kink bands in polycrystalline zirconium. Tran. Meta. Soc. AIME 1964;230:780.

[99] Freise EJ, Kelly A. Twinning in Graphite. Proc. Phys. Soc. A 1961;264:269.

[100] Bullough R. Deformation Twinning in the Diamond Structure. Proceedings of the Royal Society of London. Series A, Mathematical and Physical Sciences 1957;241:568.

[101] Bakarian PW, Mathewson CH. Slip and twinning in magnesium single crystals at elevated temperatures. American Institute of Mining and Metallurgical Engineers, New York, NY, United States, 1943. p.28.

[102] Burke EC, Hibbard JWR. Plastic deformation of magnesium single crystals. American Institute of Mining and Metallurgical Engineers -- Journal of Metals 1952;4:295.

[103] Conrad H, Robertson WD. Effect of temperature on flow stress and strain-hardening coefficient of magnesium single crystals. Journal of Metals 1957;9:503.

[104] Roberts JM, Hartman DE. The temperature dependence of the microyield points in prestrained magnesium single crystals. Tran. AIME 1964;230:1125.

[105] Akhtar A, Teghtsoonian E. Solid solution strengthening of magnesium single crystals. II. The effect of solute on the ease of prismatic slip. Acta Metallurgica 1969;17:1351.

[106] Akhtar A, Teghtsoonian E. Solid solution strengthening of magnesium single crystals. I. Alloying behaviour in basal slip. Acta Metallurgica 1969;17:1339.

[107] Sheely WF, Nash RR. Mechanical properties of magnesium monocrystals. Metallurgical Society of American Institute of Mining, Metallurgical and Petroleum Engineers -- Transactions 1960;218:416.

[108] Partridge PG, Roberts E. The microhardness anisotropy of magnesium and zinc single crystals. Journal of the Institute of Metals 1963;92:50.

[109] Hauser FE, Starr CD, Tietz L, Dorn JE. Deformation mechanisms in polycrystalline aggregates of magnesium. Trans. Am. Soc. Metals. 1955;47:102.

[110] Koike J, Kobayashi T, Mukai T, Watanabe H, Suzuki M, Maruyama K, Higashi K. The activity of non-basal slip systems and dynamic recovery at room temperature in fine-grained AZ31B magnesium alloys. Acta Materialia 2003;51:2055.

[111] Agnew SR, Brown DW, Vogel SC, Holden TM. In-situ measurement of internal strain evolution during deformation dominated by mechanical twinning. Ecrs 6: Proceedings of the 6th European Conference on Residual Stresses, vol. 404-4. Zurich-Uetikon: Trans Tech Publications Ltd, 2002. p.747.

[112] Brown DW, Agnew SR, Bourke MAM, Holden TM, Vogel SC, Tome CN. Internal strain and texture evolution during deformation twinning in magnesium. Materials Science and Engineering a-Structural Materials Properties Microstructure and Processing 2005;399:1.

[113] Partridge PG, Roberts E. The formation and behaviour of incoherent twin boundaries in hexagonal metals. Acta Metallurgica 1964;12:1205.

[114] Reed-Hill RE, Robertson WD. Additional modes of deformation twinning in magnesium. Acta Mat. 1957;5:717.

[115] Jillson DC. An Experimental Survey of Deformation and Annealing Processes in Zinc. Transactions AIME 1950;188:1009.

[116] Moore AJW. Accommodation Kinking Associated with the Twinning of Zinc. Proc. Phys. Soc., vol. 65, 1952. p.956.

[117] Mann GE, Sumitomo T, Caceres CH, Griffiths JR. Reversible plastic strain during cyclic loading-unloading of Mg and Mg-Zn alloys. Materials Science and Engineering a-Structural Materials Properties Microstructure and Processing 2007;456:138.

[118] Agnew SR, Horton JA, Yoo MH. Transmission electron microscopy investigation of <c+a> dislocations in Mg and α-solid solution Mg-Li alloys. Met. Mat. Tran. A 2002;33A:851.

[119] Couret A, Caillard D. An in situ study of prismatic glide in magnesium. I. The rate controlling mechanism. Acta Metallurgica 1985;33:1447.

[120] Bechade J-L. Post-Creep Ti3SiC2 Microstructure Studied by Electron-Backscattered Diffraction and Transmission Electron Microscopy. submitted.

[121] Mann G, Griffiths JR, Caceres CH. Hall-Petch parameters in tension and compression in cast Mg-2Zn alloys. Journal of Alloys and Compounds 2004;378:188.

[122] Agnew SR, Tome CN, Brown DW, Holden TM, Vogel SC. Study of slip mechanisms in a magnesium alloy by neutron diffraction and modeling. Scripta Materialia 2003;48:1003.

[123] Brown DW, Jain A, Agnew SR, Clausen B. Twinning and Detwinning During Cyclic Deformation of Mg Alloy AZ31B. Materials Science Forum 2007;539-543:3407.

[124] Drits ME, Rokhlin LL, Sheredin VV, Shul'ga YN. Magnesium alloys with high damping capacity. Metal science and heat treatment 1970;11:939.

[125] Riehemann W, El-Al FA. Influence of ageing on the internal friction of magnesium. Journal of Alloys and Compounds 2000;310:127.

[126] Watanabe H, Mukai T, Sugioka M, Ishikawa K. Elastic and damping properties from room temperature to 673 K in an AZ31 magnesium alloy. Scripta Materialia 2004;51:291.

[127] Barsoum MW, Farber L. Room Temperature De-Intercalation and Self-extrusion of Ga from Cr_2GaN. Science 1999;284:937.

[128] Bell RL, Cahn RW. The Dynamics of Twinning and the Interrelation of Slip and Twinning in Zinc Crystals. Proceedings of the Royal Society of London. Series A, 1957. p.494.

[129] Brown DW, Agnew SR, Abeln SP, Blumenthal WR, Bourke MAM, Mataya MC, Tome CN, Vogel SC. The role of texture, temperature, and strain rate in the activity of deformation twinning. Icotom 14: Textures of Materials, Pts 1and 2, vol. 495-497. 2005. p.1037.

[130] Vander Voort GF. Examination of some grain size measurement problems. In: Voort GFV, Warmuth FJ, Purdy SM, Szirmae A, editors. Metallography: Past, Present, and Future (75th anniversary volume). Philadelphia: ASTM, 1993. p.266.

[131] Zhou AG, Basu B, Barsoum MW. Kinking Nonlinear Elasticity, Damping and Microyielding of Hexagonal Close-Packed Metals. Acta Mat. 2008;56:60.

[132] Brown DW, Bourke MAM, Dunn PS, Field RD, Stout MG, Thoma DJ. Uniaxial tensile deformation of uranium 6 wt pct niobium: A neutron diffraction study of deformation twinning. Metall. Mater. Trans. A-Phys. Metall. Mater. Sci. 2001;32:2219.

[133] Salem A, Kalidindi S, Doherty R, Semiatin S. Strain hardening due to deformation twinning in α-titanium: Mechanisms. Met. Mat. Trans. A 2006;37:259.

[134] Agnew SR, Yoo MH, Tome CN. Application of texture simulation to understanding mechanical behavior of Mg and solid solution alloys containing Li or Y. Acta Materialia 2001;49:4277.

[135] Wonsiewicz BC, Backofen WA. Plasticity of magnesium crystals. TMS-AIME 1967;239:1422.

[136] Koike J. Enhanced deformation mechanisms by anisotropic plasticity on ploycrystalline Mg alloys at room temperature. Met. Mat. Tran. A 2005;36A:1689.

[137] Agnew SR, Horton JA, Lillo TM, Brown DW. Enhanced ductility in strongly textured magnesium produced by equal channel angular processing. Scripta Materialia 2004;50:377.

[138] Lou XY, Li M, Boger RK, Agnew SR, Wagoner RH. Hardening evolution of AZ31B Mg sheet. International Journal of Plasticity 2007;23:44.

[139] Barnett MR, Keshavarz Z, Ma X. A semianalytical Sachs model for the flow stress of a magnesium alloy. Metall. Mater. Trans. A-Phys. Metall. Mater. Sci. 2006;37A:2283.

[140] Kalidindi SR, Zhen T, Barsoum MW. Macroscale constitutive modeling of kinking nonlinear elastic solids Mater. Sci. Eng. A 2006;418:95.

[141] Barsoum MW, Zhou AG, Brown DW, Vogel SC. in preparation.

[142] Li Y, Enoki M. Deformation and anelastic recovery of pure magnesium and AZ31B alloy investigated by AE. Materials Transactions 2007;48:2343.

[143] Freise EJ, Kelly A. Twinning in graphite. Proc. Roy. Soc. A 1961;264:269.

[144] Wagoner RH, Lou XY, Li M, Agnew SR. Forming behavior of magnesium sheet. Journal of Materials Processing Technology 2006;177:483.

[145] Yang XY, Miura HM, Sakai T. Dynamic evolution of new grains in magnesium alloy AZ31 during hot deformation. Materials Transactions 2003;44:197.

[146] Amini S, Zhou A, Gupta S, DeVillier A, Finkel P, Barsoum M. Synthesis and Elastic and Mechanical Properties of Cr2GeC. Submitted.

[147] Brown DW, Abeln SP, Blumenthal WR, Bourke MAM, Mataya MC, Tome CN. Development of crystallographic texture during high rate deformation of rolled and hot-pressed beryllium. Metall. Mater. Trans. A-Phys. Metall. Mater. Sci. 2005;36A:929.

[148] Radovic M, Barsoum MW, El-Raghy T, Wiederhorn SM. Tensile creep of coarse-grained Ti3SiC2 in the 1000-1200 degrees C temperature range. Journal of Alloys and Compounds 2003;361:299.

[149] Barsoum MW, Radovic M, Finkel P, El-Raghy T. Ti3SiC2 and ice. Applied Physics Letters 2001;79:479.

[150] Duval P, Ashby MF, Anderman I. RATE-CONTROLLING PROCESSES IN THE CREEP OF POLYCRYSTALLINE ICE. Journal of Physical Chemistry 1983;87:4066.

[151] Davis KG, Teghtsoonian E. Deformation twins in cobalt. Acta Metallurgica 1962;10:1189.

[152] Vaidya S, Mahahan S, Preece CM. ROLE OF TWINNING IN THE CAVITATION EROSION OF COBALT SINGLE CRYSTALS. Metallurgical Transactions A (Physical Metallurgy and Materials Science) 1980;11A:1139.

[153] Street R. The variation with magnetization of Young's modulus for cobalt. Proceedings of the Physical Society 1948;60:236.

[154] Toledano P, Krexner G, Prem M, Weber HP, Dmitriev VP. Theory of the martensitic transformation in cobalt. Physical Review B 2001;64:144104.

[155] Guyer RA, McCall KR, Boitnott GN, Hilbert LB, Jr., Plona TJ. Quantitative implementation of Preisach-Mayergoyz space to find static and dynamic elastic moduli in rock. Journal of Geophysical Research 1997;102:5281.

[156] McCall KR, Guyer RA. Equation of state and wave propagation in hysteretic nonlinear elastic materials. Journal of Geophysical Research 1994;99:23887.

[157] Guyer RA, Johnson PA. Nonlinear mesoscopic elasticity: Evidence for a new class of materials. Physics Today 1999;52:30.

[158] Preisach F. Magnetic after-effect. Zeitschrift fur Physik 1935;94:277.

[159] Mayergoyz I, editor Mathematical models of hysteresis and their applications: Elsevier, 2003.

[160] Mayergoyz ID. Mathematical Models of Hysteresis. Physical Review Letters 1986;56:1518.

[161] Guyer RA, McCall KR, Boitnott GN. Hysteresis, Discrete Memory, and Nonlinear Wave Propagation in Rock: A New Paradigm. Physical Review Letters 1995;74:3491.

[162] Ortin J. Preisach modeling of hysteresis for a pseudoelastic Cu-Zn-Al single crystal. Journal of Applied Physics 1992;71:1454.

[163] Zhou AG, Basu B, Barsoum MW. Kinking Nonlinear Elasticity, Damping and Microyielding of Hexagonal Close-Packed Metals. Acta Mat.;Accepted.

[164] Amini S, Barsoum MW. Synthesis and mechanical properties of oriented MAX Phases. In preparation.

[165] Basu S, Zhou A, Finkel P, Barsoum MW. A method for structural health monitoring using a smart sensor system. USA, Pending.

[166] Basu S, Moseson A, Barsoum MW. On the determination of spherical nanoindentation stress-strain curves. Journal of Materials Research 2006;21:2628.

[167] Fischer-Cripps AC. A review of analysis methods for sub-micron indentation testing. Vacuum 2000;58:569.

[168] Zhen T. Compressive Behavior of Kinking Nonlinear Elastic Solids - Ti3SiC2, Graphite, Mica and BN. Department of Materials Science and Engineering. Philadelphia: Drexel University, 2004. p.132.

[169] Oliver WC, Pharr GM. Measurement of hardness and elastic modulus by instrumented indentation: Advances in understanding and refinements to methodology. J. Mat. Res. 2004;19:3.

Appendix A: Stress-Strain Curve of Nanoindentation

Nanoindentation measures a sample's load-displacement curves. In order to compare with uniaxial compression, the load-displacement curves need be transformed to stress-strain curves by a method development by our group [19-22, 166]. Indentation stress (mean indentation pressure) and indentation strain are defined here as $\frac{P}{\pi a^2}$ and $\frac{a}{R}$ respectively, where P is the applied load, a is the corresponding radius of the indentation in the contact plane, and R is the radius of indenter (Fig. 11.1) [167].

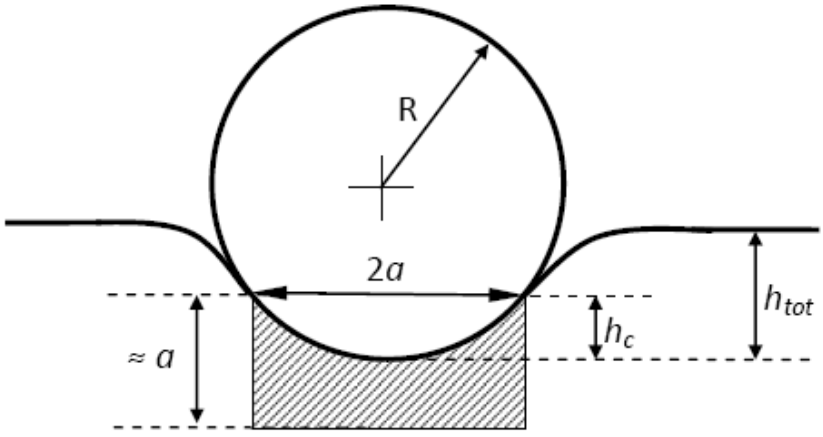

Figure A0.1: Schematic diagram of indentation with a spherical indenter. Shaded area is the material disturbed by the indenter.

Here we are only comparing the energy dissipated in a loading-unloading cycle measured from the experiment with the corresponding predictions from our micromechanical models. The approach used here amounts to taking the energy dissipated in the measured load-displacement curve in the indentation experiment and dividing it by an equivalent volume of the material under the indenter that is experiencing much of the deformation imposed in the indentation. The normalization by volume is essential because the model described in Chapter 2 predicts dissipation energy per unit volume. The approach used here is tantamount to idealizing the affected volume under a spherical indenter to a cylinder of radius *a* and height *a* (see Fig. 11.1).

For Hertzian contact, the well known stress-strain relationship [167] can be recast as:

$$\frac{P}{\pi a^2} = K(\frac{a}{R}), \qquad K = \frac{4}{3\pi} E^*, \qquad \frac{1}{E^*} = \frac{1-\nu_s^2}{E_s} + \frac{1-\nu_i^2}{E_i} \qquad (11.1)$$

where E_s and ν_s denote the sample's Young modulus and Poisson's ratio and E_i and ν_i denote the indenter's Young modulus (1140GPa) and Poisson's ratio (0.07) [166]. *K* is the linear response of the sample which is the equivalent to Young's modulus E in a uniaxial compression test. Given that the Young's modulus of Ti_2AlC is 278 GPa and Poisson's ration is 0.17 [168], it follows that E^*=229GPa and *K* = 98 GPa, which is identical to the slope of the unloading curves shown in Fig. 3.6b.

With the CSM (Continuous Stiffness Measurement) option – in addition to P and the total penetration depth, h_{tot} – the harmonic contact stiffness S_H is obtained directly. Consequently, *a* was assumed [169]:

$$h_c = h_{tot} - 0.75\frac{P}{S_H}, \quad \text{and} \quad a = \sqrt{2Rh_c - h_c^2} \tag{11.2}$$

The definitions of h_c and h_{tot} are expressed in Fig. 11.1. After a was obtained, the stress ($\frac{P}{\pi a^2}$) and strain ($\frac{a}{R}$) in Eq. 11.1 are calculated and plotted.

Appendix B: Obtain KNE Parameters from Literatures

The KNE parameters of Gharghouri et al.'s paper [44] were obtained from the unloading curves of that paper's Fig. 4. A loading curve was generated - assuming the loading and unloading curves were symmetric - which is not a bad assumption. The parameters of the Mann et al. [117] and Caceres et al. [45] paper were directly obtained from the hysteresis loops shown in their papers. The figure numbers listed in Table 7.4 refer to the figures in the original papers.

Since these authors did not report nested loops, the following procedure was adopted to obtain the pertinent parameters (σ, ε_{NL}, W_d and U_{NL}). The first step was to draw a line bisecting the loop in half. Another straight line with a slope of 42 GPa was then drawn and the various parameters determined. For stresses lower than the maximum stress of any of the published loops, the line bisecting the latter was pivoted and rotated counterclockwise – i.e. towards the linear elastic line - and the various parameters determined. The maximum stress after the rotation was the point of intersection of the rotated line with the loop. In other words, a universal loading trajectory and symmetrical loops were assumed, which based on our experiment hysteretic loops in this thesis.

Vita

Aiguo Zhou

DOB: 10/22/1975

Education
Ph.D. in Material Engineering, Drexel University, Philadelphia, PA, Jun 2008.
M.S. in Materials Science, Tsinghua University, Beijing, China, Jul 2003.
B.S. in Material Engineering, Wuhan University of Technology, Wuhan, China, Jul 1997

Experience
Teacher in Materials Engineering, Henan Polytechnic University, Jiaozuo, China, Jul 1997-Sep 2000

Refereed Publications
Total: 14 published and 4 submitted or in preparation; first author: 9; second author: 5; corresponding author: 5; times cited according to ISI: 91

Presentations and Patent
4 oral presentations in international conferences, 1 provisional patent filed.